

Systems-level modeling and analysis of cell cycle and metabolic network to study proliferative diseases

Thesis submitted in partial fulfillment of the requirements for the degree of

Doctor of Philosophy

in BIOINFORMATICS

by

NISHTHA PANDEY

20162146

nishtha.pandey@research.iiit.ac.in



International Institute of Information Technology, Hyderabad

(Deemed to be University)

Hyderabad - 500 032, INDIA

February, 2023

Copyright © Nishtha Pandey, 2023
All Rights Reserved

International Institute of Information Technology

Hyderabad, India

CERTIFICATE

It is certified that the work contained in this thesis, titled “Systems-level modeling and analysis of cell cycle and metabolic network to study proliferative diseases” by Nishtha Pandey, has been carried out at the Center for Computational Natural Sciences and Bioinformatics, International Institute of Information Technology, Hyderabad, India, under my supervision and is not submitted elsewhere for a degree.

Date

Advisor: Dr. Vinod P. K.

To Mummy, Papa, Didi, Jiju and Babu for being my pillars of strength

ACKNOWLEDGMENTS

गुरुर्ब्रह्मा गुरुर्विष्णुः गुरुर्देवो महेश्वरः ।

गुरुर्साक्षात् परब्रह्म तस्मै श्री गुरवे नमः ॥

First and foremost, I thank all my teachers, starting from my mother, who gave me अक्षर ज्ञान, to my Ph.D. supervisor, Dr. Vinod P.K., who taught me what research truly means. I earnestly believe their cumulative hard work has helped me achieve this feat.

I express my deepest gratitude to my supervisor for his thorough guidance and motivation. He believed in my potential, gave me the opportunity to pursue research, and supported me financially. He enhanced my research aptitude and channeled my efforts in the correct direction by asking the right questions. I sincerely thank him for the enormous time and energy he devoted in guiding me through this journey. Our extensive, detailed discussions and brainstorming sessions always led to the generation of new ideas. The years spent under his mentorship have been a transforming phase of my life. I was always intrigued by his secret behind the zeal that stayed unbeatable against all odds. He leads by example; his actions taught me composure, patience, perseverance, and openness are some of the most important qualities required to pursue research.

I also want to thank the Center for Computational Natural Sciences and Bioinformatics at the International Institute of Information Technology, Hyderabad, for supporting me in various forms throughout my research. I would like to thank the faculty members of the center, Dr. Abhijit Mitra, Dr. Nita Parekh, Dr. U. Deva Priyakumar, Dr. Prabhakar Bhimalapuram, Dr. Harjinder Singh, Dr. Gopalakrishnan Bulusu, Dr. Marimuthu Krishnan, Dr. Tapan Kumar Sau, and Dr. Lini Thomas for their valuable suggestions, advice, encouragement, and learnings that helped me enhance my knowledge across various fields. They have contributed significantly to my success in the DBT-BINC exam. I thank the Department of Biotechnology (DBT), Government of India, for financial support through DBT BINC JRF/SRF fellowship. I especially thank Dr. Prabhakar Bhimalapuram, Dr. Vinod P.K., Mr. Nadeem Hussain Mohd. and Mrs. Aradhana Vinod for providing medical and mental support during the COVID-19 infection. I am thankful to the R&D office staff, Ms. Prathima Mandapati and Mr. Bal Santosh B.

I thank my group members Noor, Prakrati, Manisri, Gayathri, and Vinay for their valuable inputs in my research work. I am also thankful to all Ph.D. research scholars with whom I have shared lab space; I have learnt something from everyone. I was fortunate to find mentors and friends like Broto, Preethi and Antarip. I started my journey with determination; they helped me with the orientation. I have no hesitation in admitting that I would not have applied for the BINC exam in the first place if it wasn't for Broto. I thank him for the encouragement, confidence, and guidance. It is often said that it is the company that makes our tea special; my tea breaks turned into stress buster sessions because of Antarip, Sohini, Rameez, Preethi, Broto, Mohan, Navneet, and Shweta. Sohini & Rameez's home was always my favorite weekend hangout place. I am thankful to my friends later in the journey, Shweta, Srilakshmi, Akansha, Rami, Shruti, Vishal, Pradeep, and Rohit, for creating a healthy work environment bustling with positive energy. My dear friend Preethi always reminded me that Ph.D. is one's lone journey, but I was lucky to share every moment with Manisri. I am blessed to have Shilpa, Sana, Ritika, and Swati,

who remained by my side for decades despite my terribly awkward social skills. Thank you for always going out of the way to stay connected. I also sincerely acknowledge the contribution of those who criticized me and told me that I can't and I shouldn't. They kept me focused and determined till the end.

I am grateful to Maa, Papa, Didi, Jiju and Yaachu babu. My parents and sister have put me first in all their endeavors throughout their life and made selfless sacrifices with a smile on their faces. I can't thank God enough for blessing me with my little angel, the most wonderful child. I was fortunate to be raised by two women who are the epitome of strength. Thanks to them, giving up on anything has never been an option for me. Love you to the moon and back, Maa and Didi. Unfortunately, my parents have always borne the heat of my ill temper because I knew I had their back. I apologize. I feel responsible and regret that my mother couldn't be with my grandfather on his deathbed. Last but not the least, I owe this degree to Jiju; without his belief and necessary push, I would not have considered enrolling for Ph.D. at this stage of life. On a lighter note, I also owe him a treat for funding my laptops.

I conclude by quoting and thanking Late Prof. Randy Pausch (CMU) for his life-changing words:

“The brick walls are there for a reason. The brick walls are not there to keep us out. The brick walls are there to give us a chance to show how badly we want something. Because the brick walls are there to stop the people who don't want it badly enough. They're there to stop the other people.” – An excerpt from The Last Lecture.

List of publications

Journal Publications

1. **Pandey N**, Vinjamuri G, Vinod P.K., Mathematical modelling of naïve T lymphocyte activation in adaptive immune response (Manuscript under preparation).
2. **Pandey N**, Vinod P. K., Model scenarios for cell cycle re-entry in Alzheimer's disease, *iScience*, 25 (7), 2022.
3. Dangarh P, **Pandey N**, Vinod P. K., Modeling the control of meiotic cell divisions: Entry, Progression, and Exit, *Biophysical Journal*, 119 (5), 1015-1024, 2020.
4. **Pandey N**, Lanke V, Vinod P. K., Network-based metabolic characterization of renal cell carcinoma, *Scientific Reports*, 10 (1), 1-13, 2020.
5. **Pandey N**, Vinod P. K., Mathematical modelling of reversible transition between quiescence and proliferation, *PLoS ONE*, 13 (6), 2018.

Oral Presentations

1. Oral presentation titled “Mathematical modelling of neuronal cell cycle re-entry in Alzheimer's disease” at *Society for Mathematical Biology (SMB) 2021 Annual Meeting (Virtual)*, University of California Riverside (UCR), June 13-17, 2021.

Poster Presentations

1. “Systems-level modelling of meiosis regulatory network”, Prakrati Dangarh, Nishtha Pandey, Vinod P. K., at 20th *International Conference on Systems Biology (ICSB 2019)*, Okinawa Institute of Science and Technology Graduate School, Okinawa, Japan, Nov 1 - 5, 2019.

Abstract

Cell division refers to the process by which cells grow, replicate their genetic material, and divide to form daughter cells. Major biological processes, namely reproduction, development, wound healing and tissue regeneration, require cell division. Cells switch between quiescence and proliferation states for maintaining tissue homeostasis and regeneration. The cell division process is regulated by a wide range of extracellular and intracellular cues like growth factors, stress, and reactive oxygen species (ROS). The decision to exit or enter quiescence is dysregulated in proliferative and degenerative diseases. Hence, understanding the molecular mechanisms that control the reversible transition between quiescence and proliferation is crucial. In this thesis, we study the regulatory network involved in this decision-making in normal and disease (cancers and Alzheimer's Disease) conditions and characterize the metabolic adaptation of cancers using systems biology approach.

At the restriction point (R-point), cells become irreversibly committed to the completion of the cell cycle independent of mitogen. The mechanism involving hyper-phosphorylation of retinoblastoma (Rb) and activation of transcription factor E2F is linked to the R-point passage. However, stress stimuli trigger exit from the cell cycle back to the mitogen-sensitive quiescent state after Rb hyper-phosphorylation, but only until APC/C-Cdh1 inactivation. In the work presented here, we developed a mathematical model to investigate the reversible transition between quiescence and proliferation in mammalian cells with respect to mitogen and stress signals. The model integrates the current mechanistic knowledge and accounts for the recent experimental observations with cells exiting quiescence and proliferating cells. We show that Cyclin E-Cdk2 couples Rb-E2F and APC/C-Cdh1 bistable switches and temporally segregates the R-point and the G1/S transition. A redox-dependent mutual antagonism between APC/C-Cdh1 and its inhibitor Emi1 makes the inactivation of APC/C-Cdh1 bistable. We show that the levels of Cdk inhibitor (CKI) and mitogen control the reversible transition between quiescence and proliferation. Further, we propose that shifting of the mitogen-induced transcriptional program to G2-phase in proliferating cells might result in an intermediate Cdk2 activity at the mitotic exit and the immediate inactivation of APC/C-Cdh1. Our study builds a coherent framework and generates hypotheses that have been

confirmed by experimental findings.

Proliferative diseases like cancer arise due to alterations in the regulation of the cell cycle. An emerging hallmark of cancer is metabolic reprogramming, which presents opportunities for cancer diagnosis and treatment based on metabolism. A comprehensive metabolic network analysis of renal cell carcinoma (RCC) subtypes, including clear cell, papillary, and chromophobe, was performed by integrating transcriptome data with the human genome-scale metabolic model to understand the coordination of metabolic pathways in cancer cells. We identified metabolic alterations of each subtype with respect to tumor-adjacent normal samples and compared them to understand the differences between subtypes. We found that genes of amino acid metabolism and redox homeostasis are significantly altered in RCC subtypes. Chromophobe showed metabolic divergence compared to other subtypes with upregulation of genes involved in glutamine anaplerosis and aspartate biosynthesis. A difference in transcriptional regulation involving HIF1A is observed between subtypes. We identified E2F1 and FOXM1 as other major transcriptional activators of metabolic genes in RCC. These results highlight the crosstalk between metabolism and cell division. Further, the co-expression pattern of metabolic genes in each patient showed variations in metabolism within RCC subtypes. We also found that co-expression modules of each subtype have tumor stage-specific behavior, which may have clinical implications.

Intriguingly, cell cycle dysregulation triggers not only proliferative diseases such as cancers but also drives degenerative diseases like Alzheimer's disease (AD). Aberrant production and aggregation of amyloid beta oligomers ($A\beta$) into plaques is a frequent feature of AD. However, therapeutic approaches targeting $A\beta$ accumulation fail to reverse or inhibit disease progression. The approved cholinesterase inhibitor drugs are also mostly symptomatic treatments. During human brain development, the progenitor cells differentiate into neurons and switch to a postmitotic, resting state. However, cell cycle re-entry often precedes the loss of neurons. In this study, we developed mathematical models of multiple routes leading to cell cycle re-entry in neurons that incorporate the crosstalk between cell cycle, neuronal and apoptotic signaling mechanisms. We show that the integration of multiple feedback loops influences the severity of disease and makes the switch to pathological state irreversible. We observe that the transcriptional changes

associated with this transition are also characteristics of the AD brain. We propose targeting multiple arms of the feedback loop may bring about disease-modifying effects in AD.

Cell cycle re-entry during infection is also the underlying process of the adaptive immune response. Naïve T cells get activated on antigen priming and proliferate to form effector and memory cells. However, unlike other mammalian cells, these cells go through an extended lag phase followed by rapid division cycles. The cells undergo extensive metabolic reprogramming in the lag phase, which equips them for extensive clonal expansion. Some common regulators of metabolism and cell cycle coordinate cell growth with proliferation. In the final section of the work, we have developed a mathematical model to explore the crosstalk between metabolism and cell cycle in T cell activation and expansion. We demonstrate the interplay of multiple feedback loops in sustaining Myc levels for T cell activation, expansion, and metabolic reprogramming. This proposed model integrates information across literature and high throughput expression data (proteome) to provide systems-level insights.

Overall, we studied the regulatory network involved in quiescence versus proliferation decision-making in physiological and pathological conditions. We present a consensus picture that bridges different experimental studies and propose hypotheses that can help in further experimentation. Since proliferation and metabolism go hand in hand, we also characterized the metabolic adaptations of cancer that showed subtype-specific changes. This thesis expands the understanding of multiple pathological states that may aid in developing clinical applications.

CONTENTS

Chapter 1	Introduction	1
1.1	Background	1
1.2	Mammalian cell cycle	2
1.2.1	Molecular components of the quiescence to proliferation reversible transition network	3
1.2.2	Pathological consequences of cell cycle dysregulation	6
1.3	Network motifs in the cell cycle control system	6
1.4	Theoretical approaches to study cell cycle	6
1.4.1	Mathematical modeling	7
1.5	Experimental techniques for high throughput data generation	9
1.5.1	Transcriptome data	10
1.5.2	Transcriptome data analysis	11
1.6	Organization of Thesis	13
Chapter 2	Modeling of reversible transition between quiescence and proliferation	15
2.1	Introduction	15
2.2	Model description	17
2.3	Methods	19
2.4	Results	20
2.5	Discussion	26
Chapter 3	Network based metabolic characterization of cancers	31
3.1	Introduction	31
3.2	Methods	33
3.3	Results	36
3.3.1	RCC shows high variation in metabolism compared to other cancer types	36
3.3.2	Reporter metabolic pathways in RCC subtypes	37
3.3.3	Co-expression of metabolic genes in RCC	44
3.4	Discussion	49
Chapter 4	Modeling cell cycle re-entry in neurodegeneration	57
4.1	Introduction	57

4.2	Model description	60
4.2.1	Module 1: A β -induced hyperactivation of extracellular signal-regulated kinases (ERK) in neurons.....	61
4.2.2	Module 2: Intracellular Ca ²⁺ -dependent APC/C-Cdh1 inactivation, Rb hyperphosphorylation and E2F induction in neurons.....	62
4.2.3	Module 3: DNA damage dependent increase in CycD-Cdk4/6 and E2F accumulation in neurons.....	64
4.3	Methods	65
4.4	Results	68
4.4.1	Competition between CycD and p35 controls Cdk5 activity.....	68
4.4.2	Ca ²⁺ and ROS nexus in Rb and APC/C-Cdh1 inactivation.....	72
4.4.3	DNA damage-induced cell cycle re-entry: repair versus apoptosis.....	74
4.4.4	Sensitivity of models to parametric variation.....	79
4.4.5	Expression profile of cell cycle and redox regulators in the AD brain and transgenic mouse model of AD.....	80
4.4.6	Neurodegeneration versus cancer.....	83
4.5	Discussion	84
Chapter 5 Modeling T-cell activation and clonal expansion in adaptive immune response		89
5.1	Introduction	89
5.2	Model description	94
5.2.1	Activation of naïve T cells on antigen recognition.....	94
5.2.2	Myc protein stability model.....	95
5.3	Methods	97
5.4	Results	99
5.4.1	Antiproliferative response triggered by antigen recognition regulate T cell activation threshold.....	99
5.4.2	Quiescent state is programmed differently in naïve CD4 ⁺ and CD8 ⁺ T cells.....	101
5.4.3	TCR priming drives rapid induction of Myc independent of amino acid transporter.....	102
5.4.4	Temporal dynamics of Myc depends on post translational modification.....	104
5.4.5	Positive and negative feedback loop regulation of Myc.....	105
5.4.6	SLC7A5 expression is altered in pan-cancer.....	107
5.5	Discussion	109

Chapter 6 Conclusion.....	113
Bibliography.....	117
Appendix A.....	142
Appendix B.....	146
Appendix C.....	155

LIST OF FIGURES

Figure 1.1: Four phases of the cell cycle. The cell grows during the interphase (G1, S, and G2). Cytokinesis usually follows mitosis (M phase); P, M, A, T represent prophase, metaphase, anaphase, and telophase respectively. Cells can switch between cycling and resting (quiescence – G0) state.2

Figure 1.2: Cell cycle phase specific activity of Myc, E2F, CDKI and Cyc-Cdk complex.....5

Figure 1.3: Positive (a, b, c, d) and negative feedback motifs (e, f) in biological networks. \oplus presents activation and \ominus presents inhibition.....7

Figure 1.4: Signal-response curve (left) and one parameter saddle node bifurcation (right). With variation in the signal strength S the response R varies. R turns on abruptly with gradual increase in S (threshold-type response). On slowly decreasing S the gene expression may turn off (a) at the same threshold signal strength or, (b) lower than the threshold for gene activation (θ_{act}) or, (c) the gene may not be inactivated even after lowering the signal strength zero (irreversible transition). The one parameter saddle node bifurcation (right) corresponds to (b)[60].10

Figure 1.5: Microarray technique and RNA Sequencing technique workflow and comparison [75].12

Figure 2.1: The molecular mechanism controlling the commitment points in the mid and late G1 phase of the mammalian cell cycle.....19

Figure 2.2: (a) The mechanism of Rb phosphorylation and dephosphorylation. Rbp and Rbpp represent the mono-phosphorylated and hyper-phosphorylated forms respectively. (b) The mechanism of APC/C-Cdh1 activation and inactivation, Cdh1^P and Cdh1^{DP} represent the phosphorylated and dephosphorylated forms respectively.19

Figure 2.3: Temporal dynamics of quiescence to proliferation in the presence of mitogens. (a) E2F activation depends on its initial levels at the time of Rb hyper-phosphorylation. (b) Inhibition of CycD ($k_{scycdm} = 0$, $k_{scycds} = 0$) post-G1 entry doesn't delay the dynamics much. Simulations are shown for $S = 1$ (mitogen level). The arrow represents the time of CycD inhibition. RBpp, E2F, CycD_T, CycE, CycA_T, Cdh1, Emi1_T, CKI_T represent hyper-phosphorylated Rb, free E2F, total CycD, free CycE, total CycA, APC/C-Cdh1, total Emi1 and total CDK inhibitor respectively.21

Figure 2.4: Temporal dynamics of quiescence to proliferation in the presence of mitogens. (a) E2F activation depends on Myc-dependent synthesis of E2F, (b) G1/S transition is delayed in the absence of CycD ($k_{scycdm} = 0$, $k_{scycds} = 0$).22

Figure 2.5: Temporal dynamics of proliferation to quiescence in the presence of stress (a) before and (b) after APC/C-Cdh1 inactivation. The arrow represents the time of exposure to stress ($k_{scki} = 0.6$).....22

Figure 2.6: The dynamics of APC/C-Cdh1 inactivation in the absence of Emi1 ($k_{semi} = 0$). The dynamics is shown in the absence (solid line) and presence (dashed line) of Cdk2 inhibition ($k_{dcyce} = 0.01$, $k_{dcyca} = 0.01$). The arrow represents the time of Cdk2 inhibition.23

Figure 2.7: Bifurcation analysis of Rb-E2F subsystem. (a) The effect of increasing the levels of mitogen on Rb hyper-phosphorylation (Rb_{pp}). Filled circle represents the stable steady state and empty circle represents the unstable steady state. The arrow shows the transition from mitogen- dependent to independent state. (b) Two parameters bifurcation diagram with different levels of mitogen and total CKI. The monostable and bistable regions are shown (E2F on and off). Q represents quiescence and P represents proliferation.....23

Figure 2.8: (a) The sensitivity of Rb inactivation/E2F activation threshold to 5-fold change in parameter values. The shift in the saddle node corresponding to Rb inactivation/E2F activation threshold is shown for 5-fold increase/decrease in base parameter value. (b) The sensitivity of APC/C-Cdh1 inactivation threshold to 5-fold change in parameter values. The shift in the saddle node corresponding to APC/C-Cdh1 inactivation threshold is shown for 5-fold increase/decrease in base parameter value. The dashed lines (- -) indicate the two-fold change in the threshold and dotted lines (...) indicate the normalized base parameter value and threshold.....24

Figure 2.9: Bifurcation analysis of G1/S transition. The effect of increasing CycE-Cdk2 activity on (a) Cdh1 inactivation and (b) Emi1 accumulation are shown. CycE_t represents the total CycE-Cdk2 activity since, Cdk levels are considered abundant and kinase activity is regulated by the binding partner. Filled circle represents the stable steady state and empty circle represents the unstable steady state. The arrow shows the transition from G1 to S-phase.25

Figure 3.1: Principal component analysis (PCA) of 14 cancer types. The log fold-change in expression of top 10% highly varying HMR2 genes (361) between tumor and matched normal samples was used to perform the PCA.36

Figure 3.2: Box and whisker plot representing sample wise distribution of (a) E2F1 and (b) FOXM1 expression data for RCC subtypes. As the values are log transformed to the base 2, four-fold change is measured as 2. The lower and upper whiskers represent minimum and maximum value respectively, circles represent outliers. Boundary of box represents first and third quartile range, mean is represented by 'x' and median by '—'.38

Figure 3.3: Survival analysis using E2F1 and FOXM1 as a prognostic marker. Overall survival between low expression group (red) and high expression group (black) for (a) KICH (b) KIRC (c) KIRP show significant difference; the high expression group has a lower survival probability. The survival difference between low and

high expression group was evaluated by Kaplan-Meier (KM) method [187] using the survival package in R [188].	39
Figure 3.4: Reporter pathways of KICH, KIRC and KIRP. Red denotes upregulated and blue denotes downregulated pathways. The prefix c, m and s correspond to cytosol, mitochondria and extra-cellular compartment, respectively. p-values are log transformed ($-\log_{10}p$) and minus (-) was used to represent the downregulation of pathway.....	40
Figure 3.5: One carbon metabolism is affected in KICH. The expression of genes involved in folate cycle, methionine cycle and glutathione synthesis are altered. Downregulated genes are shown in blue while upregulated genes are shown in red color.	42
Figure 3.6: Mitochondrial metabolism is altered in KICH; genes of malate-aspartate shuttle, aspartate synthesis and TCA cycle are upregulated (red) while glutamine metabolism genes are downregulated (blue).....	44
Figure 3.7: Eigengene (ME) expression profile (y-axis) of KICH metabolic modules M3_CH and M5_CH, x axis represents 25 normal and 81 KICH samples.	46
Figure 3.8: Eigengene (ME) expression profile (y-axis) of alanine, aspartate and glutamate metabolism; glutathione metabolism; propanoate metabolism in KICH (x axis represents 25 normal and 81 tumor samples).....	48
Figure 4.1: Molecular network representing competition between p35 and CycD for Cdk5 binding. $A\beta$, through nuclear export of p27 (dashed double headed black arrows), controls ERK activity; red color line with blunt end indicates inhibition and green arrow indicates transcriptional activation, discontinuous lines indicate indirect control. Solid lines with double headed arrows denote reversible association and dissociation of complexes.	61
Figure 4.2: Molecular network representing Rb and APC/C-Cdh1 role in neuroprotection; red color line with blunt end indicates inhibition and green arrow indicates transcriptional activation, discontinuous lines indicate indirect control. Solid lines with double headed arrows denote reversible association and dissociation of complexes. The underlying mechanism is shown with +p for phosphorylation and Ub for ubiquitination.....	63
Figure 4.3: Molecular network representing DNA damage-induced route to cell cycle re-entry and subsequent apoptosis. The red color line with blunt end indicates inhibition. Arrows represent activation with green color indicating transcriptional regulation. Double headed arrows denote reversible association and dissociation of complexes. The underlying mechanism is shown with +p for phosphorylation and Ub for ubiquitination.....	64
Figure 4.4: $A\beta$ mediated activation of MEK-ERK signaling pathway. (a) Temporal dynamics of state variables is shown in the presence of $A\beta$, which induces p27 nuclear export. At $t=500$, the $A\beta$ level (marked by arrow) was set to 0.05 from	

zero. (b) Temporal dynamics of state variables on including the additional effect of $A\beta$ on p35-Cdk5-p27 trimer dissociation. Relative level of state variable $CycD_{Total}$ is represented on the right y-axis. a.u. represents arbitrary units..... 69

Figure 4.5: Bifurcation diagram showing the effect of $A\beta$ level on the ERK activation. The response curve is shown in the absence (red) and presence (blue) of additional effect of $A\beta$ on p35-Cdk5-p27 trimer dissociation in the (a) control and (b) $CycD$ KO conditions. The response curve of ERK shows bistable characteristics (two stable steady states and one unstable steady state for same value of $A\beta$ marked by black filled circles and open circle respectively). Solid lines represent stable steady states, while dashed line represents unstable steady state. SN1 and SN2 represent the saddle nodes corresponding to ERK activation and inactivation, respectively. a.u. represents arbitrary units..... 71

Figure 4.6: Two-parameter bifurcation plots showing how saddle nodes (SN1 and SN2) of bistable switch corresponding to ERK activation and inactivation, respectively, shift with parametric variation. (a) The $A\beta$ threshold for ERK activation and inactivation reduces with increase in p27 ($CDKI_{Total}$). (b) An increase in the $p35_{Total}$ increases the $CycD$ requirement to activate ERK ($A\beta=0.005$). $p35_{Total}$ below a certain threshold fails to suppress ERK and saddle nodes disappear via cusp bifurcation. a.u. represents arbitrary units..... 71

Figure 4.7: An alternate route to cell cycle re-entry via Rb hyper-phosphorylation and APC/C-Cdh1 inactivation (a) Temporal dynamics of state variables is shown in the presence of $A\beta$ by setting its level (marked by arrow) to 0.1 from zero at $t=500$. p25-Cdk5 hyperactivity relieves both Rb and APC/C-Cdh1 barrier. (b) The bifurcation diagram showing the effect of $A\beta$ on ROS accumulation. An irreversible transition to pathological state (oxidative stress) occurs with increase in $A\beta$ level. (c) An increase in glutamate level by increasing k_{sglub} (glutamate excitotoxicity) also shows the irreversible transition to pathological state (oxidative stress). Solid lines represent stable steady states, while dashed line represents unstable steady state. (d) Blocking the individual feedback loops (red: Glis KO, $k_{sgls}=0$; blue: $CycB$ KO, $k_{scycb}=0=k_{scyc}$) turned on by APC/C-Cdh1 inactivation leads to a drop in the magnitude of oxidative stress and makes the transitions to pathological state reversible. Inhibition of p25-Cdk5 activity (green: $k_{sp25}=0$) or termination of the downstream feedbacks (cyan: $k_{sgls}=0$ AND $k_{scycb}=0=k_{scyc}$) rescue the transition to pathological state. SN1 and SN2 represent the saddle nodes corresponding to APC/C-Cdh1 inactivation and activation, respectively. a.u. represents arbitrary units..... 75

Figure 4.8: Cell cycle re-entry via DNA damage dependent E2F activation (a) Temporal dynamics of state variables is shown by setting the DNA damage to intermediate level (0.5 a.u.) from zero at $t=500$ (marked by arrow). (b) Temporal dynamics of state variables is shown for higher level of DNA damage (2.5 a.u.) at $t=500$ (marked by arrow). (c) The bifurcation diagram showing the bistable activation of E2F for lower values of DNA damage (shown in semi-log scale for better resolution). (d) Bistable activation of $p53_{killer}$ for higher values of DNA damage. Solid lines represent stable steady states, while dashed line represents

unstable steady state. SNs represent saddle node corresponding to E2F and p53 killer activation/inactivation. a.u. represents arbitrary units.....	78
Figure 4.9: (a) The bifurcation diagram showing the variation in E2F levels for lower and higher DNA damage levels. E2F levels corresponding to an intermediate level of DNA damage (above SN1 but below SN3) may play a role in DNA repair. SN1 and SN3 correspond to DNA damage threshold for E2F and p53 killer activation, respectively. (b) The two-parameter bifurcation analysis showing the effect of altering the stability of E2F (fac2) on the DNA damage threshold for p53 killer activation (SN3) and inactivation (SN4).	79
Figure 4.10: Parameter sensitivity analysis for module 1. The bars represent the fold change in saddle node values for change in parameter (increase or decrease) from default values (fold change = SN(new)/SN(default)). Fold change in SN1 with increase (blue) and decrease (orange) in parameter values and fold change in SN2 with increase (grey) and decrease (yellow) in parameter values are shown.....	80
Figure 4.11: Parameter sensitivity analysis for module 2. The bars represent the fold change in saddle node values for change in parameter (increase or decrease) from default values (fold change = SN(new)/SN(default)). Fold change in SN1 with increase (blue) and decrease (orange) in parameter values are shown.	81
Figure 4.12: Parameter sensitivity analysis for module 3. The bars represent the fold change in saddle node values for change in parameter (increase or decrease) from default values (fold change = SN (new)/SN (default)). SN1: increase (blue) and decrease (orange); SN3: increase (light blue) and decrease (green); and SN4: increase (navy blue) and decrease (brown).....	82
Figure 5.1: Mitogen signaling (marked by ↓) turns on both proliferative and antiproliferative signal. The continuous presence of mitogen can be substituted with mitogen pulses since the downstream effector shows biphasic activation.	91
Figure 5.2: The molecular mechanism controlling the cell cycle re-entry in the presence of antigen in T cells.....	94
Figure 5.3: Molecular network showing the incoherent feedforward loop regulated by Myc. Metabolites are represented by rectangles, proteins are denoted by yellow-colored ovals. Green arrows represent translational regulation, protein synthesis depletes and degradation generates \bar{a}_{pool}	96
Figure 5.4: Molecular network that regulates Myc accumulation. Blue colored rectangles with rounded corners represent inputs to the model, yellow-colored circles and ovals represent the underlying mechanism. Met1 in model and figure 5.3 represents UDP-GlcNAC.....	97
Figure 5.5: Antigen triggered temporal dynamics of naïve T cell activation (quiescence exit) (TCR = 1) (a) in the presence ($k_{sp53}=0.01$) and (b) in the absence of antiproliferative signaling ($k_{sp53}=0$); and (c) in the absence of Dcaf1 ($k_{sp53}=0.01$, $k_{sdcaf1}=0$). (d) Bifurcation analysis of Rb-E2F subsystem. The effect of increasing	

the TCR signal strength on Rb hyper-phosphorylation is shown for three different values of p53 synthesis rate ($k_{sp53}=0, 0.001, 0.002$). The TCR signal strength required for Rb inactivation increases (shifts right) with increase in k_{sp53} . Filled circle represents the stable steady state and empty circle represents the unstable steady state. 100

Figure 5.6: Parameter sensitivity analysis for T cell quiescence exit. The bars represent the fold change in saddle node values for change in parameter (increase or decrease) from default values (fold change = $SN(new)/SN(default)$). Fold change in SN1 with increase (blue) and decrease (orange) in parameter values are shown. 101

Figure 5.7: Proteome data analysis of naïve and activated CD4+ and CD8+ T cells. (a) Naïve CD8+ T cells have higher concentration of cumulative CDKI and cyclins. Error bars represent standard deviation across biological replicates. (b) Activated CD8+ T cells synthesize inhibitors of CDKI (Mdm2, Dcaf1) and amino acid transporters (SLC1A5, SLC7A5) rapidly than CD4+ T cells (24 hrs data). 102

Figure 5.8: Antigen triggered temporal dynamics of different forms of Myc (a) in the presence and (b) in the absence of amino acid transporter ($k_{sslc}=0$). Different forms of Myc are colored on the basis of post translational modification; p represents phosphorylation, M represents glycosylation at sites Ser62 and/or Thr58. 103

Figure 5.9: Antigen triggered temporal dynamics of different forms of Myc (a) in the absence of ERK activity ($Erk_{max}=Erk_{residual}=0$) and (b) in the absence of OGT activity ($V_{max}=V_{maxn}=0$). Different forms of Myc are colored on the basis of post translational modification; p represents phosphorylation, M represents glycosylation at sites Ser62 and/or Thr58. 105

Figure 5.10: Temporal dynamics of intracellular amino acid pool on activation in wild type T cells (green) and in presence of transporter blocker (red, $k_{imp}=0$). Myc triggers negative feedback loops that deplete cells of amino acids. 106

Figure 5.11: Parameter sensitivity analysis for Myc protein stability model. The bars represent the fold change in steady state value of Myc for change in parameter (increase or decrease) from default values. Fold change with increase (blue) and decrease (orange) in parameter values are shown. 107

Figure 5.12: Box and whisker plot representing sample wise distribution of SLC7A5 expression data for 14 tumor types. As the values are log transformed to the base 2, four-fold change is measured as 2. The lower and upper whiskers represent minimum and maximum value respectively, circles represent outliers. Boundary of box represents first and third quartile range, mean is represented by 'x' and median by '—'. 108

Figure 5.13: Among the 14 tumor types studied in gene expression data analysis, LUSC and LUAD show the most frequent alteration in Myc proximal network. The LUSC and LUAD tumor samples also show high \log_2 (fold change value) reported in figure 5.12 (figure reproduced from [405]). 109

Figure 5.14: Survival analysis using SLC7A5 as a prognostic marker. Overall survival probability between low (black) and high expression group (red) for (a) KIRC (b) KIRP show significant difference (hazard ratio HR > 2, p value < 0.01); the high expression group has a lower survival probability. (c) LUSC and (d) LUAD don't show significant difference in survival probability of the two groups (hazard ratio HR < 2, p value > 0.01). 110

LIST OF TABLES

Table 3.1: Number of tumor and tumor-adjacent normal samples of 14 cancer types used for the principal component analysis. BLCA - Bladder Urothelial Carcinoma, BRCA - Breast invasive carcinoma, COAD - Colon adenocarcinoma, HNSC - Head and Neck squamous cell carcinoma, KICH - Kidney Chromophobe, KIRC - Kidney renal clear cell carcinoma, KIRP - Kidney renal papillary cell carcinoma, LIHC - Liver hepatocellular carcinoma, LUAD - Lung adenocarcinoma, LUSC - Lung squamous cell carcinoma, PRAD - Prostate adenocarcinoma, STAD - Stomach adenocarcinoma, THCA - Thyroid carcinoma, UCEC - Uterine Corpus Endometrial Carcinoma.	34
Table 3.2: Differentially expressed genes ($ \log_2(FC) \geq 1$ and adj p-value ≤ 0.05) between normal and cancer samples.....	37
Table 3.3: Transcription factor enrichment of downregulated genes using Enrichr [181].....	37
Table 3.4: Transcription factor enrichment of upregulated genes using Enrichr [181].	38
Table 3.5: Pearson correlation value between module eigengene expression value and disease, stages and overall survival for KICH. p-value is given inside the bracket; HMR2 metabolic pathways associated with each module and their corresponding p-value are provided.	47
Table 3.6: Correlation between module eigengene (ME) expression value and disease, stages and overall survival for KIRP. Pearson correlation is given with p-values inside the bracket. HMR2 metabolic pathways associated with each module are given with corresponding p-value inside the bracket.	50
Table 3.7: Correlation between module eigengene (ME) expression value and disease, stages and overall survival for KIRC. Pearson correlation is given with p-values inside the bracket. HMR2 metabolic pathways associated with each module are given with corresponding p-value inside the bracket.	51
Table 4.1: Summary of experimental data used to develop the framework of module 1. ..	72
Table 4.2: Summary of experimental data used to develop the framework of module 2. ..	76
Table 4.3: Summary of experimental data used to develop the framework of module 3. ..	77
Table 4.4: Cell cycle and redox metabolism gene expression pattern in AD and GBM. Pearson correlation coefficient and corresponding Student asymptotic p value for eigen gene expression profile with disease is given, *represents correlation of expression profile between wild type and transgenic mice, #represents correlation of expression profile with transgenic mice age.....	84

Chapter 1 INTRODUCTION

1.1 Background

Cell cycle refers to the series of events through which cells grow, replicate their genome, and eventually divide into two daughter cells by mitosis. It is the underlying process necessary for growth, development, and reproduction. The precise regulation of the cell cycle is critical to maintain the genetic integrity of the cell. The cell cycle regulation is under the control of a complex regulatory network that processes a wide range of extracellular and intracellular signals to trigger cell cycle re-entry or arrest cell cycle, or trigger cell death. This complex regulatory network is responsible for the timely execution of cell cycle events in an ordered manner. Dysregulation of the cell cycle is the hallmark of proliferative diseases like cancer [1–3]. Therefore, cell cycle control has been an area of intense research for several decades. Such studies focus on mechanisms that influence not only the timing but also the frequency of DNA replication and cell division [4]. Several factors, such as stress, carcinogenic toxicants, and radiations that cause DNA damage, can considerably alter the cell cycle specific events [1]. A systems-level study of cell cycle control may provide an understanding of disease mechanisms and their treatment strategies.

The entire cell cycle can be divided into four phases (Figure 1.1). Mother cells divide to form daughter cells which undergo a period of growth (G1). Most of the cellular proteins, RNA, other macromolecules, and membranes are synthesized in G1. It is followed by the S phase, which is the period of DNA synthesis. The next phase (G2) is another period of growth. Mitosis (M) follows the G2 phase. In the M phase, chromosome condenses, the nuclear envelope breaks down, mitotic spindles form, chromosomes attach to the mitotic spindles, and finally, separation of the sister chromatids occurs. G1 phase to G2 phase is also known as the interphase. The process completes with cytokinesis, i.e., separation of the daughter cells. The gap phases (G1, G2) are usually much longer (Figure 1.1) than the S or M phase [5]. This provides sufficient time for cell growth. Additionally, they also function as crucial regulatory transition points that can control progression to the subsequent cell cycle phase via the processing of various intracellular and extracellular signals [2, 3, 6].

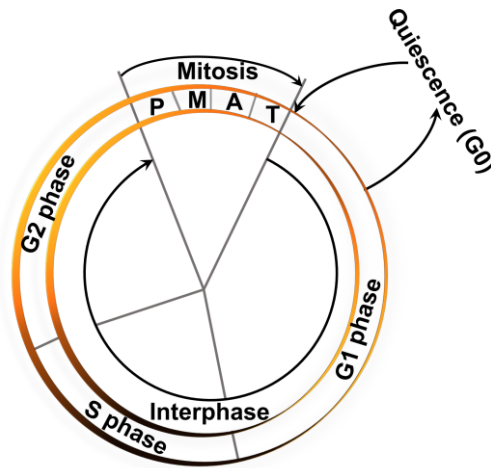


Figure 1.1: Four phases of the cell cycle. The cell grows during the interphase (G1, S, and G2). Cytokinesis usually follows mitosis (M phase); P, M, A, T represent prophase, metaphase, anaphase, and telophase respectively. Cells can switch between cycling and resting (quiescence – G0) state.

1.2 Mammalian cell cycle

The passage of mammalian cells through the cell cycle is controlled primarily by various extracellular growth factors which signal cell proliferation. When cells are starved of growth factors, they withdraw from the cell cycle, cease to proliferate, and enter into a quiescent state (G0) [7, 8]. On restimulation, usually with serum, they resume cycling. However, in comparison to rapidly proliferating cells, they pass through a longer lag phase [8, 9]. Though the stimulus has widespread effects on cellular growth and metabolism, the length of the lag phase appears to be independent of the levels of serum or growth factors [9–11]. After the lag phase, the cells start to enter the S phase asynchronously [10, 11]. On being stimulated with growth factor, cells cross a decision point that may be located even before the end of lag, after which they continue to divide without further stimulation [8, 9, 11, 12]. Hence, cells become committed to divide sometime before the transition from G1 to S phase. Normal cells are growth factor-dependent, and they must pass through the critical decision point in every cell cycle [13]. Molecular machinery underlying this decision point appears to be dysregulated in many cancers emphasizing its importance [14]. Interestingly, the factor(s) that determine the timing of this critical decision point remains unclear. On restimulation, some quiescent cells have higher growth factor requirements than others [15]. Even on stimulation at maximum strength, the cells cross the decision point to enter the S phase in an asynchronous manner [10, 11]. Though often considered to be merely a nuisance, the variability may be a consequence of the regulatory mechanism for cell cycle commitment.

Hence, understanding the origin of this variability is necessary for a complete understanding of the cell cycle control.

1.2.1 Molecular components of the quiescence to proliferation reversible transition network

The molecular players of the quiescence to proliferation reversible transition network broadly belong to two classes viz the cell cycle activators and inhibitors. They differ in their mode of action to either promote proliferation or maintain quiescence. Myc and E2F are the key transcription factors of the G1 phase that promote the exit from quiescence. Cyclin dependent protein-kinases (Cdk) are a class of cell cycle activators that function in complex with their regulatory Cyclin subunits (Cyc). Progression of the cell cycle is also regulated negatively by several molecular brakes, e.g., Cdk inhibitors (CDKI), p53 tumor suppressor, retinoblastoma proteins (Rb), and ubiquitin ligase (APC/C-Cdh1) [16, 17]. A brief overview of the network components follows:

Myc

Myc family proteins (c-Myc, N-Myc, and L-Myc) are a class of transcription factors with oncogenic functions. Myc is the downstream effector of multiple signal transduction pathways which sense growth factors and nutrient availability or the cellular microenvironment, e.g., cellular adherence with the extracellular matrix. Myc promotes the cell cycle by inducing E2F, Cyc-Cdk activity (Figure 1.2). In addition to direct transcriptional regulation of Cyc, Myc hyperactivates Cyc-Cdk complexes through activation of the Cdk activating kinases and Cdc25 phosphatase. Myc further promotes replication by binding to origins of replication and through upregulation of gene products required for initiation of replication [18, 19].

E2F protein

E2F family proteins, typically E2F1-3a, regulate the expression of many genes required for cell cycle progression, DNA synthesis, DNA repair, and apoptosis in a context-dependent manner (Figure 1.2) [20, 21]. E2F1 functions as a master regulator of the G1/S phase genes. While knockout (KO) of E2F proteins prevents cell cycle re-entry from quiescence [22], aberrant overexpression drives quiescent cells into the cell cycle [23]. E2F

activity is suppressed by Rb in the quiescent state by Rb-E2F complex formation, elimination of repression on E2F by Rb KO prevents exit to quiescence [24].

Cyclin-Cdk complex

The cell cycle is controlled by multiple Cyc and Cdks, which belong to the family of serine/threonine kinases. Cdks form complexes with their cyclin binding partners and activate Cyc-Cdk kinase activity. The complexes regulate cell-cycle progression by phosphorylation of substrates like Rb. Cdk levels are considered to be comparatively constant and in excess of Cyc levels through the entire cell cycle. The oscillations in the expression level of Cyc result in the oscillations of Cyc-Cdk complexes levels. Different Cyc-Cdk complex gets activated in different phases of the cell cycle (Figure 1.2). Cyclins may be classified into different classes based on the temporal profile of protein expression and the corresponding cell-cycle control function, e.g., G1 cyclins, G1/S cyclins, S cyclins, and M cyclins. Growth factor stimulation activates the CycD-Cdk4/6 complex, whereas E2F activates CycE, CycA, and CycB dependent Cdk activity through direct or indirect transcriptional regulation of cyclins. Cdk activity is regulated by the Cdk inhibitors (CDKI) [25, 26].

Cdk inhibitors (CDKI)

The Cyc-Cdk complexes are negatively regulated by CDKIs belonging to two major classes. Cdk4/6 specific inhibitors include p16INK4a, p15INK4b, p18INK4c, and p19INK4d and are classified as INK4 proteins. The other class of inhibitors is called Cdk-interacting protein/kinase inhibitory proteins (Cip/Kip), e.g., p21^{CIP1}, p27^{KIP1}, and p57^{Kip2}. CDKIs form trimer complex with Cyc-Cdk and inhibit their kinase activity. On the other hand, they are also known to stabilize the Cyc-Cdk complex association [21, 25, 26]. The INK4 protein level is usually high in the quiescent state, whereas p21^{CIP1} gets activated in response to DNA damage checkpoint activation. Tumor suppressor p53 is the transcriptional regulator of p21^{CIP1} and is one of the most frequent mutations observed in cancer [27].

p53

p53 is a tumor suppressor transcription factor that is induced by stress signals like DNA damage, nutrient deprivation, oncogene activation, etc. p53 drives cell-cycle arrest and provides an opportunity for DNA repair primarily by transcriptional activation of p21^{CIP1} and

apoptosis by induction of pro-apoptotic genes such as Noxa, Bad, Apaf1 [27, 28]. Further, p53 triggers antiproliferative signaling in response to growth factor stimulation which facilitates the filtering of signal versus noise [29].

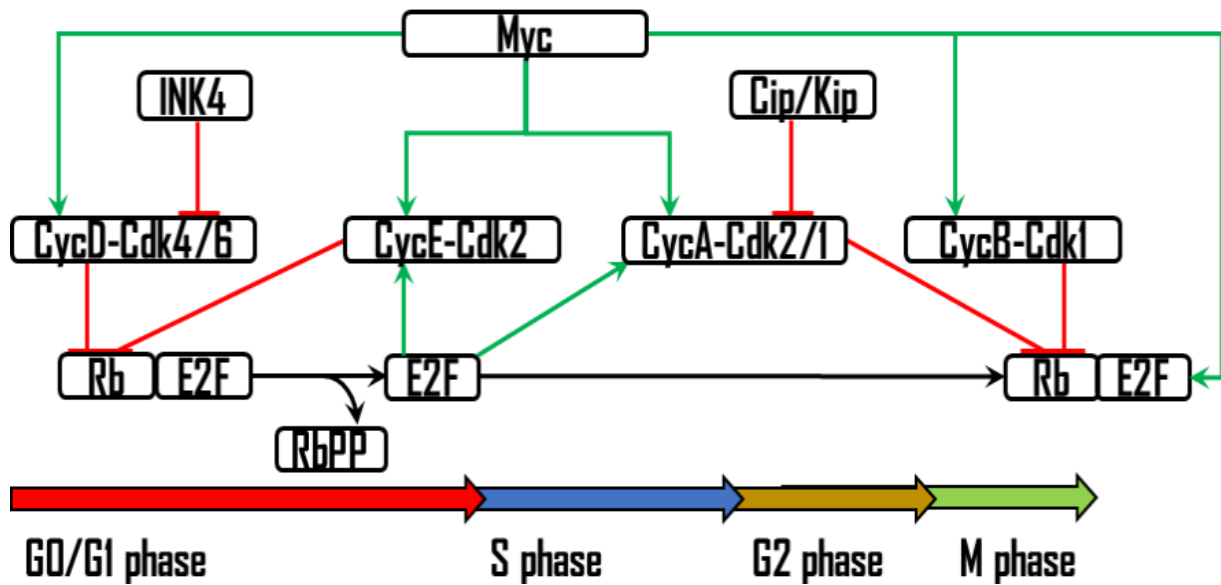


Figure 1.2: Cell cycle phase specific activity of Myc, E2F, CDKI and Cyc-Cdk complex.

Rb protein

Rb, or the retinoblastoma protein, functions as a tumor suppressor, and it belongs to the family of pocket proteins. Other members of the family include p130 and p107 [30]. Rb family proteins form complex with transcription factors of the E2F family and repress expression of the E2F-target genes (Figure 1.2) [30–32].

Anaphase promoting complex/cyclosome (APC/C)

The anaphase promoting complex/cyclosome (APC/C), another tumor suppressor, is a multi-subunit E3 ubiquitin ligase that plays essential functions in the cell cycle. It is a highly conserved protein across multiple species and depends on two adaptor proteins, Cdh1 and Cdc20, for substrate recognition and enzyme activity. Both APC/C-Cdc20 and APC/C-Cdh1 critically control the cell cycle by targeting proteins for proteasomal degradation through ubiquitination of important cell cycle regulators such as cyclins (CycA, CycB). Additionally, APC/C-Cdh1 prevents premature entry into the S phase by protecting CDKIs from degradation and keeping resultant Cdk activity low [33, 34].

1.2.2 Pathological consequences of cell cycle dysregulation

The cell cycle control system regulates tissue homeostasis; most cells undergo up to 40–60 cycles before they cease to proliferate and become senescent [35]. Alternatively, they may also exit the cell cycle during differentiation [36]. Dysregulation of the cell cycle control system results in abnormal phenotype [37]. Cancer is one such disorder that is associated with a defective cell cycle. In most cases, cancer cells fail to switch from proliferation to quiescence [38, 39]. Additionally, cell death machinery that controls apoptosis may also fail [40]. Other disorders associated with cell cycle dysregulation include neurodegeneration; terminally differentiated neurons re-enter the cell cycle, which then triggers cell death [41, 42]. Hence, understanding the molecular basis of cell cycle dysregulation becomes critical for therapeutic intervention.

1.3 Network motifs in the cell cycle control system

Cell cycle progression can be considered as a collection of unidirectional state transitions. The cell cycle control system operates through the integration and coordination of multiple feedback loops, which ensure these phase transitions are irreversible, i.e., even after the removal of transient triggering signals, the cell continues to move forward through the G1-S-G2-M stages. The feedback motifs may have a positive or negative effect. Accordingly, the output of the system amplifies or represses the input leading to a sustained or transient response. The frequently encountered motifs are shown below; both double positive (Figure 1.3b) as well as double negative (Figure 1.3a) feedback loops result in positive feedback. Figure 1.3e and f have an odd number of negative effects (\ominus), which make them negative feedback network motifs [43].

1.4 Theoretical approaches to study cell cycle

Cell cycle control mechanisms have been studied in detail by various biochemical and molecular biological methods [16]. However, traditional wet-lab experiments are often insufficient to build a complete understanding at the systems-level. Hence, alternative methods like mathematical modeling are being widely applied for the analysis of dynamic systems and deriving logical and convincing interpretations of different experimental observations [44, 45].

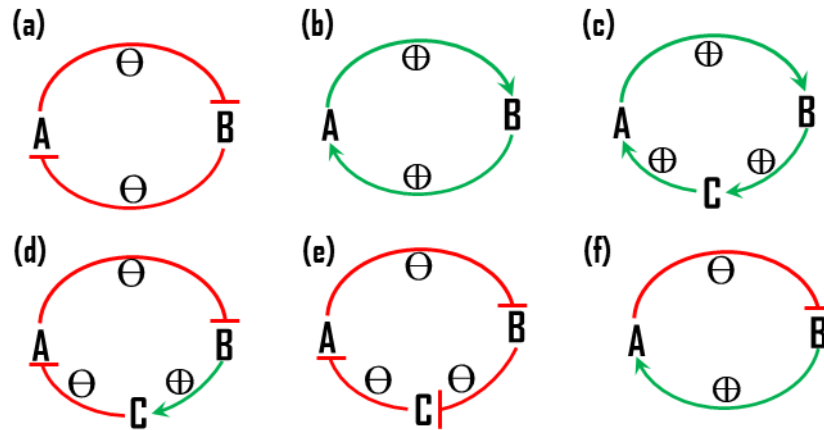


Figure 1.3: Positive (a, b, c, d) and negative feedback motifs (e, f) in biological networks. \oplus presents activation and \ominus presents inhibition.

1.4.1 Mathematical modeling

Mathematical modeling is a tool used to translate biomolecular networks into mathematical formulations, which help in a detailed analysis of the dynamical behavior of the components and their interactions [46]. It helps answer complex questions which cannot be addressed by intuition alone, gives insights into the systemic response, and facilitates the formulation of hypotheses for testing in the future. The most frequently used formulation is ordinary differential equations (ODEs), which is a deterministic modeling approach [47, 48]. The solutions of deterministic models are predetermined and predictable for a given set of equations, parameters and initial conditions [49, 50].

Ordinary differential equations (ODEs)

ODEs calculate the temporal evolution of the state variables that describe the biomolecular network. The collection of ODEs usually characterizes a nonlinear dynamic system that is difficult to solve analytically and requires computers to obtain numerical solutions. The mathematical model captures the relationship among state variables. ODEs are suitable for the modeling of systems that are properly mixed, perfectly homogeneous, have a sufficiently large number of chemical components, and the reactions take place simultaneously; such assumptions hold true in many biological systems [44, 51]. The change in the concentration profile of a component (e.g., protein) with respect to time ($[C_j(t)]$) is described below:

$$\frac{d[C_j]}{dt} = V_{\text{synthesis}} + V_{\text{activation}} - V_{\text{degradation}} - V_{\text{inactivation}} \quad (\text{Eqn. 1.1})$$

The right-hand side of each ODE contains positive terms (synthesis and activation) and negative terms (degradation and inactivation) for each of the reactions in which C participates as a product or a reactant. The rate expressions (V) on the right-hand side can follow the standard rules of biochemical reaction kinetics (law of mass action (Eqn. 1.2) [52], Hill-equation (Eqn. 1.3) [53], or Michaelis-Menten rate law (Eqn. 1.4)) [54]. Different equations are adopted depending on the type of regulation of protein, e.g., complex formation (Eqn. 1.2), synthesis (Eqn. 1.3), inactivation (Eqn. 1.4). It can be noted that the same protein can also be subjected to all three regulations.

$$\text{Law of mass action: } \frac{d[A]}{dt} = k_{dis} * [AB] - k_{as} * [A] * [B] \quad (\text{Eqn. 1.2})$$

The concentration of protein A ([A]) at any time t is determined by the concentration of reactants ([A], [B], [AB]) and the rate at which protein A and inhibitor/activator B associate (k_{as}) and dissociate (k_{dis}).

$$\text{Hill function: } \frac{d[A]}{dt} = k_s * \frac{[B]^n}{K^n + [B]^n} - k_d * [A] \quad (\text{Eqn. 1.3})$$

The concentration of protein A ([A]) at any time t is determined by the rate of synthesis (k_s), rate of degradation (k_d), the concentration of transcription factor B [B], Hill coefficient (n) that controls the steepness of the activation function, and activation coefficient K , which is the concentration of B that is needed to significantly activate the expression of [A]. The half-maximal expression value is reached when $B = K$.

Michaelis Menten kinetics:

$$\frac{d[Ap]}{dt} = k_p * [Ek_T] * \frac{[Adp]}{K_{mp} + [Adp]} - k_{dp} * [Ep_T] * \frac{[Ap]}{K_{mdp} + [Ap]} \quad (\text{Eqn. 1.4})$$

The concentration of the phosphorylated form of protein A ([Ap]) at any time t is determined by the rate of phosphorylation/dephosphorylation (k_p/k_{dp}), the total concentration of respective enzymes ([Ek_T], [Ep_T] representing the kinase and phosphatase, respectively), the concentration of substrate ([Adp]/[Ap]), and Michaelis constant (K_{mp} , K_{mdp}). Both

phosphorylation and dephosphorylation follow Michaelis-Menten kinetics, and values of K_m control the steepness of activation/inactivation as proposed by Goldbeter and Koshland [55].

Data obtained from various wet-lab experiments provide information about the parameter values. However, not all parameters have experimentally measured values, and some values can be estimated depending on the availability of temporal data. They can also be guessed in an iterative manner with the aim to simulate the qualitative behavior/dynamics of the biological system [56, 57]. The model developed may be minimal and relatively simple with only a few ODEs or elaborate and complex with many variables depending on which form closely captures the real behavior of cells [58, 59].

Bifurcation theory

The values of the parameters can be varied to study their effect on the response variable (sensitivity analysis) or to study how the qualitative behavior of the system changes from one state to the other state (bifurcation analysis). The parameters used in an ODE mathematical model capture specific biological processes and mimic different cellular functions. Changing these parameter values simulate the cellular response to various stimuli such as protein deletion or over-expression. Bifurcation diagrams or the “signal-response curves” show the steady state responses with respect to alteration in specific parameters in particular ranges or input signal S (Figure 1.4) [60]. An interesting characteristic of the signal-response curve is that a shift in parameter value can lead to a very dramatic change in the response of the system. A one-parameter bifurcation diagram and signal response curve are shown in Figure 1.4 [60]. In the bifurcation plot, the stable steady states are presented with solid lines, whereas the unsteady states are presented as dotted lines. The activation and inactivation thresholds (saddle nodes, SN) of the system are different (change in p_j values). The saddle-node bifurcation occurs with both stable and unstable steady states coming together and disappearing with parametric changes [60–64].

1.5 Experimental techniques for high throughput data generation

Several high throughput methods focus on characterizing meaningful biological information at the multiomics level (genome, epigenome, transcriptome, proteome, metabolome, etc.). The functional aspects of genomic changes are well understood by

routinely analyzing the gene expression (transcriptome), proteome, or metabolome data. The analysis of high-throughput data helps in understanding the molecular mechanisms and in differentiating the phenotype of interest (e.g., normal versus disease). It helps to draw a holistic picture of the biological system by understanding the crosstalk among biological processes [65–68].

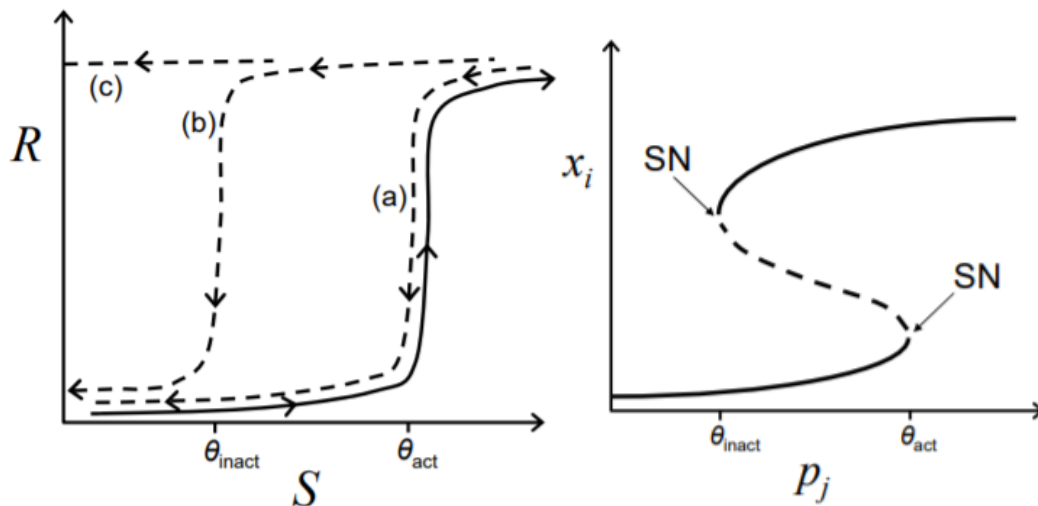


Figure 1.4: Signal-response curve (left) and one parameter saddle node bifurcation (right). With variation in the signal strength S the response R varies. R turns on abruptly with gradual increase in S (threshold-type response). On slowly decreasing S the gene expression may turn off (a) at the same threshold signal strength or, (b) lower than the threshold for gene activation (θ_{act}) or, (c) the gene may not be inactivated even after lowering the signal strength zero (irreversible transition). The one parameter saddle node bifurcation (right) corresponds to (b)[60].

1.5.1 Transcriptome data

Transcriptomics, as the name suggests, is the study of transcriptome or complete set of RNAs transcribed under defined conditions. The biological information encoded in the genome is decoded by gene transcription. Thus, quantification of the transcriptome reveals how genes are regulated under different conditions. It also bridges the gap between genotypic and phenotypic association [69]. The transcriptome data analyzed in this study were obtained using Microarrays and RNA sequencing (RNA-Seq) techniques.

Microarray

Microarrays are basically a set of genes or oligonucleotides on a chip that usually characterize the genome/transcriptome of a species. The chip is divided into grids or arrays, also known as features, each of which has specific oligonucleotide sequences attached. The

sequences serve as probes and detect the presence of gene specific transcripts by complementary base pairing or hybridization. Messenger RNA (mRNA) samples from different systems, e.g., healthy and disease, are extracted, reverse transcribed into complementary (cDNA), and simultaneously fluorescently labeled. After hybridization of the labeled cDNA samples, the features on the microarray are identified by scanning. The intensity of fluorescence correlates with the expression level of the gene. The design and specificity of probes have advanced with time, allowing improvement in measurement accuracy of even the low abundance transcripts [70–74] (Figure 1.5).

RNA sequencing

RNA sequencing (RNA-Seq) is another method for quantifying transcript levels more precisely. Similar to the microarray technique first, the extracted RNA is reverse transcribed into cDNAs fragments. Next, adaptors are attached to either one or both ends of the cDNA fragments. Each cDNA molecule is then sequenced in a high throughput manner to generate short sequence reads, usually 30-400 bp long from one (single-end) or both ends (pair-end) (Figure 1.5) [75]. The sequence reads are aligned to the reference genome, and transcribed regions of the genome are identified. This method provides higher coverage and better resolution of the dynamic transcriptome profile compared to microarray. It is an open system that also detects novel transcripts, alternatively spliced genes, and allele-specific expression. Common sequencing platforms include Illumina IG, Applied Biosystems, and Roche 454 [76–79].

1.5.2 Transcriptome data analysis

In this section, an overview of different approaches adopted in this work for the analysis of transcriptome data is discussed.

Differential gene expression analysis

Differential gene expression analysis facilitates the identification of the genes that show a difference in expression patterns under different conditions (time, disease state, etc.) [80]. Statistical analysis methods are applied to the gene expression data to quantify the magnitude (log fold change) and significance (p-value) of change in gene expression levels.

Commonly used R packages for the identification of differentially expressed genes include DESeq2 [81] and EdgeR [82] for RNA-Seq transcriptome data analysis.

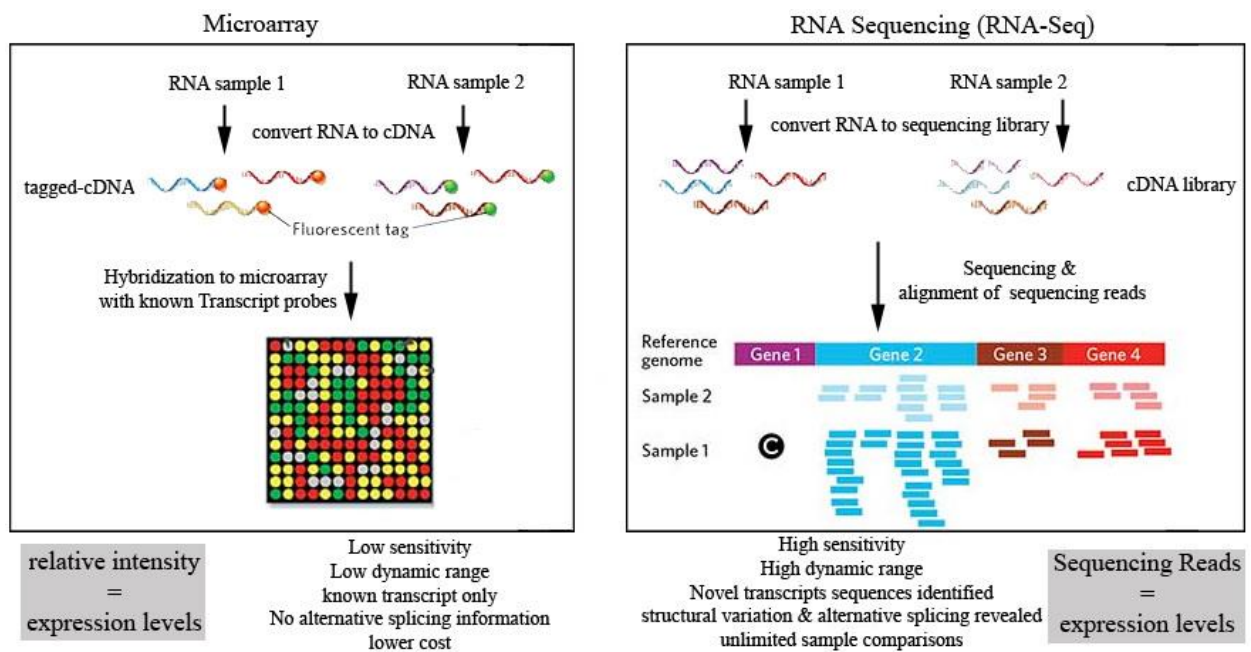


Figure 1.5: Microarray technique and RNA Sequencing technique workflow and comparison [75].

Gene co-expression network

The reconstruction of a biological network using genome-wide measurement provides a framework for interpretation at the systems-level. Gene co-expression networks (GCNs) are built from transcriptome data by computing co-expression scores between pairs of genes and defining a significance threshold. It generates an undirected graph; the nodes represent genes, and edges connect gene pairs that are significantly correlated. Densely connected gene modules usually share related biological functions. Intermodular connectivity signifies a higher-order organization of biological relationships, whereas intra-modular connectivity recognizes highly connected hub genes within modules. The network hubs may be molecular drivers like transcription factors [83]. GCNs cluster genes that are active simultaneously and are often active in the same or related biological processes.

Genome-scale metabolic model

Genome-scale metabolic models (GEMs) represent a comprehensive picture of metabolism at the species/genome level [84]. These models organize information about

enzymes, their associated stoichiometric reactions, substrates, products, interactions with metabolites in *in silico* form. Transcriptome data can be integrated with GEMs to obtain tissue specific or disease specific metabolic networks [85–87]. This integrated approach aids the interpretation of how alterations at the transcriptome level map to the metabolome and associated pathways. Thus, GEMs facilitate metabolic response analysis as well as flux simulation at the systems-level [88]. Such interpretation is not possible by using metabolic pathway databases like the Kyoto Encyclopedia of Genes and Genomes (KEGG) pathway [89, 90]. Several tissue specific GEMs, including hepatocyte, kidney, brain, adipocyte, have been archived for public access [84, 91–94]. The earliest GEMs developed for humans are Recon1 [95, 96] and the Edinburgh Human Metabolic Network (EHMN) [97, 98]. Later, the human metabolic reaction (HMR) and HMR2 database encompassing Recon1, EHMN, and KEGG were created [91, 99]. The genome scale metabolic models are progressively updated with new features, e.g., the latest version of Recon (Recon3D) includes three-dimensional structure data of metabolites and proteins. It enables the characterization of disease associated mutations and identification of metabolic response signatures in response to certain drugs [100].

1.6 Organization of Thesis

The cell cycle control system ensures the flawless execution of growth, development, morphogenesis, regeneration, and homeostasis. An orchestrated operation of the components controls the cellular fate; consequently, the cells may choose to rest in a dormant state (quiescence), actively cycle (proliferation), differentiate to attain specialized structure and function (differentiation), or cease to proliferate (senescence) and/or die (apoptosis).

The central theme of the work presented here is to explore the mechanism at the heart of the quiescence versus proliferation decision-making process and understand the adaptations in different cellular and pathological contexts. This thesis presents systems-level modeling and analysis of the reversible transition between quiescence and proliferation and commitment to the cell cycle. We have modeled a temporal window of reversibility where cells can switch between quiescence and proliferation depending on the mitogen and stress signals. The crossing of this temporal window leads to an irreversible commitment to proliferation, and the cells become independent of input signals. Redox state and metabolic

adaptations also contribute to cellular decision-making. For instance, redox imbalance drives oxidative stress and alters the cell cycle progression. Similarly, metabolism supports the biosynthetic and bioenergetic demands of proliferating cells. Hence, the interaction between the cell cycle, metabolism, and redox has also been explored, and the crosstalk mechanisms are highlighted. A deterministic modeling framework has been adopted to develop mathematical models of cell cycle re-entry in different contexts, which include epithelial, neuronal, immune cell lines, and normal and proliferative disease conditions. Additionally, transcriptome data of proliferative diseases and neurodegeneration, have been analyzed using different computational approaches to get network-level insights and to relate our models with clinical observations. Chapter 2 presents the mathematical model of quiescence to proliferation reversible transition and an irreversible commitment to the cell cycle in a normal mammary epithelial cell line. Chapter 3 reports a pan-cancer comparative analysis of G1/S dysregulation and metabolic adaptations, focusing especially on renal cell carcinoma. Chapter 4 presents the mathematical model of aberrant cell cycle re-entry and apoptosis in neurodegeneration. Chapter 5 presents the mathematical model for cell cycle re-entry in naïve T-cell activation during an adaptive immune response with an emphasis on the temporal regulation of Myc in T-cell activation and clonal expansion. The last chapter summarizes the major conclusions of the thesis.

Chapter 2 MODELING OF REVERSIBLE TRANSITION BETWEEN QUIESCENCE AND PROLIFERATION

2.1 Introduction

Tissue homeostasis depends on the ability of mammalian cells to reversibly switch between quiescence (G0) and proliferation. Cells remain quiescent in the absence of mitogen and under stress conditions. Cells exit quiescence on mitogen stimulation and enter the G1 phase of the cell cycle; later, they become committed to the completion of the cell cycle. The decision-making mechanism to exit or enter quiescence is dysregulated in proliferative and degenerative diseases [101, 102]. Proliferating tumor cells also heterogeneously switch to quiescence in response to anti-cancer drugs [103, 104]. The quiescent tumor cells persist, leading to relapse [105]. Hence, understanding the molecular mechanisms that control the reversible transition between quiescence and proliferation is crucial.

The term restriction point (R-point) was coined to define the time point when cells become irreversibly committed to the completion of the cell cycle in the absence of mitogen. It was considered an early G1 event based on pulsing the mitogen to mitogen-starved (G0) cells [106, 107]. The underlying molecular mechanism of R-point involves the regulation of transcription factor E2F by a pocket protein retinoblastoma (Rb) [23, 108, 109], but recent experimental observations suggest the canonical view should be revisited. Conventionally, mitogen induced, Cyclin D-Cdk4/6 (CycD-Cdk4/6) driven, hypo-phosphorylation of Rb is believed to release E2F [110–112]. This E2F is considered indispensable to drive Cdk2 dependent hyper-phosphorylation of Rb and full release of E2F via CycE transcription. The double negative feedback loop between Rb and E2F mediated through CycE-Cdk2 is proposed to ensure irreversible commitment to proliferation [113]. However, this view is challenged by the observations that hypo-phosphorylated/mono-phosphorylated Rb forms act as an inhibitor of E2F, and hyper-phosphorylation of Rb is required for the E2F activation [114–118]. Moreover, though selective inhibition of Cdk2 by chemical genetics approach

blocks R-point passage [119], major phosphorylation of Rb and CycE accumulation is detectable only after the R-point [120, 121]. These findings question the Cdk2 activity threshold needed for irreversibility.

While R-point is located in the G1 phase of cells exiting quiescence, continuously cycling cells may overcome mitogen requirement in the G2 phase of the previous cycle. In the presence of mitogen, cycling cells are found to bifurcate into two populations as they exit mitosis [122]. The majority of cells (80%) immediately commit to the cell cycle since they have Cdk2 activity at an intermediate level, while other cells with low Cdk2 activity experience transient quiescence. In the absence of mitogen, cells exit mitosis with low Cdk2 activity to enter quiescence state and require mitogen for the cell cycle re-entry. Whether the R-point operates in the G1 or G2 phase of cycling cells is dependent on the cell type. The majority of cycling Swiss 3T3 cells exit mitosis with low Cdk2 activity (subjected to G1 R-point) compared to MCF10A cells, which show intermediate Cdk2 activity (subjected to G2 R-point) [122]. The proliferation to quiescence decision is controlled by the Cdk inhibitor p21. Endogenous DNA damage during the S-phase is shown to induce the synthesis of p21 in cycling cells [123, 124].

Further, a recent finding by Cappell et al. (2016) suggests that APC/C-Cdh1 inactivation at the G1/S transition serves as a commitment point that prevents re-entry into quiescence. This is based on the evidence that cells re-enter the quiescence state in the presence of stress after Rb hyper-phosphorylation and before APC/C-Cdh1 inactivation. The cycling cells with intermediate Cdk2 activity immediately inactivate APC/C-Cdh1 and enter the S phase [125]. The molecular mechanism proposed for the commitment at the G1/S boundary depends on the irreversible inactivation of APC/C-Cdh1 by its inhibitor Emi1 [125, 126]. CycE-Cdk2 is shown to initiate APC/C-Cdh1 inactivation before Emi1 promotes the accelerated inactivation. Studies have also shown that the proliferation to quiescence decision is controlled by double negative feedback loops between Cdk2 and p21, which control the degradation of p21 via the activation of two ubiquitin ligases, CRL4^{Cdt2} and SCF^{Skp2} [123, 127, 128]. The regulation of APC/C-Cdh1 and p21 is linked via APC/C-Cdh1 dependent degradation of Skp2 [129, 130]. Further, Dong et al. (2014) showed that the levels of E2F increase in a Myc-dependent manner, and crossing an E2F threshold determines the cell cycle commitment. In this case, G1 phase Cyc-Cdks control the timing of E2F crossing the

threshold [131]. However, the inhibition of Cdk2 blocks APC/C-Cdh1 inactivation and the S-phase entry [125].

How these regulations depending on mitogen and stress are integrated is yet to emerge. The complexity of the regulation coupled with different experimental setup/cell types makes it difficult to understand this problem by intuition alone. The mathematical modeling approach provides a scope to develop a coherent framework that will help to generate hypotheses for further exploration by experiments. Previous studies on mathematical modeling of R-point and G1/S transition have shown the bistable activation of E2F and inactivation of p21, respectively [113, 123, 127]. R-point models show how cells emerging out of quiescence become mitogen independent, and G1/S transition models show how p21 controls heterogeneity in cycling and quiescence states. It is important to revisit these models in the light of newer findings [115, 125, 132–135].

In this study, we developed a mathematical model to investigate the reversible transition between quiescence and proliferation in mammalian cells. The model integrates the current mechanistic knowledge and accounts for the recent experimental observations with cells emerging out of quiescence and cycling cells. We propose model scenarios for the cell cycle entry and exit with respect to mitogen and stress. We show that CycE-Cdk2 couples Rb-E2F and APC/C-Cdh1 bistable switches and temporally segregates the R-point and the G1/S transition. A mutual antagonism between APC/C-Cdh1 and its inhibitor Emi1 can make the inactivation of APC/C-Cdh1 bistable. We propose Emi1 can switch from a substrate to an inhibitor of APC/C-Cdh1 in a redox-dependent manner.

2.2 Model description

The model proposed here incorporates all the essential features controlling the reversible transition between quiescence and proliferation. At the heart of quiescence to proliferation transition is the regulation of Myc, E2F, Rb, CycD-Cdk4/6, CycE-Cdk2, APC/C-Cdh1, and Cdk inhibitors such as p21 (represented as CKI) (Figure 2.1). Mitogen stimulates early and late phases of signaling events that promote Myc stabilization [136]. Though Myc is activated with the early phase of mitogen signaling, the synthesis of Myc-dependent proteins occurs only with the late phase of mitogen signaling. This delay might be due to the presence of anti-proliferative signals, which have to be inhibited by the late phase

of signaling. It is shown that p53-controlled anti-proliferative genes are induced by the early phase of mitogen signaling. This acts as restraint mechanism to prevent the commitment to the cell cycle until the late phase of mitogen signaling [29]. We consider mitogen as an input to the model, which promotes Myc-dependent synthesis of CycD, CycE, and E2F through the late phase of mitogen signaling.

In the model, CycD-Cdk4/6 mono-phosphorylates Rb, but this does not relieve the inhibitory effect of Rb on E2F. Rb inhibits E2F by forming a stoichiometric inhibitory complex (Figure 2.2a). CycE-Cdk2 hyper-phosphorylates the mono-phosphorylated form and relieves E2F inhibition [115]. The hyper-phosphorylation of Rb is required for relieving the Rb inhibition of E2F. We considered that higher levels of Cdk2 activity can hyper-phosphorylate Rb independent of mono-phosphorylation (by higher levels of CycE-Cdk2 or CycA-Cdk2). The release of E2F promotes its own synthesis and the synthesis of CycE, CycA, and Emi1. We attempted to answer interesting questions such as how E2F gets activated initially and what sets the time window. The hyper-phosphorylation of Rb/activation of E2F is controlled by CKI, which forms a complex with CycD-Cdk4/6, CycE-Cdk2, and CycA-Cdk2 [26]. Stress raises the Cdk activity barrier by escalating CKI accumulation. We considered a higher threshold of CycE-Cdk2 is required to initiate APC/C-Cdh1 inactivation by phosphorylation. Emi1 subsequently inactivates APC/C-Cdh1 by forming a stoichiometric inhibitory complex (Figure 2.2b). Although Emi1 and CycE both are E2F targets, Emi1 accumulates only in the late G1 phase. Such a delay in Emi1 accumulation might be due to post-transcriptional/translational controls [137–139]. It has been proposed that Emi1 can be an APC/C-Cdh1 target similar to CycA [140]. Since Emi1 regulation in G1 is largely unknown, we hypothesized that Emi1 is an APC/C-Cdh1 substrate (Figure 2.1) and explored the dynamical consequences. Post-APC/C-Cdh1 inactivation, the activation of SCF^{Skp2} and CRL4^{Cdt2} ubiquitin ligases target CKI for proteolysis in a Cdk2 dependent manner [141, 142]. Since SCF^{Skp2} is an APC/C-Cdh1 substrate and CRL4^{Cdt2} dependent proteolysis is coupled to DNA replication via PCNA, we consider that both ubiquitin ligases are directly regulated by APC/C-Cdh1 [129, 130, 143]. We assume that the degradation of CycE and E2F is promoted by the accumulation of CycA [144–146].

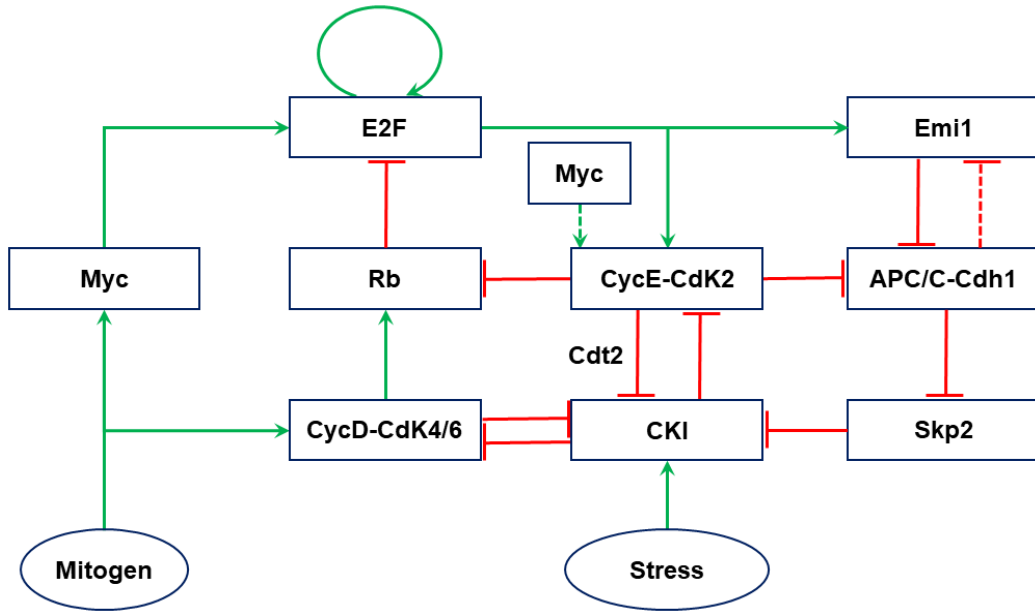


Figure 2.1: The molecular mechanism controlling the commitment points in the mid and late G1 phase of the mammalian cell cycle.

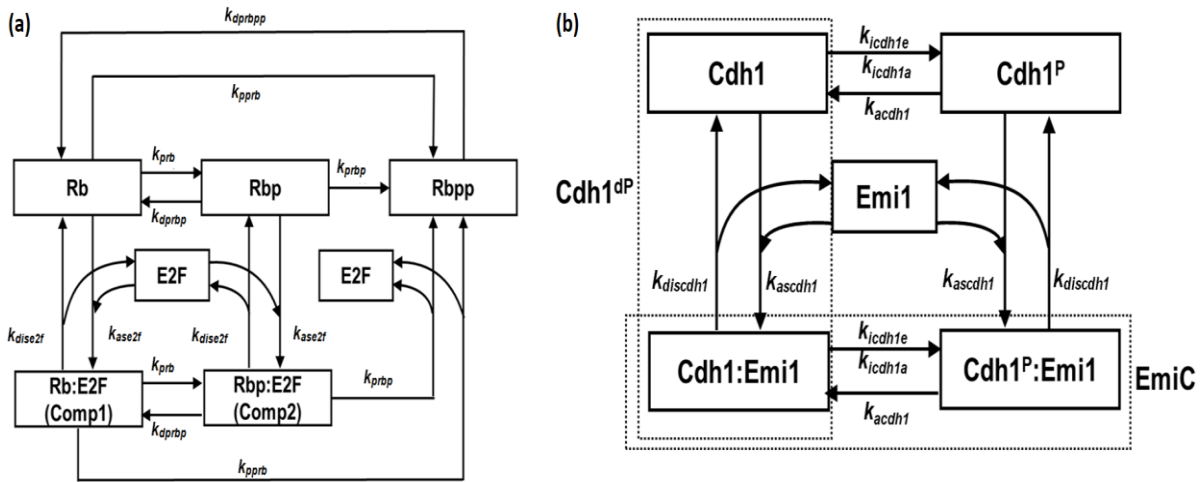


Figure 2.2: (a) The mechanism of Rb phosphorylation and dephosphorylation. Rbp and Rbpp represent the mono-phosphorylated and hyper-phosphorylated forms respectively. (b) The mechanism of APC/C-Cdh1 activation and inactivation, Cdh1^P and Cdh1^{dP} represent the phosphorylated and dephosphorylated forms respectively.

2.3 Methods

The network described in figure 2.1 was translated into a set of non-linear ordinary differential equations (ODEs), which describe the dynamics of individual components. Multi-site phosphorylation and dephosphorylation of Rb and APC/C-Cdh1 were described using Michaelis-Menten kinetics, and E2F dependent synthesis of components (E2F, CycE, Emi1, CycA) were described by Hill equations ($n = 1$), while all other reactions were represented by

the law of mass action. The parameter values were initially taken from an existing mammalian cell cycle model [145]. Model parameter values were refined by simulating the model to capture the single-cell dynamics of reversible transition between quiescence and proliferation in the presence/ absence of mitogen and stress and qualitative behavior of various perturbations [122, 125, 127, 131, 147]. One- and two-parameter bifurcation analyses were performed to study the effect of different parameter values. Models were simulated numerically using XPPAUT, available from <http://www.math.pitt.edu/~bard/xpp/xpp.html>, to obtain the temporal profiles and bifurcation diagrams. The equations and parameter values are presented at the end, in the appendix section (APPENDIX A).

2.4 Results

Different model scenarios were considered based on initial signals (“trigger”) for E2F activation. Earlier models considered that CycD-Cdk4/6 dependent phosphorylation of Rb relieves some E2F that promotes its further increase and CycE accumulation. However, recent evidence showed that CycD-Cdk4/6 promotes the inhibition of E2F by Rb [115]. We explored how CycD and CKI control the Rb-E2F switch under this circumstance. In the presence of mitogen, levels of Myc and CycD increase, CycD overcomes the stoichiometric inhibition by CKI, leading to mono-phosphorylation of Rb. However, the Rb hyper-phosphorylation can depend on the activation of existing CycE-Cdk2 by the inactivation of CKI or/ and on Myc- dependent synthesis of CycE [148]. Similarly, E2F activation after Rb hyper-phosphorylation can depend on its initial levels at the time of Rb hyper-phosphorylation or/ and on Myc-dependent synthesis of E2F [131]. In the first scenario (no Myc-dependent synthesis), Rb hyper-phosphorylation and E2F activation occur prior to the major accumulation of CycE and E2F (Figure 2.3a), which is consistent with the experimental observations by Ekholm et al. (2001) [120]. We also checked the CycD requirement post-G1 entry. Hitomi and Stacey (1999) analyzed at what point in G1 the anti-CycD antibody treatment becomes ineffective for cells emerging out of quiescence and cycling cells [147]. We found that the inhibition of CycD (mimicking anti-Cyclin D treatment) had no effect from the point when the CycE exceeds CKI levels to sustain Rb hyper-phosphorylation and E2F activation (Figure 2.3b). At very low CKI levels, this point coincides with the R-point when cells become independent of mitogen. Therefore, we conclude that CKI levels determine whether mitogen withdrawal and CycD inhibition

become ineffective at the same or different time points in the G1. Such difference has been reported for cells emerging out of quiescence and cycling cells [147].

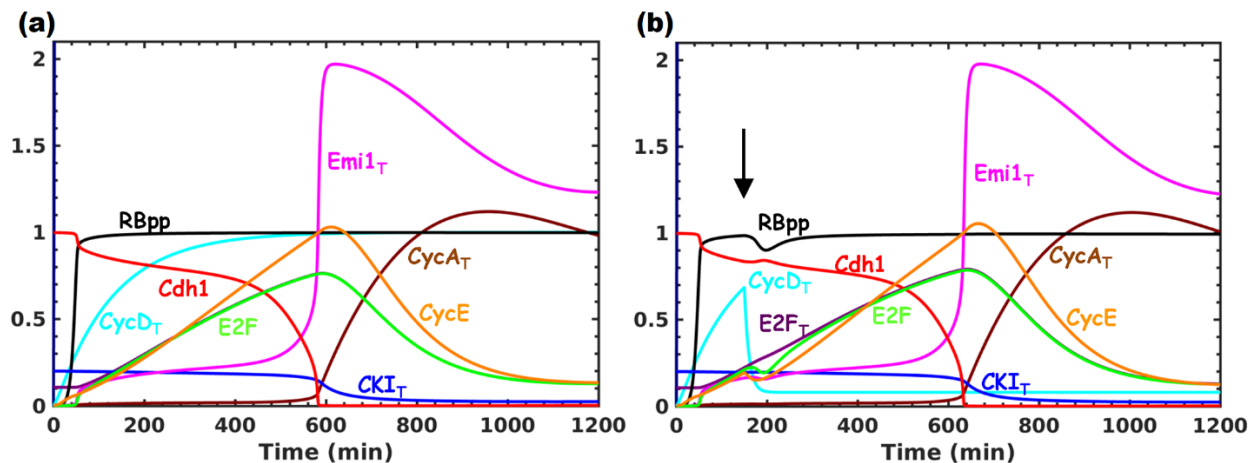


Figure 2.3: Temporal dynamics of quiescence to proliferation in the presence of mitogens. (a) E2F activation depends on its initial levels at the time of Rb hyper-phosphorylation. (b) Inhibition of CycD ($k_{seycdm} = 0$, $k_{seyeds} = 0$) post-G1 entry doesn't delay the dynamics much. Simulations are shown for $S = 1$ (mitogen level). The arrow represents the time of CycD inhibition. RBpp, E2F, CycD_T, CycE, CycA_T, Cdh1, Emi1_T, CKI_T represent hyper-phosphorylated Rb, free E2F, total CycD, free CycE, total CycA, APC/C-Cdh1, total Emi1 and total CDK inhibitor respectively.

In the second scenario (E2F/CycE is not present initially), the E2F (and CycE) accumulation and Rb hyper-phosphorylation are delayed compared to the CycD accumulation and Rb mono-phosphorylation (Figure 2.4a). The exit from quiescence becomes independent of CycD (Figure 2.4b). Recent evidence from the MCF10A cell line and in vivo mice model demonstrate CycE-Cdk2 alone can hyper-phosphorylate Rb at a higher Cdk2 activity threshold in the absence of CycD-Cdk4/6 activity [149]. The location of the mitogen sensitive R-point in these two model scenarios will differ if Rb hyper-phosphorylation and E2F activation are required for the passage of the R-point.

Further, we show that a rise in CycE-Cdk2 activity (in an E2F-dependent manner) initiates APC/C-Cdh1 inactivation and accumulation of Emi1. The upregulation of Emi1 leads to accelerated inactivation of APC/C-Cdh1 and degradation of CKI (Figure 2.3a). Here, the temporal separation between Rb hyper-phosphorylation and APC/C-Cdh1 inactivation is achieved due to the low and high Cdk2 threshold requirement for the substrates, respectively. A slow rise in CycE-Cdk2 activity is important for separating these two phases. A step-wise inactivation of APC/C-Cdh1 is achieved by coupling Emi1 accumulation to the CycE-Cdk2 activity dependent inhibition of APC/C-Cdh1. In the presence of stress signals prior to the

inactivation of APC/C-Cdh1, CKI levels increase, leading to inactivation of CycE-Cdk2 and Rb dephosphorylation (Figure 2.5a). On the other hand, APC/C-Cdh1 inactivation leads to an increase in the degradation rate of CKI in the S-phase, which counteracts the CKI accumulation in the presence of stress, making the G1/S transition irreversible (Figure 2.5b). In the absence of Emi1, APC/C-Cdh1 inactivation slows down (Figure 2.6, solid line), and the inhibition of Cdk2 leads to the re-activation of APC/C-Cdh1 (Figure 2.6, dashed line). This is consistent with the experimental observation by Cappell et al. (2016) [125].

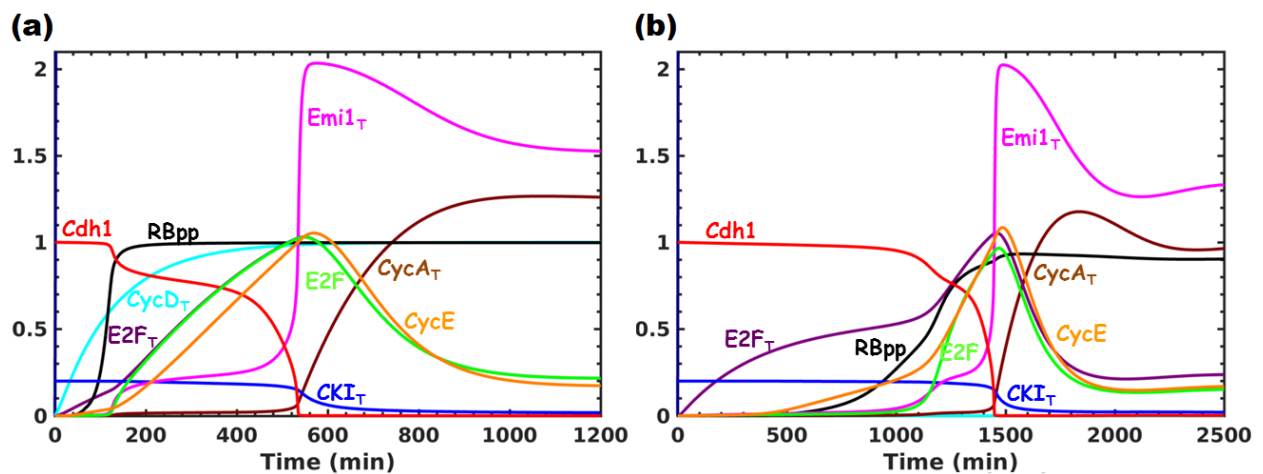


Figure 2.4: Temporal dynamics of quiescence to proliferation in the presence of mitogens. (a) E2F activation depends on Myc-dependent synthesis of E2F, (b) G1/S transition is delayed in the absence of CycD ($k_{scycdm} = 0$, $k_{scyeds} = 0$).

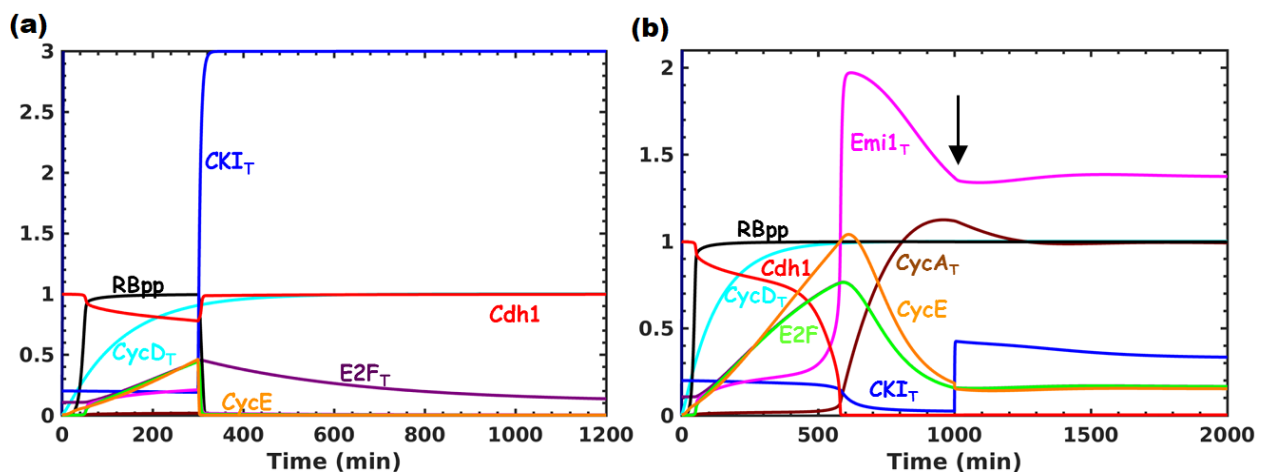


Figure 2.5: Temporal dynamics of proliferation to quiescence in the presence of stress (a) before and (b) after APC/C-Cdh1 inactivation. The arrow represents the time of exposure to stress ($k_{seki} = 0.6$).

We performed the one-parameter bifurcation analysis of Rb-E2F regulation to understand the reversible transition between quiescence and proliferation. We show that the

hyper-phosphorylation of Rb/activation of E2F is irreversible with respect to mitogen, as observed previously (Figure 2.7a) [113]. At higher levels of mitogen, the system is monostable (high E2F state), while at low/intermediate levels of mitogen, the system is bistable (low and high E2F states coexist). We studied the effect of increasing the CKI levels by performing the two-parameter bifurcation analysis. With an increase in the CKI levels, as observed in the presence of stress, the system transits from a high E2F state via bistable region to a low E2F state (shown by an arrow in Figure 2.7b). However, this can be counteracted by increasing the levels of mitogen, which overcomes the CKI stoichiometric inhibition. In the absence of CKI, the system is bistable only for very low levels of mitogen, and for intermediate and high levels of mitogen, the system is in a high E2F state.

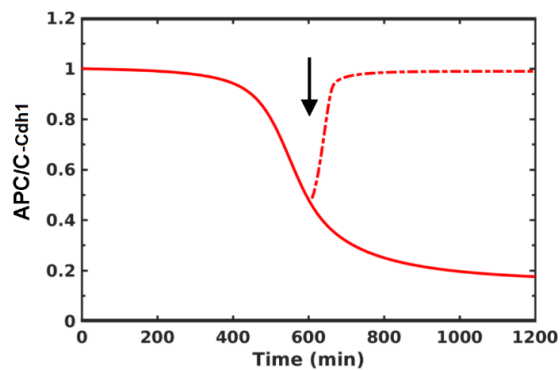


Figure 2.6: The dynamics of APC/C-Cdh1 inactivation in the absence of Emi1 ($k_{semi1} = 0$). The dynamics is shown in the absence (solid line) and presence (dashed line) of Cdk2 inhibition ($k_{deyce} = 0.01$, $k_{deyca} = 0.01$). The arrow represents the time of Cdk2 inhibition.

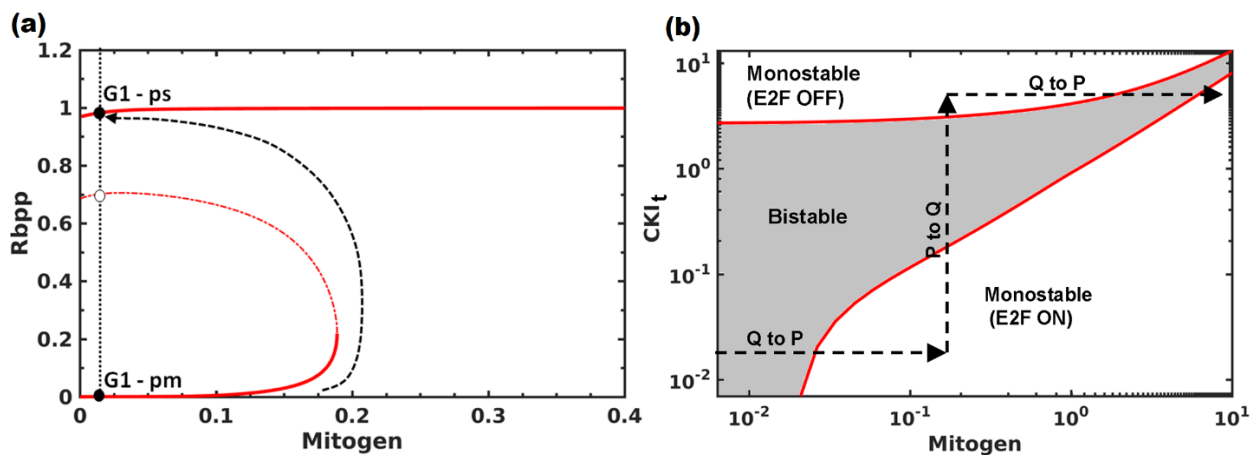


Figure 2.7: Bifurcation analysis of Rb-E2F subsystem. (a) The effect of increasing the levels of mitogen on Rb hyper-phosphorylation (Rbpp). Filled circle represents the stable steady state and empty circle represents the unstable steady state. The arrow shows the transition from mitogen-dependent to independent state. (b) Two parameters bifurcation diagram with different levels of mitogen and total CKI. The monostable and bistable regions are shown (E2F on and off). Q represents quiescence and P represents proliferation.

We also studied the sensitivity of the Rb inactivation/E2F activation threshold to a 5-fold change in parameter values by performing two-parameter bifurcation analyses. The Rb inactivation threshold is most sensitive (steep change in threshold for a small fold change in parameter values) to synthesis/degradation rate of CycE ($k_{scycceb}$, k_{dcyce}) and E2F (k_{se2fb} , k_{de2f}), and Rb total (Figure 2.8a). Further, the Rb inactivation threshold changes gradually (higher slope) with respect to CKI total and degradation rate of CycD (k_{dcycd}). On the other hand, the Rb activation/E2F inactivation threshold is sensitive (for less than 5-fold change) to the dephosphorylation rate of Rb (k_{dprbp}) and shifts to the right (a positive value), bringing mitogen dependence with an increase in k_{dprbp} .

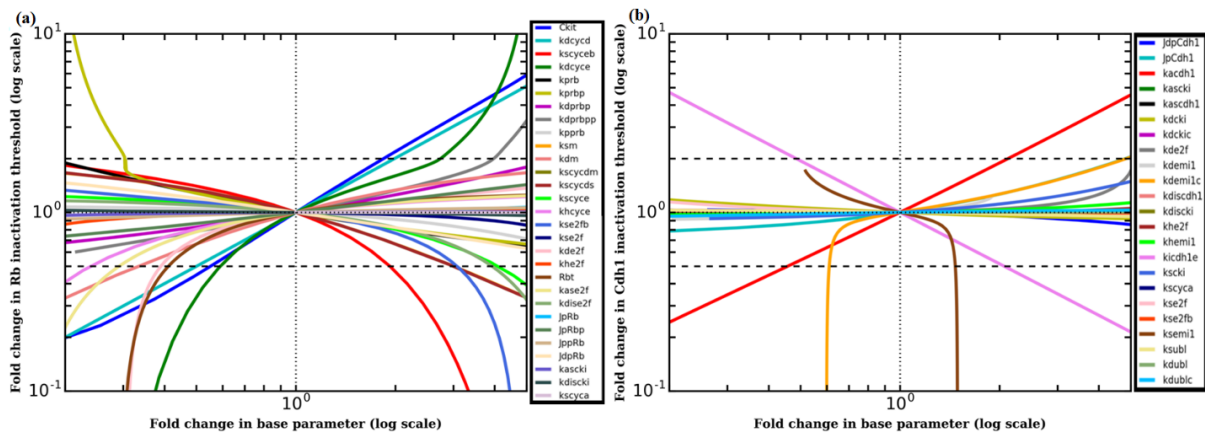


Figure 2.8: (a) The sensitivity of Rb inactivation/E2F activation threshold to 5-fold change in parameter values. The shift in the saddle node corresponding to Rb inactivation/E2F activation threshold is shown for 5-fold increase/decrease in base parameter value. (b) The sensitivity of APC/C-Cdh1 inactivation threshold to 5-fold change in parameter values. The shift in the saddle node corresponding to APC/C-Cdh1 inactivation threshold is shown for 5-fold increase/decrease in base parameter value. The dashed lines (- -) indicate the two-fold change in the threshold and dotted lines (...) indicate the normalized base parameter value and threshold.

Further, we performed the bifurcation analysis of APC/C-Cdh1 regulation at the G1/S transition. Figure 2.9a shows that the CycE-Cdk2 activity initiates APC/C-Cdh1 inactivation but is not required to maintain its inhibition. This depends on the Emi1 accumulation, which is irreversible with respect to CycE-Cdk2 (Figure 2.9b). We also studied the sensitivity of APC/C-Cdh1 inactivation threshold to 5-fold change in parameter values by performing two parameter bifurcation analyses. We observed that the APC/C-Cdh1 inactivation threshold changes steeply with respect to the synthesis (k_{semi1}) and degradation (k_{demi1c}) rates of Emi1 (Figure 2.8b). The APC/C-Cdh1 inactivation threshold also changes gradually with respect to activation (k_{acdh1}) and inactivation (k_{icdh1e}) rates of APC/C-Cdh1. Further, the time window

between Rb hyper-phosphorylation and APC/C-Cdh1 inactivation is also sensitive to these parameter values along with the synthesis rate of CycE (k_{scycE}).

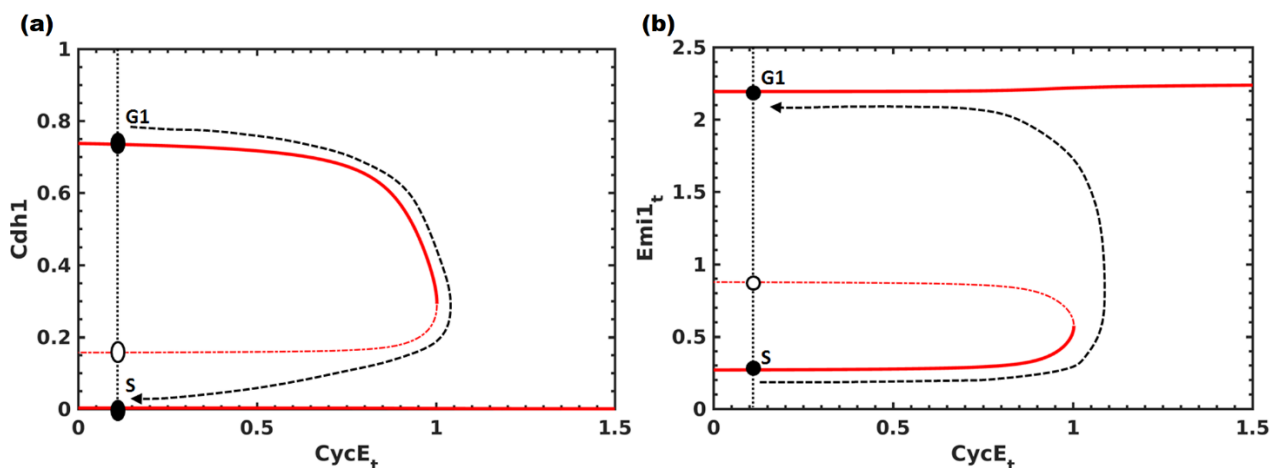


Figure 2.9: Bifurcation analysis of G1/S transition. The effect of increasing CycE-Cdk2 activity on (a) Cdh1 inactivation and (b) Emi1 accumulation are shown. CycE_t represents the total CycE-Cdk2 activity since, Cdk levels are considered abundant and kinase activity is regulated by the binding partner. Filled circle represents the stable steady state and empty circle represents the unstable steady state. The arrow shows the transition from G1 to S-phase.

We also analyzed the behavior of cycling cells that sense the presence of mitogen during the G2 phase of the preceding cell cycle. It is shown that many cells exit mitosis with intermediate Cdk2 activity, keep Rb phosphorylated, and increase the Cdk2 activity to commit immediately to the next cell cycle. On the other hand, a small fraction of cells enters a transient state of quiescence with low Cdk2 activity, and Rb is dephosphorylated [123, 125]. We used the developed framework to understand the control of proliferation to quiescence decision by bifurcation in Cdk2 activity at the mitotic exit. We re-interpret Figure 2.3a by shifting the Y-axis to an intermediate Cdk2 activity where Rb is hyper-phosphorylated to replicate the mitotic exit initial conditions (APC/C-Cdh1 is active, Cdk2 is at an intermediate level, and Emi1 is low) as observed in experiments. The position of the Y-axis is chosen based on the experimental observation that cycling cells commit to the next cycle immediately (~ 4 hrs) by inactivating APC/C-Cdh1 compared to cells coming out of quiescence (~ 8 hrs post R-point) [125]. The initial phase before the mitotic exit (left-hand side of Y-axis) is interpreted as the G2/M phase with re-accumulation of Myc and CycD in the presence of mitogen. Both of them are known to decrease after G1/S transition and increase in G2 only if the mitogen is present [134, 150, 151]. Similarly, in this framework, we assume that both E2F and CycE also re-accumulate after they are degraded in the G1/S

transition. In the absence of mitogen/CycD, the re-accumulation of E2F/CycE is affected, and cells enter into quiescence after mitotic exit even in the absence of CKI. Further, increasing the CKI levels, mimicking the effect of increase in DNA damage that occurs naturally during the DNA replication, also promote entry into quiescence and this can be transient if the CKI levels decrease due to the DNA repair in G1. This picture suggests that an intermediate Cdk2 activity at the mitotic exit is due to an increase in CycE levels through G2/M. However, the recent mapping of protein dynamics has shown that CycE accumulates only after the mitotic exit, which contradicts our interpretations [134]. This can be reconciled if we hypothesize that there is an accumulation of CycE/E2F mRNA, which gets translated at/after the mitotic exit. E2F and CycE levels decrease in S/G2/M due to CycA-Cdk2 activation. However, a rapid inactivation of CycA-Cdk2 at the mitotic exit might lead to a faster rise in CycE that helps maintain an intermediate Cdk2 state. This is also supported by the evidence that in cycling cells, the accumulation of CycE is driven by the re-accumulation of Myc in G2 [148].

Another interesting observation that emerges is whether Cdk2 activity at the mitotic exit exceeds Rb hyper-phosphorylation threshold. This is assumed to explain the immediate inactivation of APC/C-Cdh1 in cycling cells. Alternatively, an increase in the rate of synthesis of proteins in cycling cells compared to cells emerging from quiescence can also explain the faster activation of Cdk2 and inactivation of APC/C-Cdh1. The transcriptional difference can be attributed to the difference in the extent of chromosomal condensation in cells emerging out of quiescence and cycling cells [135].

2.5 Discussion

A mathematical modeling framework was developed to analyze how CycD and CKI control Rb-E2F regulation in two different contexts: quiescence to proliferation and proliferation to quiescence. We also explored how early (E2F activation) and late (APC/C-Cdh1 inactivation) events of G1 are coupled to order the cell cycle progression in cells emerging out of mitogen starvation and in cycling cells. We studied the dynamics in the presence and absence of mitogen and stress.

We showed that CycD-Cdk4/6 by sequestering CKI tilts the CycE-Cdk2 and CKI dynamic balance towards the activation of CycE-Cdk2 and hyper-phosphorylation of Rb (Figure 2.1 and Figure 2.3a). This occurs in spite of CycD-Cdk4/6-dependent mono-phosphorylation of Rb being inhibitory to E2F. Under this condition, we observed that the

length of the G1 phase is controlled by the rate of synthesis of CycE and Emi1. This provides an explanation for the observation that overexpression of CycD does not significantly alter the length of G1 [133]. However, increasing the rate of Myc-dependent synthesis of CycE and E2F makes CycD dispensable for the G0 to G1 transition as observed in some cellular contexts [149, 152, 153]. The entry is delayed, and the activity of E2F (free E2F) shows a delay relative to the total concentration of E2F (Figure 2.4b). Such a delay has been observed experimentally using a reporter for the E2F activity [154].

In CycD dependent situation, we also showed that the point in G1 when cells become independent of CycD is determined by CKI levels. This point coincides (at low CKI levels) or differs (at high CKI levels) with the point in G1 when cells become independent of mitogen (R-point). A difference can emerge since CycD is stable after mitogen withdrawal until S-phase entry. The slow response time ascertains alleviation of the CKI barrier even in the absence of the stimulus. We propose that such a scenario exists in cycling cells due to the endogenous stress in the S-phase or in cells emerging out of quiescence after longer treatment of mitogen withdrawal, both resulting in high CKI levels [123, 132]. Our analysis provides insights into the experimental observations obtained with mitogen withdrawal, anti-CycD treatment, and Cdk4/6 inhibition in cells emerging out of quiescence and in cycling cells [132, 147]. We also showed that increasing mitogen levels overcome the effect of increase in CKI and promote the cell cycle entry (Figure 2.7b). Such a picture explains the observation that longer treatment of mitogen withdrawal requires stronger re-stimulation to exit quiescence [135]. This view is also consistent with the observation that mitogen and DNA-damage mediated signaling compete in G2 to control the cell cycle of daughter cells [132].

At the G1/S boundary, we showed that a double negative feedback loop regulation between APC/C-Cdh1 and Emi1 could make the transition bistable with respect to CycE-Cdk2 (Figure 2.9). E2F-dependent accumulation of Emi1 is insufficient to explain its timely accumulation in the late G1 phase and its action only after APC/C-Cdh1 is initially inactivated by CycE-Cdk2. Further, Emi1 overexpression accelerates APC/C-Cdh1 inactivation, suggesting that its levels should be controlled for the timely inactivation of APC/C-Cdh1 [125, 126]. A delayed accumulation of Emi1 is achieved by considering Emi1 as an APC/C-Cdh1 substrate. Although Emi1 acts as a pseudo-substrate of APC/C-Cdh1 [155], evidences indicate that it can act as a substrate or inhibitor depending on the redox

status and it contains KEN and D-box motifs that are required for APC/C-dependent degradation [140]. Further, it is also shown that mRNAs of *Emi1* and *CycA* accumulate in the late G1 phase. However, proteins fail to accumulate in the anti-oxidant treated cells. This suggests a coordination of reactive oxygen species (ROS) production and metabolism in driving the G1/S transition. *Emi1* is also one of the most pronounced translationally-repressed genes, and relieving its repression is also crucial for its accumulation [156]. These experiments suggest *Emi1* levels are controlled both at the level of its synthesis and degradation for the G1/S transition. Our model prediction that a feedback loop regulation of *Emi1* is required for rapid and switch-like inactivation of APC/C-Cdh1 at the G1/S boundary has been validated [157].

The inactivation of APC/C-Cdh1 is accompanied by the degradation of CKI (Figure 2.3a), which prevents stress mediated exit to quiescence (Figure 2.5b). This explains the experimental observation that stress can induce exit to quiescence until APC/C-Cdh1 is inactivated in MCF10A cells [125]. CKI degradation in S-phase also prevents DNA re-replication [143]. A recent study shows that $CRL4^{Cdt2}$ is a major ubiquitin ligase involved in CKI degradation [123], and its activation depends on the S-phase entry [141]. Direct evidence connecting the activation of $CRL4^{Cdt2}$ to APC/C-Cdh1 inactivation is lacking, which has to be explored experimentally. Further, we showed that a distinct Cdk2 requirement for R-point (low) and APC/C-Cdh1 inactivation (high) creates a window of opportunity for stress mediated exit to quiescence after R-point passage. In cycling cells, we proposed that the Cdk2 activity is at an intermediate level between two thresholds (for Rb hyper-phosphorylation and APC/C-Cdh1 inactivation) at the mitotic exit since early G1 phase events are shifted to G2, and APC/C-Cdh1 is inactivated immediately. Therefore, two independent routes for proliferation to quiescence depending on the mitogen withdrawal (which affects transcriptional program) and replication stress (which affects CKI levels) exist.

Previously, mathematical models were proposed to account for the dynamics of the mammalian cell cycle in full or in parts [113, 123, 127, 145, 158, 159]. The cell cycle models combined Rb-E2F and APC/C-Cdh1 through E2F dependent synthesis of *CycA* that promotes S-phase entry by inactivating APC/C-Cdh1 [145, 158]. However, the kinetics of APC/C-Cdh1 inactivation is unaffected after *CycA* knockdown in MCF10A and HeLa cells [125]. A mathematical model proposed for proliferation-quiescence decision incorporates

Emi1 dependent regulation of APC/C-Cdh1, but relies on CycA-Cdk2 for the switch-like inactivation of APC/C-Cdh1 [159]. This model shows that p21 degradation in S-phase reduces the ability of cells to enter quiescence in response to endogenous DNA damage, but it occurs independent of APC/C-Cdh1 inactivation. However, our model accounts for the experimental findings in MCF10A cells that Emi1 is required for the rapid and irreversible inactivation of APC/C-Cdh1 [125]. We demonstrated that the inactivation of APC/C-Cdh1 promotes CKI degradation to suppress the stress sensitivity. A variation in the regulation can be observed due to the cell-type differences. Further, we also studied the effect of CycD on R-point in different cellular contexts incorporating recent experimental findings [115, 132]. It will be interesting to test the model hypotheses by experiments to further understand the reversible transition between quiescence and proliferation. In summary, our study provides mechanistic insights into both mitogen and stress sensitivity of the mammalian cell cycle and is included in the BioModels database as a curated model (BIOMD0000000954) [160, 161].

In this chapter, we explored the quiescence-proliferation reversible decision-making in MCF10A, a non-transformed cell line, using the mathematical modelling approach. This model framework can be extended to study how various cancers develop and how cancer drug tolerance emerges under treatment. Recent findings suggest that the drug response controls Cyc-Cdk activity via transcription or proteolysis regulation [103–105]. Further, the model can help in the study of cell cycle re-entry in neurodegeneration.

Chapter 3 NETWORK BASED METABOLIC CHARACTERIZATION OF CANCERS

3.1 Introduction

Major biological processes, namely reproduction, development, wound healing and tissue regeneration, require cell proliferation. Cells proliferate in response to growth-promoting stimulus; however, under adverse conditions, they move into a reversible, non-proliferating state termed quiescence. Cells gauge the strength of proliferative and anti-proliferative signals through multiple molecular players described as the cell cycle control system in earlier chapters. Proliferative diseases arise as a consequence of dysregulation of the proliferation to quiescence reversible transition. Cancer is a proliferative disease that affects millions worldwide; around 19.3 million new incidences were reported last year, and 10 million individuals lost their lives [162]. The transcriptional regulation of genes may be altered in cancer due to underlying mutations in the genome or epigenetic changes. The Cancer Genome Atlas (TCGA) hosts large scale molecular data of over 20000 cancer and matched normal samples spanning 33 cancer types [163]. Several studies have analyzed TCGA transcriptome data obtained from different cancers to gain insight into the differential expression of genes in cancer [87, 164, 165].

In addition to cell cycle dysregulation, metabolic reprogramming is an emerging feature of cancer. The rapidly proliferating cancer cells need to replicate their genome, increase the protein and lipid content and assemble them into daughter cells. Hence, metabolic alterations complement proliferation by meeting the high energy and anabolic demand. Initial studies by Otto Warburg pointed to aerobic glycolysis [166]; glycolysis fulfills the ATP requirement and provides carbon for fatty acid, nucleotide synthesis [167]. However, recent advances have started to reveal other metabolic alterations and plasticity of cancer metabolism [168]. Therefore, understanding how the metabolism differs from normal to disease state can elucidate the adaptations which promote cancer progression. Further, these findings may facilitate the screening of metabolic targets for therapeutic purposes. A pan-cancer analysis of different cancer types found a convergent metabolic landscape with upregulated nucleotide synthesis and downregulated mitochondrial metabolism as the main

features [169]. Rosario et al. analyzed the gene expression of metabolic pathways in KEGG and found that pentose and glucuronate interconversions (PGI) is significantly dysregulated in many cancer types while the polyamine synthesis is uniquely upregulated in prostate adenocarcinoma (PRAD) [170]. Peng et al. identified metabolic subtypes in 33 cancer types based on seven major metabolic processes. These metabolic signatures showed clinical relevance and association with somatic drivers [171].

A recent study on TCGA data revealed that the classification of 33 cancer types is dominated by tissue-type or cell-of-origin differences. This provides a basis for a focused pan-cancer analysis of individual tissues to map the cancer subtype-specific changes in the metabolism [172]. In this chapter, we focused on renal cell carcinoma (RCC), which is a heterogeneous cancer with three major histological subtypes viz clear cell (KIRC), papillary (KIRP), and chromophobe (KICH). These RCC subtypes also differ in cell-of-origin, KIRC and KIRP originate from cells of proximal convoluted tubule, whereas KICH develops from cells of distal convoluted tubule of the nephron [173]. A multi-platform genomic data analysis on RCC supported the site of origin as one of the major determinants in the classification of these subtypes [174]. Molecular characterization of RCC further revealed the subtype-specific mutations, methylation, and pathways [175]. RCC subtypes have distinct glycolytic and mitochondrial gene expression patterns. A metabolically divergent (MDD) group with poor survival is identified in KICH. These KICH samples with aggressive nature have been reclassified from KIRC after a histologic review [175]. However, many of the RCC studies have specifically explored metabolic alterations of only KIRC [92, 176]. The pan-RCC studies have either focused on analyzing expression patterns within tumors only and/or restricted the analysis to selective metabolic pathways [174, 175]. Hence, a comprehensive metabolic characterization of RCC subtypes with respect to the normal tissue of origin and including especially the less common KICH and KIRP, is required.

First, we compared the metabolism of RCC with other cancer types using transcriptome data. To study metabolism, we used Genome-scale metabolic model (GEM) that provides a comprehensive view of metabolism and serves as a scaffold for interpreting high throughput data [177]. We observed that RCC subtypes show metabolic divergence from the other cancer samples. Further, cell cycle transcription factors emerged as important regulators of metabolic genes. The analysis showed that E2F1 and FOXM1 are the major

transcriptional activators of upregulated metabolic genes in RCC. To obtain additional insights into the metabolism of RCC subtypes, a network-based analysis was performed by integrating transcriptome data with the human genome-scale metabolic model [177, 178]. Our study revealed the role of amino acid metabolism and redox homeostasis in RCC subtypes in addition to glycolysis and TCA cycle alterations. A difference in glutamine metabolism was observed between subtypes, which is linked to the difference in transcriptional regulation involving HIF1A [179]. Heterogeneity within subtype was explored by extending the analysis to all tumor samples and identifying metabolic network modules based on the co-expression pattern of metabolic genes. We also identified metabolic modules that are linked to clinical traits of RCC subtypes. In summary, we present a comparative picture of the convergent and divergent alterations in cell cycle, metabolism, and redox regulation that support uncontrolled proliferation across RCC subtypes.

3.2 Methods

Preprocessed TCGA RNA-Sequencing (RNA-Seq) expression data spanning 20531 genes across 33 cancer types was retrieved from Genomic Data Commons (GDC) portal (<https://gdc.cancer.gov/>). The analysis was restricted to 14 cancer types based on the threshold of at least 15 tumor matched normal samples (Table 3.1). The human genome-scale metabolic model (HMR version 2.0) was used to study cancer metabolism [177]. HMR2 is a comprehensive model with 8181 reactions, 3161 unique metabolites, and 3765 genes. The log fold change difference in HMR2 gene expression between each tumor and matched normal samples was calculated. The top 10% of metabolic genes based on the variance in fold change across samples were used for performing the principal component analysis (PCA).

To specifically map the metabolic changes of RCC subtypes, the RNA-Seq raw count data of KIRC, KIRP, and KICH were obtained from the GDC portal. We used only pairs of tumor and tumor-adjacent normal samples (25 for KICH, 32 for KIRP, and 72 for KIRC) to perform differential gene expression analysis of HMR2 genes for each subtype using DESeq2, which also performs normalization internally using the median of ratios method [81]. Benjamini-Hochberg method [180] was used to adjust the p-value of genes obtained in the DESeq2 analysis. The adjusted p-value criteria were used to select differentially expressed genes in RCC (adj p-value < 0.05). Transcriptional factor enrichment analysis of these genes was performed using Enrichr [181]. The upregulated and downregulated genes

between tumor and matched normal samples of each subtype were used as target genes. Enrichr provides different gene-set libraries to identify transcription factors from the target gene list. We used multiple libraries, including ChEA and ENCODE_and_ChEA_Consensus_TFs, to identify transcriptional factors associated with upregulated and downregulated genes.

Table 3.1: Number of tumor and tumor-adjacent normal samples of 14 cancer types used for the principal component analysis. BLCA - Bladder Urothelial Carcinoma, BRCA - Breast invasive carcinoma, COAD - Colon adenocarcinoma, HNSC - Head and Neck squamous cell carcinoma, KICH - Kidney Chromophobe, KIRC - Kidney renal clear cell carcinoma, KIRP - Kidney renal papillary cell carcinoma, LIHC - Liver hepatocellular carcinoma, LUAD - Lung adenocarcinoma, LUSC - Lung squamous cell carcinoma, PRAD - Prostate adenocarcinoma, STAD - Stomach adenocarcinoma, THCA - Thyroid carcinoma, UCEC - Uterine Corpus Endometrial Carcinoma.

TCGA Project	BLCA	BRCA	COAD	HNSC	KICH	KIRC	KIRP	LIHC	LUAD	LUSC	PRAD	STAD	THCA	UCEC
Normal	19	113	40	43	25	72	32	50	58	51	52	32	59	22

The adjusted p-value of metabolic genes was also used to integrate the gene expression and the genome-scale metabolic model to identify reporter metabolites by the reporter metabolite algorithm (RMA) [178]. This method transforms the p-values into Z-scores using the inverse normal distribution function and scores a metabolite based on aggregating Z scores of its k neighboring genes:

$$Z_{metabolite} = \frac{1}{\sqrt{k}} \sum_{i=1}^k Z_i \quad (\text{Eqn. 3.1})$$

The Z score of each metabolite was corrected for background distribution. 100000 sets of k genes were chosen at random to compute mean (μ_k) and standard deviation (σ_k).

$$Z_{metabolite}^{corrected} = \frac{Z_{metabolite} - \mu_k}{\sigma_k} \quad (\text{Eqn. 3.2})$$

Corrected Z scores were used for the p-value calculation. This method assumes that genes linked to the metabolite are co-expressed. Further, reporter pathways were also identified by aggregating the score of n metabolites of a pathway [182].

$$Z_{pathway}^m = \frac{1}{\sqrt{n}} \sum_{metabolite=1}^n Z_{metabolite} \quad (\text{Eqn. 3.3})$$

We identified the direction of change of reporter pathways by performing the analysis with only upregulated or downregulated genes in each subtype.

Since RMA was performed between only tumor and tumor-adjacent normal samples, we extended our study to analyze the co-expression pattern of metabolic genes in all available RCC samples (81 KICH, 290 KIRP, and 518 KIRC samples) in the GDC portal. This was done to understand the variations within the tumor samples and to map the tumor-stage specific changes. Co-expression networks of HMR2 genes were constructed for KICH, KIRC, and KIRP by performing the Weighted Gene Co-expression Network Analysis (WGCNA) in R [183]. WGCNA organizes the co-expressing genes into modules of functional pathways. Pearson correlations between gene expression levels were computed to construct the correlation matrix. The sign of correlations was retained by performing a linear transformation using the equation given below (Eqn. 3.4).

$$S_{ij} = \frac{1 + \text{cor}(x_i, x_j)}{2} \quad (\text{Eqn. 3.4})$$

A weighted adjacency matrix was constructed using a function $a_{ij} = S_{ij}^\beta$, where β represents soft-threshold power that is calculated by a scale-free topology criterion. Biological networks have few hub nodes, which have a higher degree. Such networks adhere to a power law of degree distribution. Here, the number of nodes having degree k decreases exponentially with an increase in k . These networks are called scale free because power laws have the same functional form at all scales. The coefficient of determination (R^2) between $\log(p(k))$ and $\log(k)$ measures how well a network satisfies a scale free topology criterion. $p(k)$ is the frequency distribution of the degree k . The relationship between R^2 and β is characterized by a saturation curve. The value of β is determined by scanning over a range (say $\beta=1-20$), and the lowest value where the saturation is reached is considered for the analysis. We obtained $\beta = 14$ for KIRC and $\beta = 12$ for KIRP and KICH. A topological overlap matrix (TOM) was obtained from the adjacency matrix, and hierarchical clustering was performed using a distance measure $1-\text{TOM}$ [184]. Modules of minimum size 100 were identified using the dynamic tree cut algorithm [185]. The module eigengene (ME) expression value was obtained using Singular Value Decomposition (SVD) [186]. Pearson's correlation between ME values and clinical traits: disease (normal-0, tumor-1), stage (normal-0, stage I-1, stage II-2, stage III-3, stage IV-4), and survival data, were calculated to

identify relevant tumor modules [183]. We performed a hypergeometric test to identify HMR2 metabolic pathways associated with the modules. Eigengene expression values of individual pathways of significant modules were also visualized to confirm the stage-specific changes.

3.3 Results

3.3.1 RCC shows high variation in metabolism compared to other cancer types

We screened 14 cancer types from TCGA based on the availability of RNA-Seq data of both tumor and tumor-adjacent normal samples (668 samples) (Table 3.1). The human genome-scale metabolic model HMR2 was used to study the metabolic differences between different cancers. The fold change in the gene expression between each tumor and matched normal samples was used to cluster cancers. The degree of similarity and extent of heterogeneity in metabolic adaptations between different cancer types was explored. The log fold change was used to eliminate the tissue-of-origin differences between cancer types. The PCA across 14 cancer types revealed that RCC samples have high variance compared to other tumor samples (Figure 3.1). RCC samples KIRC and KIRP cluster together and segregate from non-RCC samples along principal component 1 (PC1) and KICH samples along PC2. Unique features of RCC subtypes make them a suitable candidate for further investigation.

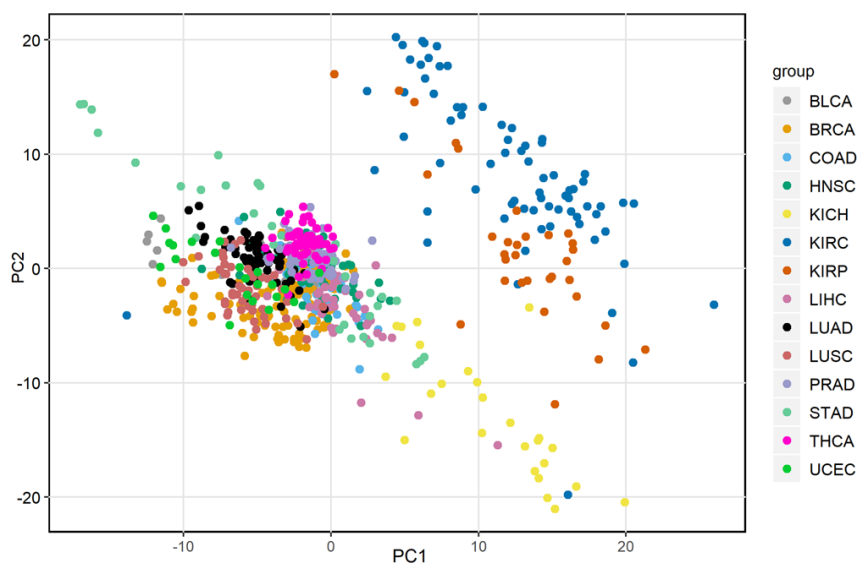


Figure 3.1: Principal component analysis (PCA) of 14 cancer types. The log fold-change in expression of top 10% highly varying HMR2 genes (361) between tumor and matched normal samples was used to perform the PCA.

3.3.2 Reporter metabolic pathways in RCC subtypes

The differential gene expression (DGE) analysis between tumor and matched normal samples showed that metabolic genes were predominately downregulated in RCC subtypes (Table 3.2). We performed the transcriptional factor enrichment analysis of differentially expressed genes [181]. The downregulated genes were associated with HNF4A, LXR, RXR, and PPARA in RCC (adj p-value < 0.05) (Table 3.3). The upregulated genes were associated with E2F1 and FOXM1 in RCC and with HIF1A in KIRC and KIRP (adj p-value < 0.05) (Table 3.4). The expression of E2F1 and FOXM1 are upregulated in the RCC samples (Figure 3.2). The survival analysis based on E2F1 and FOXM1 expression level shows a significant survival difference, with the low expression group having a higher overall survival probability (Figure 3.3). We characterized the metabolic network-based alterations of RCC by mapping the gene expression changes to the reactions in HMR2 and identified reporter metabolites and pathways [178, 182]. Figure 3.4 shows the reporter pathways of KICH, KIRC, and KIRP.

Table 3.2: Differentially expressed genes ($|\log_2(\text{FC})| \geq 1$ and adj p-value ≤ 0.05) between normal and cancer samples.

RCC subtype	No. of up regulated genes	No. of down regulated genes
KICH	516	692
KIRC	413	579
KIRP	378	483

Table 3.3: Transcription factor enrichment of downregulated genes using Enrichr [181].

Library	Terms	Gene coverage	Transcription Factor (TF)	KICH (adj p-val)	KIRC (adj p-val)	KIRP (adj p-val)
ARCHS4_TFs_Coexp	1724	25983	HNF4A	2.37E-34	2.31E-15	1.97E-17
ChEA_2016	645	49238	HNF4A	1.18E-17	1.68E-20	1.91E-15
			LXR	7.27E-17	9.34E-15	5.36E-14
			RXR	2.01E-17	8.90E-16	7.10E-15
			PPARA	1.39E-11	4.23E-11	1.27E-09
ENCODE_and_ChEA_Con sensus_TFs_from_ChIP-X	104	15562	HNF4A	4.00E-10	4.11E-06	5.41E-06
TF_Perturbations_ Followed_by_Expression	1958	19741	HNF4A	2.18E-29	1.69E-30	1.20E-27
			PPARA	1.18E-22	1.17E-34	2.53E-24

Table 3.4: Transcription factor enrichment of upregulated genes using Enrichr [181].

Library	Terms	Gene coverage	Transcription Factor (TF)	KICH (adj p-val)	KIRC (adj p-val)	KIRP (adj p-val)
ARCHS4_TFs_Coexp	1724	25983	HIF1A	-----	0.003	0.0015
			E2F1	1.87E-09	5.77E-07	5.05E-16
			FOXM1	1.16E-11	5.1E-08	3.37E-16
ChEA_2016	645	49238	HIF1A	-----	8.83E-07	-----
			E2F1	4.56E-07	-----	-----
			FOXM1	0.030571	-----	0.0415
ENCODE_and_ChEA_Con sensus_TFs_from_ChIP-X	104	15562	E2F1	3.12E-10	-----	3.12E-06
TF_Perturbations_Followed_by_Expression	1958	19741	HIF1A	-----	3.29E-10	2.01E-04
			E2F1	1.18E-07	1.34E-04	1.63E-06
			FOXM1	7.02E-06	-----	0.0148

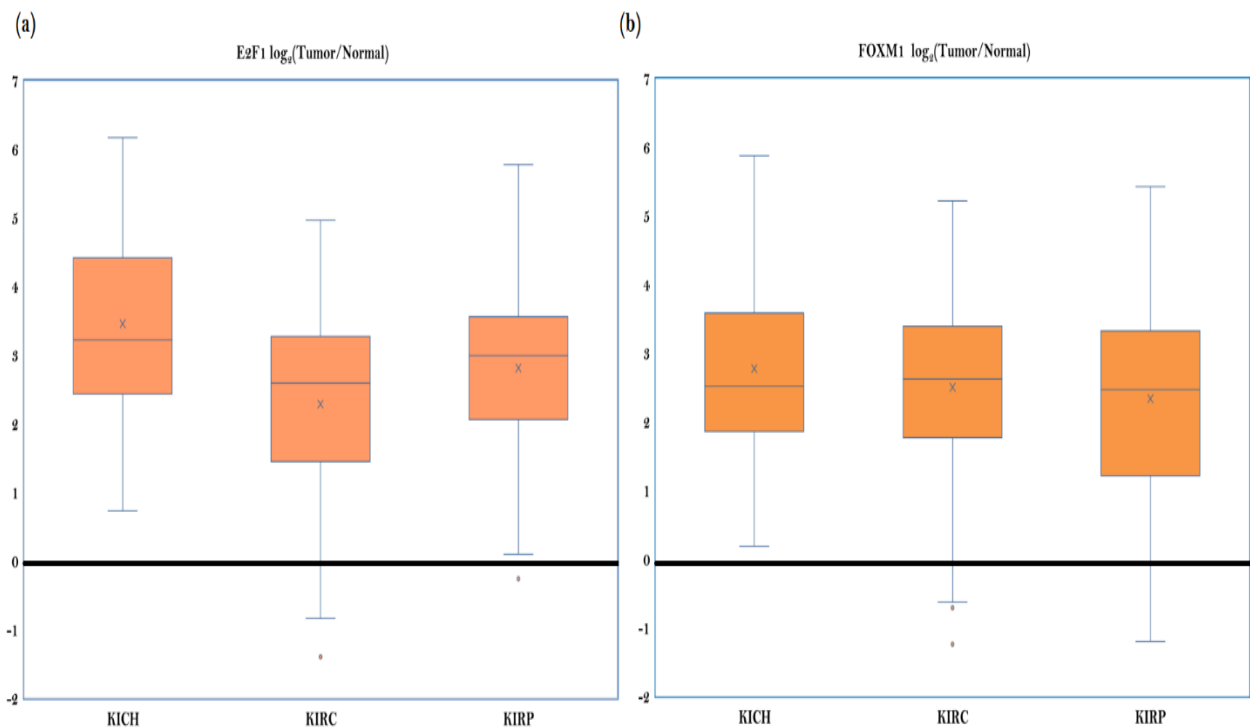


Figure 3.2: Box and whisker plot representing sample wise distribution of (a) E2F1 and (b) FOXM1 expression data for RCC subtypes. As the values are log transformed to the base 2, four-fold change is measured as 2. The lower and upper whiskers represent minimum and maximum value respectively, circles represent outliers. Boundary of box represents first and third quartile range, mean is represented by ‘x’ and median by ‘—’.

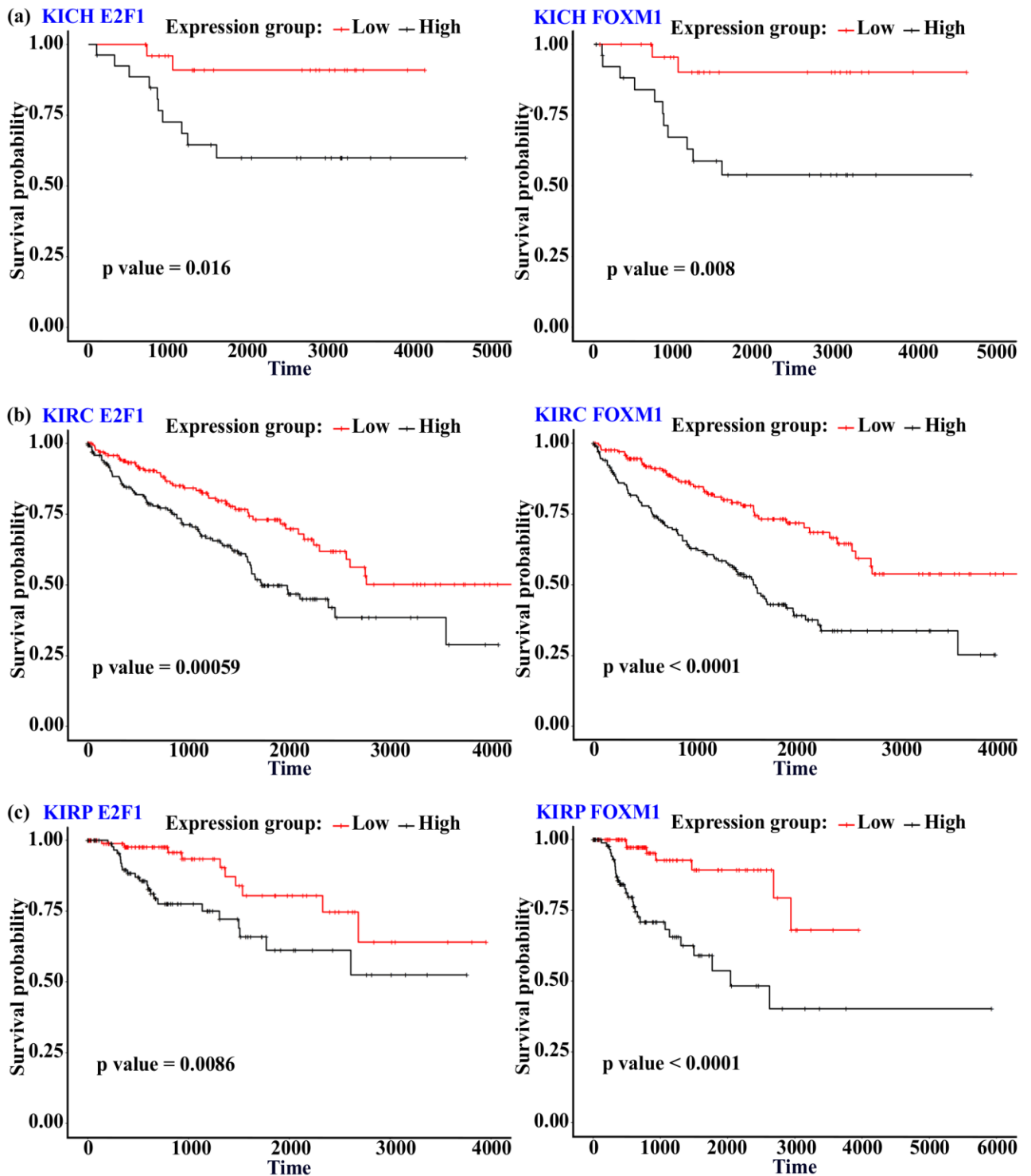


Figure 3.3: Survival analysis using E2F1 and FOXM1 as a prognostic marker. Overall survival between low expression group (red) and high expression group (black) for (a) KICH (b) KIRC (c) KIRP show significant difference; the high expression group has a lower survival probability. The survival difference between low and high expression group was evaluated by Kaplan-Meier (KM) method [187] using the survival package in R [188].

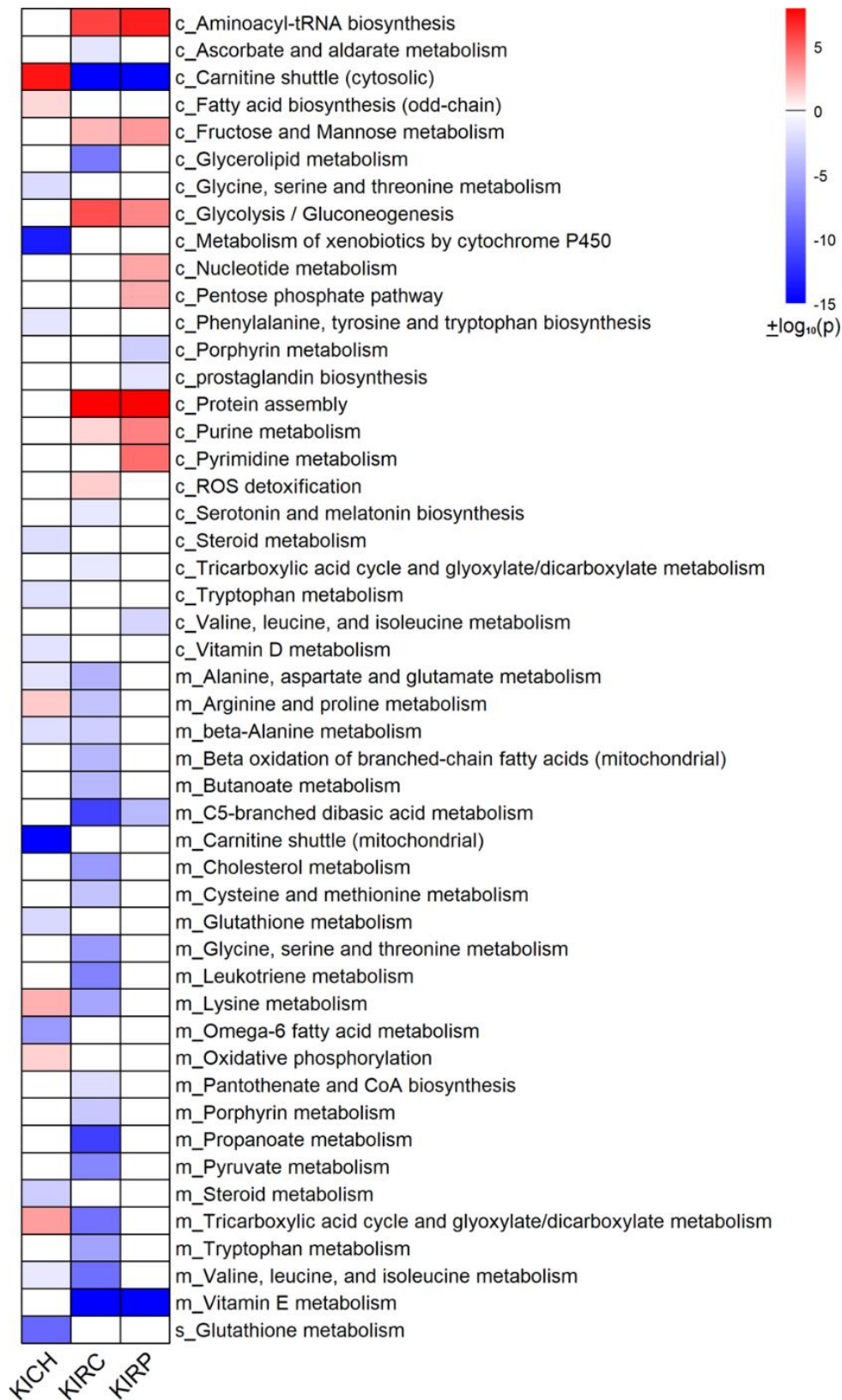


Figure 3.4: Reporter pathways of KICH, KIRC and KIRP. Red denotes upregulated and blue denotes downregulated pathways. The prefix c, m and s correspond to cytosol, mitochondria and extra-cellular compartment, respectively. p-values are log transformed ($-\log_{10}p$) and minus (-) was used to represent the downregulation of pathway.

One carbon metabolism

We found that the glycine, serine and threonine metabolism was downregulated in KICH. Serine and glycine provide one-carbon units to the folate cycle through one-carbon metabolism [189]. Further, conversion of choline, another source of one-carbon units, into glycine was downregulated (BHMT, CHDH, DMGDH, SARDH). The one-carbon metabolism was also downregulated in KIRC. However, a compartment-specific change was observed in RCC subtypes (Figure 3.4). We found that genes encoding cytosolic enzymes of the folate cycle (SHMT1, MTHFR) were downregulated while mitochondrial genes (SHMT2, MTHFD2) were upregulated in KICH (Figure 3.5). These mitochondrial genes were also upregulated in KIRP. On the other hand, both cytosolic and mitochondrial genes of the folate cycle were downregulated in KIRC. Further, genes involved in the methionine cycle (BHMT, MAT1A, MAT2A) and methionine salvage pathway (ADI1, AMD1, TAT) were downregulated in KICH. We also found most of these genes were downregulated in KIRP and KIRC.

Glutathione metabolism

Serine and glycine are also precursors for glutathione synthesis. We found that extracellular glutathione metabolism was downregulated in KICH (Figure 3.4). Genes of glutathione salvage pathway, gamma-glutamyl transferases (GGT1, GGT2, and GGT5), alanyl aminopeptidase (ANPEP), and glutathione S-transferases (GSTA1, GSTA5, GSTM1, GSTM2, GSTT2) were downregulated. However, we observed that the gene involved in the *de novo* synthesis of glutathione was upregulated (GCLC) in KICH (Figure 3.5). This pathway requires cysteine and glutamate, which in turn might depend on the extracellular uptake of these amino acids. We found that the cysteine/glutamate transporter SLC7A11 was significantly upregulated in RCC subtypes. Further, KIRP and KIRC also showed similar alterations in glutathione metabolism. However, genes of *de novo* synthesis were unaltered in KIRC.

Aromatic amino acid metabolism

The metabolism of aromatic amino acids was altered in RCC (Figure 3.4). We observed that phenylalanine, tyrosine and tryptophan biosynthesis and tryptophan metabolism were downregulated. Phenylalanine and tryptophan are essential amino acids, while tyrosine

is produced *in vivo*. Phenylalanine hydroxylase (PAH) gene involved in tyrosine synthesis from phenylalanine was significantly downregulated in RCC. Genes involved in the conversion of tryptophan into serotonin and tryptamine (TPH1, DDC) were also downregulated. However, indoleamine 2, 3-dioxygenase 1 (IDO1), and tryptophan 2, 3-dioxygenase 2 (TDO2) genes involved in the first step of the tryptophan/kynurenine pathway were upregulated in all three subtypes.

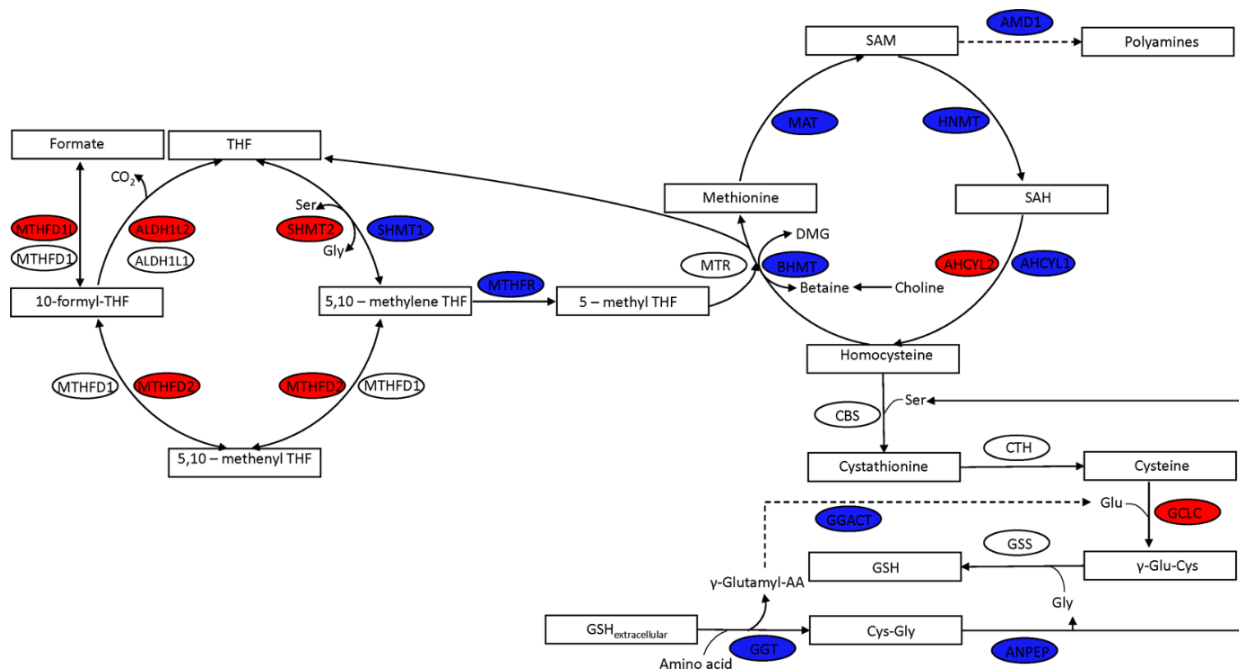


Figure 3.5: One carbon metabolism is affected in KICH. The expression of genes involved in folate cycle, methionine cycle and glutathione synthesis are altered. Downregulated genes are shown in blue while upregulated genes are shown in red color.

Alanine, aspartate and glutamate metabolism

Genes involved in the conversion of alanine to pyruvate (AGXT, AGXT2, and GPT), aspartate to L-arginino-succinate (ASS1), glutamine to glutamate (GLS), glutamate to α -ketoglutarate (GLUD2) and glutamate to succinate route (GAD, GABAT, SSADH) were downregulated in RCC. Interestingly, genes involved in the interconversion of oxaloacetate and aspartate (cytosol: GOT1, mitochondrial: GOT2) were upregulated only in KICH (Figure 3.6), while downregulated in KIRC. In this pathway, glutamate is converted to α -ketoglutarate and aspartate in mitochondria by GOT2 and aspartate is converted into oxaloacetate (OAA) in the cytosol by GOT1 [190]. ASNS involved in the conversion of

aspartate to asparagine was upregulated in RCC. Further, the gene encoding malate dehydrogenase enzyme, MDH2 was also upregulated which suggests that aspartate-malate shuttle is affected in KICH. Additionally, mitochondrial NADP-dependent malic enzyme ME3 involved in the conversion of malate to pyruvate was upregulated. This reaction is associated with NADPH production and maintenance of redox [191]. Despite overall downregulation of branched chain amino acids metabolism in RCC (Figure 3.4), the expression of branched chain aminotransferase (BCAT1), the first gene of this pathway, was upregulated in RCC (Figure 3.6). This reaction generates glutamate as a byproduct, which can support *de novo* glutathione biosynthesis or anaplerotic reactions.

Arginine and proline metabolism

Genes involved in arginine and proline metabolism and polyamine synthesis were downregulated in RCC. Ornithine decarboxylase (ODC1), the rate limiting enzyme of polyamine synthesis, was downregulated in KICH and KIRC. An alternative route to polyamines generation from arginine via agmatine was also affected since genes encoding arginine decarboxylase (AZIN2), and agmatinase (AGMAT) were downregulated. Further, genes that participate in the urea cycle, namely nitric oxide synthase (NOS), arginase 2 (ARG2) and ornithine transcarbamylase (OTC), were also downregulated in RCC. These genes control the conversion of arginine to citrulline, arginine to ornithine, and ornithine to citrulline, respectively. However, in KICH, we observed that OTC was upregulated.

Central carbon metabolism

Glycolysis/ gluconeogenesis pathway and fructose and mannose metabolism were upregulated only in KIRP and KIRC. HIF1A target genes of the glycolytic pathway (GLUT1, HK2, HK3, ALDOA, GAPDH, PGK1, ENO1, LDHA, and PDK1) were upregulated. On the other hand, the TCA cycle and oxidative phosphorylation were upregulated in KICH (Figure 3.4 and Figure 3.6). Further, genes involved in pyruvate to acetyl-CoA conversion (DLAT, PDH) and acetate to acetyl-CoA (ACSS1, ACSS3) conversion were upregulated in KICH and were downregulated in KIRC and KIRP. However, genes involved in the conversion of pyruvate to oxoacetate (PC) and oxoacetate to PEP (PCK1, PCK2) were downregulated in RCC. UDP glucuronosyltransferase family genes were mostly downregulated in KICH and KIRP while upregulated in KIRC. These genes participate in the interconversion of D-

glucuronate and UDP-D-glucuronate. The pentose phosphate pathway, purine and pyrimidine metabolism were also upregulated in KIRP (Figure 3.4).

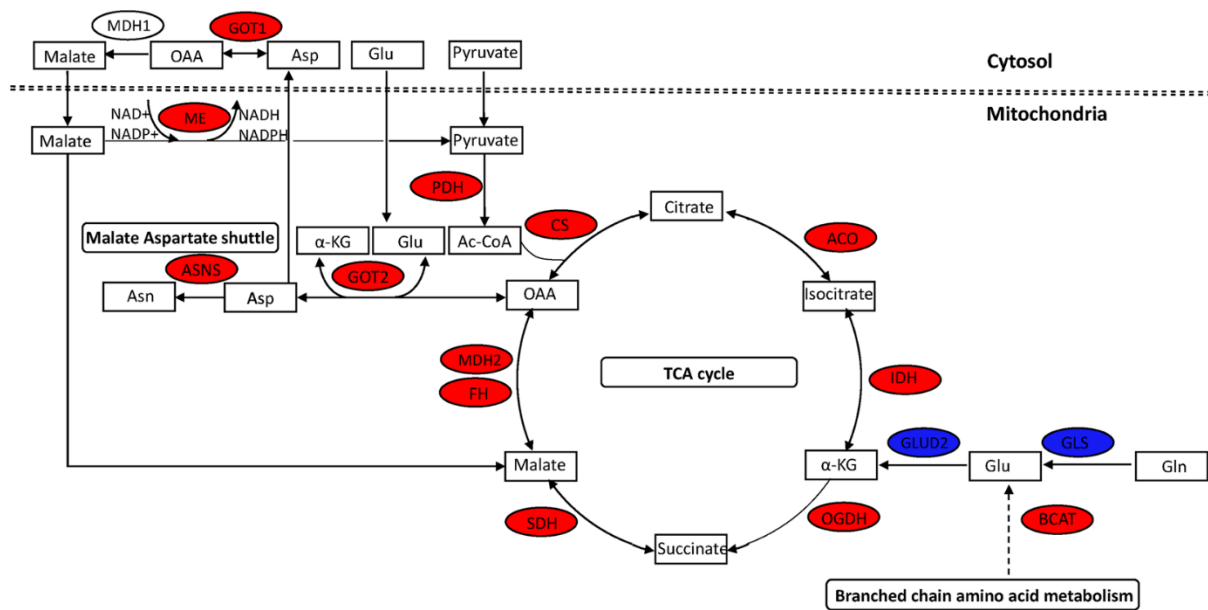


Figure 3.6: Mitochondrial metabolism is altered in KICH; genes of malate-aspartate shuttle, aspartate synthesis and TCA cycle are upregulated (red) while glutamine metabolism genes are downregulated (blue).

Fatty acid metabolism

Fatty acid synthase (FASN) was upregulated in KICH and KIRP. Genes of fatty acid degradation, ketogenesis (HMGCS2), cholesterol metabolism (CYP7A1, CYP8B1, CYP27B1), steroid hormone synthesis, lipid transport (APOA1, APOA2, and APOA5), and carnitine shuttle were downregulated, suggesting altered lipid metabolism in RCC. Further, the metabolism of xenobiotics by cytochrome P450 was also downregulated in KICH. Although most genes of this pathway were downregulated, few members of the cytochrome P450 superfamily with known links to cancer were upregulated in KICH (CYP1A1, CYP3A4, CYP3A7) [192].

3.3.3 Co-expression of metabolic genes in RCC

In the previous analysis, we considered only the tumor and matched normal samples to identify reporter metabolic pathways. We extended this study to include all the available samples of RCC to understand the variations within tumor samples at the level of

metabolism. We performed unsupervised WGCNA to identify modules of co-expressed genes and explored their variation in a cancer-stage specific manner. We identified 7 metabolic modules in KICH, which showed disease- and stage-specific changes. M5_CH, M6_CH, and M7_CH modules showed a negative correlation with the disease, while M1_CH, M2_CH, and M3_CH modules showed a positive correlation with the disease (Table 3.5). The M5_CH module was downregulated in most tumor samples (Figure 3.7), while M6_CH and M7_CH modules showed differences with respect to a few late-stage samples that resembled normal samples. Interestingly, these late-stage samples correspond to the six recently reported as the metabolically divergent KICH (KICH-MDD) samples [175]. Major pathways associated with each module are provided in Table 3.5. The M5_CH module included downregulated reporter metabolic pathways. The M6_CH module was associated with protein modification and glycosphingolipid metabolism, while the M7_CH module was associated with sphingolipid metabolism and starch and sucrose metabolism. Both these modules showed a significant correlation with the overall survival time (Table 3.5).

The upregulated M1_CH and M2_CH modules also showed differences with respect to KICH-MDD samples. These late-stage samples resembled normal samples. The M2_CH module was associated with oxidative phosphorylation, while the M1_CH module was associated with propanoate metabolism, valine, leucine, and isoleucine metabolism, tricarboxylic acid cycle, and glyoxylate dicarboxylate metabolism (Table 3.5). Further, this module included genes (GOT1, GOT2, BCAT1, and GCLC) that were found to be dysregulated in our study. We found that genes of alanine, aspartate and glutamate metabolism, glutathione metabolism, and propanoate metabolism can distinguish KICH-MDD samples (Figure 3.8). Both M1_CH and M2_CH modules showed a significant correlation with stages and overall survival time. The M3_CH module showed a higher stage-specific correlation and was associated with aminoacyl-tRNA biosynthesis and isolated reactions in HMR2 corresponding to cell cycle genes (Table 3.5). This module also included metabolic genes involved in pyrimidine metabolism (POLA2, RRM2, POLD1, POLE2, POLR3D, CAD, POLR3G, POLE), glycosaminoglycan metabolism (CHPF, CHPF2, B3GAT2, B3GALT6, CHSY3, CHST14), amino acid metabolism (DNMT1, SHMT2, MTHFD2, DNMT3B, TYMS, SRM, TDO2, ASNS) and lipid metabolism (FASN, ELOVL5, NRF1, FADS2, SQLE, CYP2R1, P4HB). We observed that the M3_CH module was specific to KICH-MDD.

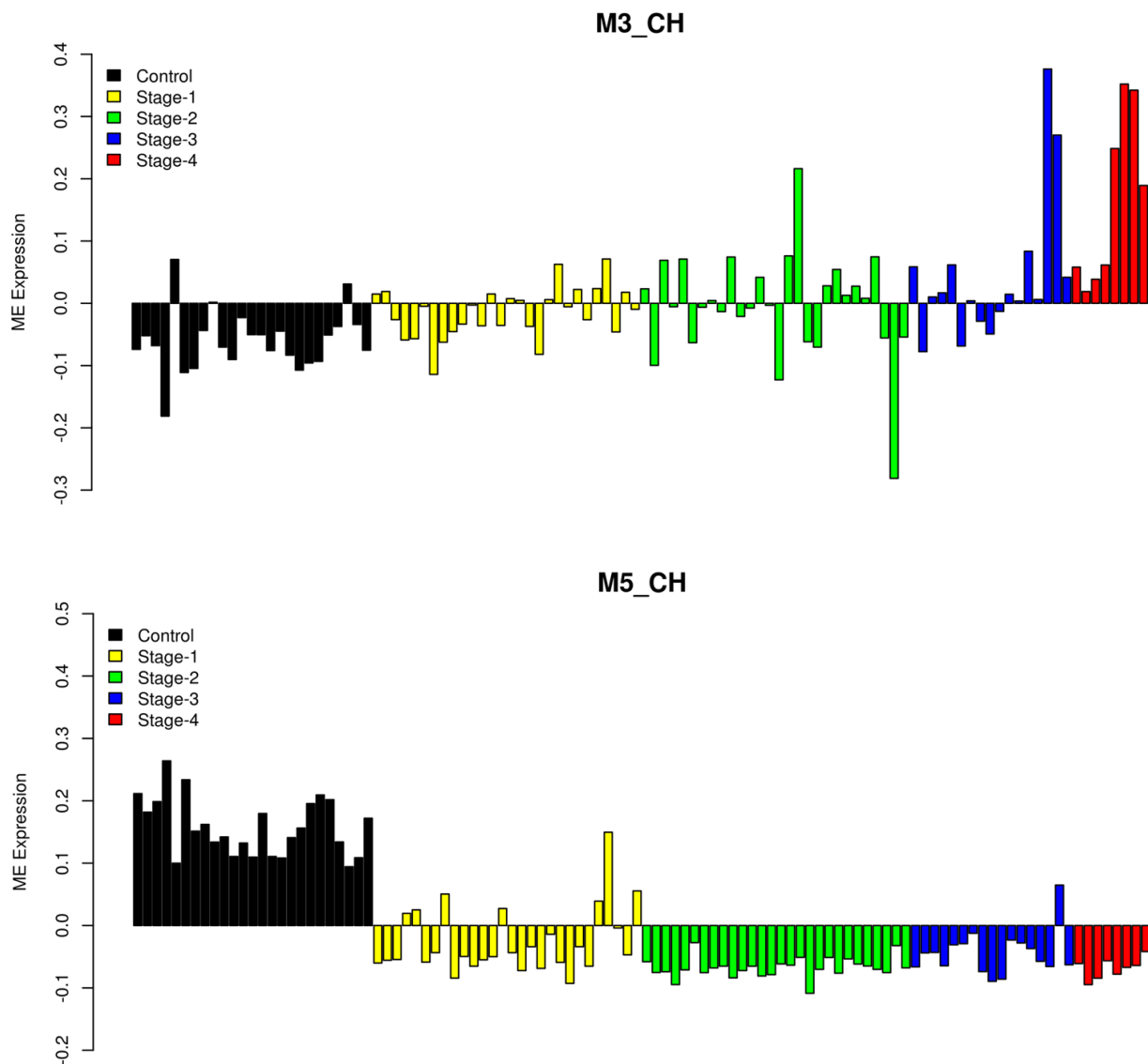


Figure 3.7: Eigengene (ME) expression profile (y-axis) of KICH metabolic modules M3_CH and M5_CH, x axis represents 25 normal and 81 KICH samples.

We identified metabolic modules of KIRP that showed disease- and stage-specific changes. M1_RP, M2_RP, M3_RP, and M4_RP modules showed a negative correlation with the disease while M5_RP, M6_RP, M7_RP, and M8_RP modules showed a positive correlation with the disease (Table 3.6). KIRP samples showed a heterogeneous behavior in different modules. The modules were either upregulated or downregulated in only some KIRP samples from different stages. The M2_RP module was associated with many reporter metabolic pathways, and the M1_RP module was associated with the tricarboxylic acid cycle and glyoxylate dicarboxylate metabolism and oxidative phosphorylation (Table 3.6).

Table 3.5: Pearson correlation value between module eigengene expression value and disease, stages and overall survival for KICH. p-value is given inside the bracket; HMR2 metabolic pathways associated with each module and their corresponding p-value are provided.

Module (Size)	Disease	Stage	Overall Survival	Pathways
M1_CH (755)	0.59 (3e-11)	0.27 (0.006)	0.31 (0.005)	Propanoate metabolism (1.9E-3), Valine, leucine, and isoleucine metabolism (3.1E-3), Tricarboxylic acid cycle and glyoxylate dicarboxylate metabolism (1.8E-2)
M2_CH (455)	0.54 (2e-9)	0.37 (9e-5)	0.34 (0.002)	Oxidative phosphorylation (1.1E-14), Nucleotide metabolism (2.2E-3), N-glycan metabolism (9.3E-3)
M3_CH (269)	0.35 (3e-4)	0.54 (2e-9)	-0.22 (0.05)	Isolated (2.8E-3), Lysine metabolism (3.5E-3), Aminoacyl-tRNA biosynthesis (8.4E-3), Chondroitin heparan sulfate biosynthesis (1.5E-2)
M4_CH (352)	-0.33 (7e-4)	-0.21 (0.03)	-0.26 (0.02)	Isolated (1.4E-12), Transport, Golgi apparatus (4.6E-4)
M5_CH (1138)	-0.9 (9e-40)	-0.72 (7e-18)	-0.18 (0.1)	Metabolism of xenobiotics by cytochrome P450 (4.6E-13), Glycine, serine and threonine metabolism (3.7E-7), Alanine, aspartate and glutamate metabolism (1.9E-4)
M6_CH (227)	-0.32 (8e-4)	-0.11 (0.2)	-0.32 (0.004)	Protein modification (2.3E-6), Chondroitin heparan sulfate biosynthesis (2.0E-3), Glycosphingolipid metabolism (4.3E-2)
M7_CH (413)	-0.69 (2e-16)	-0.39 (3e-5)	-0.44 (4e-5)	Nucleotide metabolism (2.8E-4), Sphingolipid metabolism (8.5E-3), Starch and sucrose metabolism (2.9E-2)

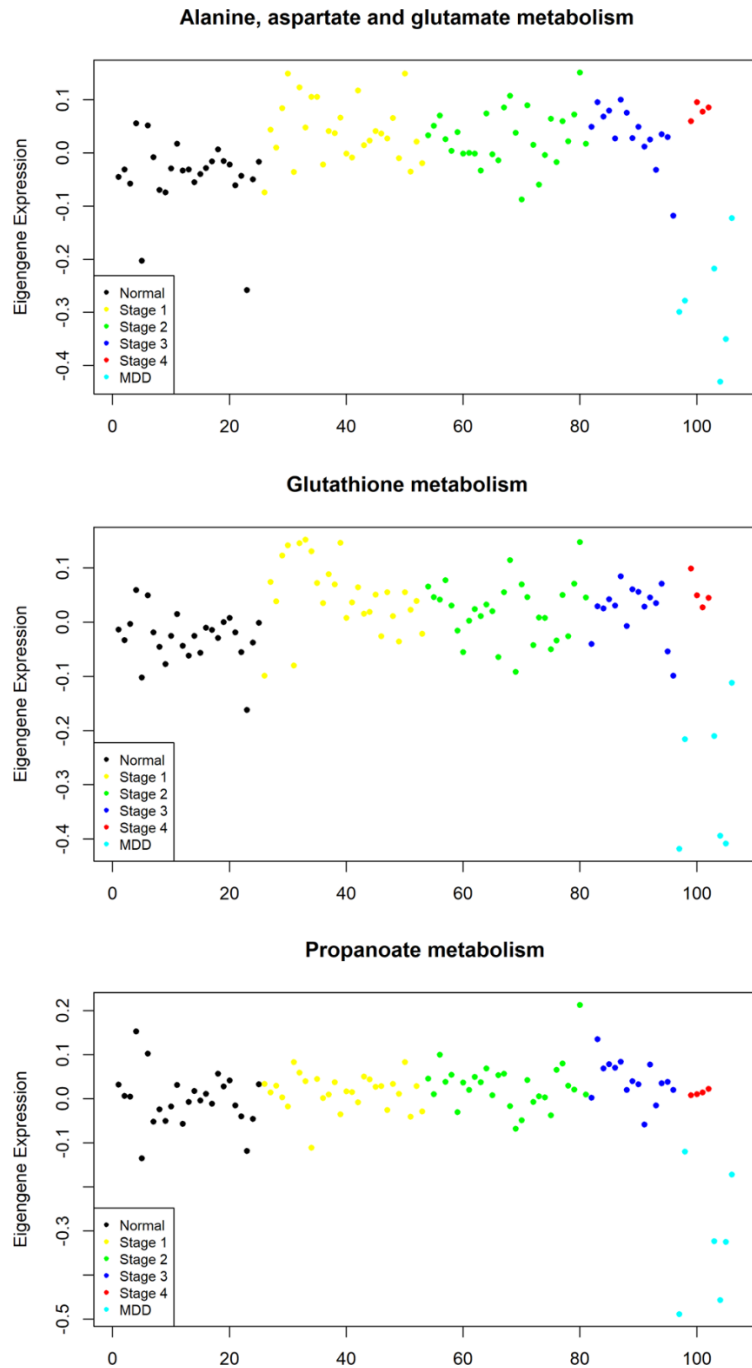


Figure 3.8: Eigengene (ME) expression profile (y-axis) of alanine, aspartate and glutamate metabolism; glutathione metabolism; propanoate metabolism in KICH (x axis represents 25 normal and 81 tumor samples).

The upregulated M5_RP module was also associated with oxidative phosphorylation suggesting a complex pattern of gene expression in this pathway. On the other hand, the M3_RP module was downregulated in most KIRP samples and is associated with O-glycan metabolism and prostaglandin biosynthesis. Further, the M8_RP module was upregulated in mostly late stages of KIRP and was associated with nucleotide metabolism (RRM2, CAD,

TYMS, POLA2, NT5E, NME7, POLE2, POLR2D, POLE3, POLR3G, TK1, POLE). This module also included genes linked to HIF1A transcriptional activity (LDHA, NT5E, CA9, HK2), carbohydrate metabolism (RPIA, PFKFB4, NUP107, NUP62, HAS3, NUP43, ENO2, PFKP, NUP37), one carbon metabolism (MTHFD1L, MTHFD2, DNMT3B, TYMS) and cell cycle.

In KIRC, modules M2_RC, M3_RC, and M4_RC showed a positive correlation with the disease, while M1_RC, M7_RC, M8_RC and M9_RC modules showed a negative correlation with the disease (Table 3.7). The M4_RC module was upregulated in most late stage KIRC samples. However, M2_RC and M3_RC modules were upregulated only in some KIRC samples. Major pathways associated with each module are provided in Table 3.7. The M4_RC module was associated with glycolysis and fructose and mannose metabolism. This module also included genes of the cell cycle, purine metabolism, and HIF1 transcriptional activity (PRKCG, PRKCB, SLC2A1, PIK3CD, ENO1, ENO2, HK2, HK1, HK3, LDHA, PGK1, ALDOA, GAPDH, PDK1). The M6_RC module showed a weak correlation with stages of KIRC, and it included genes of pentose and glucuronate interconversions (UDP Glucuronosyltransferase family genes) and glycine, serine and threonine metabolism (DMGDH, SHMT1, BHMT, BHMT2, CHDH, SARDH). Further, M8_RC and M9_RC modules were downregulated in most KIRC samples. The M8_RC module was associated with protein modification and glycine, serine and threonine metabolism, while the M9_RC module was associated with tricarboxylic acid cycle and glyoxylate dicarboxylate metabolism and other reporter metabolic pathways.

3.4 Discussion

Different evidences suggest that cancer cells reprogram the metabolism to meet the requirement of cell growth and division. This presents opportunities for cancer diagnosis and treatment based on metabolic biomarkers and targets, respectively. In this work, we executed comparative metabolomic analysis across 14 tumor types and found RCC subtypes undergo unique reprogramming of metabolism. Identifying the shared and unique metabolic features of RCC subtypes may help in differentiating subtypes for an effective treatment.

Table 3.6: Correlation between module eigengene (ME) expression value and disease, stages and overall survival for KIRP. Pearson correlation is given with p-values inside the bracket. HMR2 metabolic pathways associated with each module are given with corresponding p-value inside the bracket.

Module (Size)	Disease	Stage	Overall Survival	Pathways
M1_RP (335)	-0.38 (9e-13)	-0.24 (4e-5)	0.0088 (0.9)	Valine, leucine and isoleucine degradation (8.3E-12), Tricarboxylic acid cycle and glyoxylate dicarboxylate metabolism (1.1E-10), Propanoate metabolism (1.9E-4), Oxidative phosphorylation (0.02)
M2_RP (428)	-0.36 (4e-11)	-0.26 (6e-6)	0.068 (0.2)	Glycine, serine and threonine metabolism (6.6E-10), Pyruvate metabolism (4.8E-6), Arginine and proline metabolism (8.3E-5), Alanine, aspartate and glutamate metabolism (8.2E-4)
M3_RP (474)	-0.82 (2e-79)	-0.3 (2e-7)	-0.084 (0.2)	O-glycan metabolism (1.6E-4), prostaglandin biosynthesis (2.3E-3), Keratan sulfate biosynthesis (5.4E-3), Estrogen metabolism (7.9E-3)
M4_RP (954)	-0.27 (6e-7)	-0.07 (0.2)	-0.033 (0.6)	Isolated (2.43E-19), Inositol phosphate metabolism (0.01)
M5_RP (618)	0.28 (2e-7)	0.17 (0.004)	-0.0048 (0.9)	Oxidative phosphorylation (2.8E-5), Nucleotide metabolism (1.4E-4), Aminoacyl-tRNA biosynthesis (1.3E-3), N-glycan metabolism (0.01), Pyrimidine metabolism (0.01)
M6_RP (417)	0.34 (5e-10)	0.011 (0.9)	-0.0051 (0.9)	Glucocorticoid biosynthesis (0.03)
M7_RP (203)	0.27 (1e-6)	0.086 (0.1)	-0.032 (0.6)	Amino sugar and nucleotide sugar metabolism (2.7E-3), Purine metabolism (0.03)
M8_RP (166)	0.5 (1e-21)	0.64 (3e-35)	-0.16 (0.005)	Nucleotide metabolism (0.01), Pyrimidine metabolism (0.02)

Table 3.7: Correlation between module eigengene (ME) expression value and disease, stages and overall survival for KIRC. Pearson correlation is given with p-values inside the bracket. HMR2 metabolic pathways associated with each module are given with corresponding p-value inside the bracket.

Module (Size)	Disease	Stage	Overall Survival	Pathways
M1_RC (315)	-0.3 (1e-13)	-0.058 (0.2)	0.0044 (0.9)	Oxidative phosphorylation (1.1E-15), Arachidonic acid metabolism (2.1E-3), prostaglandin biosynthesis (2.3E-3), Pentose and glucuronate interconversions (3.1E-3)
M2_RC (516)	0.29 (4e-13)	0.32 (2e-15)	-0.086 (0.05)	Nucleotide metabolism (9.5E-3), Aminoacyl-tRNA biosynthesis (1.8E-2)
M3_RC (256)	0.31 (7e-15)	0.24 (5e-9)	-0.2 (4e-6)	Glucocorticoid biosynthesis (6.1E-4), Starch and sucrose metabolism (1.9E-2), Lysine metabolism (1.5E-2)
M4_RC (422)	0.77 (3e-118)	0.56 (8e-49)	-0.11 (0.01)	Fructose and mannose metabolism (2.2E-2), Glycolysis/ Gluconeogenesis (2.3E-2), Porphyrin metabolism (3.8E-2)
M5_RC (228)	0.18 (8e-6)	-0.043 (0.3)	0.033 (0.5)	Protein modification (1.8E-8), Chondroitin heparan sulfate biosynthesis (6.0E-6), Purine metabolism (2.0E-3)
M6_RC (323)	-0.063 (0.1)	-0.13 (0.001)	0.14 (0.001)	Metabolism of xenobiotics by cytochrome P450 (1.3E-7), Glycine, serine and threonine metabolism (2.6E-5), Pentose and glucuronate interconversions (3.7E-4).
M7_RC (728)	-0.28 (7e-12)	-0.28 (8e-12)	0.034 (0.4)	Isolated (4.9E-25), Transport, Golgi apparatus (1.3E-3), Inositol phosphate metabolism (0.01)
M8_RC (465)	-0.9 (1e-210)	-0.48 (9e-36)	-0.076 (0.09)	Protein modification (9.8E-3), Serotonin and melatonin biosynthesis (9.8E-3), Glycine, serine and threonine metabolism (1.2E-2), Retinol metabolism (2.8E-2)
M9_RC (322)	-0.71 (5e-91)	-0.48 (2e-34)	0.12 (0.007)	Valine, leucine and isoleucine degradation (1.4E-16), Tricarboxylic acid cycle and glyoxylate dicarboxylate metabolism (8.9E-12), Alanine, aspartate and glutamate metabolism (6.2E-7)

The metabolic network-based analysis of RCC subtypes revealed the systems-level alterations. The co-expression pattern of metabolic genes in each sample showed the variations in RCC metabolism. We observed that the differentially expressed metabolic genes in RCC are associated with cell cycle specific transcriptional factors E2F1 and FOXM1, suggesting that they can function at the crossroads of proliferation and metabolism. Amplification in the expression levels of E2F1 in RCC samples provides further evidence into the dysregulation around the Rb-E2F switch. Alterations in the activity of Rb-E2F switch's key components e.g., mutations in the Rb family result in heightened E2F activity. Oncogenic E2F transformation is common in many forms of cancer, which leads to mitogen insensitivity and uncontrolled proliferation [193]. We observed that the lower level of E2F1 is associated with better survival, which can be related to the trait of G1-like samples that are shown to have better survival and fewer defective cell cycle checkpoints [194].

We found that glycine, serine and threonine metabolism (one-carbon metabolism), alanine, aspartate and glutamate metabolism, aromatic amino acid and branched chain amino acid metabolism were downregulated in RCC compared to tumor-matched normal samples (Figure 3.4). One carbon metabolism fuels the synthesis of amino acids, nucleotides, and polyamines, regulates the gene expression epigenetically, and maintains redox homeostasis through the methionine cycle [195, 196]. We also found that the polyamine synthesis pathway was downregulated in RCC. However, studies have shown that the gene expression and metabolites of one-carbon metabolism are upregulated only in aggressive KIRC [92, 176]. Polyamines regulate cell proliferation and their levels are high in multiple cancers [197, 198]. These changes can be attributed to tumor or stage-specific differences. We found that the expression of genes in glutathione (GSH) metabolism was dysregulated in RCC, which can affect the GSH levels and sensitivity to the oxidative stress. Our observations are consistent with recent studies focusing on glutathione metabolism in KICH [199, 200]. We also observed that the pentose phosphatase pathway genes were upregulated in RCC. The pentose phosphatase pathway intermediates are shown to be high in a metabolomic study of KIRC [92]. Although aromatic amino acid metabolism was downregulated in RCC, the tryptophan/kynurenine pathway genes (TDO1 and IDO1) were upregulated. Kynurenines have an immunoregulatory role of restricting the T cell activation [201]. UDP glucuronosyltransferase family of genes were differentially expressed in RCC subtypes.

These genes are shown to be dysregulated to a different extent and in different directions across cancers [170].

The canonical route to generate glutamate from glutamine for anaplerotic reactions was also downregulated (Figure 3.6). However, the upregulation of glutamic-oxaloacetic transaminase enzymes GOT1 and GOT2 in KICH suggests a non-canonical route to utilize the carbon and nitrogen derived from glutamine (Figure 3.6). Coloff et al. have shown that the upregulation of transaminases and downregulation of GLUD can promote glutamine anaplerosis and non-essential amino acids (NEAA) synthesis in proliferating mammary epithelial cells [202]. Further, GOT1 and GOT2 can trigger a series of reactions involving the conversion of aspartate to pyruvate. This can potentially play a role in maintaining the redox state by increasing NADPH/NADP⁺ ratio. Human pancreatic ductal adenocarcinoma (PDAC) relies on the pathway involving GOT1, and knockdown of it is shown to increase reactive oxygen species and a decrease in growth [203].

An increase in the expression of GOT1/2 and mitochondrial genes in only KICH suggests metabolic divergence. KIRC and KIRP showed an increase in the expression of genes in the glycolytic pathway and fructose and mannose metabolism. The upregulated metabolic genes in KIRC and KIRP were linked to HIF1A, while in KICH were linked to the cell cycle transcriptional activators E2F1 and FOXM1. Von Hippel-Lindau tumor suppressor (VHL) loss and HIF1A stabilization is the hallmark of KIRC [176]. Further, HIF1A is shown to inhibit the flux from glycolysis to the TCA cycle and promote glutamine reductive carboxylation (reverse TCA flux) for citrate generation. Interestingly, HIF1A is also shown to suppress the expression of aspartate producing genes GOT1 and GOT2 [179]. We also found argininosuccinate synthase 1 (ASS1) expression was downregulated, which can increase aspartate availability and is associated with poor prognosis in multiple cancers [204, 205]. In RCC, an increase in aspartate levels can promote cell proliferation due to its role in nucleotide synthesis [206]. In KICH, genes related to the aspartate-malate shuttle were also upregulated, suggesting that aspartate can act as an anaplerotic source for the TCA cycle. Further, FOXM1 and its targets (ASNS and FASN) were upregulated in RCC [207]. ASNS promotes the synthesis of asparagine, which is shown to be a suppressor of apoptosis in response to glutamine withdrawal [208]. FASN has an important role in tumor growth and survival [209]. On the other hand, the down regulated metabolic genes are associated with

HNF4A, PPAR, and LXR. HNF4A is a proximal tubule specific transcription factor and is downregulated in the late stages of KIRP and KIRC [173]. PPAR and LXR are nuclear receptors involved in the regulation of lipid metabolism [210, 211].

The co-expression pattern of metabolic genes showed that most metabolic changes in KICH-MDD are similar to other KICH samples and normal samples. Mitochondrial/oxidative metabolism was downregulated in MDD compared to other KICH samples, consistent with the previous observation [175]. Additionally, our work also shows that the genes of glutathione metabolism, propanoate metabolism, and alanine, aspartate and glutamate metabolism were also altered in KICH-MDD samples (Figure 3.8), providing further evidence for metabolic divergence. AMPK-mTOR signaling involved in mitochondrial biogenesis is shown to be dysregulated in KICH [212]. We observed that the expression of components of the AMPK complex was significantly upregulated in KICH samples compared to MDD samples (PRKAA2, PRKAB1, PRKAG1, PRKAG2). On the other hand, we found that a module related to cell cycle, pyrimidine metabolism, and amino acid metabolism (M3_CH) showed positive correlation with stages of KICH and was specific for the MDD group. The mitochondrial one-carbon metabolic genes of this module were upregulated. This pathway helps maintain the mitochondrial redox homeostasis during tumor growth [213]. The MDD group also consists of samples that were reclassified as KICH from KIRC, and these samples displayed the characteristics of the HIF1A cluster with its targets upregulated (e.g., CA9). These observations suggest that MDD samples have low AMPK and mitochondrial activity and high cell cycle and HIF1A activity. These features can be related to the aggressiveness of RCC samples. A similar classification of hepatocellular carcinoma (HCC) samples into HIF1A and AMPK clusters with the more aggressive stage belonging to the HIF1A cluster has been shown [214]. The active and functional form of mitochondria has been associated with a less aggressive form of tumors. Damaged mitochondria lead to enhanced ROS production and a higher mutational load [215]. We also found a module related to cell cycle and HIF1 transcriptional activity was upregulated in late-stage samples of KIRC and KIRP, which can serve as a biomarker for staging. Although KIRC and KICH show distinct metabolic phenotypes (glycolytic and oxidative), KIRP showed a more heterogeneous behavior. In KIRP, the mitochondrial metabolism was not fully downregulated. This can represent a hybrid phenotype with a subclass of samples showing aggressive phenotype like KIRC and less aggressive phenotype like chromophobe. A hybrid

metabolic phenotype utilizing both glycolysis and oxidative phosphorylation is shown to exist based on the mutual antagonism between HIF1 and AMPK [216]. Notably, glycolysis was upregulated, and mitochondrial oxidative phosphorylation was downregulated in a single cell RNA-Seq (scRNA-Seq) study of the KIRC as well [217].

In summary, we observed cross talk between cell cycle and metabolism across RCC subtypes. The metabolic adaptations are coupled to cell cycle alterations, and both processes are regulated by common transcription factors. A comprehensive metabolic network-based analysis of RCC showed the metabolic differences between RCC subtypes. We specifically showed the metabolic divergence of KICH compared to other subtypes and linked the subtype-specific metabolic changes to the difference in the transcriptional regulation. The co-expression of metabolic genes showed the pattern of gene expression in each patient. KICH showed uniform metabolic changes compared to KIRC and KIRP across stages except for the MDD samples. We found co-expression modules that showed tumor stage-specific behavior. Thus, our study identifies metabolic features associated with RCC subtypes, which can help towards cancer diagnosis and prognosis. The metabolic alterations identified by integration of genome-scale metabolic model and transcriptome data of less common RCC subtypes have to be supported by global metabolomic profiling to explore new opportunities for diagnostic and therapeutic intervention. The emergence of single cell RNA-Seq (scRNA-Seq) data of cancers provides further scope for exploration of metabolic changes. It is noteworthy that the results obtained from bulk RNA-Seq (TCGA) of RCC were similar to a recent scRNA-Seq of RCC [218]. The differentially expressed metabolic genes obtained from the scRNA-Seq study were enriched for the reporter pathways identified from the bulk RNA-Seq analysis. The significantly dysregulated metabolic processes include central carbon metabolism and one carbon metabolism in RCC. The heterogeneity of RCC metabolism can be further explored with help of scRNA-Seq data.

Chapter 4 MODELING CELL CYCLE RE-ENTRY IN NEURODEGENERATION

4.1 Introduction

Neurodegeneration refers to the gradual deterioration of neuronal structure and function, leading to loss of cognitive abilities and dementia. According to the recent reports from the World Health Organization (WHO), approximately 55 million people suffer from neurodegenerative disease worldwide, with an annual rise of about 10 million. Alzheimer's disease (AD) is the most prevalent neurodegenerative disease contributing to 60–70% of the cases [219]. These cases primarily belong to two subgroups, familial AD (FAD) and sporadic AD (SAD). FAD is usually associated with mutations in the amyloid precursor protein (APP) gene or its processing enzymes (PSEN1, PSEN2). These mutants exacerbate the accumulation of A β peptide and plaque formation in the extracellular region between neurons. Clinical manifestations of neurodegeneration usually appear at an earlier age. However, FAD is a less frequent form affecting only about 5% of the patients [220]. The etiology of SAD is more complex and attributes to multiple risk factors such as age, brain injury, inefficient removal of A β , epsilon4 allele form of apolipoprotein E (APOE), midlife hypertension, high cholesterol, obesity but none of these serves as a determining factor [221–223]. AD onset is late if the cognitive impairment symptoms appear among the elderly post 65 years [220]; the frequency increases from 3% among people aged 65-74 years to 32% among 85 years and above. However, the onset of systemic changes like A β accumulation precedes the manifestation of dementia by more than a decade [223].

AD is a multifactorial disease, and in most cases, is not pinned down to a specific root. Numerous factors have been investigated for their potential as a causative agent, and several hypotheses have been proposed to provide the mechanistic detail of AD. Accordingly, various therapeutic approaches targeting the underlying molecular players have been tested [224, 225]. One of the earliest theories put forward is the cholinergic deficit hypothesis which attributes the loss of cholinergic neurons and reduction in acetylcholine synthesis to cognitive impairment in AD pathology [226]. Therefore, cholinesterase inhibitor (ChEI) drugs have

been in use for AD for decades now. However, this class of drugs is largely successful as a symptomatic therapy and has failed to fetch an overall promising disease-modifying effect in AD pathogenesis [224, 227]. ChEI manages AD symptoms by inhibiting cholinesterase, the enzyme that breaks down choline neurotransmitters. Its inability to inhibit disease progression, in general, suggests cholinergic neuronal atrophy is rather a consequence and not a mechanism of neurodegeneration [228, 229].

Another theory is the amyloid cascade hypothesis (ACH) that Hardy and Higgins proposed to describe AD pathogenesis in 1992. They hypothesized A β aggregates, the main constituent of amyloid plaque, as the causative agent of AD and other abnormalities like hyper-phosphorylation of the microtubule-associated protein tau (MAPT/tau), the formation of intracellular neurofibrillary tangles (NFT), cell loss, and dementia follow as subsequent effects of A β accumulation [230]. This hypothesis is supported by the driver mutations in FAD as well as genome-wide association studies (GWAS) in SAD. The risk genes identified in GWAS include SORL1, CLU, and APOE, which participate in the sorting and trafficking of proteins, preventing aggregate formation and clearance of deposits [231]. Other studies reported A β peptides may exist in multiple neurotoxic forms. Hence, since the proposal of ACH, numerous studies have explored the neurodegenerative effects of different forms of aggregated amyloid fibrils and soluble A β oligomers [232, 233]. Soluble A β oligomers are commonly found in AD brains and are more neurotoxic due to their diffusible nature. They can bind a wide array of protein and non-protein neuronal receptors, including glutamate receptors, and turn on downstream signaling processes. It can eventually lead to hyper-phosphorylation of tau, dysregulation of the neuronal processes, synaptic degeneration, and loss of neurons [233]. Inhibitors interfering with APP processing, A β aggregation, and therapies facilitating A β clearance are most frequently tested in clinical trials. However, despite highly efficient removal of A β from plasma and cerebrospinal fluid, they have failed to fetch promising results in clinical trials [224]. The failure of A β plaque clearance therapies points towards the self-sustaining role of downstream effectors that regulate disease progression post A β exposure. Additionally, worsening cognitive decline in some case (NCT03131453) may be attributed to the physiological role of A β in long term potentiation at lower concentration (picomolar) [234]. Hence, the amyloid cascade hypothesis has been reviewed critically time and again [235–237]. Rather than exploring the series of events

leading to a cascade, the need to identify downstream self-amplifying mechanisms that regulate AD progression and sustain pathological manifestation in the absence of the initial trigger has been felt [238–240].

Expression of cell cycle activators is significantly upregulated in postmortem samples from degenerating regions of the AD brain [41, 241–247]. These proteins also show up in individuals with mild cognitive impairment and minor A β plaque load [248]. Similar finding is recapitulated in transgenic AD mice model, where appearance of cell cycle events in vulnerable regions of brain precede pathological markers [249]. Further, neuronal cell cycle re-entry transgenic mice model manifest NFT and amyloid pathology [250], whereas double transgenic mice exhibit the development of enhanced AD-associated features like tau pathology and enhanced neurodegeneration than transgenic AD mice model [251]. In line with the animal models, overexpression of cell cycle activators/oncogenes induces AD-like changes, whereas inhibitors of cyclin-dependent kinase (Cdk) rescue cell division and subsequent apoptosis in neuronal cell lines [252–254]. Further, pathological phosphorylation of tau by Cdks increases its stability leading to destabilization of microtubular dynamics, synaptic loss and neuronal dysfunction [255–258]. These observations suggest cell cycle re-entry not only precedes neuron loss, but it also mediates and escalates the disease progression. It appears counterintuitive since neurons are known to exit proliferation permanently and maintain a postmitotic, differentiated state after human brain development [259]. High levels of Cdk inhibitors (CDKI), Retinoblastoma protein (Rb), and anaphase-promoting complex/cyclosome (APC/C)-Cdh1 ensure a non-dividing state [247, 260–262]. On the other hand, cyclins perform alternate functions such as the regulation of synaptic plasticity in neurons [263, 264]. Cdk5 is the most abundant member of the Cdk family in neurons, and it forms complexes with p35 and p39. In contrast to the function of other Cdks, it participates in cell cycle suppression. Cdk5 is also involved in brain development, cortical neuron migration, and microtubule regulation [247, 259, 265, 266].

In this chapter, we present different model scenarios for cell cycle re-entry in neurons. Mathematical models of control circuits leading to cell cycle regulated neuronal apoptosis (CRNA) were developed. We show that the integration of multiple feedback loops influences the severity of disease and makes the switch to pathological state irreversible. Based on the model predictions, we propose that simultaneous clearance of extracellular A β aggregates and

inhibition of multiple arms of the feedback loop may bring about disease-modifying effects in moderate and severe AD. The mathematical model presented here is the first such attempt to mechanistically link cell cycle re-entry with neuronal apoptosis.

Further, we show the transcriptional changes in vulnerable regions of the AD brain are in accordance with the disease state captured by the models. Though the cell cycle control mechanism is dysregulated in both cancer and AD, neurons undergo apoptosis while cancer cells continue to proliferate. Our transcriptomic studies involving glioblastoma multiforme (GBM) samples reveal some underlying differences in the two pathological states.

4.2 Model description

We reconstructed CRNA control circuits based on the available information in the literature. The critical cell cycle regulators involved in the control of CRNA include APC/C-Cdh1, Rb, E2F, p35/p25-Cdk5, Cyclin-Cdk, and CDKI (p21, p27). These proteins emerged as important players since they control a multitude of substrates. APC/C-Cdh1, Rb maintain the neurons in a nondividing, differentiated state, whereas Cyclin-Cdk, E2F drive cell cycle re-entry. Cdk5 and p27, on the other hand, act as a double-edged sword. Cdk5 activity is regulated in neurons by mechanisms involving autophosphorylation and rapid degradation [266]. Cdk5 deficient mice (Cdk5^{-/-}) fail to develop normally and die perinatally with multiple abnormalities in the cerebral cortex, hippocampus, and cerebellum. In contrast, high Cdk5 activity contributes to the complex etiology of AD by hyper-phosphorylation of various physiological and non-physiological substrates [259]. Under physiological conditions, p27, a member of the Kip family of CDKI, also contributes to sustaining mature neurons in the differentiated state in a manner analogous to APC/C-Cdh1, Rb, and Cdk5. Gene silencing experiments targeting p27 promote cell cycle re-entry (Rb phosphorylation) and apoptosis in rat cortical neurons. Inhibitors of Cdk rescue this effect of p27 silencing [267]. However, immunohistology data from AD brain report accumulation of p27 in the cytosol of both NFT bearing and histologically indistinguishable neurons [268]. A buildup of cytosolic p27 in AD seems to contradict the canonical, neuroprotective role of p27 in differentiated neurons. We describe three network modules involving these components in the control of CRNA.

4.2.1 Module 1: A β -induced hyperactivation of extracellular signal-regulated kinases (ERK) in neurons

The temporal profile of ERK activity determines cell fate. A sustained but low activity of ERK promotes differentiated state of neurons [269–271]. In differentiated neurons, the p35-Cdk5 complex indirectly limits the sustained ERK activity (Figure 4.1) by inhibiting its upstream MAP kinase kinase-1 (MEK-1) through phosphorylation [272].

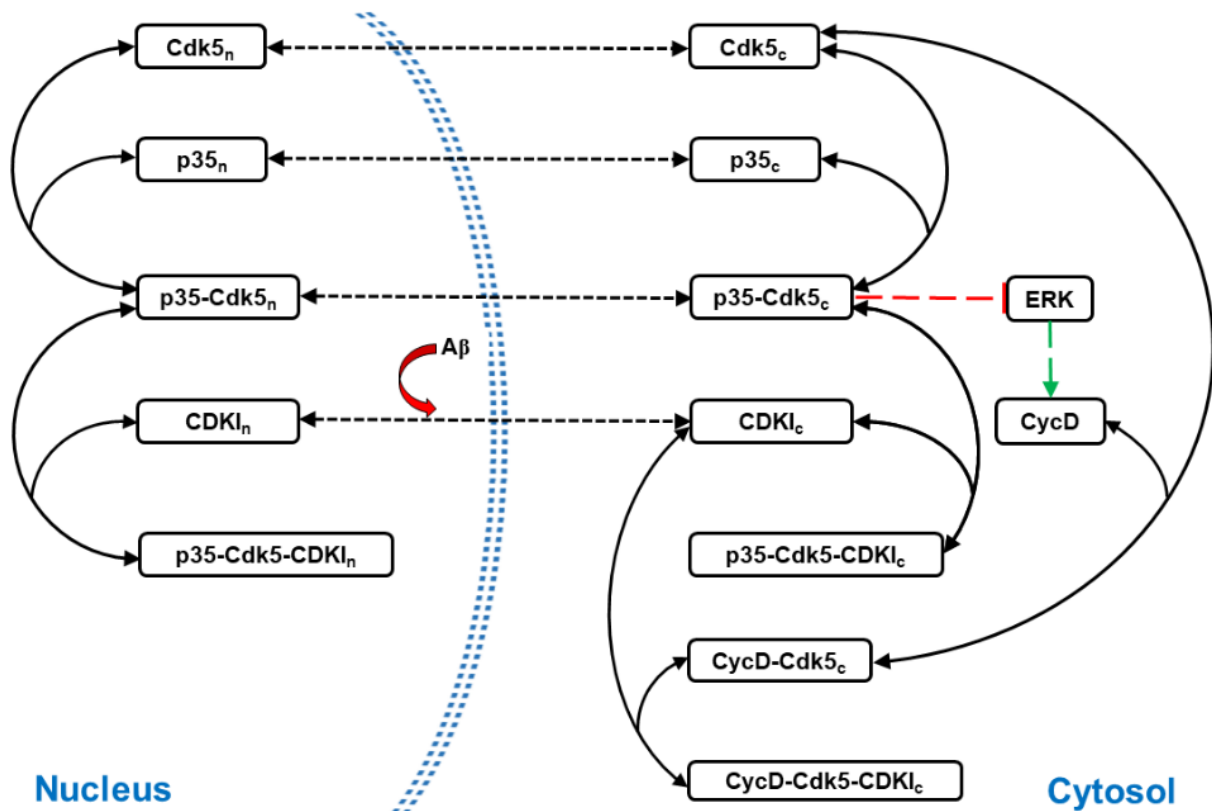


Figure 4.1: Molecular network representing competition between p35 and CycD for Cdk5 binding. A β , through nuclear export of p27 (dashed double headed black arrows), controls ERK activity; red color line with blunt end indicates inhibition and green arrow indicates transcriptional activation, discontinuous lines indicate indirect control. Solid lines with double headed arrows denote reversible association and dissociation of complexes.

Cyclin D (CycD) competes with p35 for Cdk5 binding in the presence of A β and thereby intervenes with the physiological, neuroprotective function of Cdk5. Loss of p35-Cdk5 activity dysregulates the MEK-ERK signaling pathway by relieving its repression. Hyperactivated ERK increases CycD expression further [269, 273, 274]. However, CycD, p35, and Cdk5 are abundant in postmitotic neurons [259, 263]. This raises the question of how the binding partner of Cdk5 switches from p35 to CycD on A β exposure. Cdk5 carries nuclear export signal and intrinsically tends to be localized outside nucleus [275]. In the resting neurons, p27 (CDKI) compartmentalizes p35-Cdk5 to the nucleus by trimer complex

formation. A β exposure exports p27 to the cytoplasm [275], and the relative compartment-wise distribution of these proteins changes. CycD primarily localizes in the cytoplasm of differentiated neurons [276]. Cytosolic p27 stabilizes its association with Cdk5. siRNA targeted against p27 rescues p35-Cdk5 association and is neuroprotective [277]. Hence, A β , through nuclear export of p27, topples the p35-Cdk5 balance to CycD-Cdk5 state, leading to ERK hyperactivation and CycD accumulation.

4.2.2 Module 2: Intracellular Ca²⁺-dependent APC/C-Cdh1 inactivation, Rb hyper-phosphorylation and E2F induction in neurons

Rb and APC/C-Cdh1 maintain a non-proliferating, differentiated state of neurons. Rb suppresses the cell cycle by stoichiometric inhibition of the E2F transcription factor. APC/C-Cdh1, on the other hand, belongs to the E3 ubiquitin ligase family that gets activated at the end of mitosis in cycling cells and remains active till the G1/S transition of the next cycle [125]. In the quiescent (G0) and differentiated state, APC/C-Cdh1 suppresses the cell cycle by promoting proteasomal degradation of cell cycle activators [278]. Glutamate excitotoxicity or A β exposure perturbs intracellular Ca²⁺ balance through stimulation of the ligand gated ion channel present on the membrane of differentiated neurons. Ca²⁺ dysregulation activates calpain catalyzed cleavage of p35 into p25; p25 has a slower turnover rate which increases the kinase activity of Cdk5 [233, 254, 279–281] (Figure 4.2). p25-Cdk5 inactivates Rb and APC/C-Cdh1 by phosphorylation [282, 283]. While Rb phosphorylation frees E2F and drives the synthesis of cyclins, APC/C-Cdh1 inhibition brings down their degradation. Besides its direct role in cell cycle regulation, APC/C-Cdh1 also regulates the metabolic and redox state of cells. It diverts glycolytic flux towards the pentose phosphate pathway (PPP) through degradation of 6-phosphofructo-2-kinase/fructose-2,6-bisphosphatase-3 (Pfkfb3). The nicotinamide adenine dinucleotide phosphate (NADPH) molecules produced as a by-product of PPP play a role in generating reduced glutathione (GSH) (Figure 4.2). GSH maintains redox homeostasis by scavenging reactive oxygen species (ROS) [284]. The APC/C-Cdh1 function is of prime importance in neurons since the high metabolic rate of the brain makes it susceptible to ROS generation and oxidative stress [285]. Further, E2F also contributes to ROS generation by increasing Cyclin B (CycB) accumulation (via. FOXM1) [286, 287] and APC/C-Cdh1 inactivation [125]. Mitochondrially localized CycB-Cdk1 phosphorylates Bcl-xL and interrupts ATP-synthase activity. This leads

to enhanced electron leak through the electron transport chain (ETC) and ROS accumulation (Figure 4.2) [288]. Excessive ROS adversely affects neuronal viability through oxidative DNA damage and apoptosome activation [289].

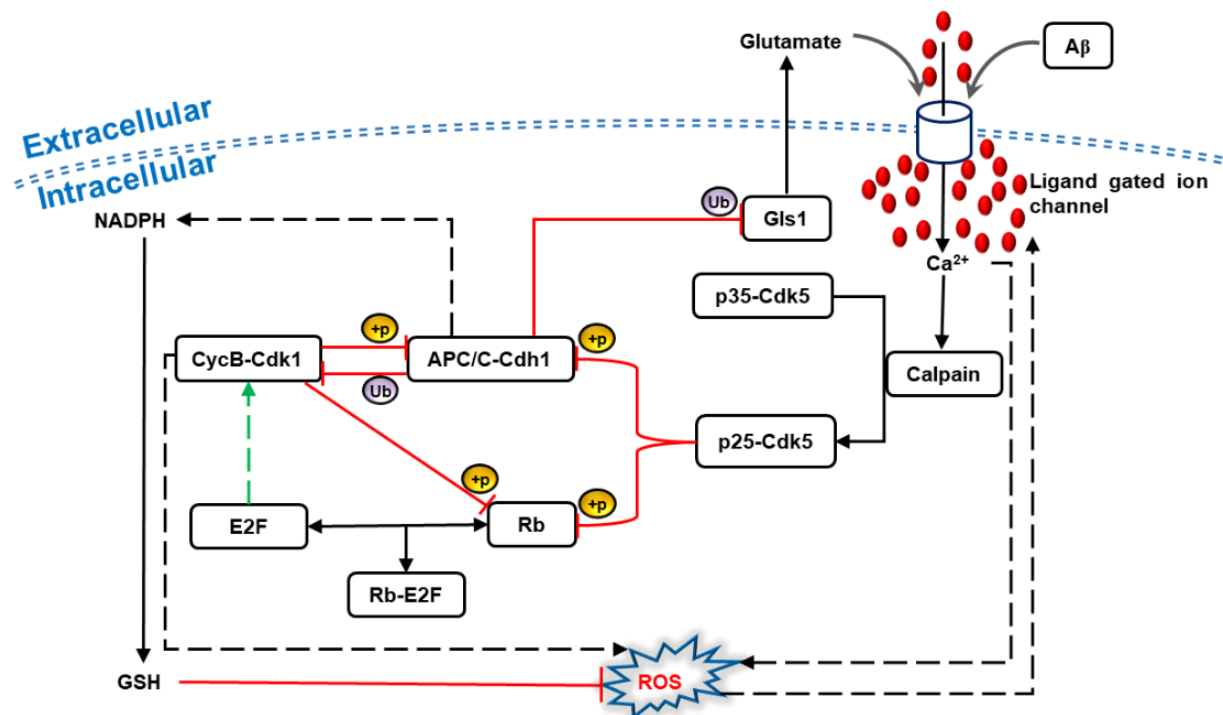


Figure 4.2: Molecular network representing Rb and APC/C-Cdh1 role in neuroprotection; red color line with blunt end indicates inhibition and green arrow indicates transcriptional activation, discontinuous lines indicate indirect control. Solid lines with double headed arrows denote reversible association and dissociation of complexes. The underlying mechanism is shown with +p for phosphorylation and Ub for ubiquitination.

APC/C-Cdh1 additionally manages neuronal activity via modulation of ligand-gated ion channels. Glutaminase (Gls1), an enzyme that catalyzes the conversion of glutamine to glutamate via glutaminolysis pathway, is an APC/C-Cdh1 substrate. In the absence of APC/C-Cdh1, Gls1 activity increases, leading to an increase in glutamate levels. The glutamate excitotoxicity triggers extended periods of receptor stimulation in neurons and dysregulation of intracellular Ca^{2+} [254, 283]. Ca^{2+} imbalance causes mitochondrial dysfunction and ROS generation. ROS accumulation alters membrane permeability by lipid peroxidation, and intracellular Ca^{2+} increases further [289–291]. Intracellular Ca^{2+} and ROS amplify each other, APC/C-Cdh1 contributes to the amplification through regulation of its substrates described above (Figure 4.2).

E2F induced CycE [115]. Rb hyper-phosphorylation further relieves stoichiometric inhibition of E2F. Free E2F also promotes APC/C-Cdh1 inactivation and accumulation of SCF^{Skp2-Cks1}(Ubl) complex that promotes CDKI degradation in CycE-Cdk2 dependent manner [128–130]. When the damage accumulates beyond repair potential, p53 and E2F coordinate the apoptotic signaling through induction of p53DINP1 that controls the conversion from p53 helper state to p53 killer state. p53 in the killer state activates multiple pro-apoptotic genes [27, 300–302]. Thus, neurons may respond to a rise in E2F levels in a graded manner. At a moderate level, p53DINP1 remains low, and E2F helps in DNA repair, while at a higher level, it switches on the killer [303]. E2F also indirectly stabilizes p53 via modulation of its Mdm2 dependent degradation. It induces tumor suppressor protein ARF that associates with p53 inhibitor Mdm2 and brings down p53 degradation [304] (Figure 4.3).

4.3 Methods

The three modules capturing alternative routes to cell cycle re-entry are regulated by complex molecular networks. These network modules presented in Figure 4.1-Figure 4.3 were translated into a set of ordinary differential equations (ODE) and algebraic equations to describe the dynamics of individual components. Unless stated otherwise, the law of mass action was used to represent the synthesis, degradation, activation, inactivation, association, dissociation reactions, and transport mechanisms.

Experimental evidence suggests that the ERK total protein levels don't change, but A β stimulation alters its activity via MEK-1 dependent phosphorylation of ERK [273]. Hence, the ERK total was modeled as a fixed parameter, and its activity was considered to be directly controlled by A β . The activation/inactivation of ERK, which is known to exhibit ultrasensitive characteristics, was modeled as Michaelis-Menten kinetics [55, 305]. Considering the physiological function and ubiquitous abundance of p35, Cdk5, and p27 in differentiated neurons, the total concentration of p35 (p35_T), Cdk5 (Cdk5_T), and p27 (CDKI_T) were modeled as fixed parameter in module 1.

Rb and APC/C-Cdh1 activity is controlled by p25-Cdk5 and CycB-Cdk1 dependent phosphorylation, with their total levels fixed. The activation/inactivation of Rb and APC/C-Cdh1 was modeled as Michaelis-Menten kinetics, and E2F dependent synthesis of E2F (autoactivation) and CycB were modeled as Hill functions. The model equations and

parameters used to describe these variables were taken from the mammary epithelial cell line quiescence to proliferation reversible transition model [306]. Ca^{2+} dependent activation of calpain in module 2 was also modeled as a Hill function since cooperative binding of two Ca^{2+} ions to calpain is known [307]. Similar to module 1, p35 was considered a fixed parameter. The activity of Cdk (Cdk5, Cdk1) was considered to be limited by its binding partner. Hence, the variables p35, p25, CycB represent the corresponding Cdk activity. We considered direct regulation of NADPH by APC/C-Cdh1, CycB regulation by E2F, ROS regulation by CycB, Ca^{2+} and ROS mutual amplification eliminating the intermediate steps involved in these regulations (Figure 4.2) to keep the model minimalistic.

Rb-E2F regulation in module 3 is modeled similar to module 2. In the E2F-p53 coordinated apoptotic signaling, p53DINP1 and p53 killer synthesis were modeled as Hill functions, based on earlier models [301, 302, 306]. The cyclin (CycD, CycE) levels control the corresponding Cdk activity (Cdk4/6, Cdk2).

$\text{A}\beta$ was varied as the input parameter in module 1 and 2 to simulate the pathological state. The translocation of p27 into the cytosol (module 1) and levels of Ca^{2+} (module 2) were regulated by $\text{A}\beta$. DNA damage was the stimulus for module 3. The degradation rates of p53 and E2F were reduced, while that of Mdm2 was increased in a DNA damage dependent manner. The synthesis rate of CycD was increased in the presence of DNA damage.

The work focused on studying the emergent properties of molecular networks and the various perturbations and rescue experiments listed in Table 4.1-4.3. The experimental data indicates consistency in the cellular response across the same set of stimuli and inhibitors, but the quantitative measure showed differences. These variations may arise due to the differences in experimental handling, intrinsic noise, differences in the cell line, etc. Therefore, we combined these observations to present models that draw a consensus across multiple studies. We started the model simulations with parameter values obtained from cell cycle and apoptosis models [301, 302, 306]. The models were integrated, and the parameter values were refined to simulate the data corresponding to $\text{A}\beta$ and DNA damage induced cell cycle re-entry and apoptosis. The models capture the qualitative picture of an increase or decrease in the number of cells undergoing apoptosis with experimental perturbations.

The complex formation is assumed to be rapid compared to synthesis, degradation, activation, inactivation, and transport rate constants. The knockout (KO) /inhibition experiments for state variables were simulated by setting either the synthesis or activation rate to zero; for fixed parameters, the KO condition was modeled by setting the total level of protein to zero. One and two-parameter bifurcation analyses were performed to characterize how the system responds to variations in the parameter values and study the effect of individual feedback loops. The default parameters were also varied in a $\pm 10\%$ range to test parameter sensitivity. The set of equations was solved numerically with XPPAUT.

The simulations represent a dynamic picture but not the actual time scale of disease progression due to the unavailability of temporal data on systemic changes in disease progression. Therefore, rate constants (k) have a dimension of time^{-1} . The state variables represent relative concentrations of respective components and are dimensionless. Michaelis constants (J) and half-saturation constants are also dimensionless. The equations and parameter values are presented at the end in the appendix section (APPENDIX B).

Different model scenarios for cell cycle re-entry in neurons may lead to transcriptional changes. Transcriptome data of AD were analyzed to study the change in gene expression related to the proposed modules. Normalized expression data across multiple datasets from different regions of AD brain postmortem samples and control samples were retrieved from <http://www.alzdata.org/> (Table 4.4) [308, 309]. Additional AD brain datasets were downloaded from gene expression omnibus (GEO) and processed using the GEO2R R script [310–314]. These datasets resolve samples into different groups: asymptomatic, incipient, moderate, and severe AD. Further, normalized temporal data from the rTg4510 transgenic mouse model was also used to study progressive changes in AD [315]. The gene expression patterns of various targets of E2F, p53, and redox metabolism were studied. The list of genes under the regulation of these transcriptional factors and redox metabolism were obtained from the literature [27, 286, 316]. E2F target genes which were associated with the cell cycle in at least one study were filtered [286]. The eigengene expression profile representing the maximum variance for the groups of genes of interest (E2F target, p53 target, and redox metabolism) were obtained for each sample using the *moduleEigengenes* function of the WGCNA package in R [183]. Correlation between the representative

eigengene expression and disease state was obtained by the Pearson correlation method using the *cor* function in *R*.

Since both neurodegeneration and cancer show aberrant cell cycle re-entry, our results from AD were also compared with the expression patterns from cancer. As RNA-Seq data of tumor matched normal glioblastoma multiforme (GBM) samples were not available in TCGA, the transcriptome data from primary tumor-derived glioblastoma multiforme stem cells (GSC) and neural stem cells (NSC) was analyzed (Table 4.4) [317]. The FPKM (Fragments Per Kilobase of transcript per Million mapped reads) data was quantile normalized using the *normalize.quantiles* function of preprocessCore package and then log transformed. GSC samples were subdivided into two distinct groups based on the classification provided by Mack et al. [317]. The eigengene expression under these conditions was also calculated to study the correlation with disease. Statistical significance of the correlation values was obtained using the *corPvalueStudent* function in *R* that computes Student asymptotic p-value for given correlations [183].

4.4 Results

4.4.1 Competition between CycD and p35 controls Cdk5 activity

We attempted to integrate different experimental findings and present a consensus model for ERK dysregulation in neurons. At first, we captured the initial condition mimicking the differentiated neuron's resting state. Initially, p35-Cdk5 is almost equally distributed between different compartments (Figure 4.4a), and the nuclear form stays in p27 bound trimer complex state. This is consistent with the observation of Zhang et al. (2010) [275], showing that p35-Cdk5 remains evenly distributed in the differentiated neurons as a nucleocytoplasmic protein with its nuclear localization dependent on p27. Conversely, CycD-Cdk5 activity stays limited to cytosol since CycD is largely cytoplasmic in postmitotic neurons [276].

A β exposure (Figure 4.4a) exports p27 to the cytosol, consequently p35 and Cdk5 also move out of the nucleus. In the presence of cytosolic p27, CycD competes with p35 for complex formation with Cdk5, resulting in a decrease in p35-Cdk5 activity and an increase in CycD-Cdk5-p27 complex formation (Figure 4.4a). A reduction in p35-Cdk5 activity leads to

hyperactivation of ERK (Figure 4.4a). An increase in ERK activity leads to the accumulation of CycD that competes with p35 to decrease the p35-Cdk5 activity further. ERK hyperactivity and high CycD (Figure 4.4a) serve as markers for pathological state and cell cycle re-entry in differentiated neurons. These simulations are consistent with the experimental observations listed in Table 4.1 [273, 275, 277].

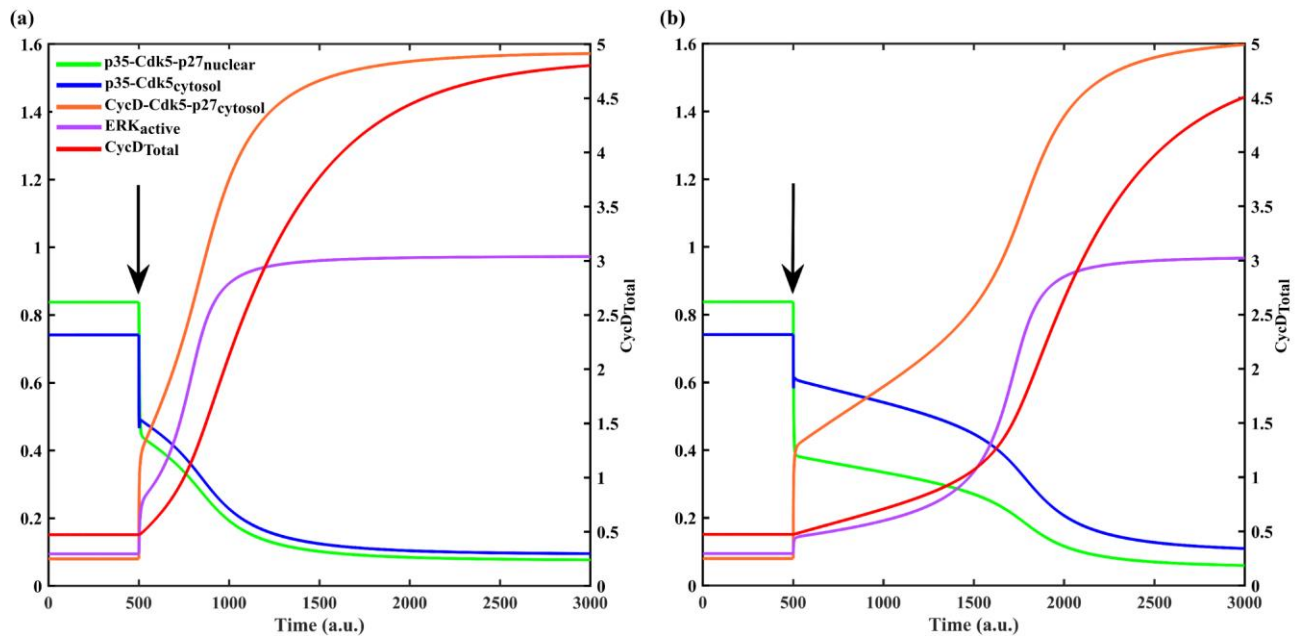


Figure 4.4: A β mediated activation of MEK-ERK signaling pathway. (a) Temporal dynamics of state variables in the presence of A β , which induces p27 nuclear export. At $t=500$, the A β level (marked by arrow) was set to 0.05 from zero. (b) Temporal dynamics of state variables on including the additional effect of A β on p35-Cdk5-p27 trimer dissociation. Relative level of state variable CycD_{Total} is represented on the right y-axis. a.u. represents arbitrary units.

Further, we show that this positive feedback between CycD and ERK sustains ERK_{active} at pathological levels and gives rise to bistability (Figure 4.5a). The saddle node 1 (SN1) corresponds to the A β threshold for transition from normal to disease state, while SN2 corresponds to the threshold for the transition back to the normal state. Thus, decreasing A β does not lead to immediate reversal to the normal state unless its level falls below SN2. MEK inhibition limits CycD to value inadequate for competition with p35; hence the system remains in a low ERK activity state, and bistability is lost (achieved by $k_{aerk}=0$, APPENDIX B). Modi et al. (2012) have shown similar cell cycle re-entry rescue experiments in primary cortical cell lines from rat (Table 4.1) [273]. Hence, we propose this A β induced cell cycle re-entry mechanism as an ERK bistable switch. A β brings about competition between CycD and p35 for Cdk5 association; this turns the switch from a low ERK_{active} state to a high ERK_{active} state.

The model was also used to simulate other rescue experiments summarized in Table 4.1. In the absence of p27, CycD fails to sequester Cdk5 away from p35, and ERK activity remains low [277]. ERK and CycD form two arms of a feedback loop, and transfection of cortical neurons with CycD siRNA or Cdk4/6 inhibitor rescues the effect of A β [252, 273]. However, our model failed to capture the CycD KO phenotype through the A β effect on the cellular localization of p27 only. In the absence of CycD, the competition for complex formation ends, and p35-Cdk5-p27 trimer formation occurs in the cytosol, leading to a decrease in p35-Cdk5 activity and an increase in ERK activity (Figure 4.5b). Thus, we hypothesized that A β also directly destabilizes p35-Cdk5-p27 by some unknown mechanism ($k_{dis35cki}$, APPENDIX B). This prevents the p35-Cdk5-p27 complex formation and blocks the transition to a high ERK_{active} state in the absence of CycD (Figure 4.5b). Evoking A β dependent trimer dissociation increases nuclear export and cytosolic activity of the p35-Cdk5 complex. As a result, ERK suppression strengthens, and the A β threshold for ERK_{active} switch shifts to the right (Figure 4.5a). The dynamics also shows a delay in p35-Cdk5 inactivation and ERK hyperactivation (Figure 4.4a vs. 4.4b), which reproduces the temporary neuroprotection provided by A β triggered rise in p35-Cdk5 activity in the cytoplasm [275].

We further studied how the levels of important regulators viz, p27, p35, and CycD affect the regulation of ERK by performing two-parameter bifurcation analysis. We analyzed the shift of the two saddle nodes, SN1 and SN2, with respect to second parametric changes. An increase in p27 (CDKI_{Total}) levels reduces the A β threshold to activate ERK, showing the inverse relationship between A β and p27 (Figure 4.6a). Elevated p27 perturbs the cytosol and nuclear distribution of p35-Cdk5, leading to the sequestration of more p35-Cdk5 in the nucleus and activation of ERK. Therefore, the saddle node shifts to the left along the x-axis (A β). However, nuclear p35-Cdk5-p27 complex formation may still suppress the cell cycle re-entry [318]. A decrease in p27 levels increases the A β threshold due to an increase in the cytosolic concentration of p35-Cdk5 and stronger inhibition of ERK (Figure 4.6a). Hence, p27 can perform both anti and pro-apoptotic functions [267, 277] by controlling the p35-Cdk5 nuclear and cytosolic concentration, respectively. A β helps in the transition from an anti to the pro-apoptotic function of p27 by altering the nuclear-cytoplasmic ratio of p35-Cdk5 in the disease state.

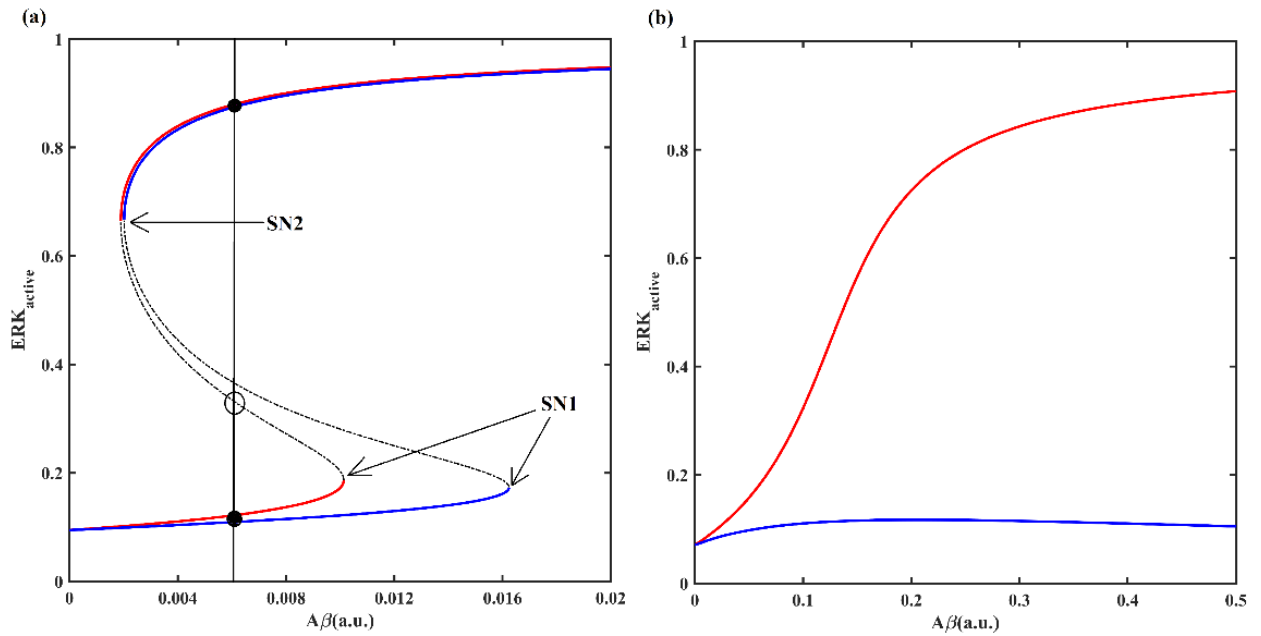


Figure 4.5: Bifurcation diagram showing the effect of $A\beta$ level on the ERK activation. The response curve is shown in the absence (red) and presence (blue) of additional effect of $A\beta$ on p35-Cdk5-p27 trimer dissociation in the (a) control and (b) CycD KO conditions. The response curve of ERK shows bistable characteristics (two stable steady states and one unstable steady state for same value of $A\beta$ marked by black filled circles and open circle respectively). Solid lines represent stable steady states, while dashed line represents unstable steady state. SN1 and SN2 represent the saddle nodes corresponding to ERK activation and inactivation, respectively. a.u. represents arbitrary units.

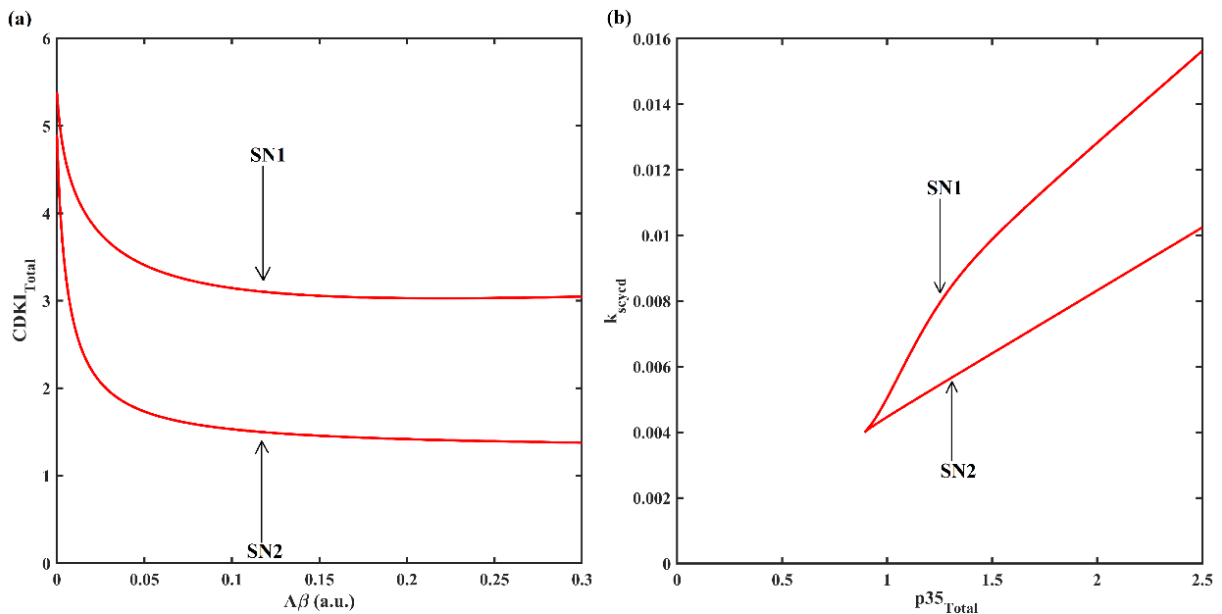


Figure 4.6: Two-parameter bifurcation plots showing how saddle nodes (SN1 and SN2) of bistable switch corresponding to ERK activation and inactivation, respectively, shift with parametric variation. (a) The $A\beta$ threshold for ERK activation and inactivation reduces with increase in p27 ($CDKI_{Total}$). (b) An increase in the $p35_{Total}$ increases the CycD requirement to activate ERK ($A\beta=0.005$). $p35_{Total}$ below a certain threshold fails to suppress ERK and saddle nodes disappear via cusp bifurcation. a.u. represents arbitrary units.

We also simulated the relation between p35 and CycD by performing the two-parameter bifurcation analysis for $A\beta=0.005$. Figure 4.6b shows that as the p35 total ($p35_{Total}$) pool increases, the CycD level (k_{scycd} , APPENDIX B) required for ERK activation also increases. Likewise, for a lower level of p35, the CycD requirement also reduces, reflecting the competition [277]. However, we observed if p35 levels drop beyond a threshold, the p35-Cdk5 activity becomes inadequate to suppress ERK activity. Under such circumstances, ERK remains constitutively hyperactive; the bistable state disappears via cusp bifurcation. Thus, the bistable activation of ERK depends on the competition between CycD and p35 for Cdk5. Decreasing this competition by p35 overexpression bestows neuroprotection.

Table 4.1: Summary of experimental data used to develop the framework of module 1.

Cell line	Stimulus	Rescue	Cell cycle entry	Apoptosis	Reference
Primary cortical neuron (Rat)	$A\beta_{42}$	-----	Yes	Yes	[273]
	$A\beta_{42}$	MEK inhibitor	No	No	
	$A\beta_{42}$	CycD siRNA	No	No	
Primary cortical neuron (Rat)	Soluble $A\beta_{1-42}$ oligomer	-----	Yes	Yes	[277]
	Soluble $A\beta_{1-42}$ oligomer	p27siRNA	Yes	No	
Primary cortical neuron (Rat)	$A\beta$ aggregate	-----	-----	Yes	[252]
	$A\beta$ aggregate	Cdk4 inhibition	-----	No	
	$A\beta$ aggregate	Cdk6 inhibition	-----	No	
Primary cortical neuron (<i>Cdk5</i> ^{-/-} Mice)	Fibrillar $A\beta_{1-42}$	Cdk5-NLS	No	Yes	[275]
		Cdk5-NES	Yes	No	

4.4.2 Ca^{2+} and ROS nexus in Rb and APC/C-Cdh1 inactivation

In the second module, we studied how different perturbations that converge on Ca^{2+} dysregulation and APC/C-Cdh1 inactivation drive transition to the disease state. This includes exposure to $A\beta$ oligomer, glutamate excitotoxicity, and CycB overexpression (Table 4.2).

The model mimics the differentiated neuron condition by maintaining Rb, APC/C-Cdh1 active (Figure 4.7a - Cdh1dp), Ca^{2+} , ROS, E2F targets, and APC/C-Cdh1 substrates low. An increase in the $A\beta$ level (Figure 4.7a) leads to a rise in the influx of Ca^{2+} and activation of p25-Cdk5, which helps to overcome the Rb and APC/C-Cdh1 barrier by phosphorylation (Figure 4.7a). This leads to amplification in Ca^{2+} and ROS levels by

feedback loops (Figure 4.2). In neurons, a rise in ROS generation has been linked to an increase in the percentage of cells undergoing apoptosis and is rescued by the addition of membrane-permeable anti-oxidants [284, 319]. Hence, we considered high ROS levels as a marker for pathological state. Rb hyper-phosphorylation, APC/C-Cdh1 inactivation marks cell cycle re-entry. We did not observe segregation of two events viz, first hyper-phosphorylation of Rb at the restriction point (RP) and later APC/C-Cdh1 inactivation at the G1/S transition as seen with the canonical model of quiescence to proliferation transition on mitogen stimulation [125]. The temporal separation of RP and G1/S is regulated by the rate at which Cdk2 activity builds up [125, 306]. The order of G1 phase events is shown to be reversed in the mammary epithelial cell line with a change in the Cdk2 threshold for Rb hyper-phosphorylation and APC/C-Cdh1 inactivation in the absence of CycD [149]. Thus, we speculate our model observation may represent a non-canonical route to cell cycle re-entry in neurodegeneration with no temporal segregation of RP and G1/S transition. p25-Cdk5 is known to inactivate APC/C-Cdh1 without requiring Cdk2 [254] and hyper-phosphorylate Rb with an efficiency comparable to Cdk2 in neurons [282].

The bifurcation analysis shows that the system is bistable and undergoes an irreversible transition to pathological state (high ROS) once A β levels cross a threshold value (Figure 4.7b). Such a transition also occurs with CycB overexpression or glutamate excitotoxicity (Figure 4.7c). These model features align with the experimental observations listed in Table 4.2 [254, 283, 288]. The pathological state arises from Rb and APC/C-Cdh1 inactivation, which increases E2F targets and APC/C-Cdh1 substrates. This module includes multiple feedback loops that can switch the system irreversibly into a state of oxidative stress implying the transition becomes independent of the A β stimulus (Figure 4.7b). We perturbed the network to study the contribution of individual feedback loops. This includes the mutual antagonism between CycB-Cdk1 and APC/C-Cdh1 (CycB-Cdk1 -----| APC/C-Cdh1 -----| CycB-Cdk1) and APC/C-Cdh1 and Gls1 (APC/C-Cdh1 ---| Gls1 \rightarrow glutamate \rightarrow Ca²⁺ \rightarrow p25-Cdk5 -----| APC/C-Cdh1). Inhibition of Gls1 ($k_{sgls}=0$) or CycB-Cdk1 ($k_{scycb}=0=k_{scyc}$) shifts the saddle nodes to the right and leads to a drop in the upper steady state values of ROS, suggesting that each feedback contributes to the strength of amplification and targeting the feedbacks can delay the onset and disease progression (Figure 4.7d). The reversible characteristic of pathological state suggests that in the presence of inhibitor of feedback

loops, targeted removal of A β peptides may alleviate the severity of the disease. The vulnerability of neurons can thus be reduced by glutaminase inhibition, CycB KO, or by the addition of membrane permeable antioxidants (achieved by increasing k_{anadphb}), which enhance the ROS scavenging capacity. Our model is consistent with rescue mechanisms that compensate for perturbations such as: addition of APC/C-Cdh1 inhibitor (achieved by making $k_{\text{acdh1}}=0$), A β oligomers, glutamate, and CycB overexpression (Table 4.2).

We then tested which nodes could be the most potential targets for therapeutic intervention. On evaluating the condition of p25-Cdk5 inhibition (Figure 4.7d) or collective downstream feedback loop blockade by glutaminase and CycB-Cdk1 inhibition (Figure 4.7d), we observe the jump to pathological state is lost. Intracellular Ca²⁺ influx initiates APC/C-Cdh1 inactivation by p25-Cdk5 and accumulation of its targets. APC/C-Cdh1 is the central regulator of this network module, and therefore, perturbations around it have a significant effect on the phenotype [320] than the direct role of A β on Ca²⁺ influx and oxidative stress. This property of the model is in line with the “two-hit hypothesis” proposed for AD. Dual insult in the form of mitogenic stimulation (Rb and APC/C-Cdh1 inactivation) and oxidative stress (depletion of antioxidants and ROS generation) plays a crucial role in disease progression. On a single insult, cells adapt to a new steady but vulnerable state [321]. As glutamate excitotoxicity and CycB dysregulation converge on APC/C-Cdh1 deactivation, they may induce the irreversible transition to a pathological state.

4.4.3 DNA damage-induced cell cycle re-entry: repair versus apoptosis

Several physiological processes like ATP intensive neuronal activity makes the normal brain vulnerable to oxidative stress and DNA damage [285, 297]. Damage sensing kinases elevate p53 and E2F levels in an attempt to arrest and repair [294]. However, E2F and p53 can cooperate to trigger apoptosis when the damage is beyond repair [295, 300, 304, 322]. An unscheduled S-phase entry creates replication stress that escalates the degree of DNA damage [323].

In the third module, we explored how the DNA damage-induced cell cycle re-entry occurs in neurons in an attempt to repair, but as a consequence, may lead to apoptosis. The differentiated neuron state is represented by dephosphorylated Rb (RbPP=0), E2F under

stoichiometric inhibition of Rb ($E2F_{free}=0$), and dephosphorylated/inactive p53. Accordingly, the repair phase is represented by active p53 helper state, high p21 ($CDKI_{Total}$), and cell cycle re-entry (marked by hyper-phosphorylated Rb) whereas, apoptotic state is represented by p53 killer state, intermediate p21 ($CDKI_{Total}$) and cell cycle re-entry (marked by hyper-phosphorylated Rb).

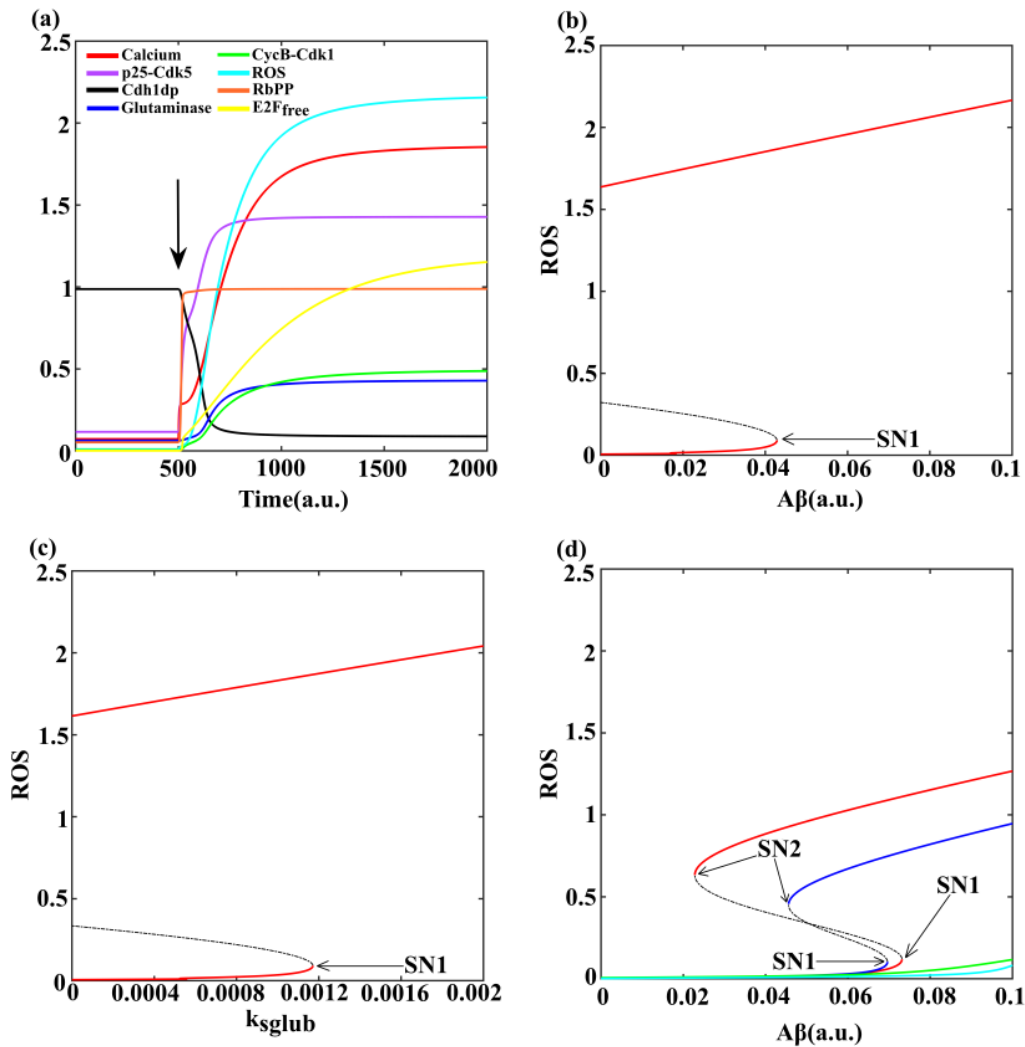


Figure 4.7: An alternate route to cell cycle re-entry via Rb hyper-phosphorylation and APC/C-Cdh1 inactivation (a) Temporal dynamics of state variables is shown in the presence of $A\beta$ by setting its level (marked by arrow) to 0.1 from zero at $t=500$. p25-Cdk5 hyperactivity relieves both Rb and APC/C-Cdh1 barrier. (b) The bifurcation diagram showing the effect of $A\beta$ on ROS accumulation. An irreversible transition to pathological state (oxidative stress) occurs with increase in $A\beta$ level. (c) An increase in glutamate level by increasing k_{sglub} (glutamate excitotoxicity) also shows the irreversible transition to pathological state (oxidative stress). Solid lines represent stable steady states, while dashed line represents unstable steady state. (d) Blocking the individual feedback loops (red: Glis KO, $k_{sgls}=0$; blue: CycB KO, $k_{scyeb}=0=k_{seyc}$) turned on by APC/C-Cdh1 inactivation leads to a drop in the magnitude of oxidative stress and makes the transitions to pathological state reversible. Inhibition of p25-Cdk5 activity (green: $k_{sp25}=0$) or termination of the downstream feedbacks (cyan: $k_{sgls}=0$ AND $k_{scyeb}=0=k_{seyc}$) rescue the transition to pathological state. SN1 and SN2 represent the saddle nodes corresponding to APC/C-Cdh1 inactivation and activation, respectively. a.u. represents arbitrary units.

Table 4.2: Summary of experimental data used to develop the framework of module 2.

Cell line	Stimulus	Rescue	Cell cycle entry (Approx.)	Apoptosis (Approx.)	Reference
Primary cortical neuron (Rat)	Glutamate excitotoxicity	-----	-----	Yes	[288]
		Cyclin B1 inhibition	-----	No	
		CDK inhibition	-----	No	
	Cyc B1 expression	-----	-----	Yes	
		CDK inhibition	-----	No	
		Phospho-defective Bcl-xL expression	-----	No	
		Phospho-mimetic Bcl-xL expression	-----	Yes	
Primary cortical neuron (Rat)	Glutamate excitotoxicity	-----	Yes	Yes	[254]
		p27 expression	No	-----	
		Cyclin B1 inhibition	No	-----	
		Phospho-mimetic Cdh1 (inactive)	Yes	Yes	
		Phospho-defective Cdh1 (active)	No	No	
		Cdk5 inhibition	No	No	
Primary cortical neuron (Rat)	Soluble A β ₁₋₄₂ oligomer	-----	Yes		[283]
		Glutaminase inhibitor	No		
	Glutamate	-----	Yes		
		Glutaminase inhibitor	No		
	APC/C-Cdh1 inhibitor	-----	Yes		
Glutaminase inhibitor		No			
Primary cortical neuron (Rat)	APC/C-Cdh1 inhibitor	-----	-----	Yes	[284]
		Cyc B1 inhibition	-----	No	
		Pfkfb3 inhibition	-----	No	
		Cyc B1 + Pfkfb3 inhibition	-----	No	
	Pfkfb3 expression	-----	-----	Yes	
		Glutathione	-----	No	

Analogous to mitogen, DNA damage induces the nuclear activity of CycD-Cdk4/6. DNA damage also increases the half-life of E2F by bringing down the degradation rate. However, DNA damage simultaneously induces the expression of p53 helper and its downstream target p21. At a lower extent of DNA damage, the cells remain arrested since the CDKI barrier exceeds total Cdk activity despite an increase in CycD-Cdk4/6, and E2F levels do not exceed the Rb level. At an intermediate level of DNA damage (Figure 4.8a), Rb is hyper-phosphorylated (Figure 4.8a), and E2F attains a higher steady state value since DNA damage-induced rise in CycD-Cdk4/6 helps cyclins (CycD_{Total} + CycE_{Total}) overcome the

CDKI barrier ($CDKI_{Total}$). Thus, the relative abundance of activators and inhibitors (cyclins and CDKI; E2F and Rb) determines the cellular state. A higher level of DNA damage (Figure 4.8b) leads to the accumulation of p53 killer ($p53_{killer}$) that, together with E2F, can induce the expression of apoptotic proteins. The DNA damage dependent module dynamics captures the observations compiled in Table 4.3 [297, 303, 323, 324].

Table 4.3: Summary of experimental data used to develop the framework of module 3.

Cell line	Stimulus	Rescue	Cell cycle entry (Approx.)	Apoptosis (Approx.)	Reference
Primary cortical neuron (Mice)	Camptothecin	-----	Yes	Yes	[303]
	E2F1 transfection	-----	Yes	Yes	
SH-SY5Y cells	H ₂ O ₂	-----	-----	Yes	[297]
	H ₂ O ₂	E2F inhibitor	-----	Yes	
U2OS cells	E2F1 transfection (low)	-----	Yes	-----	[324]
	E2F1 transfection (medium)	-----	Yes (and DNA repair)	-----	
	E2F1 transfection (high)	-----	Yes	Yes	
Primary hippocampal neurons (Mice)	CycE-Cdk2 transfection	-----	Yes	Yes	[323]
	CycE-Cdk2 transfection	p53DN (dominant negative)	Yes	No	

Bifurcation analysis with respect to variation in the level of DNA damage shows a separation of thresholds for Rb inactivation by hyper-phosphorylation (E2F activation) (Figure 4.8c) and p53 killer activation (Figure 4.8d). Rb gets inactivated at a lower threshold, while p53 killer gets activated at a higher threshold level of DNA damage. At an intermediate level between the two thresholds, the activation of E2F may indicate its functional role in DNA repair, as shown in Figure 4.9a [324]. The activation of E2F is irreversible with respect to DNA damage (Figure 4.8c) due to the feedback loop regulation involving Rb and E2F ($Rb \dashv E2F \rightarrow CycE-Cdk2 \dashv Rb$). This suggests that once neurons commit to cell cycle re-entry, then there is no point-of-return and may undergo polyploidization [325]. p53 killer activation shows bistable activation at a higher level of DNA damage (Figure 4.8d). The activation of p53 killer depends on the activation of the positive feedback loop via p53DINP1, which promotes the conversion between p53 helper to killer. p53DINP1 levels begin to rise initially due to the rise in E2F levels, which, together with p53 killer, amplifies its levels further.

Since E2F levels required to activate cell cycle genes differ from the activation of pro-apoptotic genes, the two bistable switches are separated, creating two different thresholds (Figure 4.8c, Figure 4.8d). This emergent dynamics delays the activation of apoptosis genes until DNA damage accumulates in neurons to higher levels.

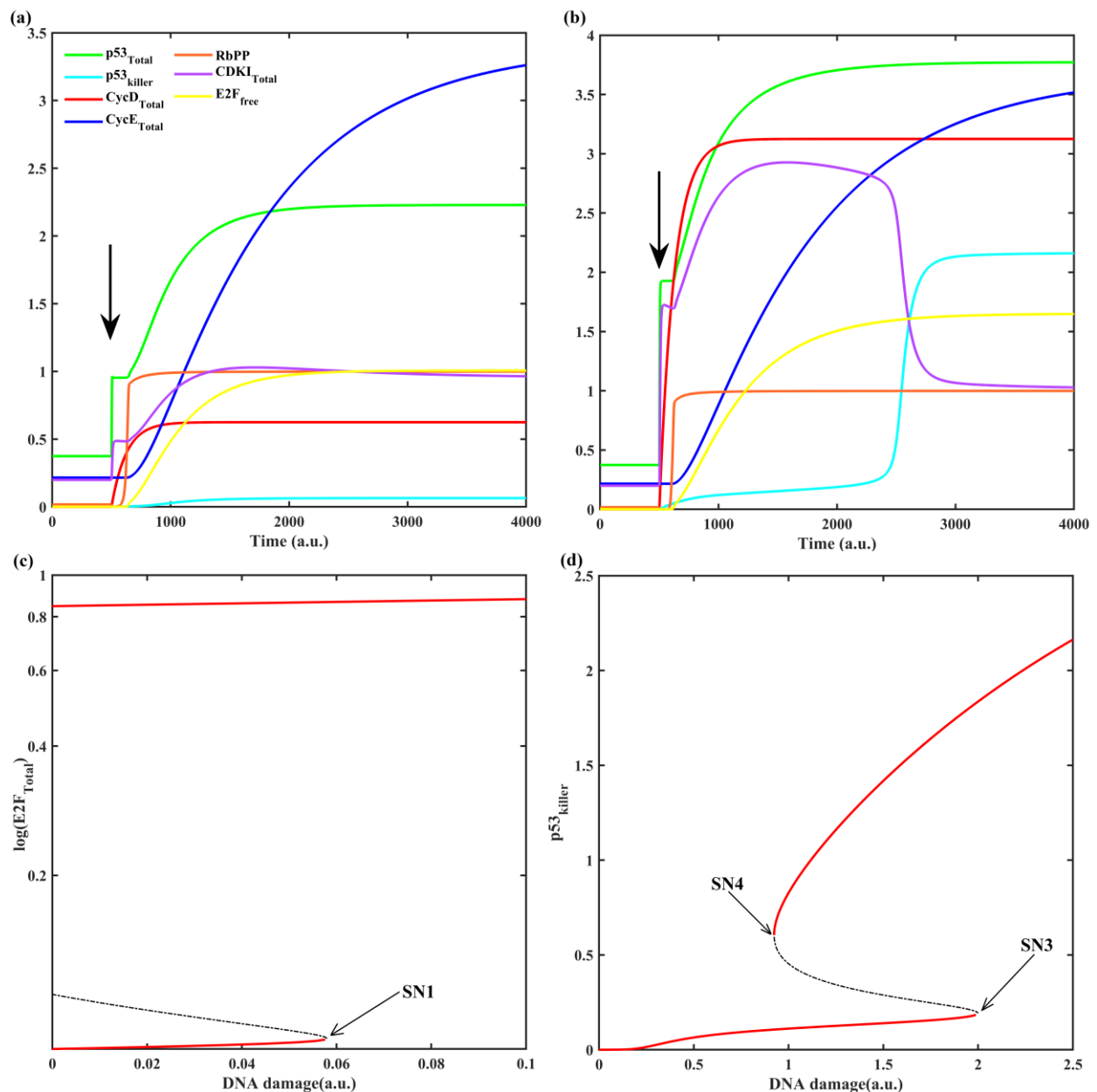


Figure 4.8: Cell cycle re-entry via DNA damage dependent E2F activation (a) Temporal dynamics of state variables is shown by setting the DNA damage to intermediate level (0.5 a.u.) from zero at t=500 (marked by arrow). (b) Temporal dynamics of state variables is shown for higher level of DNA damage (2.5 a.u.) at t=500 (marked by arrow). (c) The bifurcation diagram showing the bistable activation of E2F for lower values of DNA damage (shown in semi-log scale for better resolution). (d) Bistable activation of p53_{killer} for higher values of DNA damage. Solid lines represent stable steady states, while dashed line represents unstable steady state. SNs represent saddle node corresponding to E2F and p53 killer activation/inactivation. a.u. represents arbitrary units.

An increase in E2F stabilization by DNA damage (fac2) shifts the saddle nodes of p53 killer activation to lower DNA damage levels reducing the delay in activation of apoptosis (Figure 4.9b). Thus, the graded increase in E2F levels in neurons controls the cell fate decision [324].

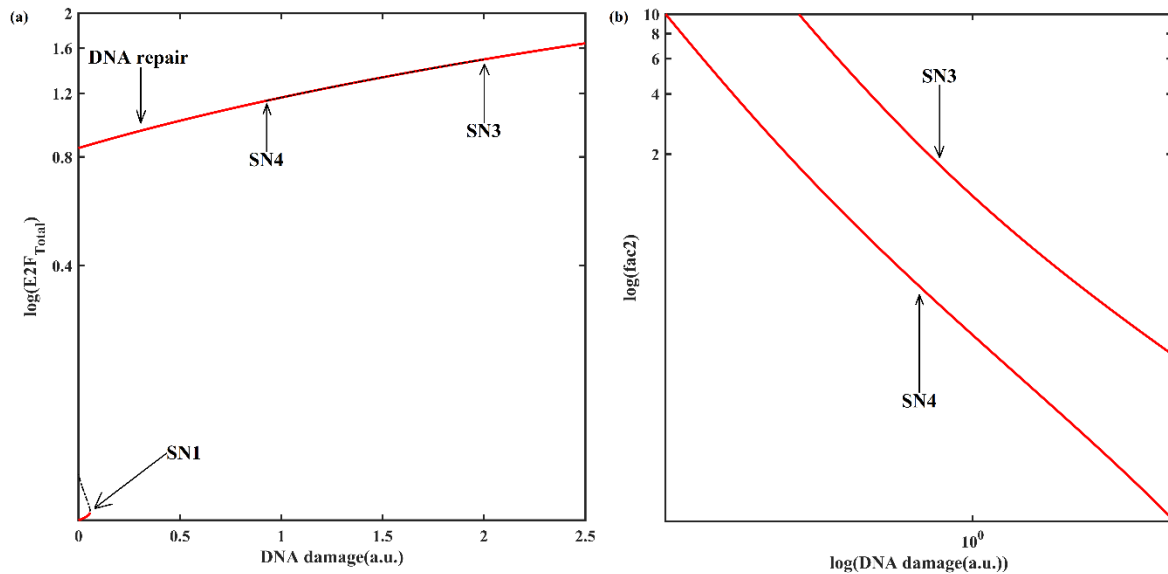


Figure 4.9: (a) The bifurcation diagram showing the variation in E2F levels for lower and higher DNA damage levels. E2F levels corresponding to an intermediate level of DNA damage (above SN1 but below SN3) may play a role in DNA repair. SN1 and SN3 correspond to DNA damage threshold for E2F and p53 killer activation, respectively. (b) The two-parameter bifurcation analysis showing the effect of altering the stability of E2F (fac2) on the DNA damage threshold for p53 killer activation (SN3) and inactivation (SN4).

4.4.4 Sensitivity of models to parametric variation

We presented a set of models that draw an integrated picture across various experimental observations. The set of parameters used in this study is one such example that describes the physiological and pathological phenotypes. Thus, we tested our choice of parameters by evaluating the model sensitivity after varying each parameter in a $\pm 10\%$ range. We quantified alteration in the bifurcation diagram by computing the fold change in threshold value (location of saddle node) with variation in the parameter values for each module (Figure 4.10– Figure 4.12). 132 out of the 136 total parameters tested from the three modules showed less than two-fold change in threshold value. Four parameters viz CKI_T ($p27_{Total}$), $Cdk5_T$ ($Cdk5_{Total}$), k_{ierk} , and k_{aerk} (ERK inactivation and activation rate) that directly control the competition between p35 and CycD in module 1 show more than two-fold change in threshold values in both directions on parameter variation. The irreversible characteristic of

the transition from normal to pathological state is preserved for all parameters under these perturbations in module 2 and module 3.

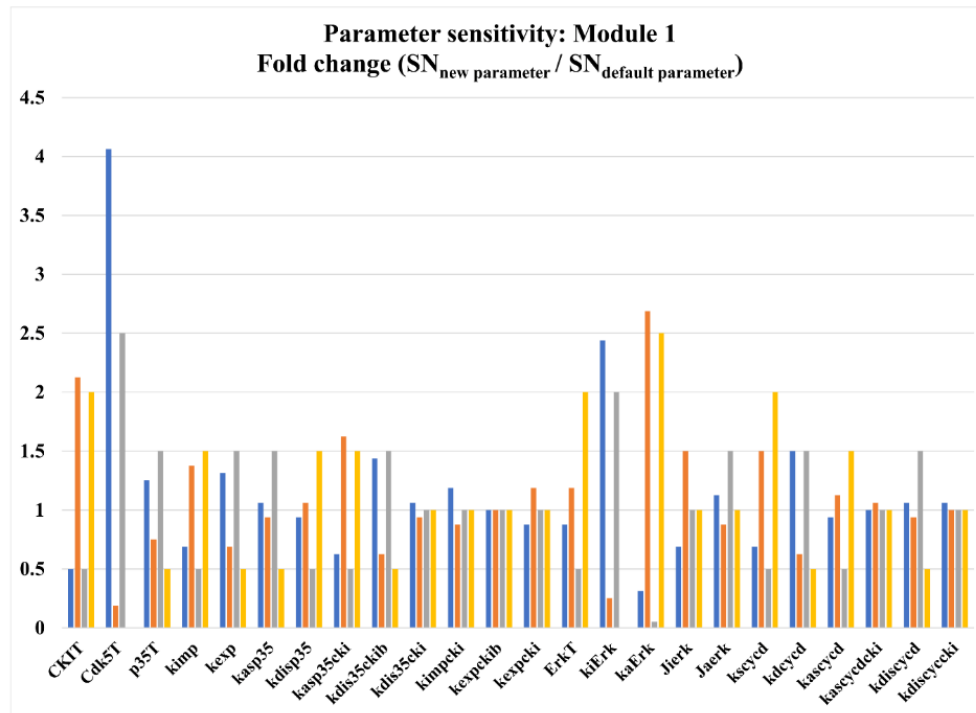


Figure 4.10: Parameter sensitivity analysis for module 1. The bars represent the fold change in saddle node values for change in parameter (increase or decrease) from default values (fold change = $SN(\text{new})/SN(\text{default})$). Fold change in SN1 with increase (blue) and decrease (orange) in parameter values and fold change in SN2 with increase (grey) and decrease (yellow) in parameter values are shown.

4.4.5 Expression profile of cell cycle and redox regulators in the AD brain and transgenic mouse model of AD

The experimental data used in this study mostly represent characteristics of different neuronal cell lines. Therefore, we also analyzed clinical data emerging from AD patients. We studied the transcriptional changes associated with the model outcome in the hippocampus and entorhinal cortex (EC) regions of the AD brain. The beginning of memory loss and cognitive dysfunction are linked to neurodegeneration in EC and hippocampus [326–329]. The eigengene expression profile [186] of cell cycle genes under the transcriptional control of E2F shows a positive correlation with AD compared to normal samples in the EC and hippocampal regions (Table 4.4). Further, we analyzed the expression pattern of p53 activated pro-apoptotic genes such as Noxa, Bax, p53, p73, p53DINP1, Apaf1, Casp6, p21, and Mdm2 [27]. The eigengene expression profile of these genes also shows a positive

correlation with the disease state (Table 4.4). Additionally, E2F and p53 transcriptional dysregulation is observed in the transgenic mouse model of AD (rTg4510) (Table 4.4).

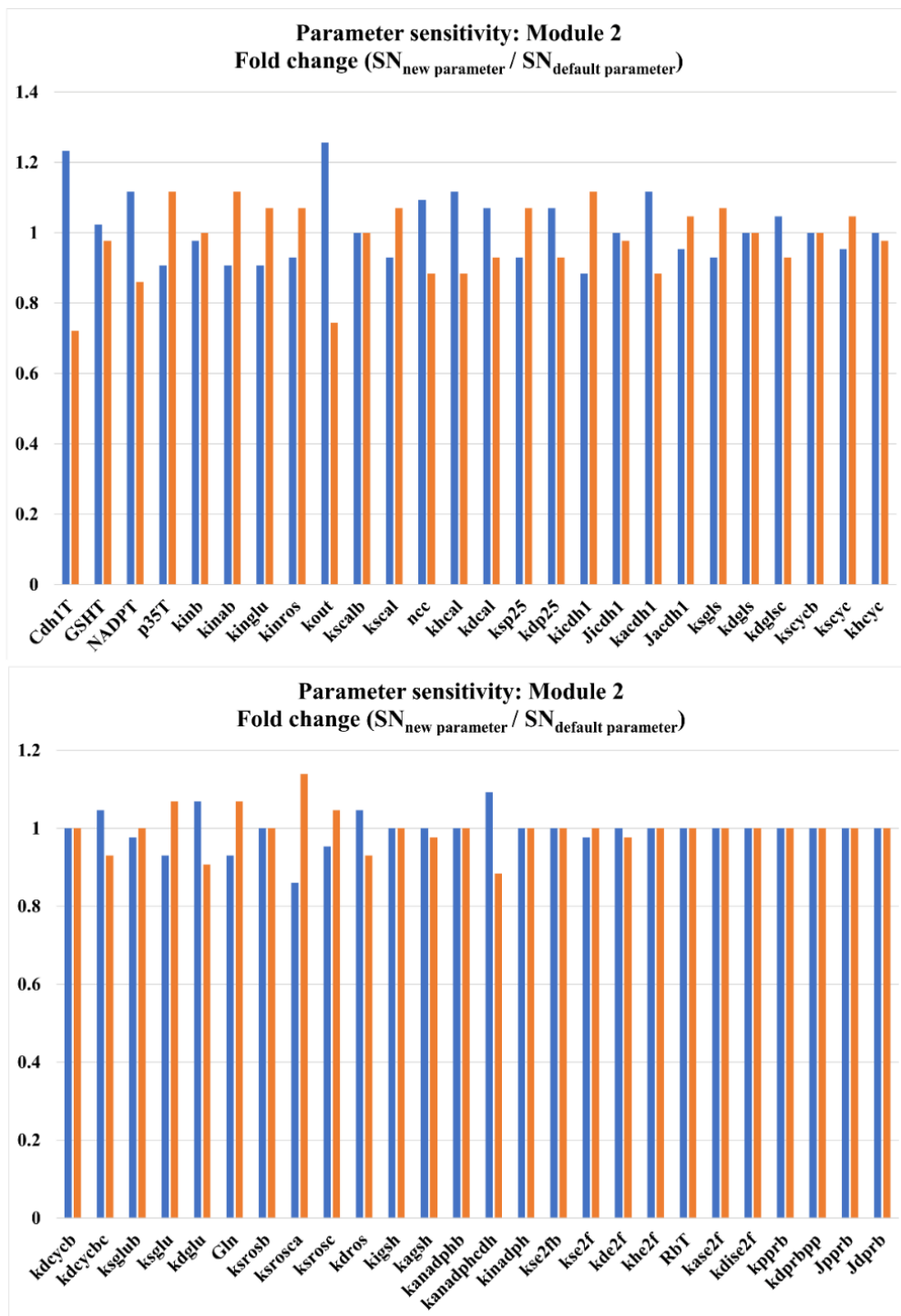


Figure 4.11: Parameter sensitivity analysis for module 2. The bars represent the fold change in saddle node values for change in parameter (increase or decrease) from default values (fold change = $SN(\text{new})/SN(\text{default})$). Fold change in SN1 with increase (blue) and decrease (orange) in parameter values are shown.

These findings are consistent with immunoblotting observations showing the activation of p53 in the AD brain [330, 331]. p53 is also activated in the Tg2576 transgenic mouse model of AD and with soluble A β treatment [332]. p53 expression in neurons is accompanied by DNA fragmentation [333]. Neurons from different brain regions of the 3x-transgenic AD mice show colocalization of Rb hyperphosphorylation (E2F activation) with a tau pathology marker. Further, the appearance of Rb hyperphosphorylation precedes the appearance of the tau pathology markers in the hippocampus of the AD brain [334]. Loss of APC/C-Cdh1 function disturbs the balance between pro-oxidants and antioxidants leading to perturbation of redox homeostasis and oxidative stress. Analysis of eigen gene expression profile with genes involved in redox metabolism shows a significant dysregulation (Table 4.4). Most of the AD brain datasets from EC and hippocampus show a negative correlation with the pathological state. However, we also found evidence for a positive correlation with redox metabolism genes in the rTg4510 transgenic mouse model of AD and in one of the AD brain datasets from the EC region (Table 4.4). The upregulation of redox metabolism may result from a stress-responsive compensatory mechanism. NFT performs an alternative function via induction of a secondary neuroprotective mechanism [335–338]. The expression pattern of genes controlled by E2F, p53, and redox metabolism genes is in accordance with the different states captured by our models. Upregulation of E2F and p53 target genes in AD point towards probable apoptosis signaling whereas, downregulation of redox metabolism gene suggests oxidative stress. The clinical data analysis provides supporting evidence in patients and confirms these as relevant role players in AD pathogenesis.

4.4.6 Neurodegeneration versus cancer

Dysregulation of the cell cycle marks the pathological state of both AD and cancers, but neurons die while attempting to divide, whereas cancer cells continue to divide uncontrollably [339]. Similar to the expression analysis in AD, we studied eigengene expression of p53 activated genes and redox metabolism genes in glioblastoma multiforme (GBM) to understand the underlying molecular difference [317, 340]. GSC derived from primary tumors contrasted strikingly from their progenitor NSC in the expression of p53 activated genes (Table 4.4). Unlike AD, p53 target genes showed significant downregulation in GBM. p53 gene mutations are frequently observed in different cancers [225, 341]. Redox metabolism genes too showed heterogeneity across two GBM groups. The group with

classical, proliferative features showed upregulation (Pearson Correlation: 0.905; p-value: 1.5e-06), whereas the second group with mesenchymal features exhibited downregulation of redox metabolism (Pearson Correlation: -0.669; p-value: 0.009). These differences attribute to differences in metabolic reprogramming among the subgroups [342].

Table 4.4: Cell cycle and redox metabolism gene expression pattern in AD and GBM. Pearson correlation coefficient and corresponding Student asymptotic p value for eigen gene expression profile with disease is given, *represents correlation of expression profile between wild type and transgenic mice, #represents correlation of expression profile with transgenic mice age.

Disease	Region/Group	Gene set	Pearson correlation coefficient	p-value	Identifier
AD	Hippocampus	E2F target	0.306	2.4e-4	GSE28146, GSE29378, GSE36980, GSE48350, GSE5281
		p53 target	0.381	3.4e-6	
		Redox metabolism	-0.359	1.3e-5	
	Entorhinal cortex	E2F target	0.367	9.6e-4	GSE26927, GSE26972, GSE48350, GSE5281
		p53 target	0.35	1.7e-3	
		Redox metabolism	-0.404	2.5e-4	
	Hippocampus	E2F target	0.459	9.4e-3	GSE1297
		p53 target	0.518	2.8e-3	
		Redox metabolism	-0.517	2.9e-3	
	Entorhinal cortex	E2F target	0.718	9.3e-17	GSE118553
		p53 target	0.742	2.2e-18	
		Redox metabolism	0.465	1.5e-6	
Transgenic mouse model of AD	Entorhinal cortex	E2F target	0.372*	3.7e-3*	GSE125957
		p53 target	0.548*	7.0e-6*	
		Redox metabolism	0.533*	1.4e-5*	
		E2F target	0.731#	6.6e-6#	
		p53 target	0.865#	1.4e-9#	
		Redox metabolism	0.789#	3.8e-7#	
GBM	Group 1	p53 target	-0.823	9.2e-5	GSE119834
		Redox metabolism	0.905	1.5e-06	
	Group 2	p53 target	-0.941	5.6e-7	
		Redox metabolism	-0.669	0.009	

4.5 Discussion

Cell division plays an important role in tissue regeneration and development. However, unlike most of the other cell types, differentiated neurons are perceived to have entered a permanent postmitotic quiescent state. In AD, neurons undergo atrophy, and this loss is often associated with cell cycle re-activation. We studied the different routes to cell cycle re-entry in postmitotic neurons. The emergent properties of cell cycle control networks

were analyzed using a mathematical modeling approach. We showed how multiple feedback loops combine to make the transition from normal to pathological state irreversible and explored the effect of different perturbations that provide insights into drug targeting strategies.

The first network module focused on A β induced positive feedback between ERK and CycD, which promotes a switch-like activation of ERK activity in neurons. We speculated that A β induces dissociation of p35-Cdk5-p27 nuclear complex and translocation of p27 leads to the activation of ERK by eliminating the competition between CycD and p35 for Cdk5. Further, in the resting neurons, the p35-Cdk5-p27 nuclear complex suppresses expression of proliferation promoting E2F1-DP1 target genes by competing with DP1 for E2F1 binding [318]. p27 also plays a role in stabilizing the CycD and Cdk4/6 interaction [21]. An increase in CycD accumulation with ERK activation can lead to an increase in CycD-Cdk4/6 activity, which influences the Rb-E2F switch by mono-phosphorylating Rb. CycD-Cdk4/6 derepresses genes under the control of RbL2/p130-E2F4 complex by phosphorylation. RbL2/p130-E2F4 is known to suppress the pro-apoptotic gene B-Myb in healthy neurons [343]. This complex also participates in the formation of the DREAM complex, which suppresses MMB-FOXO1 target genes, including CycB [286]. In addition, ERK also controls cell cycle progression by regulating Cdk2 location and Cdk1 activity [269, 344, 345]. CycB-Cdk1 is known to trigger phosphorylation of pro-apoptotic proteins BAD and FOXO1. In the absence of Akt signaling, CycB-Cdk1 dependent phosphorylation relieves the inhibition of these proteins by scaffold protein 14-3-3, leading to apoptosis in neurons [346–349]. Interestingly, A β is also known to inhibit Akt activity [350, 351].

An alternate route to CRNA centered around APC/C-Cdh1 inactivation mediated by A β -dependent Ca²⁺ dysregulation and oxidative stress. We showed an irreversible transition to a high ROS state at higher levels of A β due to the multiple feedback regulations of APC/C-Cdh1. The irreversible transition also suggests that decreasing A β alone may not have the desired effect. We modeled inhibition of Gls1 and/or CycB that helps to reduce the levels of ROS, resulting in rescue. We observed glutaminase inhibitor completely abolishes the effect of APC/C-Cdh1 inhibitor but not of A β [283]. On the contrary, MEK inhibition appears to completely rescue CRNA induced by A β [273], which suggests crosstalk between these network modules and the ERK switch probably acts as an initiator module for apoptosis. We

proposed a scenario of how these two modules can crosstalk via Cdk5 regulation. The autophosphorylation of p35-Cdk5 protects it from calpain protease activity, but A β dependent rise in the CycD-Cdk5-p27 complex dissociates the p35-Cdk5 complex and makes p35 more susceptible to cleavage [266, 352]. Hence, CycD induction reduces p35 and Cdk5 association (module 1) and helps in Ca²⁺ dependent generation of p25, which binds Cdk5 strongly compared to CycD [273]. Subsequently, p25-Cdk5 inhibits APC/C-Cdh1 (module 2) and also phosphorylates substrates nuclear lamin, anti-apoptotic protein Mcl-1, and cytoskeletal proteins that can promote a transition to the apoptotic state [259, 353]. These mechanisms suggest that cell cycle re-entry may activate multiple routes to apoptosis. However, A β induced cell cycle re-entry also protects some proportion of neurons from apoptosis [354]. This indicates that cell fate decisions may be influenced by the heterogeneity in the stress levels (oxidative stress and DNA damage) experienced by individual neurons.

The third passage to CRNA focused on DNA damage mediated CycD induction and E2F stabilization. Neurons make an irreversible commitment to the cell cycle with an increase in the level of E2F. This may play a role in DNA repair [295] and polyploidization [325] that protects them from cell death under DNA damage and oxidative stress. A further increase in E2F level in a graded manner with an increase in DNA damage may lead to pro-apoptotic gene expression in cooperation with p53 [322, 324]. We showed that the different thresholds for activation of DNA repair and apoptosis emerge by combining two bistable switches. The extent of DNA damage can exceed repair threshold if ROS (as observed with module 2) levels rise, which can induce oxidative DNA damage.

In chapter 2, we captured the dynamics of how stress signals like oxidative stress and DNA damage induced transition back to quiescence after crossing the restriction point and before the G1/S boundary in mammary epithelial cell cycle model [306]. In contrast, we observed a scenario of how stress signals drive cell cycle re-entry in neurons. We attribute this difference to the defense mechanism in neurons against DNA damage since the levels of repair proteins are very low in the mature neuron state [296, 355]. This view differs from the recently proposed “cell cycle inertia” driven mechanism for the G1/S transition in the presence of stress signals close to the G1/S boundary in mammary epithelial cells. Here, cells commit to S-phase due to an inertia from rising Cdk2 activity with a slower accumulation of CDKI [356].

The work presented here investigated the network modules that set off CRNA and studied the role of different feedback loops in pushing the system into an irrevocable pathological state. The mathematical models were developed to simulate the multiple scenarios for cell cycle re-entry with a minimal number of state variables. Hence, it does not account for all the A β induced effects in neurons and amplification in A β levels due to feedback loop regulation [239]. A β amplifying loops may help to cross the threshold (saddle node) for an irreversible transition to the pathological state. Nevertheless, the pre-clinical phase of AD is characterized by neurons entering the cell cycle. The irreversible nature of AD points towards the need for understanding the disease progression mechanism in greater detail. The failure of therapeutic measures at various phases of clinical trials reflects mere removal of the causative agent is not sufficient for efficient treatment. We showed the convergence of cell cycle re-entry onto the activation of self-amplifying positive feedback loops, and shutting off feedback signals may serve as an efficient disease-modifying therapy. We also proposed mechanisms through which crosstalk between different routes to CRNA may take place and compared the scenario with cell cycle progression in other mammalian cells.

Chapter 5 MODELING T-CELL ACTIVATION AND CLONAL EXPANSION IN ADAPTIVE IMMUNE RESPONSE

5.1 Introduction

The immune system comprises several types of cells and chemical signals that collectively defend a host from foreign invaders such as viruses, microbes, toxins, and cancer cells [357]. The immune response is classified into two categories, viz innate and adaptive response. The innate immunity elicits a nonspecific defense mechanism that distinguishes foreign agent, but is independent of its nature and source. It acts within a few hours of encountering an invasion. However, it doesn't create any memory to facilitate immunity for future exposure. On the contrary, the adaptive immune response is specific to the foreign agent or antigen. This antigen dependent process culminates in the memorization of infection history. The memory of an earlier encounter equips the host for a rapid and efficient response in the future. The innate immune responses evoke adaptive immunity, and they work together to get rid of the pathogens [358, 359].

T cells are a crucial constituent of the adaptive defense mechanism. They develop from the hematopoietic stem cells in the bone marrow and migrate to mature in the thymus. T cells present antigen-binding receptors called the T-cell receptor (TCR) on their membrane; every T cell expresses TCR of a unique type. Hence, a large repertoire of T cells that present a wide array of TCR forms the basis of antigen-specific adaptive immunity. T cells recognize antigens that are presented on the surface of antigen presenting cells (APC) by major histocompatibility proteins (MHC). MHC protein flags fragments of phagocytosed foreign proteins, microbes, or antigens when a cell gets infected with some intracellular pathogen. Post maturation in the thymus, the progenitor T cells further differentiate and undergo several divisions to become lineage restricted based on the MHC coreceptor CD4 or CD8 expression. These naïve CD4⁺ and CD8⁺ T cells remain in a dormant state, predominately localized within the lymph nodes until an antigen encounter. Once activated, T cells pass through a

major expansion phase where they rapidly proliferate to clear the infection. The proliferating cells differentiate to execute specific functions. While most of the effector cells undergo the contraction phase after the clearance of infection, some cells differentiate to create a memory of the infection [358, 360, 361]. Nevertheless, cell proliferation forms the ground for adaptive immunity, and its dysregulation can lead to immunodeficiency or autoimmunity.

Naïve T cells exit quiescence on antigenic stimulation in a manner analogous to growth factor signaling of MCF10A cells described in chapter 2. However, T cells spend significantly more time in the G1 phase preparing to divide [362]. Though even genetically identical cells show asynchronous behavior, most non-immune quiescent cells from multiple cell lines commit to division and enter S-phase within 8-16hrs [125]. On the contrary, T cells take about 24-30hrs to commit and enter the S phase for the first round of division [362]. G0 exit to G1/S transition in naïve CD4⁺ T cells require 25-30hrs, but naïve CD8⁺ T cells show variability and may commit faster than CD4⁺ in the presence of stronger antigen stimulus [363]. In the continuous presence of growth factors, mammalian cells continue to cycle. These cells can overcome growth factor requirement and cross the restriction point (mitogen sensitive checkpoint) in the G2 phase of the earlier cycle, causing a short G1 phase [122, 127, 134]. The next cycle has an accelerated S-phase entry within 4-8hrs [125]. T cells, on the other hand, complete subsequent divisions once every 4hrs and drive rapid clonal expansion by curtailing the gap phases and multiplying several times [362, 364]. Further, evaluation of mitogen requirement in different cell lines reports that the continuous presence of growth factor can be substituted with two pulses of growth factor stimulation [29, 365, 366]. Despite continuous stimulation of growth factors, their downstream effectors such as ERK and PI3K/Akt manifest dynamic activation profiles in two waves form [29, 136, 367–370]. The first wave turns on both proliferative and antiproliferative signals triggered by p53 signaling. The second phase of activation suppresses the antiproliferative signal and is dispensable in p53 null mutants [29] (Figure 5.1). Whether such control of restriction point exists in T cells or not is unclear. Analogous to growth factors, antigen also triggers an immediate antiproliferative response in T cells involving activation of p53 [371, 372]. Antigen priming of TCR for 24hrs is required to activate T cells for proliferation. These cells undergo expansion driven by cytokine (Interleukin-2/IL-2) signaling [373–375]. Naïve T cells do not express IL-2 receptor (IL2R) alpha subunit (CD25), leading to the formation of dimeric IL2R

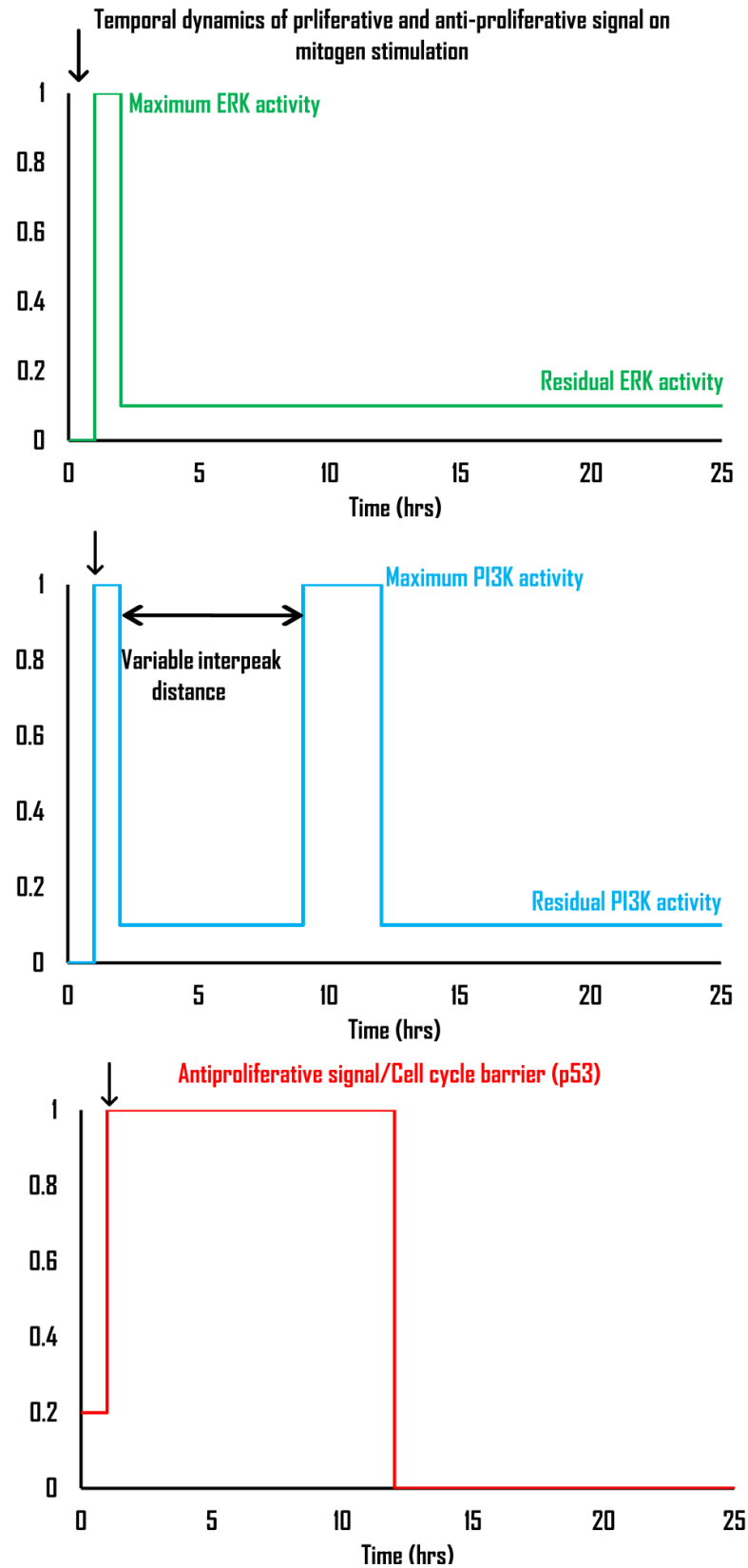


Figure 5.1: Mitogen signaling (marked by ↓) turns on both proliferative and antiproliferative signal. The continuous presence of mitogen can be substituted with mitogen pulses since the downstream effector shows biphasic activation.

complex with an intermediate ligand affinity. TCR signaling induces NFAT, Nf- κ B, and AP-1 driven transcription of IL-2 and IL2R α [362, 376]. IL2R α in complex with IL2R β and IL2R γ gives rise to high affinity cytokine signaling [377]. Though TCR stimulation alone activates proliferation, lack of IL-2 signaling results in suboptimal clonal expansion and slower cell cycle progression [362]. In addition to IL2R α , naïve CD4⁺ T cells also express inadequate IL2R β . Therefore, exogenous addition of IL2 can reduce the TCR signaling threshold in CD8⁺ but not in CD4⁺ T cells [378]. These observations highlight despite being derived from a common lineage; the naïve states are programmed differently.

The proliferation of activated T cells is preceded by the growth phase and characterized by major metabolic rewiring in which cell size increases about 3 to 4-fold. Myc functions as a critical transcription factor for the global metabolic reprogramming in activated, primary T lymphocytes [379]. Recent evidence highlights Myc deficient T cells fail to increase cell size substantially and do not proliferate on stimulation with an antigen of adequate strength. Mass spectrometry data shows that despite immune activation, expression of most but not all proteins is compromised in Myc knockout (KO) T cells as compared to the wild type cells [380]. These observations establish Myc as a global proteome modulator too. Myc is also known to control the “division destiny” of T cells proliferative response i.e., the number of times T cells would divide depends on the Myc level; division ceases when Myc drops below a threshold value [381]. Hence, the adaptive immune response is largely coordinated by the temporal activity profile of proto-oncoprotein Myc. The temporal profile of Myc coincides with two phase activation of ERK, PI3K/Akt (Figure 5.1) on growth factor signaling in various mammalian cell lines [29, 136, 382]. Its levels rise rapidly to peak around 2hrs, which then decreases to an intermediate value followed by another rise around 6hrs before dropping to a low level. ERK phosphorylates Myc at Ser62, which protects Myc from degradation and increases its half-life. Myc S62 phosphorylation promotes its phosphorylation at Thr 58 by GSK3 β . Dual phosphorylation of Myc makes it a substrate for Pin1 catalyzed *cis* to *trans* conformational change at S62-P63 peptide bond. PP2A phosphatase recognizes this substrate in *trans* conformation and dephosphorylates Myc at S62. T58 mono-phosphorylated Myc subsequently undergoes ubiquitinylation and proteasomal degradation. PI3K/Akt inactivates GSK3 β by phosphorylation and has a positive effect on Myc levels [383]. ERK and PI3K/Akt activity also rapidly increase on antigen

stimulation of TCR and show transient behavior in T cells [372, 384–386]. Myc rapidly accumulates within the first 4hrs of TCR stimulation and continues to increase thereof, albeit at a slower rate. Although the qualitative features remain identical in both CD4⁺ and CD8⁺ T cells, Myc rises to significantly higher levels in CD8⁺ T cells [380, 381]. Myc and mTORC1 signaling targets e.g., proteins involved in translation, ribosome, nucleotide synthesis, glucose metabolism, show a delayed induction but continue to accumulate between 8-16hrs. IL2 signaling components IL-2, IL2R α follow similar behavior [372]. This pathway is known to control PI3K/Akt activity. However, IL2 signaling is dispensable for activation and becomes critical during expansion [362]. Further, overall GSK3 β activity is modulated by multiple inhibitory and activatory phosphorylation. Inhibitory phosphorylation of GSK3 β goes down, whereas activatory phosphorylation goes up as an immediate response to TCR stimulation. Different experimental observations have studied the phosphorylation status of distinct residues that collectively suggest GSK3 β kinase activity downregulates between 12 - 24 hrs of TCR stimulation [372, 386, 387]. These data show apparent differences between GSK3 β kinase activity and Myc profile which may be explained by alternate mechanisms e.g., enhanced production and stabilization of Myc by other means [380, 388, 389]. Further, new findings report that unlike previously believed, neither Akt-mediated N-terminal phosphorylation of GSK3 β completely inhibit its activity nor is it the only regulatory kinase for GSK3 β [386]. Several other kinases, including mTOR targets p70 S6 kinase and p90 Rsk, negatively regulate GSK3 β [387].

In this chapter, we modeled the quiescence to proliferation transition in the presence of antigen, which triggers both proliferative and antiproliferative responses. Myc serves as a central regulator of the network by controlling proliferative and antiproliferative signals to drive entry into the proliferation phase. We showed a feature of dynamic change in the threshold for quiescence exit in T cells. To gain further insights into how Myc levels are maintained for an extended duration during T cell activation, we also developed a detailed model of Myc regulation that integrates transcriptional, translational, and post-translational controls. We showed that positive feedback loop regulation of Myc helps to sustain Myc levels and meet the metabolic demand. Interruption of the positive feedback between Myc and amino acid import interferes with immune cell activation. Finally, we also extended the

study to explore the gene expression pattern of Myc and amino acid transporters in other rapidly proliferating cells like cancer.

5.2 Model description

5.2.1 Activation of naïve T cells on antigen recognition

Quiescent naïve T cells get activated on antigen recognition by TCR and commit to proliferation [390]. We explored the quiescence to proliferation transition model [306] in the context of T cells. The underlying network remains the same, with antigen serving as an input signal to the model. Antigen priming turns on a series of events analogous to growth factor signaling. Myc repression gets relieved, and synthesis is turned on [391–393], which in turn promotes transcription of cell cycle activators E2F and cyclins (CycD, CycE) [19, 131, 149, 345]. CycD in complex with cyclin dependent kinases (Cdk4/6) monophosphorylates Rb (RbP), the stoichiometric inhibitor of E2F. E2F autoregulates itself and drives CycE transcription. CycE-Cdk2 inactivates Rb by hyperphosphorylation (RbPP). Naïve T cells express a varying degree of Cdk inhibitor (CDKI) [362, 394], which forms complex with Cyc-Cdk and inhibits its activity. APC/C-Cdh1 also maintains the G1 state by degradation of cyclins and Skp2, which promote CDKI degradation [129, 130]. APC/C-Cdh1 and Emi1, another E2F target, control G1/S transition through mutual inhibition [157] (Figure 5.2).

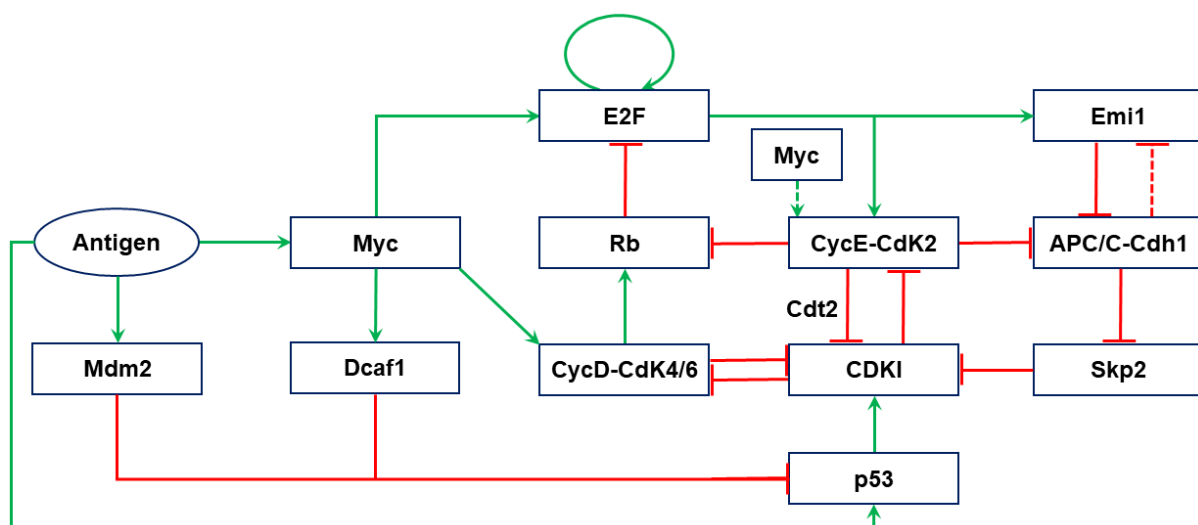


Figure 5.2: The molecular mechanism controlling the cell cycle re-entry in the presence of antigen in T cells.

Antigen recognition by TCR triggers an immediate antiproliferative response mediated by the expression of the p53 tumor suppressor [371, 372]. p21, a CDKI of the Cip/Kip protein family, is the transcriptional target of p53 [286]. Its accumulation at the G0 exit and early G1 further increases the barrier against Cdk activity. However, TCR signaling also induces Mdm2 [371], which forms complex with p53 and facilitates its rapid degradation by CRL4 E3 ubiquitin ligase [395, 396]. Dcaf1, an essential substrate receptor of CRL4, is induced by antigen stimulation driven Myc accumulation (Figure 5.2) [397, 398]. Hence, antigen recognition by TCR turns on an incoherent feed forward loop that delays the commitment to proliferation. We integrated the antiproliferative mechanism with our quiescence to proliferation reversible transition model [306] to explore how the relative abundance of inhibitors and activators impact system dynamics.

5.2.2 Myc protein stability model

Naïve T cells actively maintain the state of quiescence through repressive chromatin modifications or transcriptional repression of cell cycle activators [390–392]. Further, these cells are not dormant; they actively transcribe several genes and translate the transcripts to sustain the non-proliferative state. Additionally, maintenance of quiescence is supported by high rates of mRNA, protein turnover e.g., the transcription factor that actively retains the quiescent state and blocks proliferation has shorter half-life [390]. Although it works like a futile cycle, this helps to quickly respond to antigen stimulation. c-Myc mRNA and protein levels increase within 2-4hrs of TCR signaling [380, 381, 391]. The cycle of protein synthesis and degradation is complemented by autophagy in nutrient limiting conditions [399]. Naïve T cells perform autophagy at a basal level, and this activity increases in activated T cells [400]. We consider that autophagy is activated by TCR signaling (Figure 5.3), which provides amino acids for translation. Myc aids glucose and amino acid metabolism by driving the expression of their transporters (SLC2A1, SLC1A5, SLC7A5) [379, 380, 401]. The intracellular glutamine facilitates transport across obligate exchanger SLC7A5: efflux of glutamine is coupled to the influx of essential amino acids such as leucine, methionine [380, 402, 403]. The nutrient transporters are collectively represented as SLC in the model that contributes to an increase in the intracellular amino acid pool ($a\bar{a}_{pool}$), and Myc drives its synthesis (Figure 5.3). The localization of the amino acid transporter also depends on TCR signaling [380, 402]. The model considers the concurrent activation of ERK and Akt with

TCR signaling that can protect Myc from degradation (Figure 5.4). Unphosphorylated and GSK3 β phosphorylated (Thr58) forms of Myc are rapidly degraded compared to ERK (S62) phosphorylated form.

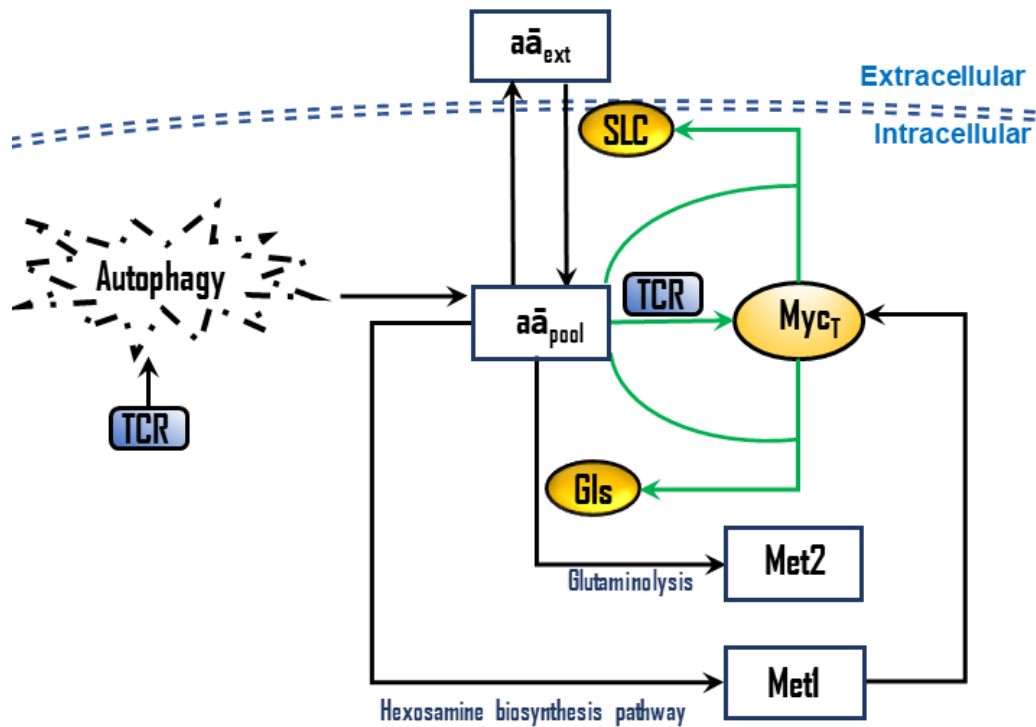


Figure 5.3: Molecular network showing the incoherent feedforward loop regulated by Myc. Metabolites are represented by rectangles, proteins are denoted by yellow-colored ovals. Green arrows represent translational regulation, protein synthesis depletes and degradation generates aa_{pool} .

The uptake of amino acids is also accompanied by their utilization in different pathways. The glutamine gets utilized in the hexosamine pathway in the presence of glucose and produces uridine diphosphate N-acetylglucosamine (UDP-GlcNAc). This metabolite (represented as Met1 in the model) donates N-acetylglucosamine (GlcNAc) to Myc for glycosylation at Thr58 in the O-GlcNAc transferase (OGT) catalyzed reaction. OGT competes with GSK3 β for post translational modification of Myc at 58 and protects Myc from ubiquitinylation followed by proteasomal degradation (Figure 5.4).

The continuous supply of amino acids supports the synthesis of proteins, including Myc. Thus, Myc dependent uptake of amino acids supports its own synthesis and stabilization, forming a positive feedback circuit. Blocking either SLC1A5 or SLC7A5 reduces the Myc levels at 20-24hrs [380, 401, 402]. The diverse functions of glutamine make it a conditionally essential amino acid in activated T cells [404]. On the other hand, many of

the glutamine metabolism enzymes are also Myc targets (e.g., Gls) [379]. This forms a negative feedback loop since glutamine depletion leads to a decrease in Myc levels.

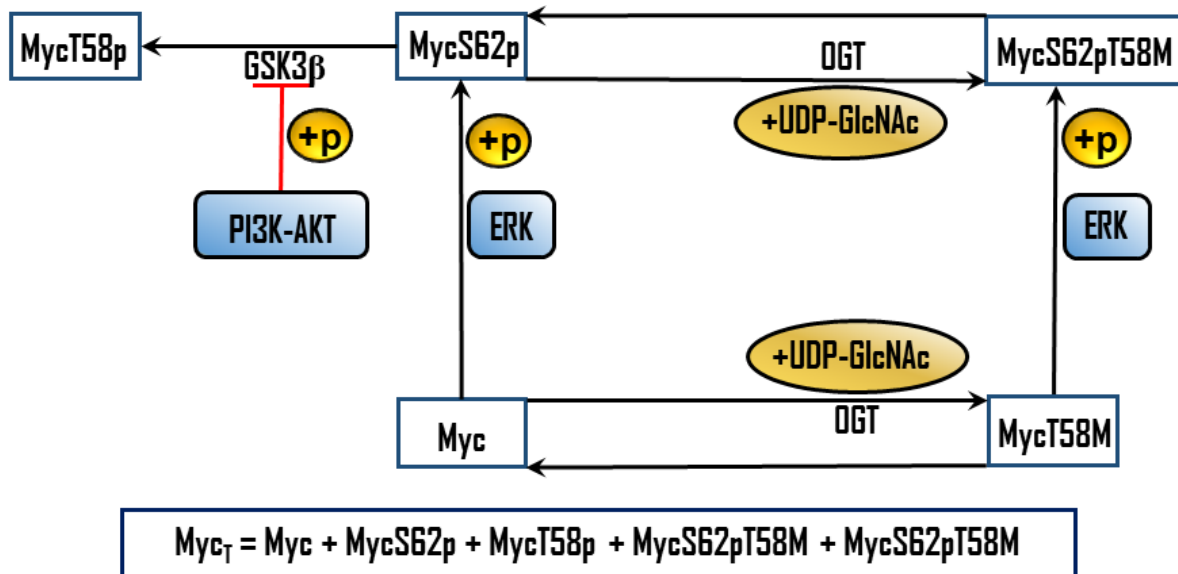


Figure 5.4: Molecular network that regulates Myc accumulation. Blue colored rectangles with rounded corners represent inputs to the model, yellow-colored circles and ovals represent the underlying mechanism. Met1 in model and figure 5.3 represents UDP-GlcNAc.

We consider Gls as a representative of these enzymes which metabolize glutamine. Hence, Myc turns on an incoherent feed forward loop that promotes both increase and decrease in intracellular amino acid level by transport and utilization, respectively (Figure 5.3). Most of the metabolites generated from glutamine are used for biosynthetic and bioenergetic needs and are collectively represented by state variable Met2 in the model. The model presented here explores how the different feedback loops cross talk to control the levels of Myc based on the recent experimental observations [29, 377, 380, 383, 388, 389, 402]. Based on the available data compiled from several sources, we also hypothesize a temporal order for the Myc protective mechanisms [372, 386, 387].

5.3 Methods

The wiring diagrams presented above (Figure 5.2-5.4) were translated into a set of ordinary differential equations (ODE) and algebraic equations to describe the dynamics of naïve T cell activation on antigen priming and Myc accumulation on T cell activation.

The proposed quiescence-proliferation reversible transition model presented in chapter 2 [306] was extended to include TCR signaling dependent synthesis of Myc, p53 and Mdm2, p53 dependent synthesis of CDKI, and Myc dependent synthesis of Dcaf1. The synthesis and degradation of new components were modeled by the law of mass action, and the new parameters were optimized to capture the temporal characteristics of naïve T cells quiescence exit. One parameter bifurcation analysis was performed to study the effect of variation in parameter value on the activation threshold (strength of TCR signal). The sensitivity of the model towards new parameters was evaluated by measuring the fold change in activation threshold with a $\pm 10\%$ change in the values. We performed proteome data analysis to compare CD4⁺ and CD8⁺ T cells. Temporal data of naïve and activated T cells were taken from Howden et al. [394] to explore the shared and unique features of the two T cell subsets. We used average expression from biological replicates for naïve and activated (post-24hr) CD4⁺ and CD8⁺ T cells to compute the fold-change in the expression. The expression profile of individual proteins along with their standard deviation (σ) is given in figure S1 to S3 (APPENDIX C).

Next, we considered an existing dynamic model of Myc in the presence of growth factor signaling and expanded it to include alternate mechanisms that support Myc accumulation on T cell activation in the presence of antigen [136]. Lee et al. modeled the post translational modifications of Myc by ERK and GSK3 β that influence its stability. Myc phosphorylation was modeled as enzyme catalyzed reactions following Michaelis-Menten kinetics. The extended model also included Myc regulation at the transcription, translation, and post translation levels (Figure 5.3 and 5.4). The enzyme catalyzed reactions were similarly modeled as Michaelis-Menten kinetics. Other reactions like import, export, synthesis, and degradation were modeled by the law of mass action. Myc dependent synthesis of glutaminase (Gls) and amino acid transporter (SLC) were modeled as Hill functions. The model parameters used to describe Myc phosphorylation by ERK and GSK3 β were taken from the earlier model [136]. The parameter values were tuned to match the dynamics of Myc accumulation on T cell activation in normal and mutant conditions. TCR was used as the input parameter to simulate antigen exposure. Additionally, ERK and PI3K activity that is regulated by TCR were also considered as an input to the system. The knockout (KO)/inhibition experiments for state variables were simulated by setting the synthesis rate to

zero. The final steady state of Myc represents the model output. The sensitivity of the model with $\pm 10\%$ change in parameter values was tested by computing fold change in Myc total levels $\left(\frac{Myc_{Total\ new\ parameter}}{Myc_{Total\ default\ parameter}}\right)$.

The state variables represent relative concentrations of respective components. The rate constants (k) have a dimension of $time^{-1}$, and Michaelis constants (J) and half-saturation constants are dimensionless. The set of equations was solved numerically with XPPAUT. The equations and parameter values are presented in the appendix section (APPENDIX C).

The model presented here aimed to study the adaptive immune response mediated by T cells on antigen stimulation. We also tested if the Myc and amino acid transporter relationship described in our model holds true in other rapidly proliferating cells like tumors. Transcriptome data of the different cancer types (Table 3.1) were analyzed to understand the expression pattern of amino acid transporter in cancers and examine its association with cancer types showing frequent dysregulation around Myc proximal network [405].

5.4 Results

5.4.1 Antiproliferative response triggered by antigen recognition regulate T cell activation threshold

The simulation of the model in the presence of antigen shows that CDKI ($CDKI_T$) initially increases and then decreases at the G1/S transition. The time required for cell cycle re-entry increases due to an increase in the barrier for Cdk activation (Figure 5.5a). This delay is reduced in the absence of an antiproliferative response mediated by p53 (Figure 5.5b). In the absence of Dcaf1, the incoherent feed forward loop is broken, and the G1/S transition is blocked due to the high CDKI barrier (Figure 5.5c). One parameter bifurcation analysis shows an irreversible T cell activation with an increase in TCR signal strength. The saddle node (SN1) shifts to the right with an increase in the TCR dependent p53 synthesis (k_{sp53}), transiently blocking cells in G1 (Figure 5.5d). SN1 denotes the TCR signal threshold required for commitment to the cell cycle (Rb hyperphosphorylation/ E2F activation). Elimination of p53 is required to reduce the threshold for cell cycle re-entry (shifting SN1 to the left). Withdrawal of antigen stimulus doesn't switch the system back to the quiescent state

(low RBpp) after transition, leading to an irreversible commitment to the cell cycle. This picture assumes that nutrient availability is not rate limiting in the control of protein levels.

Further, the new set of parameters was also varied in a range of $\pm 10\%$ to study their effect on the activation threshold. We observed that the activation threshold shifted by less than 10% (Figure 5.6) with parametric variations.

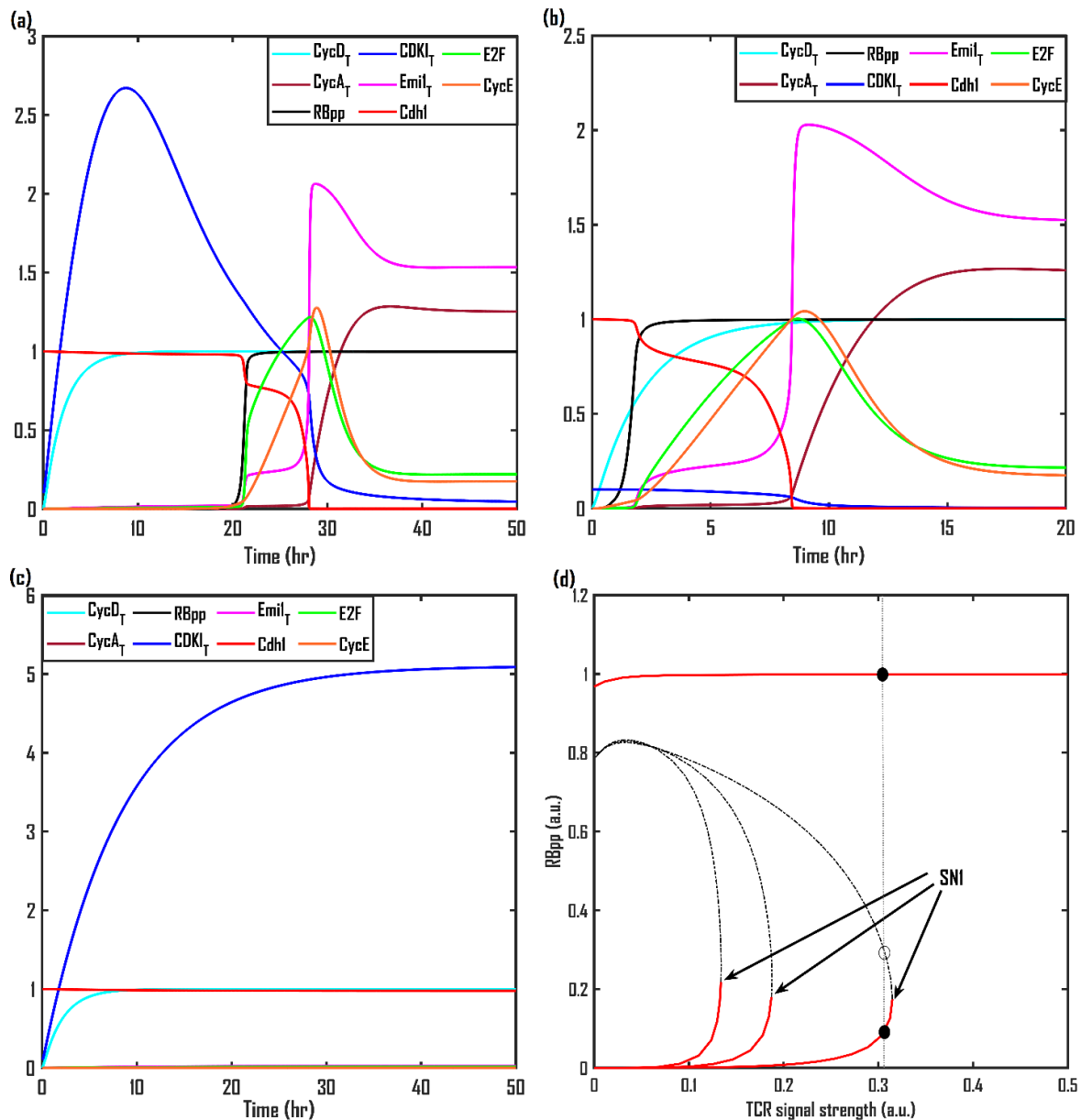


Figure 5.5: Antigen triggered temporal dynamics of naïve T cell activation (quiescence exit) (TCR = 1) (a) in the presence ($k_{sp53}=0.01$) and (b) in the absence of antiproliferative signaling ($k_{sp53}=0$); and (c) in the absence of Dcaf1 ($k_{sp53}=0.01$, $k_{sdcaf1}=0$). (d) Bifurcation analysis of Rb-E2F subsystem. The effect of increasing the TCR signal strength on Rb hyper-phosphorylation is shown for three different values of p53 synthesis rate ($k_{sp53}=0, 0.001, 0.002$). The TCR signal strength required for Rb inactivation increases (shifts right) with increase in k_{sp53} . Filled circle represents the stable steady state and empty circle represents the unstable steady state.

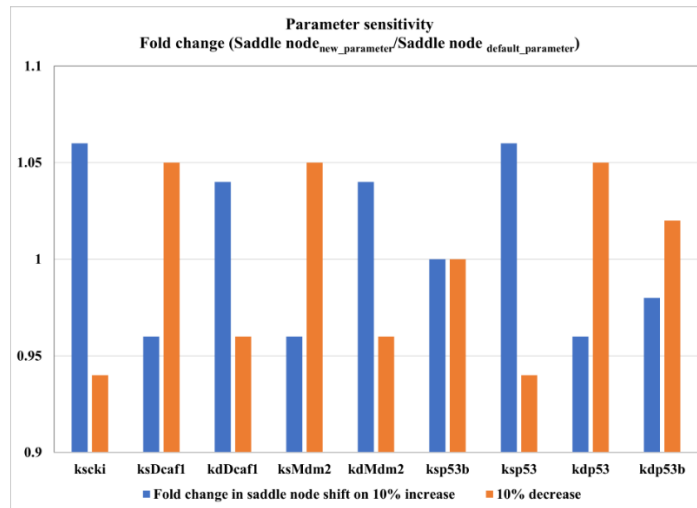


Figure 5.6: Parameter sensitivity analysis for T cell quiescence exit. The bars represent the fold change in saddle node values for change in parameter (increase or decrease) from default values (fold change = $SN(\text{new})/SN(\text{default})$). Fold change in SN1 with increase (blue) and decrease (orange) in parameter values are shown.

5.4.2 Quiescent state is programmed differently in naïve $CD4^+$ and $CD8^+$ T cells

The model presented above represents a generic network scheme of naïve T cell activation in the adaptive immune response. We analyzed proteome data from the two subsets of T cells, i.e., $CD4^+$ and $CD8^+$, to compare their state of quiescence [394]. The average protein concentration of total CDKI (cumulated p15, p18, p19, p21, p27) was around 7.5-fold higher in $CD8^+$ T cells compared to $CD4^+$ (Figure 5.7a). Thus, $CD8^+$ T cells appeared to have a higher CDKI barrier against quiescence exit. However, experiments suggest that $CD8^+$ T cells exit quiescence more rapidly than $CD4^+$ T cells under identical conditions and achieved higher clonal expansion with a greater mean division number [406, 407]. Differences in the cellular response of $CD8^+$ and $CD4^+$ cells have been linked to IL2 signaling responsiveness [378, 408], but the impact of IL2 signaling becomes evident only after cell cycle entry [362, 407, 409]. These observations motivated us to explore other possibilities that explain $CD8^+$ versus $CD4^+$ difference in timing. We observed from proteome data that $CD8^+$ T cells not only express a higher CDKI barrier but also larger total cyclins when compared to $CD4^+$ T cells. Despite elevated expression of cyclins, $CD8^+$ cells still remain trapped in the quiescent state because of a sizable inhibitor to activator ratio ($CD8^+$ T cells: 7.2 ± 2.4 , $CD4^+$ T cells: 3.5 ± 1.4) (Figure 5.7a). The overall protein abundance suggests that naïve $CD8^+$ T cells are translationally more active, but the high CDKI barrier halts them in quiescence. Accordingly,

we observed that Myc shows 4-fold higher induction in CD8⁺ T cells 24 hrs post activation (Figure 5.7b). It controls both arms of the cell cycle entry network (Figure 5.2); it suppresses the negative arm by Myc dependent accumulation of Dcaf1 and promotes the positive arm by transcription of cyclins [149, 397]. CD8⁺ T cells also accumulate p53 inhibitor Mdm2 at a comparatively faster rate (Figure 5.7b). These observations suggest that activated CD8⁺ T cells may rapidly overcome the CDKI barrier and enter into the proliferative state. We have shown earlier that the slope of Cdk2 activity determines the temporal dynamics of G1 phase events [306]. A steeper slope of cell cycle activators in CD8⁺ T cells would imply a reduction in time for APC/C-Cdh1 inactivation and G1/S transition overcoming CDKI barrier. The inhibitor ratio of CD8⁺ to CD4⁺ shows a rapid decrease (Figure 5.7b). Myc also aids rapid proteome remodeling of CD8⁺ T cells through maintenance of amino acid supply (Figure 5.7b). The amino acids support T cell activation and proliferation by performing a multitude of tasks, e.g., meeting biosynthetic demand for macromolecule synthesis, mTORC1 activation, etc. [380, 410].

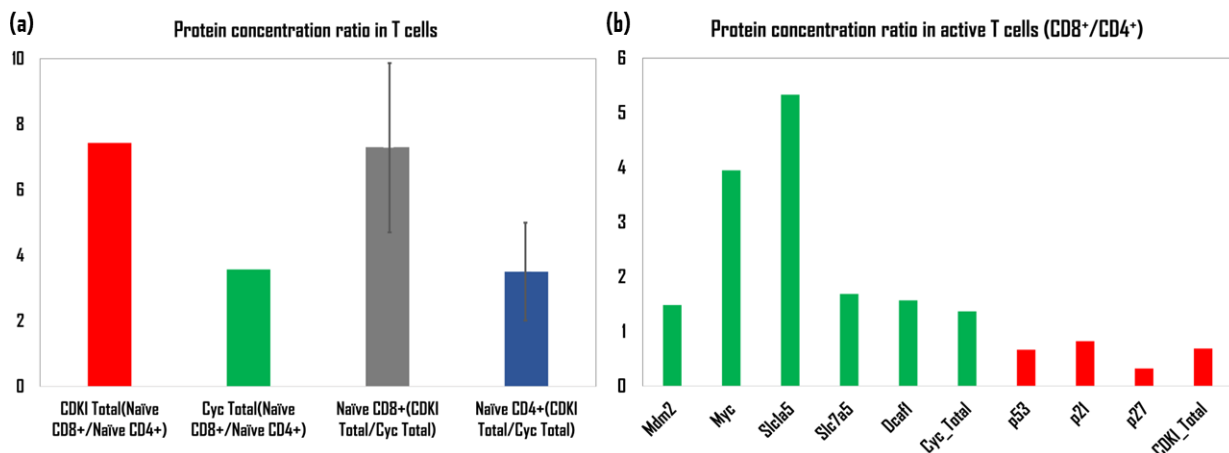


Figure 5.7: Proteome data analysis of naïve and activated CD4⁺ and CD8⁺ T cells. (a) Naïve CD8⁺ T cells have higher concentration of cumulative CDKI and cyclins, high CDKI versus cyclins level promote quiescence in T cells. Error bars represent standard deviation across biological replicates. (b) Activated CD8⁺ T cells synthesize inhibitors of CDKI (Mdm2, Dcaf1) and amino acid transporters (SLC1A5, SLC7A5) rapidly than CD4⁺ T cells (24 hrs data).

5.4.3 TCR priming drives rapid induction of Myc independent of amino acid transporter

Antigen recognition by TCR induces different downstream cascades; Myc is one of the early responders to this signal. In this model, we explored the plausible mechanisms that regulate Myc on TCR engagement. On antigen recognition by TCR, Myc rapidly accumulates within 2 to 3hrs and further gradually increases to reach a higher steady state value. TCR

rapidly promotes Myc synthesis by controlling its transcription and increasing the amino acid levels (Figure 5.8a). Our model efficiently simulates the temporal profile of Myc activation in both CD4⁺ and CD8⁺ T cells.

Naïve T cells repress Myc by several independent mechanisms, which include a low level of promoter usage, a block to transcriptional elongation, and fast degradation of c-myc mRNA. Stimulation of naïve cells causes accumulation of mRNA within 2hrs. TCR priming activates protein kinase C and increases intracellular calcium. Intracellular calcium coordinates early rise in c-myc gene expression by increasing transcription initiation [391]. Moreover, antigen stimulation rapidly phosphorylates and drives degradation of FOXO1, the upstream regulator of Lung Kruppel like transcription factor (LKLF). LKLF is highly expressed in naïve T cells. It is an important player that programs and maintains the quiescent state by negatively regulating Myc expression [390, 392].

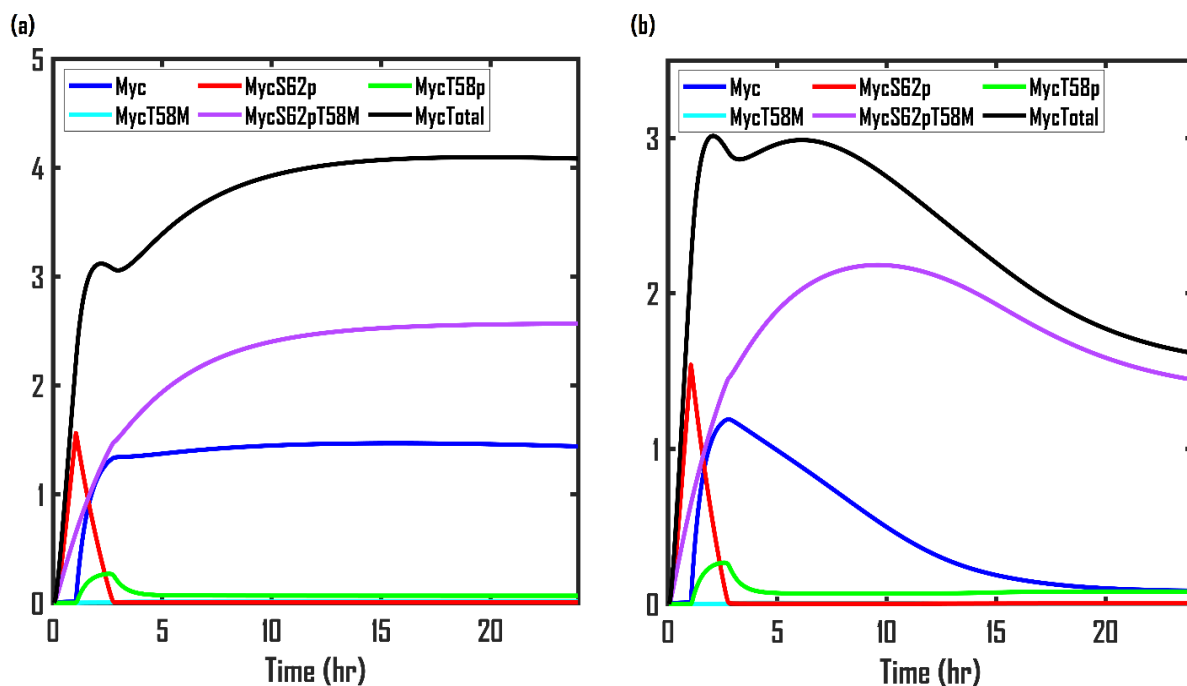


Figure 5.8: Antigen triggered temporal dynamics of different forms of Myc (a) in the presence and (b) in the absence of amino acid transporter ($k_{sslc}=0$). Different forms of Myc are colored on the basis of post translational modification; p represents phosphorylation, M represents glycosylation at sites Ser62 and/or Thr58.

The increasing bioenergetic and biosynthetic demand of T cells requires a continuous supply of nutrients. However, the early rise of Myc is found to be unperturbed in the absence of essential amino acid transporter [380, 401]. We model this experimental observation by considering that the early demand of monomer units for protein synthesis is satisfied by the intracellular pool. Figure 5.8b simulates the transporter knockout condition ($k_{sslc}=0$). This

shows that continuous replenishment of amino acids becomes crucial to sustain Myc at the later stage (24hrs).

These observations are supported by the results showing an active proteolysis mechanism in T cells. T cells activation induces autophagy rapidly to support the biosynthetic demand of these cells [400]. Autophagy generates amino acids to fuel new protein synthesis as well as ATP to provide energy for peptide bond formation [399]. It becomes important, especially at the earlier time point prior to the transcription induced metabolic reprogramming of T cells.

5.4.4 Temporal dynamics of Myc depends on post translational modification

Next, we studied the impact of posttranslational modification on the temporal profile of Myc. Although we observe that an increase in Myc synthesis rate with TCR signaling account for its rapid accumulation, this may also depend on the change in its stability due to posttranslational regulation. We observe that, similar to growth factor signaling [136], our model output is also modulated by the profile of ERK (Figure 5.9a). ERK brings down Myc degradation by S62 protective phosphorylation. Indeed, antigen recognition by TCR evokes ERK activity within minutes, and Myc level is significantly compromised in the presence of PD184352, a highly specific inhibitor of MEK, an upstream regulator of ERK [377].

Additionally, Myc levels are also determined by PI3K-Akt activity in multiple cell lines. PI3K-Akt signaling axis protects ERK phosphorylated Myc from GSK3 β inhibitory phosphorylation (Figure 5.1). However, in T cells, GSK3 β activity does not decrease immediately with TCR signal compared to mitogen stimulation experiments [372, 386, 387]. We modeled an alternate mechanism that may account for Myc stability. This involves competition between OGT and GSK3 β . OGT adds N-acetylglucosamine at Thr58 and masks Myc from phosphorylation at that site [388, 389]. We hypothesized glycosylation may protect Myc at an early time point when GSK3 β activity is still high. The model simulation shows that in the absence of OGT, there is a reduction in Myc level by 6hrs (Figure 5.9b). It efficiently mimics experimental results of reduction in Myc level after 6hrs of antigen stimulation of naïve T cells in the presence of OGT inhibitor [388].

5.4.5 Positive and negative feedback loop regulation of Myc

While glycosylation plays a role in Myc accumulation by protecting Myc from degradation, this may not be the sole mechanism since amino acid transporter is required for sustaining Myc levels [380]. This raises the question of why glycosylation alone can't protect Myc or when and how the amino acid transporters become crucial for Myc. We hypothesized Myc turns on negative feedback loop(s) that evoke dependence on additional means to sustain the Myc levels.

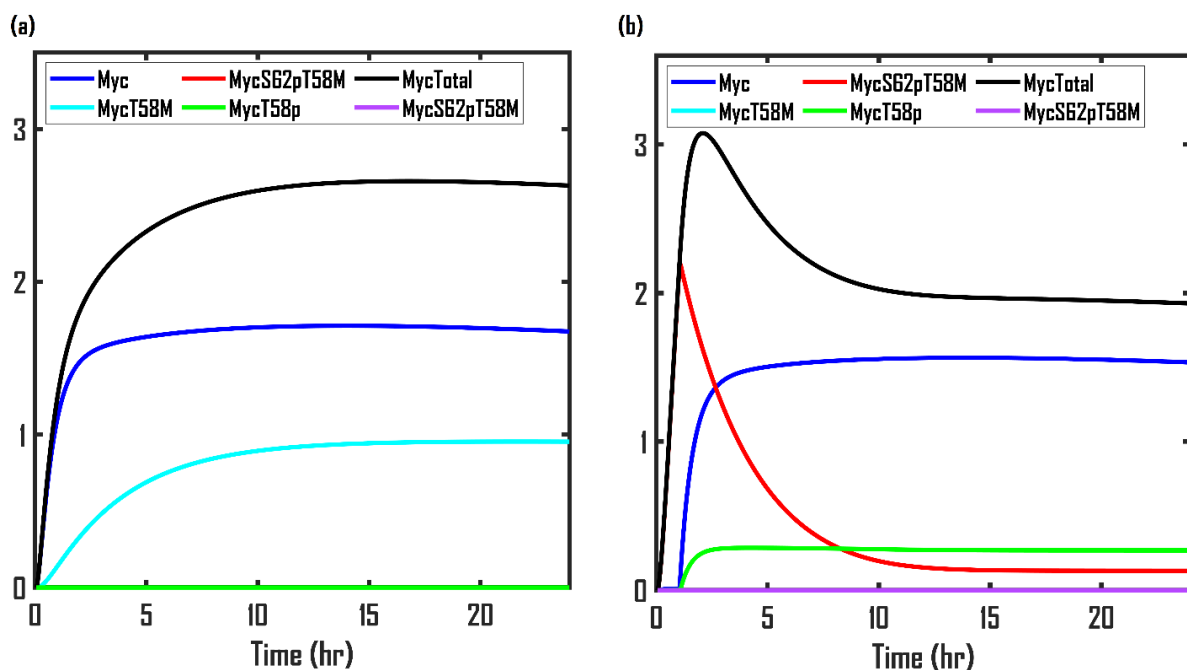


Figure 5.9: Antigen triggered temporal dynamics of different forms of Myc (a) in the absence of ERK activity ($Erk_{max}=Erk_{residual}=0$) and (b) in the absence of OGT activity ($V_{max}=V_{maxn}=0$). Different forms of Myc are colored on the basis of post translational modification; p represents phosphorylation, M represents glycosylation at sites Ser62 and/or Thr58.

Our simulation shows a gradual depletion of the amino acid pool with an increase in Myc levels in the absence of amino acid transporter (Figure 5.10). This is due to the presence of the negative feedback loop: $a\bar{a}_{pool} \rightarrow Myc \dashv a\bar{a}_{pool}$. A fraction of glutamine channels through the hexosamine biosynthesis pathway, which uses glutamine as a substrate and generates N-acetylglucosamine as a product [379, 388], thereby reducing the intracellular amino acid pool. In addition to protection of Myc, glutamine supports the biosynthetic demand of proliferating T-cells by providing intermediate metabolites for the TCA cycle, nucleotides, other amino acids, lipid, polyamines, and anti-oxidant synthesis. Enzymes involved in glutamine metabolism are also the transcriptional targets of Myc. Glis is one such

enzyme that is a Myc target and catalyzes glutaminolysis. Other enzymes also show similar trait e.g., Cad, Ppat, Odc, Oat, Glud, Got, Pfk1, Pfkfb3, Aldoa, Gpi, Ldha [379]. Further, Myc being a central regulator of metabolic reprogramming and proteome remodeling drives large scale protein synthesis [379, 380]. Thus, the intracellular amino acid pool can decrease with Myc induced metabolic reprogramming. Hence, the nutrient limiting state needs to be continuously replenished, and we show that this negative feedback loop is counter-acted by a positive feedback loop driven by Myc induced expression of essential amino acid transporters (Myc \rightarrow SLC \rightarrow $a\bar{a}_{pool}$ \rightarrow Myc). Thus, T cells under antigen stimulation are unable to meet an increase in high anabolic rate and protein synthesis on essential amino acid transporter KO or withdrawal of amino acid supply. External amino acid supply plays an important role in T-cell activation (Figure 5.10).

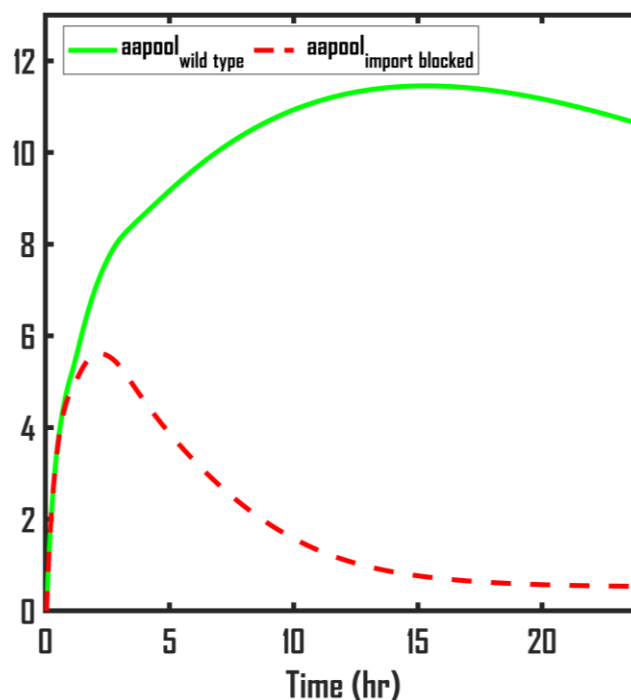


Figure 5.10: Temporal dynamics of intracellular amino acid pool on activation in wild type T cells (green) and in presence of transporter blocker (red, $k_{imp}=0$). Myc triggers negative feedback loops that deplete cells of amino acids.

We also tested how the steady state value of Myc is affected by the alternate mechanism of Myc stabilization by varying corresponding parameter values in the range of $\pm 10\%$ of their base value. The steady state value of Myc changed by less than 10% with variation in parameter value (Figure 5.11).

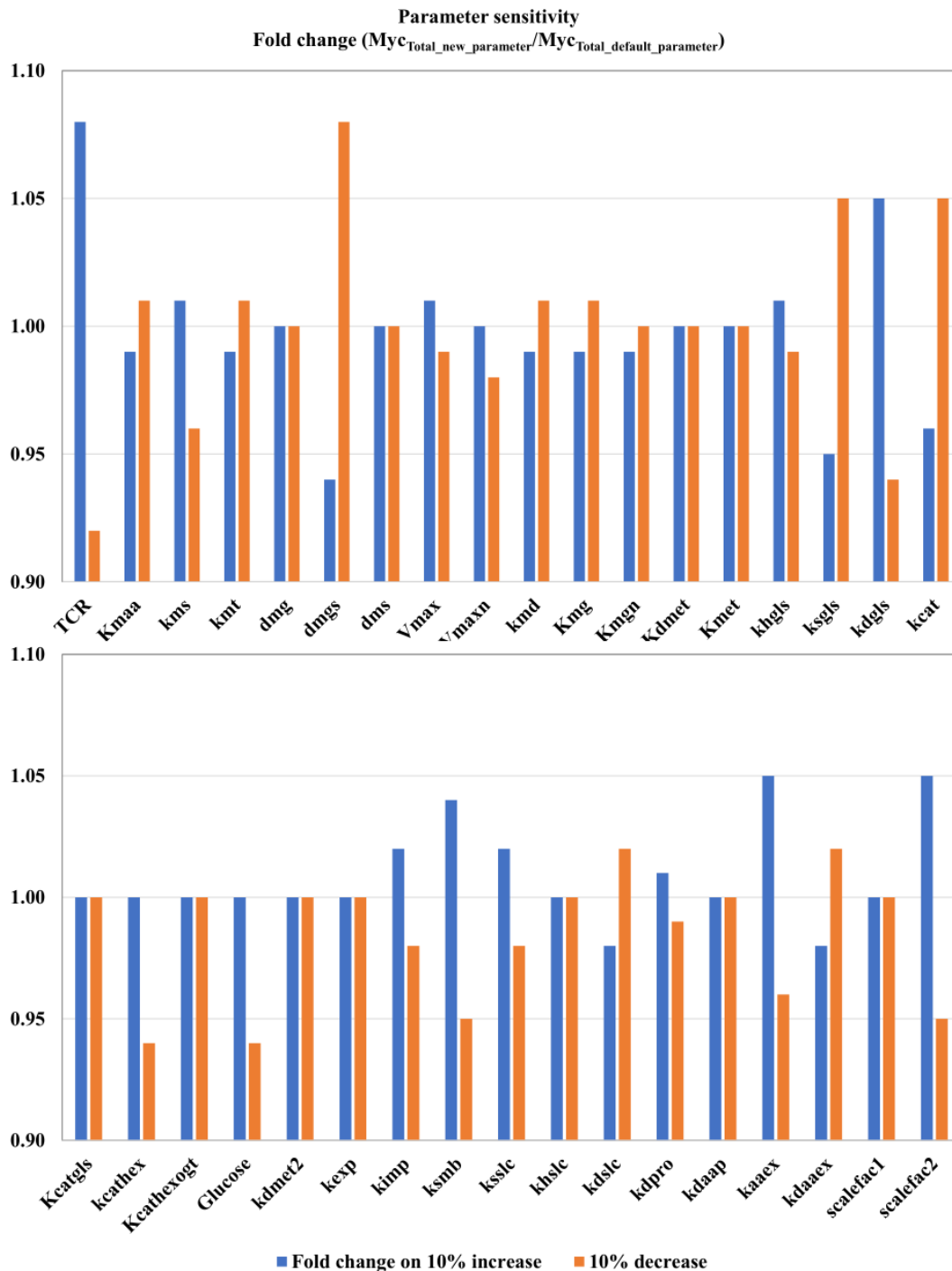


Figure 5.11: Parameter sensitivity analysis for Myc protein stability model. The bars represent the fold change in steady state value of Myc for change in parameter (increase or decrease) from default values. Fold change with increase (blue) and decrease (orange) in parameter values are shown.

5.4.6 SLC7A5 expression is altered in pan-cancer

We also explored whether the relationship between Myc and amino acid transporter is specific to T cells or is a generic scheme. We extended the model observations to tumor cells

since both proliferate fast and show convergent metabolic changes. Most of the 14 tumor types described earlier show upregulation of the SLC7A5 transporter. The sample wise fold change in expression of tumor versus matched normal samples (Table 3.1) show that SLC7A5 is upregulated in different cancers (Figure 5.12). We compared this transcriptome data analysis results with available information about the Myc proximal network dysregulation in TCGA tumor samples. Myc proximal network includes Myc itself, its related transcription factors, and its co-regulatory proteins that collectively form a single transcriptional module regulating the expression of Myc targets [405]. Upregulation of SLC7A5 (Figure 5.12), a Myc transcriptional target, is observed in the tumor types with the most frequent occurrence of alterations such as focal deletion of suppressors (MXDs, MNT, MGA), amplification of drivers (MYC paralogs, MAX, MLX), or mutations of network members in the Myc proximal network (Figure 5.13 [405]).

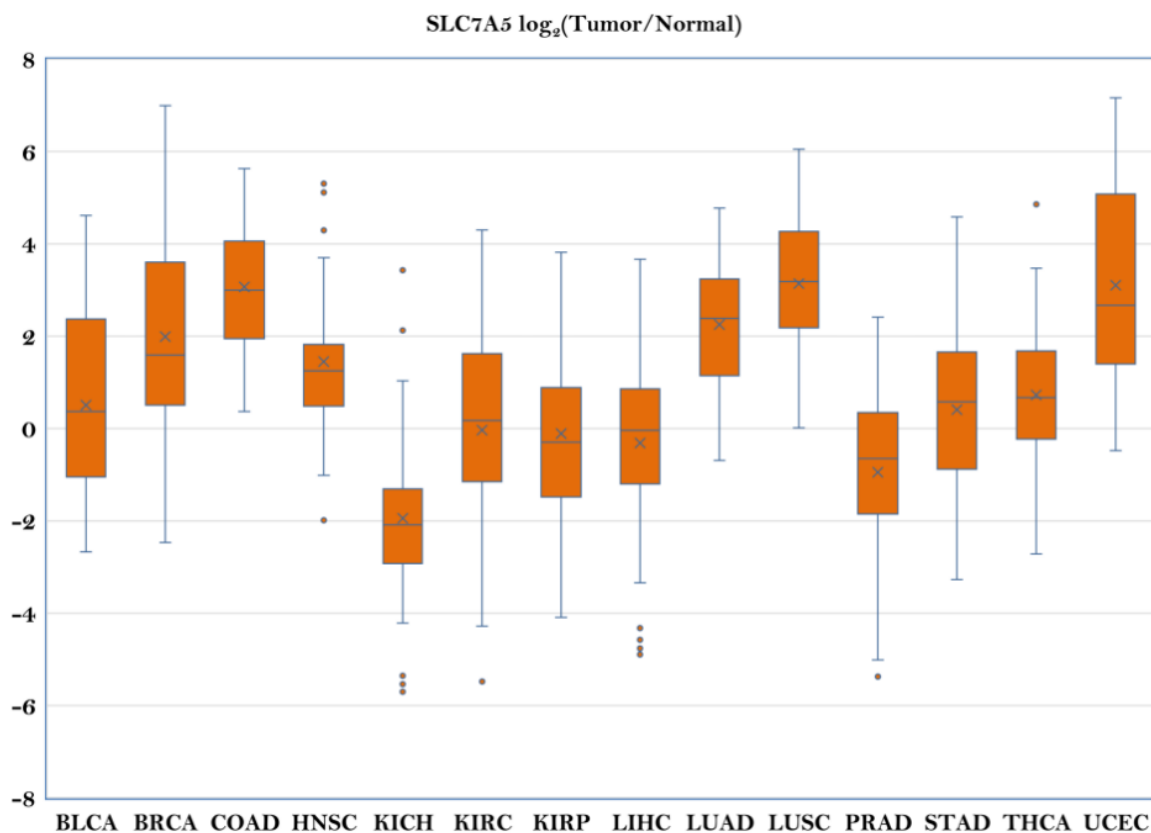


Figure 5.12: Box and whisker plot representing sample wise distribution of SLC7A5 expression data for 14 tumor types. As the values are log transformed to the base 2, four-fold change is measured as 2. The lower and upper whiskers represent minimum and maximum value respectively, circles represent outliers. Boundary of box represents first and third quartile range, mean is represented by 'x' and median by '—'.

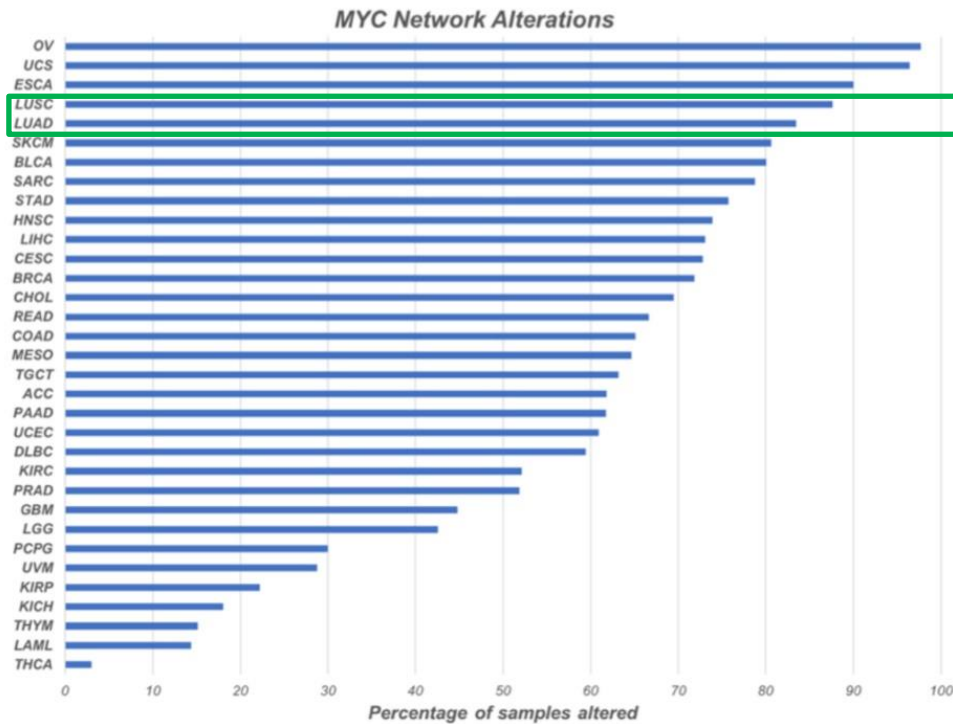


Figure 5.13: Among the 14 tumor types studied in gene expression data analysis, LUSC and LUAD show the most frequent alteration in Myc proximal network. The LUSC and LUAD tumor samples also show high $\log_2(\text{fold change value})$ reported in figure 5.12 (figure reproduced from [405]).

Intriguingly, comparison of survival probability based on SLC7A5 expression shows better discrimination in tumor types where Myc proximal network mutation frequency isn't high in population e.g., KIRC, KIRP. On the contrary, LUSC and LUAD do not show significant survival difference based on the expression of SLC7A5 (Figure 5.14). We attribute this observation to uniform upregulation of Myc and its target (Figure 5.13), thereby limiting its potential in disease prognosis.

5.5 Discussion

The work presented here focuses on the transition of naïve T cells to the activated state. Naïve T cells remain quiescent until they are challenged by antigen priming [390]. An array of cell cycle inhibitors, e.g., Cip/Kip family CDKI operate to maintain quiescence [394].

We studied the initial 24hrs of naïve T cell activation, which is known to be dependent on TCR priming [373]. As an early response to antigen recognition, T cells turn on an anti-proliferative response [371] that raises the CDKI barrier further and transiently blocks

the cells from immediately entering into a proliferative state by increasing the threshold for E2F activation. An immediate rise in inhibitors could be the cells' mechanism to filter random noise in the form of transient stimulus from a meaningful, sustained biological signal. In case of adequate and persistent signal, the inhibitors would gradually be removed or overcome by the activators. Alternately, an initial rise in CDKI barrier may provide cells with sufficient time window to grow and prepare for multiple rounds of division, also termed clonal expansion. Myc expression is turned on within 2 hrs [391]. It drives extensive metabolic reprogramming of T cells and cell growth [379, 380]. Thus, an early transient arrest could be crucial for clonal expansion.

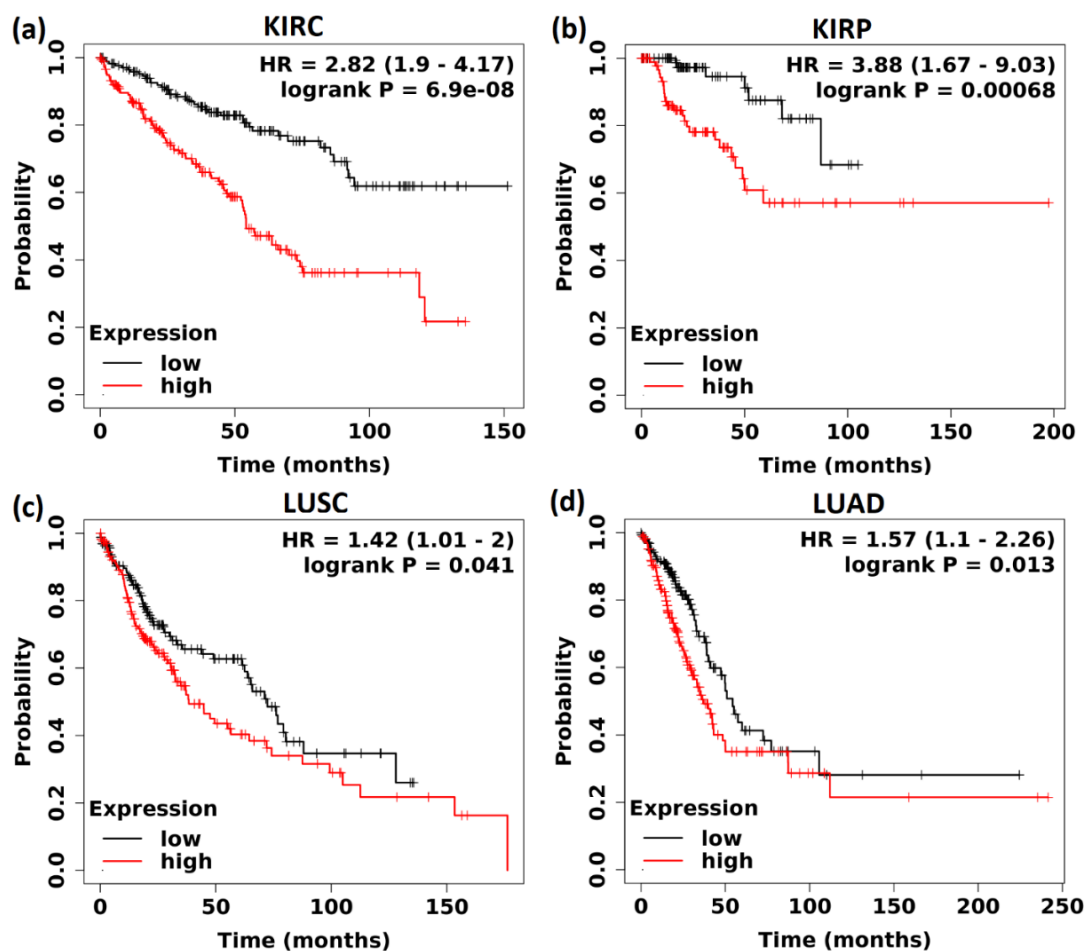


Figure 5.14: Survival analysis using SLC7A5 as a prognostic marker. Overall survival probability between low (black) and high expression group (red) for (a) KIRC (b) KIRP show significant difference (hazard ratio HR > 2, p value < 0.01); the high expression group has a lower survival probability. (c) LUSC and (d) LUAD don't show significant difference in survival probability of the two groups (hazard ratio HR < 2, p value > 0.01).

We also observed that despite the higher CDKI barrier, the CD8⁺ T cells progress faster through the cell cycle. This picture differs from Kwon et al. (2017), who showed that

fibroblast cells move deeper into quiescence with increase in CDKI levels on extended periods of mitogen starvation or contact inhibition. These cells take longer to exit quiescence [135]. However, CD8⁺ T cells have higher ribosome and translational complex numbers compared to CD4⁺ T cells [394]. Our proteome data analysis suggests that the possession of greater biosynthetic capacity may help naïve CD8⁺ T cells to accumulate cell cycle proteins rapidly than naïve CD4⁺ T cells. Cell cycle activators serve as accelerators, and inhibitors operate as brakes; they collectively ensure that the CD8⁺ T cells maintain a quiescent but prepared state. On stimulation, these cells swiftly build up not only the activators but also “inhibitors of inhibitors” and rapidly get rid of the molecular brakes. A similar strategy has been proposed in earlier studies where an apparently futile cycle of protein synthesis and degradation forms the basis of a rapid response system. These cells are continuously “running to stand still” [390, 411]. We propose translationally active CD8⁺ T cells are programmed to be stuck in quiescence by keeping the inhibitor’s barrier up. The differences between response dynamics of T cells subsets could be an adaptation that supports their effector functions. CD8⁺ cells differentiate into antigen specific cytotoxic T cells [412, 413]. Antigen specificity, clubbed with the ability of rapid expansion, makes them ideal for providing immunity against numerous virulent viral invasion [407]. Moreover, CD8⁺ T cells vary based on specific antigen receptor presented on their surface, so only a subset of the starting naïve cell population proliferates on antigen recognition. This further necessitates the need for a rapid quiescence exit. On the other hand, CD4⁺ T cells activate nonspecific immune response. CD4⁺ T cells differentiate into T_H1 or T_H2 helper T cells that produce cytokines, e.g., interferon (INF) – γ , IL-4, etc. [414]. Although cytokine-mediated immunity is primarily beneficial, under certain conditions, it can cause hyperinflammatory response [408]. Hence, delayed activation of CD4⁺ T cells would impose a more stringent commitment to proliferation and ensure a balance between protective and proinflammatory function. Remarkably, along similar lines, extensive regulatory mechanisms are put in place to constrain the differentiation of CD4⁺ T cells into large numbers of effector cells [412, 415]. On the contrary, CD8⁺ T cells readily develop into effector cytotoxic T cells even after brief stimulation [412, 416, 417].

Myc regulates proteome remodeling of T cells on TCR activation. Its knockout severely compromises overall growth and protein synthesis. The Myc stability model

explains the underlying principle involved in the rapid accumulation and maintenance of Myc levels with antigen stimulation. We show that Myc dependent metabolic adaptations create a situation of active accumulation and utilization (incoherent feedforward loop) of amino acids that are crucial for T cell activation. Myc facilitates its own transcription and translation by inducing amino acid uptake and ribosome machinery [379, 380, 401]. The imported amino acids provide the raw material for protein synthesis and also help in the activation of nutrient sensor mTORC1 (Met, Leu) [418, 419]. mTORC1 promotes protein translation by phosphorylating and activating translation factors [420, 421]. Further, glutamine also specifically controls the translation of Myc mRNA. Its 3'UTR region senses the unavailability of glutamine through metabolic intermediate and suppresses protein synthesis [422]. Myc also promotes the utilization of amino acids; therefore, an influx of amino acids plays a decisive role in T cell activation [379]. We show that a positive feedback loop between Myc and amino acid transporter is required to drive the sustained presence of Myc for T cell activation. Furthermore, Myc dampens the inhibitors that antigen stimulation sets off and drives proliferation.

In summary, we extended our quiescence-proliferation reversible transition model in the context of T cells to present a comprehensive picture of quiescence exit by including the dynamic regulation of CDKI barrier. We proposed a molecular basis for the differences in naïve CD4⁺ and CD8⁺ T cells activation. Further, we showed how multiple feedback loops function together in an ordered, non-redundant manner at the systems-level to maintain Myc levels in proliferating T cells. The Myc stability model incorporated the transcriptional, translational, and post-translational regulation of Myc controlled by antigen and amino acid metabolism. We also showed that cancer cells with frequent mutations around Myc proximal network also dysregulate essential amino acid transporters. Hence, the model presented here might also be a universal feature of Myc-induced tumors.

Chapter 6 CONCLUSION

The work presented in this thesis focused on mathematical modeling and analysis of the cell cycle regulation at a systems-level and exploring its crosstalk with metabolism and redox homeostasis. In the first part of the work, we studied the molecular basis of decision-making points: reversible transition between quiescence to G1 and irreversible G1/S phase transition in normal mammalian cell lines. The model provided mechanistic insights into both mitogen and stress sensitive commitment points of the mammalian cell cycle and accounted for the recent experimental findings. The underlying principle of commitment points is irreversibility, which emerges due to positive feedback loops giving rise to bistable characteristics. Thus, the system maintains an activated/inactivated steady state despite the withdrawal of the stimulus. While the irreversibility at the restriction (R)-point is a consequence of double negative feedback loop between E2F and Rb ($E2F \rightarrow CycE \dashv Rb \dashv E2F$), the G1/S commitment point becomes irreversible due to the novel double negative feedback between APC/C-Cdh1 and Emi1 ($APC/C-Cdh1 \dashv Emi1 \dashv APC/C-Cdh1$). We showed that the major G1-phase events are coupled via sequential activation of two bistable switches. The CycE-Cdk2 activity couples early (R-point) and late events of the G1 phase (APC/C-Cdh1 inactivation). The difference in inactivation threshold for Rb and APC/C-Cdh1 phosphorylation by CycE-Cdk2 temporally segregates the two toggle switches. Thus, interlocking multiple bistable switches forms the basis for unidirectional progression through G1. The model has been included as a curated entry in the BioModels database [160, 161], and part of our model hypothesis is validated by experimental observations of an independent group [157].

Extension of the normal cell cycle model to pathological context forms the basis of the next part of the work. Dysregulation of the decision-making points leads to proliferative diseases like cancers. The uncontrolled cellular division in cancer is supported by extensive metabolic reprogramming. We carried out transcriptome data analysis of different cancer types and found the metabolism of the RCC subtypes to be uniquely altered. Specifically, we observed metabolic divergence in KICH compared to other RCC subtypes. RCC subtypes can be broadly classified into three metabolic states viz oxidative, glycolytic, and hybrid. KICH,

the less aggressive form, showed oxidative phosphorylation phenotype, whereas the KIRC subtype mapped to the aerobic glycolysis state. KIRP, on the other hand, behaved heterogeneously, representing a hybrid phenotype with a subclass showing an aggressive phenotype like KIRC and another like chromophobe. We mapped these subtype-specific metabolic changes to the difference in the transcriptional regulation. The cell cycle transcription factors (E2F and FOXM1) [194] were identified as key regulators of metabolism, hinting at their cross talk. Network modules constructed based on co-expression profiles of genes aided the investigation of intragroup diversity. Unlike KIRC and KIRP, KICH showed uniform behavior across samples in most cases. Segregation of six KICH samples with respect to specific metabolic pathways facilitated recognition of metabolic divergence in an aggressive form of the disease. KICH being the less frequently studied subtype of RCC, our metabolic-network based study contributes to further understanding of cancer metabolism.

Another spectrum of cell cycle dysregulation is neurodegeneration. Loss of neurons in Alzheimer's disease is also attributed to dysregulated proliferation [246]. The existing therapies for AD attempt to target the root cause but remain limited as a symptomatic therapy [228]. In this part of the thesis, we explored the systemic regulation and consequence of several cell cycle re-entry mediated self-amplifying feedback loops through mathematical modeling. The modeling showed that integration of multiple feedback loops leads to an irreversible transition from low to high ROS pathological state. The in-silico perturbation experiments provide insights into drug targeting strategies. The transcriptional changes predicted by the model are consistent with transcriptome data from AD patients. We showed the emergence of different thresholds of E2F activation for DNA repair and apoptosis through coupling of multiple bistable switches, which emerges due to the double negative feedback loop regulation between Rb and E2F and positive feedback loop via p53/DINP1. DNA damage controls E2F levels that maintain the balance between pro-survival and pro-apoptotic fate. Our study also highlights the role of APC/C-Cdh1 in controlling the redox and metabolic state of differentiated neurons. Thus, G1/S bistable switch (APC/C-Cdh1^{On/Off}) also applies in the context of neuroprotection and neurodegeneration. The framework presented here is the first theoretical attempt to mechanistically model the link between cell cycle re-entry and neuronal apoptosis.

In the last section of the thesis, we extended the quiescence to proliferation reversible transition model to simulate naïve T cell activation as part of the adaptive immune response. We also proposed the rationale behind the differences in CD8⁺ versus CD4⁺ T cells response. Since Myc resides at the junction of metabolism and cell cycle, a detailed mathematical model of Myc regulation was developed that explains the rapid activation and maintenance of its level during T cell activation. The model showed that the positive feedback loop regulation of Myc via amino acid uptake is required to sustain its levels during T cell activation. Such a regulation helps to counteract an increase in Myc-dependent metabolic reprogramming and growth, which leads to amino acid utilization.

Overall, the thesis attempted to generate novel mechanistic insights into the cell cycle control system (G0-G1/S) in different cellular contexts and in normal and disease conditions using systems biology and bioinformatic approaches. These serve as a useful hypothesis for further experiments. A coherent picture of cell cycle control was developed by bringing together vast literature that may help in improving the understanding of proliferative diseases and development of drug treatment strategies.

BIBLIOGRAPHY

1. Cell Cycle - an overview | ScienceDirect Topics. <https://www.sciencedirect.com/topics/biochemistry-genetics-and-molecular-biology/cell-cycle>. Accessed 19 Feb 2022
2. Wang Z (2021) Regulation of Cell Cycle Progression by Growth Factor-Induced Cell Signaling. *Cells* 10:3327. <https://doi.org/10.3390/CELLS10123327>
3. Cell Cycle Checkpoint - an overview | ScienceDirect Topics. <https://www.sciencedirect.com/topics/biochemistry-genetics-and-molecular-biology/cell-cycle-checkpoint>. Accessed 19 Feb 2022
4. Cell Cycle and Cell Division | Learn Science at Scitable. <https://www.nature.com/scitable/topic/cell-cycle-and-cell-division-14122649/>. Accessed 19 Feb 2022
5. Brody LC Cell Cycle. <https://www.genome.gov/genetics-glossary/Cell-Cycle>. Accessed 19 Feb 2022
6. Cooper GM (2000) *The Eukaryotic Cell Cycle*, 2nd ed. Sinauer Associates (<https://www.ncbi.nlm.nih.gov/books/NBK9839/>)
7. Holley RW, Kiernan JA (1968) “Contact inhibition” of cell division in 3T3 cells. *Proc Natl Acad Sci* 60:300–304. <https://doi.org/10.1073/PNAS.60.1.300>
8. Bürk RR (1970) One-step growth cycle for BHK21/13 hamster fibroblasts. *Exp Cell Res* 63:309–316. [https://doi.org/10.1016/0014-4827\(70\)90218-1](https://doi.org/10.1016/0014-4827(70)90218-1)
9. Temin HM (1971) Stimulation by serum of multiplication of stationary chicken cells. *J Cell Physiol* 78:161–170. <https://doi.org/10.1002/JCP.1040780202>
10. Brooks RF (1975) The kinetics of serum-induced initiation of DNA synthesis in BHK 21/C13 cells, and the influence of exogenous adenosine. *J Cell Physiol* 86:369–377. <https://doi.org/10.1002/JCP.1040860409>
11. Brooks RF (1976) Regulation of the fibroblast cell cycle by serum. *Nature* 260:248–250. <https://doi.org/10.1038/260248a0>
12. Todaro GJ, Lazar GK, Green H (1965) The initiation of cell division in a contact-inhibited mammalian cell line. *J Cell Physiol* 66:325–333. <https://doi.org/10.1002/JCP.1030660310>
13. Planas-Silva MD, Weinberg RA (1997) The restriction point and control of cell proliferation. *Curr Opin Cell Biol* 9:768–772. [https://doi.org/10.1016/S0955-0674\(97\)80076-2](https://doi.org/10.1016/S0955-0674(97)80076-2)
14. Malumbres M, Barbacid M (2009) Cell cycle, CDKs and cancer: a changing paradigm. *Nat Rev Cancer* 9:153–166. <https://doi.org/10.1038/NRC2602>
15. Brooks RF, Richmond FN, Riddle PN, Richmond KMV (1984) Apparent heterogeneity in the response of quiescent swiss 3T3 cells to serum growth factors: implications for the transition probability model and parallels with “cellular senescence” and “competence.” *J Cell Physiol* 121:341–350. <https://doi.org/10.1002/JCP.1041210211>
16. Schafer KA (1998) The Cell Cycle: A Review. *Vet Pathol* 35:461–478. <https://doi.org/10.1177/030098589803500601>
17. Nakayama KI, Nakayama K (1998) Cip/Kip cyclin-dependent kinase inhibitors: Brakes of the cell cycle engine during development. *BioEssays* 20:1020–1029

18. García-Gutiérrez L, Delgado MD, León J (2019) Myc oncogene contributions to release of cell cycle brakes. *Genes (Basel)* 10:244. <https://doi.org/10.3390/genes10030244>
19. Bretones G, Delgado MD, León J (2015) Myc and cell cycle control. *Biochim Biophys Acta - Gene Regul Mech* 1849:506–516. <https://doi.org/10.1016/j.bbagr.2014.03.013>
20. Bertoli C, Skotheim JM, De Bruin RAM (2013) Control of cell cycle transcription during G1 and S phases. *Nat Rev Mol Cell Biol* 14:518–528. <https://doi.org/10.1038/NRM3629>
21. Xia P, Liu Y, Chen J, Cheng Z (2019) Focus: Death: Cell Cycle Proteins as Key Regulators of Postmitotic Cell Death. *Yale J Biol Med* 92:641
22. Wu L, Timmers C, Malti B, et al (2001) The E2F1-3 transcription factors are essential for cellular proliferation. *Nature* 414:457–462. <https://doi.org/10.1038/35106593>
23. Johnson DG, Schwarz JK, Cress WD, Nevins JR (1993) Expression of transcription factor E2F1 induces quiescent cells to enter S phase. *Nature* 365:349–352. <https://doi.org/10.1038/365349a0>
24. Sage J, Mulligan GJ, Attardi LD, et al (2000) Targeted disruption of the three Rb-related genes leads to loss of G1 control and immortalization. *Genes Dev* 14:3037–3050. <https://doi.org/10.1101/gad.843200>
25. Ding L, Cao J, Lin W, et al (2020) The roles of cyclin-dependent kinases in cell-cycle progression and therapeutic strategies in human breast cancer. *Int. J. Mol. Sci.* 21:1960
26. Obaya AJ, Sedivy JM (2002) Regulation of cyclin-Cdk activity in mammalian cells. *Cell. Mol. Life Sci.* 59:126–142
27. Fischer M (2017) Census and evaluation of p53 target genes. *Oncogene* 36:3943–3956. <https://doi.org/10.1038/onc.2016.502>
28. Chen J (2016) The Cell-Cycle Arrest and Apoptotic Functions of p53 in Tumor Initiation and Progression. *Cold Spring Harb Perspect Med* 6:a026104. <https://doi.org/10.1101/CSHPERSPECT.A026104>
29. Zwang Y, Sas-Chen A, Drier Y, et al (2011) Two Phases of Mitogenic Signaling Unveil Roles for p53 and EGR1 in Elimination of Inconsistent Growth Signals. *Mol Cell* 42:524–535. <https://doi.org/10.1016/j.molcel.2011.04.017>
30. Cobrinik D (2005) Pocket proteins and cell cycle control. *Oncogene* 24:2796–2809. <https://doi.org/10.1038/sj.onc.1208619>
31. Choi YJ, Anders L (2014) Signaling through cyclin D-dependent kinases. *Oncogene* 33:1890–1903. <https://doi.org/10.1038/onc.2013.137>
32. Engel BE, Cress WD, Santiago-Cardona PG (2014) The retinoblastoma protein: a master tumor suppressor acts as a link between cell cycle and cell adhesion. *Cell Health Cytoskeleton* 7:1–10. <https://doi.org/10.2147/CHC.S28079>
33. Li M, Zhang P (2009) The function of APC/CCdh1 in cell cycle and beyond. *Cell Div* 4:2. <https://doi.org/10.1186/1747-1028-4-2>
34. Penas C, Ramachandran V, Ayad NG (2012) The APC/C ubiquitin ligase: From cell biology to tumorigenesis. *Front. Oncol.* 1:60
35. Hayflick L, Moorhead PS (1961) The serial cultivation of human diploid cell strains. *Exp Cell Res* 25:585–621. [https://doi.org/10.1016/0014-4827\(61\)90192-6](https://doi.org/10.1016/0014-4827(61)90192-6)
36. Kumari R, Jat P (2021) Mechanisms of Cellular Senescence: Cell Cycle Arrest and Senescence Associated Secretory Phenotype. *Front. Cell Dev. Biol.* 9:485
37. Marescal O, Cheeseman IM (2020) Cellular Mechanisms and Regulation of Quiescence. *Dev Cell* 55:259–271. <https://doi.org/10.1016/J.DEVCEL.2020.09.029>
38. Stewart ZA, Westfall MD, Pietsenpol JA (2003) Cell-cycle dysregulation and

- anticancer therapy. *Trends Pharmacol Sci* 24:139–145. [https://doi.org/10.1016/S0165-6147\(03\)00026-9](https://doi.org/10.1016/S0165-6147(03)00026-9)
39. Matthews HK, Bertoli C, de Bruin RAM (2022) Cell cycle control in cancer. *Nat Rev Mol Cell Biol* 23:74–88. <https://doi.org/10.1038/s41580-021-00404-3>
 40. Zhivotovsky B, Orrenius S (2010) Cell cycle and cell death in disease: past, present and future. *J Intern Med* 268:395–409. <https://doi.org/10.1111/J.1365-2796.2010.02282.X>
 41. Joseph C, Mangani AS, Gupta V, et al (2020) Cell cycle deficits in neurodegenerative disorders: Uncovering molecular mechanisms to drive innovative therapeutic development. *Aging Dis* 11:946–966. <https://doi.org/10.14336/AD.2019.0923>
 42. Bonda DJ, Bajić VP, Spremo-Potparevic B, et al (2010) Review: Cell cycle aberrations and neurodegeneration. *Neuropathol Appl Neurobiol* 36:157. <https://doi.org/10.1111/J.1365-2990.2010.01064.X>
 43. He E (2012) Stochastic modelling of the cell cycle [PhD thesis]. Oxford University, UK
 44. Alves R, Antunes F, Salvador A (2006) Tools for kinetic modeling of biochemical networks. *Nat Biotechnol* 24:667–672. <https://doi.org/10.1038/nbt0606-667>
 45. Beard DA (2010) Simulation of cellular biochemical system kinetics. *Wiley Interdiscip Rev Syst Biol Med* 3:136–146. <https://doi.org/10.1002/WSBM.116>
 46. Tyson JJ, Csikasz-Nagy A, Novak B (2002) The dynamics of cell cycle regulation. *BioEssays* 24:1095–1109. <https://doi.org/10.1002/bies.10191>
 47. Tyson JJ, Chen K, Novak B (2001) Network dynamics and cell physiology. *Nat Rev Mol Cell Biol* 2:908–916. <https://doi.org/10.1038/35103078>
 48. Sible JC, Tyson JJ (2007) Mathematical modeling as a tool for investigating cell cycle control networks. *Methods* 41:238–247. <https://doi.org/10.1016/J.YMETH.2006.08.003>
 49. Robinson JC (2004) *An Introduction to Ordinary Differential Equations*. Cambridge University Press
 50. Wilkinson DJ (2009) Stochastic modelling for quantitative description of heterogeneous biological systems. *Nat Rev Genet* 10:122–133. <https://doi.org/10.1038/nrg2509>
 51. Resat H, Petzold L, Pettigrew MF (2009) Kinetic modeling of biological systems. *Methods Mol Biol* 541:311–335. https://doi.org/10.1007/978-1-59745-243-4_14
 52. Berline S, Bricker C (1969) The law of mass action. *J Chem Educ* 46:499–501. <https://doi.org/10.1021/ED046P499>
 53. Hill A V (1910) The possible effects of the aggregation of the molecules of haemoglobin on its dissociation curves. *J Physiol* 40:iv–vii
 54. Michaelis VL, Maud Menten ML, Goody RS, Johnson KA (1913) The Kinetics of Invertase Action. *Biochem Z* 49:333–369
 55. Goldbeter A, Koshland DE (1981) An amplified sensitivity arising from covalent modification in biological systems. *Proc Natl Acad Sci* 78:6840–6844. <https://doi.org/10.1073/pnas.78.11.6840>
 56. Motta S, Pappalardo F (2013) Mathematical modeling of biological systems. *Brief Bioinform* 14:411–422. <https://doi.org/10.1093/BIB/BBS061>
 57. Ratushny A V., Ramsey SA, Aitchison JD (2011) Mathematical Modeling of Biomolecular Network Dynamics. *Methods Mol Biol* 781:415. https://doi.org/10.1007/978-1-61779-276-2_21
 58. Ingalls BP (2013) *Mathematical Modelling in Systems Biology: An Introduction*. MIT

- press (<https://www.math.uwaterloo.ca/~bingalls/MMSB/Notes.pdf>)
59. King J, Eroumé KS, Truckenmüller R, et al (2021) Ten steps to investigate a cellular system with mathematical modeling. *PLOS Comput Biol* 17:e1008921. <https://doi.org/10.1371/JOURNAL.PCBI.1008921>
 60. Tyson JJ (2011) Cell Cycle Vignettes Analysis of Cell Cycle Dynamics by Bifurcation Theory (http://mpf.biol.vt.edu/tyson_department_page/lectures/Vignette_Cell_Cycle_Modeling/)
 61. Bifurcation Theory - an overview | ScienceDirect Topics. <https://www.sciencedirect.com/topics/computer-science/bifurcation-theory>. Accessed 21 Feb 2022
 62. Haragus M, Iooss G (2004) Bifurcation Theory. *Encycl Math Phys* 275–281. <https://doi.org/10.1016/B0-12-512666-2/00218-2>
 63. Faye G (2011) An introduction to bifurcation theory. NeuroMathComp Laboratory, INRIA, Sophia Antipolis, CNRS, ENS Paris, France (https://www.math.univ-toulouse.fr/~gfaye/ENS11/chap_bif.pdf)
 64. Chong KH, Samarasinghe S, Kulasiri D, Zheng J (2015) Computational techniques in mathematical modelling of biological switches. In: *Proceedings - 21st International Congress on Modelling and Simulation, MODSIM 2015*. pp 578–584
 65. Wu S, Chen D, Snyder MP (2022) Network biology bridges the gaps between quantitative genetics and multi-omics to map complex diseases. *Curr Opin Chem Biol* 66:102101. <https://doi.org/10.1016/J.CBPA.2021.102101>
 66. Soon WW, Hariharan M, Snyder MP (2013) High-throughput sequencing for biology and medicine. *Mol Syst Biol* 9:640. <https://doi.org/10.1038/MSB.2012.61>
 67. Pezoulas VC, Hazapis O, Lagopati N, et al (2021) Machine Learning Approaches on High Throughput NGS Data to Unveil Mechanisms of Function in Biology and Disease. *Cancer Genomics Proteomics* 18:605–626. <https://doi.org/10.21873/CGP.20284>
 68. High-throughput experimental methods in genomics. <http://compgenomr.github.io/book/high-throughput-experimental-methods-in-genomics.html#the-general-idea-behind-high-throughput-techniques>. Accessed 21 Feb 2022
 69. Lowe R, Shirley N, Bleackley M, et al (2017) Transcriptomics technologies. *PLOS Comput Biol* 13:e1005457. <https://doi.org/10.1371/JOURNAL.PCBI.1005457>
 70. Heller MJ (2002) DNA microarray technology: devices, systems, and applications. *Annu Rev Biomed Eng* 4:129–153. <https://doi.org/10.1146/ANNUREV.BIOENG.4.020702.153438>
 71. Shalon D, Smith SJ, Brown PO (1996) A DNA microarray system for analyzing complex DNA samples using two-color fluorescent probe hybridization. *Genome Res* 6:639–645. <https://doi.org/10.1101/GR.6.7.639>
 72. Lockhart DJ, Dong H, Byrne MC, et al (1996) Expression monitoring by hybridization to high-density oligonucleotide arrays. *Nat Biotechnol* 14:1675–1680. <https://doi.org/10.1038/nbt1296-1675>
 73. Auburn RP, Kreil DP, Meadows LA, et al (2005) Robotic spotting of cDNA and oligonucleotide microarrays. *Trends Biotechnol* 23:374–379. <https://doi.org/10.1016/J.TIBTECH.2005.04.002>
 74. Irizarry RA, Bolstad BM, Collin F, et al (2003) Summaries of Affymetrix GeneChip probe level data. *Nucleic Acids Res* 31:e15. <https://doi.org/10.1093/NAR/GNG015>
 75. RNA Sequencing VS Microarray - Otagenetics. <https://www.otogenetics.com/rna->

- sequencing-vs-microarray/. Accessed 21 Feb 2022
76. Wang Z, Gerstein M, Snyder M (2009) RNA-Seq: a revolutionary tool for transcriptomics. *Nat Rev Genet* 10:57–63. <https://doi.org/10.1038/NRG2484>
 77. Kukurba KR, Montgomery SB (2015) RNA sequencing and analysis. *Cold Spring Harb Protoc* 2015:951–969. <https://doi.org/10.1101/pdb.top084970>
 78. Metzker ML (2010) Sequencing technologies the next generation. *Nat. Rev. Genet.* 11:31–46
 79. Liu L, Li Y, Li S, et al (2012) Comparison of next-generation sequencing systems. *J. Biomed. Biotechnol.* 2012:11
 80. Carulli JP, Artinger M, Swain PM, et al (1998) High throughput analysis of differential gene expression. *J Cell Biochem* 72:286–296. [https://doi.org/10.1002/\(sici\)1097-4644\(1998\)72:30/31+<286::aid-jcb35>3.0.co;2-d](https://doi.org/10.1002/(sici)1097-4644(1998)72:30/31+<286::aid-jcb35>3.0.co;2-d)
 81. Love MI, Huber W, Anders S (2014) Moderated estimation of fold change and dispersion for RNA-seq data with DESeq2. *Genome Biol* 15:1–21. <https://doi.org/10.1186/s13059-014-0550-8>
 82. Robinson MD, McCarthy DJ, Smyth GK (2010) edgeR: a Bioconductor package for differential expression analysis of digital gene expression data. *Bioinformatics* 26:139–140. <https://doi.org/10.1093/BIOINFORMATICS/BTP616>
 83. van Dam S, Vösa U, van der Graaf A, et al (2018) Gene co-expression analysis for functional classification and gene-disease predictions. *Brief Bioinform* 19:575–592. <https://doi.org/10.1093/bib/bbw139>
 84. Mardinoglu A, Gatto F, Nielsen J (2013) Genome-scale modeling of human metabolism - a systems biology approach. *Biotechnol J* 8:985–996. <https://doi.org/10.1002/biot.201200275>
 85. Gatto F, Ferreira R, Nielsen J (2020) Pan-cancer analysis of the metabolic reaction network. *Metab Eng* 57:51–62. <https://doi.org/10.1016/j.ymben.2019.09.006>
 86. Yizhak K, Gaude E, Le Dévédec S, et al (2014) Phenotype-based cell-specific metabolic modeling reveals metabolic liabilities of cancer. *Elife* 3:1–23. <https://doi.org/10.7554/eLife.03641>
 87. Muzny DM, Bainbridge MN, Chang K, et al (2012) Comprehensive molecular characterization of human colon and rectal cancer. *Nature* 487:330–337. <https://doi.org/10.1038/nature11252>
 88. Moolamalla STR, Vinod PK (2020) Genome-scale metabolic modelling predicts biomarkers and therapeutic targets for neuropsychiatric disorders. *Comput Biol Med* 125:103994. <https://doi.org/10.1016/j.compbimed.2020.103994>
 89. Kanehisa M, Furumichi M, Tanabe M, et al (2017) KEGG: new perspectives on genomes, pathways, diseases and drugs. *Nucleic Acids Res* 45:D353. <https://doi.org/10.1093/NAR/GKW1092>
 90. Kanehisa M, Goto S (2000) KEGG: kyoto encyclopedia of genes and genomes. *Nucleic Acids Res* 28:27–30. <https://doi.org/10.1093/NAR/28.1.27>
 91. Mardinoglu A, Agren R, Kampf C, et al (2014) Genome-scale metabolic modelling of hepatocytes reveals serine deficiency in patients with non-alcoholic fatty liver disease. *Nat Commun* 5:1–11. <https://doi.org/10.1038/ncomms4083>
 92. Hakimi AA, Reznik E, Lee CH, et al (2016) An Integrated Metabolic Atlas of Clear Cell Renal Cell Carcinoma. *Cancer Cell* 29:104–116. <https://doi.org/10.1016/j.ccell.2015.12.004>
 93. Martín-Jiménez CA, Salazar-Barreto D, Barreto GE, González J (2017) Genome-scale reconstruction of the human astrocyte metabolic network. *Front Aging Neurosci* 9:23.

- <https://doi.org/10.3389/fnagi.2017.00023>
94. Wang Y, Eddy JA, Price ND (2012) Reconstruction of genome-scale metabolic models for 126 human tissues using mCADRE. *BMC Syst Biol* 6:1–16. <https://doi.org/10.1186/1752-0509-6-153>
 95. Duarte NC, Becker SA, Jamshidi N, et al (2007) Global reconstruction of the human metabolic network based on genomic and bibliomic data. *Proc Natl Acad Sci* 104:1777–1782. <https://doi.org/10.1073/PNAS.0610772104>
 96. Mo ML, Jamshidi N, Palsson B (2007) A genome-scale, constraint-based approach to systems biology of human metabolism. *Mol Biosyst* 3:598–603. <https://doi.org/10.1039/B705597H>
 97. Hao T, Ma HW, Zhao XM, Goryanin I (2010) Compartmentalization of the Edinburgh Human Metabolic Network. *BMC Bioinformatics* 11:. <https://doi.org/10.1186/1471-2105-11-393>
 98. Ma H, Sorokin A, Mazein A, et al (2007) The Edinburgh human metabolic network reconstruction and its functional analysis. *Mol Syst Biol* 3:135. <https://doi.org/10.1038/MSB4100177>
 99. Agren R, Bordel S, Mardinoglu A, et al (2012) Reconstruction of Genome-Scale Active Metabolic Networks for 69 Human Cell Types and 16 Cancer Types Using INIT. *PLoS Comput Biol* 8:e1002518. <https://doi.org/10.1371/journal.pcbi.1002518>
 100. Brunk E, Sahoo S, Zielinski DC, et al (2018) Recon3D: A Resource Enabling A Three-Dimensional View of Gene Variation in Human Metabolism. *Nat Biotechnol* 36:272. <https://doi.org/10.1038/NBT.4072>
 101. Nevins JR (2001) The Rb/E2F pathway and cancer. *Hum Mol Genet* 10:699–703. <https://doi.org/10.1093/hmg/10.7.699>
 102. Chen HZ, Tsai SY, Leone G (2009) Emerging roles of E2Fs in cancer: An exit from cell cycle control. *Nat Rev Cancer* 9:785–797. <https://doi.org/10.1038/nrc2696>
 103. Sharma S V., Lee DY, Li B, et al (2010) A Chromatin-Mediated Reversible Drug-Tolerant State in Cancer Cell Subpopulations. *Cell* 141:69–80. <https://doi.org/10.1016/J.CELL.2010.02.027>
 104. Jia M, Zheng D, Wang X, et al (2020) Cancer Cell enters reversible quiescence through Intracellular Acidification to resist Paclitaxel Cytotoxicity. *Int J Med Sci* 17:1652–1664. <https://doi.org/10.7150/IJMS.46034>
 105. Kadonosono T, Miyamoto K, Sakai S, et al (2022) AGE/RAGE axis regulates reversible transition to quiescent states of ALK-rearranged NSCLC and pancreatic cancer cells in monolayer cultures. *Sci Reports* 2022 12:1–13. <https://doi.org/10.1038/s41598-022-14272-0>
 106. Pardee AB (1974) A restriction point for control of normal animal cell proliferation. *Proc Natl Acad Sci* 71:1286–90. <https://doi.org/10.1073/pnas.71.4.1286>
 107. Zetterberg A, Larsson O, Wiman KG (1995) What is the restriction point? *Curr Opin Cell Biol* 7:835–842. [https://doi.org/10.1016/0955-0674\(95\)80067-0](https://doi.org/10.1016/0955-0674(95)80067-0)
 108. Harbour JW, Dean DC (2000) The Rb/E2F pathway: expanding roles and emerging paradigms. *Genes Dev* 14:2393–2409. <https://doi.org/10.1101/GAD.813200>
 109. Frolov M V., Dyson NJ (2004) Molecular mechanisms of E2F-dependent activation and pRB-mediated repression. *J Cell Sci* 117:2173–2181. <https://doi.org/10.1242/JCS.01227>
 110. Johnson A, Skotheim JM (2013) Start and the restriction point. *Curr Opin Cell Biol* 25:717–723. <https://doi.org/10.1016/J.CEB.2013.07.010>
 111. Burkhardt DL, Sage J (2008) Cellular mechanisms of tumour suppression by the

- retinoblastoma gene. *Nat Rev Cancer* 8:671–682. <https://doi.org/10.1038/nrc2399>
112. Massagué J (2004) G1 cell-cycle control and cancer. *Nature* 432:298–306. <https://doi.org/10.1038/nature03094>
 113. Yao G, Lee TJ, Mori S, et al (2008) A bistable Rb-E2F switch underlies the restriction point. *Nat Cell Biol* 10:476–482. <https://doi.org/10.1038/ncb1711>
 114. Harbour JW, Luo RX, Santi AD, et al (1999) Cdk Phosphorylation Triggers Sequential Intramolecular Interactions that Progressively Block Rb Functions as Cells Move through G1. *Cell* 98:859–869
 115. Narasimha AM, Kaulich M, Shapiro GS, et al (2014) Cyclin D activates the Rb tumor suppressor by mono-phosphorylation. *Elife* 3:1–21. <https://doi.org/10.7554/eLife.02872>
 116. Fisher RP (2016) Getting to S: CDK functions and targets on the path to cell-cycle commitment. *F1000Research* 5:2374. <https://doi.org/10.12688/f1000research.9463.1>
 117. Matson JP, Cook JG (2017) Cell cycle proliferation decisions: the impact of single cell analyses. *FEBS J* 284:362–375. <https://doi.org/10.1111/febs.13898>
 118. Ezhevsky SA, Nagahara H, Vocero-Akbani AM, et al (1997) Hypo-phosphorylation of the retinoblastoma protein (pRb) by cyclin D:Cdk4/6 complexes results in active pRb. *Proc Natl Acad Sci* 94:10699–10704. <https://doi.org/10.1073/pnas.94.20.10699>
 119. Merrick KA, Wohlbold L, Zhang C, et al (2011) Switching Cdk2 On or Off with Small Molecules to Reveal Requirements in Human Cell Proliferation. *Mol Cell* 42:624–636. <https://doi.org/10.1016/j.molcel.2011.03.031>
 120. Ekholm S V, Zickert P, Reed SI, Zetterberg A (2001) Accumulation of Cyclin E Is Not a Prerequisite for Passage through the Restriction Point. *21:3256–3265*. <https://doi.org/10.1128/MCB.21.9.3256–3265.2001>
 121. Martinsson HS, Starborg M, Erlandsson F, Zetterberg A (2005) Single cell analysis of G1 check points - The relationship between the restriction point and phosphorylation of pRb. *Exp Cell Res* 305:383–391. <https://doi.org/10.1016/j.yexcr.2005.01.023>
 122. Spencer SL, Cappell SD, Tsai FC, et al (2013) The proliferation-quiescence decision is controlled by a bifurcation in CDK2 activity at mitotic exit. *Cell* 155:369–383. <https://doi.org/10.1016/j.cell.2013.08.062>
 123. Barr AR, Cooper S, Heldt FS, et al (2017) DNA damage during S-phase mediates the proliferation-quiescence decision in the subsequent G1 via p21 expression. *Nat Commun* 8:14728. <https://doi.org/10.1038/ncomms14728>
 124. Arora M, Moser J, Phadke H, et al (2017) Endogenous Replication Stress in Mother Cells Leads to Quiescence of Daughter Cells. *Cell Rep* 19:1351–1364. <https://doi.org/10.1016/j.celrep.2017.04.055>
 125. Cappell SD, Chung M, Jaimovich A, et al (2016) Irreversible APCCdh1 Inactivation Underlies the Point of No Return for Cell-Cycle Entry. *Cell*. <https://doi.org/10.1016/j.cell.2016.05.077>
 126. Hsu JY, Reimann JDR, Sørensen CS, et al (2002) E2F-dependent accumulation of hEmi1 regulates S phase entry by inhibiting APC(Cdh1). *Nat Cell Biol* 4:358–366. <https://doi.org/10.1038/ncb785>
 127. Overton KW, Spencer SL, Noderer WL, et al (2014) Basal p21 controls population heterogeneity in cycling and quiescent cell cycle states. *Proc Natl Acad Sci*. <https://doi.org/10.1073/pnas.1409797111>
 128. Barr AR, Heldt FS, Zhang T, et al (2016) A Dynamical Framework for the All-or-None G1/S Transition. *Cell Syst*. <https://doi.org/10.1016/j.cels.2016.01.001>
 129. Bashir T, Dorello HV, Amador V, et al (2004) Control of the SCFSkp2-Cks1 ubiquitin

- ligase by the APC/C Cdh1 ubiquitin ligase. *Nature* 428:190–193. <https://doi.org/10.1038/nature02330>
130. Wei W, Ayad NG, Wan Y, et al (2004) Degradation of the SCF component Skp2 in cell-cycle phase G1 by the anaphase-promoting complex. *Nature* 428:194–198. <https://doi.org/10.1038/nature02381>
 131. Dong P, Maddali M V., Srimani JK, et al (2014) Division of labour between Myc and G1 cyclins in cell cycle commitment and pace control. *Nat Commun.* <https://doi.org/10.1038/ncomms5750>
 132. Yang HW, Chung M, Kudo T, Meyer T (2017) Competing memories of mitogen and p53 signalling control cell-cycle entry. *Nature* 549:404–408. <https://doi.org/10.1038/nature23880>
 133. Zerjatke T, Gak IA, Kirova D, et al (2017) Quantitative Cell Cycle Analysis Based on an Endogenous All-in-One Reporter for Cell Tracking and Classification. *Cell Rep* 19:1953–1966. <https://doi.org/10.1016/j.celrep.2017.05.022>
 134. Gookin S, Min M, Phadke H, et al (2017) A map of protein dynamics during cell-cycle progression and cell-cycle exit. *PLoS Biol* 15:1–25. <https://doi.org/10.1371/journal.pbio.2003268>
 135. Kwon JS, Everetts NJ, Wang X, et al (2017) Controlling Depth of Cellular Quiescence by an Rb-E2F Network Switch. *Cell Rep* 20:3223–3235. <https://doi.org/10.1016/j.celrep.2017.09.007>
 136. Lee T, Yao G, Nevins J, You L (2008) Sensing and integration of Erk and PI3K signals by Myc. *PLoS Comput Biol* 4:. <https://doi.org/10.1371/journal.pcbi.1000013>
 137. Eldridge AG, Loktev A V., Hansen D V., et al (2006) The Evi5 oncogene regulates cyclin accumulation by stabilizing the anaphase-promoting complex inhibitor Emil. *Cell* 124:367–380. <https://doi.org/10.1016/j.cell.2005.10.038>
 138. Ma HT, Tsang YH, Marxer M, Poon RYC (2009) Cyclin A2-cyclin-dependent kinase 2 cooperates with the PLK1-SCFbeta-TrCP1-EMI1-anaphase-promoting complex/cyclosome axis to promote genome reduplication in the absence of mitosis. *Mol Cell Biol* 29:6500–14. <https://doi.org/10.1128/MCB.00669-09>
 139. Moshe Y, Boulaire J, Pagano M, Hershko A (2004) Role of Polo-like kinase in the degradation of early mitotic inhibitor 1, a regulator of the anaphase promoting complex/cyclosome. *Proc Natl Acad Sci* 101:7937–42. <https://doi.org/10.1073/pnas.0402442101>
 140. Havens CG, Ho A, Yoshioka N, Dowdy SF (2006) Regulation of late G1/S phase transition and APC Cdh1 by reactive oxygen species. *Mol Cell Biol* 26:4701–4711. <https://doi.org/10.1128/MCB.00303-06>
 141. Abbas T, Sivaprasad U, Terai K, et al (2008) PCNA-dependent regulation of p21 ubiquitylation and degradation via the CRL4Cdt2 ubiquitin ligase complex. *Genes Dev* 22:2496–2506. <https://doi.org/10.1101/GAD.1676108>
 142. Lu Z, Hunter T (2010) Ubiquitylation and proteasomal degradation of the p21Cip1, p27Kip1 and p57Kip2 CDK inhibitors. <https://doi.org/104161/cc91211988> 9:2342–2352. <https://doi.org/10.4161/CC.9.12.11988>
 143. Havens CG, Walter JC (2011) Mechanism of CRL4Cdt2, a PCNA-dependent E3 ubiquitin ligase. *Genes Dev* 25:1568–1582. <https://doi.org/10.1101/GAD.2068611>
 144. Xu M, Sheppard KA, Peng CY, et al (1994) Cyclin A/CDK2 binds directly to E2F-1 and inhibits the DNA-binding activity of E2F-1/DP-1 by phosphorylation. *Mol Cell Biol* 14:8420–31. <https://doi.org/https://doi.org/10.1128/mcb.14.12.8420-8431.1994>
 145. Novák B, Tyson JJ (2004) A model for restriction point control of the mammalian cell

- cycle. *J Theor Biol* 230:563–579. <https://doi.org/10.1016/j.jtbi.2004.04.039>
146. Kalaszczynska I, Geng Y, Iino T, et al (2009) Cyclin A Is Redundant in Fibroblasts but Essential in Hematopoietic and Embryonic Stem Cells. *Cell* 138:352–365. <https://doi.org/10.1016/j.cell.2009.04.062>
 147. Hitomi M, Stacey DW (1999) Cellular ras and cyclin D1 are required during different cell cycle periods in cycling NIH 3T3 cells. *Mol Cell Biol* 19:4623–4632. <https://doi.org/10.1128/MCB.19.7.4623>
 148. Naetar N, Soundarapandian V, Litovchick L, et al (2014) PP2A-mediated regulation of ras signaling in G2 is essential for stable quiescence and normal G1 length. *Mol Cell* 54:932–945. <https://doi.org/10.1016/j.molcel.2014.04.023>
 149. Liu C, Konagaya Y, Chung M, et al (2020) Altered G1 signaling order and commitment point in cells proliferating without CDK4/6 activity. *Nat Commun* 11:1–13. <https://doi.org/10.1038/s41467-020-18966-9>
 150. Stacey DW (2003) Cyclin D1 serves as a cell cycle regulatory switch in actively proliferating cells. *Curr Opin Cell Biol* 15:158–163. [https://doi.org/10.1016/S0955-0674\(03\)00008-5](https://doi.org/10.1016/S0955-0674(03)00008-5)
 151. Yang K, Hitomi M, Stacey DW (2006) Variations in cyclin D1 levels through the cell cycle determine the proliferative fate of a cell. *Cell Div* 1:32. <https://doi.org/10.1186/1747-1028-1-32>
 152. Kozar K, Ciemerych MA, Rebel VI, et al (2004) Mouse Development and Cell Proliferation in the Absence of D-Cyclins. *Cell* 118:477–491. <https://doi.org/10.1016/J.CELL.2004.07.025>
 153. Sherr CJ, Roberts JM (2004) Living with or without cyclins and cyclin-dependent kinases. *Genes Dev* 18:2699–2711. <https://doi.org/10.1101/GAD.1256504>
 154. Dong P, Zhang C, Parker BT, et al (2018) Cyclin D/CDK4/6 activity controls G1 length in mammalian cells. *PLoS One* 13:e0185637. <https://doi.org/10.1371/JOURNAL.PONE.0185637>
 155. Miller JJ, Summers MK, Hansen D V., et al (2006) Emi1 stably binds and inhibits the anaphase-promoting complex/cyclosome as a pseudosubstrate inhibitor. *Genes Dev* 20:2410–2420. <https://doi.org/10.1101/gad.1454006>
 156. Tanenbaum ME, Stern-Ginossar N, Weissman JS, Vale RD (2015) Regulation of mRNA translation during mitosis. *Elife* 4:1–19. <https://doi.org/10.7554/eLife.07957>
 157. Cappell SD, Mark KG, Garbett D, et al (2018) EMI1 switches from being a substrate to an inhibitor of APC/CCDH1 to start the cell cycle. *Nature* 558:313–317. <https://doi.org/10.1038/s41586-018-0199-7>
 158. Gérard C, Goldbeter A (2009) Temporal self-organization of the cyclin/Cdk network driving the mammalian cell cycle. *Proc Natl Acad Sci* 106:21643–21648. <https://doi.org/10.1073/PNAS.0903827106>
 159. Heldt FS, Barr AR, Cooper S, et al (2018) A comprehensive model for the proliferation–quiescence decision in response to endogenous DNA damage in human cells. *Proc Natl Acad Sci* 115:2532–2537. <https://doi.org/10.1073/pnas.1715345115>
 160. Le Novère N, Bornstein B, Broicher A, et al (2006) BioModels Database: a free, centralized database of curated, published, quantitative kinetic models of biochemical and cellular systems. *Nucleic Acids Res* 34:D689–D691. <https://doi.org/10.1093/NAR/GKJ092>
 161. Malik-Sheriff RS, Glont M, Nguyen TVN, et al (2020) BioModels—15 years of sharing computational models in life science. *Nucleic Acids Res* 48:D407–D415. <https://doi.org/10.1093/NAR/GKZ1055>

162. Sung H, Ferlay J, Siegel RL, et al (2021) Global Cancer Statistics 2020: GLOBOCAN Estimates of Incidence and Mortality Worldwide for 36 Cancers in 185 Countries. *CA Cancer J Clin* 71:209–249. <https://doi.org/10.3322/CAAC.21660>
163. TCGA (2006) The Cancer Genome Atlas - Publications - National Cancer Institute. Natl Inst Heal
164. McLendon R, Friedman A, Bigner D, et al (2008) Comprehensive genomic characterization defines human glioblastoma genes and core pathways. *Nature* 455:1061–1068. <https://doi.org/10.1038/nature07385>
165. Bell D, Berchuck A, Birrer M, et al (2011) Integrated genomic analyses of ovarian carcinoma. *Nat* 2011 4747353 474:609–615. <https://doi.org/10.1038/nature10166>
166. Warburg O (1925) The metabolism of carcinoma cells. *J Cancer Res* 9:148–163. <https://doi.org/10.1158/jcr.1925.148>
167. Romero-Garcia S, Lopez-Gonzalez JS, Báez-Viveros JL, et al (2011) Tumor cell metabolism: An integral view. *Cancer Biol Ther* 12:939. <https://doi.org/10.4161/CBT.12.11.18140>
168. Zhu J, Thompson CB (2019) Metabolic regulation of cell growth and proliferation. *Nat Rev Mol Cell Biol* 20:436–450. <https://doi.org/10.1038/s41580-019-0123-5>
169. Gaude E, Frezza C (2016) Tissue-specific and convergent metabolic transformation of cancer correlates with metastatic potential and patient survival. *Nat Commun* 7:1–9. <https://doi.org/10.1038/ncomms13041>
170. Rosario SR, Long MD, Affronti HC, et al (2018) Pan-cancer analysis of transcriptional metabolic dysregulation using The Cancer Genome Atlas. *Nat Commun* 9:. <https://doi.org/10.1038/s41467-018-07232-8>
171. Peng X, Chen Z, Farshidfar F, et al (2018) Molecular Characterization and Clinical Relevance of Metabolic Expression Subtypes in Human Cancers. *Cell Rep* 23:255–269.e4. <https://doi.org/10.1016/j.celrep.2018.03.077>
172. Hoadley KA, Yau C, Hinoue T, et al (2018) Cell-of-Origin Patterns Dominate the Molecular Classification of 10,000 Tumors from 33 Types of Cancer. *Cell* 173:291–304.e6. <https://doi.org/10.1016/j.cell.2018.03.022>
173. Lindgren D, Eriksson P, Krawczyk K, et al (2017) Cell-Type-Specific Gene Programs of the Normal Human Nephron Define Kidney Cancer Subtypes. *Cell Rep* 20:1476–1489. <https://doi.org/10.1016/j.celrep.2017.07.043>
174. Chen F, Zhang Y, Şenbabaoğlu Y, et al (2016) Multilevel Genomics-Based Taxonomy of Renal Cell Carcinoma. *Cell Rep* 14:2476–2489. <https://doi.org/10.1016/j.celrep.2016.02.024>
175. Ricketts CJ, De Cubas AA, Fan H, et al (2018) The Cancer Genome Atlas Comprehensive Molecular Characterization of Renal Cell Carcinoma. *Cell Rep* 23:313–326.e5. <https://doi.org/10.1016/j.celrep.2018.03.075>
176. Gatto F, Nookaew I, Nielsen J (2014) Chromosome 3p loss of heterozygosity is associated with a unique metabolic network in clear cell renal carcinoma. *Proc Natl Acad Sci* 111:1–10. <https://doi.org/10.1073/pnas.1319196111>
177. Pornputtpong N, Nookaew I, Nielsen J (2015) Human metabolic atlas: An online resource for human metabolism. *Database* 2015:1–9. <https://doi.org/10.1093/database/bav068>
178. Patil KR, Nielsen J (2005) Uncovering transcriptional regulation of metabolism by using metabolic network topology. *Proc Natl Acad Sci* 102:2685–2689. <https://doi.org/10.1073/pnas.0406811102>
179. Meléndez-Rodríguez F, Urrutia AA, Lorendeau D, et al (2019) HIF1 α Suppresses

- Tumor Cell Proliferation through Inhibition of Aspartate Biosynthesis. *Cell Rep* 26:2257–2265.e4. <https://doi.org/10.1016/j.celrep.2019.01.106>
180. Benjamini Y, Hochberg Y (1995) Controlling the False Discovery Rate: A Practical and Powerful Approach to Multiple Testing. *J R Stat Soc Ser B* 57:289–300. <https://doi.org/10.1111/J.2517-6161.1995.TB02031.X>
 181. Kuleshov M V., Jones MR, Rouillard AD, et al (2016) Enrichr: a comprehensive gene set enrichment analysis web server 2016 update. *Nucleic Acids Res* 44:W90–W97. <https://doi.org/10.1093/nar/gkw377>
 182. Çakir T (2015) Reporter pathway analysis from transcriptome data: Metabolite-centric versus Reaction-centric approach. *Sci Rep* 5:1–10. <https://doi.org/10.1038/srep14563>
 183. Langfelder P, Horvath S (2008) WGCNA: An R package for weighted correlation network analysis. *BMC Bioinformatics* 9:. <https://doi.org/10.1186/1471-2105-9-559>
 184. Zhang B, Horvath S (2005) A general framework for weighted gene co-expression network analysis. *Stat Appl Genet Mol Biol* 4:. <https://doi.org/10.2202/1544-6115.1128>
 185. Langfelder P, Zhang B, Horvath S (2008) Defining clusters from a hierarchical cluster tree: The Dynamic Tree Cut package for R. *Bioinformatics* 24:719–720. <https://doi.org/10.1093/bioinformatics/btm563>
 186. Alter O, Brown PO, Botstein D (2000) Singular value decomposition for genome-wide expression data processing and modeling. *Proc Natl Acad Sci* 97:10101–10106. <https://doi.org/10.1073/PNAS.97.18.10101>
 187. Stalpers LJA, Kaplan EL (2018) Edward L. Kaplan and the Kaplan-Meier Survival Curve. *BSHM Bull* 33:109–135. <https://doi.org/10.1080/17498430.2018.1450055>
 188. Therneau TM, Grambsch PM (2000) Modeling Survival Data: Extending the Cox Model. <https://doi.org/10.1007/978-1-4757-3294-8>
 189. Yang M, Vousden KH (2016) Serine and one-carbon metabolism in cancer. *Nat Rev Cancer* 16:650–662. <https://doi.org/10.1038/nrc.2016.81>
 190. Monné M, Miniero DV, Bisaccia F, Fiermonte G (2013) The mitochondrial oxoglutarate carrier: from identification to mechanism. *J Bioenerg Biomembr* 45:1–13. <https://doi.org/10.1007/s10863-012-9475-7>
 191. Cairns RA, Harris IS, Mak TW (2011) Regulation of cancer cell metabolism. *Nat Rev Cancer* 11:85–95. <https://doi.org/10.1038/nrc2981>
 192. Rodriguez-Antona C, Ingelman-Sundberg M (2006) Cytochrome P450 pharmacogenetics and cancer. *Oncogene* 25:1679–1691. <https://doi.org/10.1038/sj.onc.1209377>
 193. Kent LN, Leone G (2019) The broken cycle: E2F dysfunction in cancer. *Nat Rev Cancer* 2019 19:326–338. <https://doi.org/10.1038/s41568-019-0143-7>
 194. Dominguez D, Tsai YH, Gomez N, et al (2016) A high-resolution transcriptome map of cell cycle reveals novel connections between periodic genes and cancer. *Cell Res* 26:946–962. <https://doi.org/10.1038/cr.2016.84>
 195. Locasale JW (2013) Serine, glycine and the one-carbon cycle: cancer metabolism is full circle. *Nat Rev Cancer* 13:572–583. <https://doi.org/10.1038/nrc3557>. Serine
 196. Ducker GS, Rabinowitz JD (2017) One-Carbon Metabolism in Health and Disease. *Cell Metab* 25:27–42. <https://doi.org/10.1016/j.cmet.2016.08.009>
 197. Thomas T, Thomas TJ (2001) Polyamines in cell growth and cell death: Molecular mechanisms and therapeutic applications. *Cell Mol Life Sci* 58:244–258. <https://doi.org/10.1007/PL00000852>
 198. Casero RA, Murray Stewart T, Pegg AE (2018) Polyamine metabolism and cancer:

- treatments, challenges and opportunities. *Nat Rev Cancer* 18:681–695. <https://doi.org/10.1038/s41568-018-0050-3>
199. Priolo C, Khabibullin D, Reznik E, et al (2018) Impairment of gamma-glutamyl transferase 1 activity in the metabolic pathogenesis of chromophobe renal cell carcinoma. *Proc Natl Acad Sci* 115:E6274–E6282. <https://doi.org/10.1073/pnas.1710849115>
 200. Lim JKM, Delaidelli A, Minaker SW, et al (2019) Cystine/glutamate antiporter xCT (SLC7A11) facilitates oncogenic RAS transformation by preserving intracellular redox balance. *Proc Natl Acad Sci* 116:9433–9442. <https://doi.org/10.1073/pnas.1821323116>
 201. Platten M, Wick W, Van Den Eynde BJ (2012) Tryptophan catabolism in cancer: Beyond IDO and tryptophan depletion. *Cancer Res* 72:5435–5440. <https://doi.org/10.1158/0008-5472.CAN-12-0569>
 202. Coloff JL, Murphy JP, Braun CR, et al (2016) Differential Glutamate Metabolism in Proliferating and Quiescent Mammary Epithelial Cells. *Cell Metab* 23:867–880. <https://doi.org/10.1016/j.cmet.2016.03.016>
 203. Son J, Lyssiotis CA, Ying H, et al (2013) Glutamine supports pancreatic cancer growth through a KRAS-regulated metabolic pathway. *Nature* 496:101–105. <https://doi.org/10.1038/nature12040>
 204. Silberman A, Goldman O, Assayag OB, et al (2019) Acid-induced downregulation of ASS1 contributes to the maintenance of intracellular pH in cancer. *Cancer Res* 79:518–533. <https://doi.org/10.1158/0008-5472.CAN-18-1062>
 205. Tao X, Zuo Q, Ruan H, et al (2019) Argininosuccinate synthase 1 suppresses cancer cell invasion by inhibiting STAT3 pathway in hepatocellular carcinoma. *Acta Biochim Biophys Sin (Shanghai)* 51:263–276. <https://doi.org/10.1093/abbs/gmz005>
 206. Hoerner CR, Chen VJ, Fan AC (2019) The ‘Achilles Heel’ of Metabolism in Renal Cell Carcinoma: Glutaminase Inhibition as a Rational Treatment Strategy. *Kidney Cancer* 3:15–29. <https://doi.org/10.3233/kca-180043>
 207. Arceci A, Bonacci T, Wang X, et al (2019) FOXM1 Deubiquitination by USP21 Regulates Cell Cycle Progression and Paclitaxel Sensitivity in Basal-like Breast Cancer. *Cell Rep* 26:3076-3086.e6. <https://doi.org/10.1016/j.celrep.2019.02.054>
 208. Zhang J, Fan J, Venneti S, et al (2014) Asparagine plays a critical role in regulating cellular adaptation to glutamine depletion. *Mol Cell* 56:205–218. <https://doi.org/10.1016/j.molcel.2014.08.018>
 209. Buckley D, Duke G, Heuer TS, et al (2017) Fatty acid synthase – Modern tumor cell biology insights into a classical oncology target. *Pharmacol Ther* 177:23–31. <https://doi.org/10.1016/j.pharmthera.2017.02.021>
 210. Ding X, Zhang W, Li S, Yang H (2019) The role of cholesterol metabolism in cancer. *Am J Cancer Res* 9:219–227
 211. Munir R, Lisec J, Swinnen J V., Zaidi N (2019) Lipid metabolism in cancer cells under metabolic stress. *Br J Cancer* 120:1090–1098. <https://doi.org/10.1038/s41416-019-0451-4>
 212. Chaux A, Albadine R, Schultz L, et al (2013) Dysregulation of the mammalian target of rapamycin pathway in chromophobe renal cell carcinomas. *Hum Pathol* 44:2323–2330. <https://doi.org/10.1016/j.humpath.2013.05.014>
 213. Ye J, Fan J, Venneti S, et al (2014) Serine catabolism regulates mitochondrial redox control during hypoxia. *Cancer Discov* 4:1406–1417. <https://doi.org/10.1158/2159-8290.CD-14-0250>
 214. Ye F, Jia D, Lu M, et al (2018) Modularity of the metabolic gene network as a

- prognostic biomarker for hepatocellular carcinoma. *Oncotarget* 9:15015–15026. <https://doi.org/10.18632/oncotarget.24551>
215. Bartesaghi S, Graziano V, Galavotti S, et al (2015) Inhibition of oxidative metabolism leads to p53 genetic inactivation and transformation in neural stem cells. *Proc Natl Acad Sci* 112:E1401. <https://doi.org/10.1073/pnas.1503132112>
 216. Yu L, Lu M, Jia D, et al (2017) Modeling the genetic regulation of cancer metabolism: Interplay between glycolysis and oxidative phosphorylation. *Cancer Res* 77:1564–1574. <https://doi.org/10.1158/0008-5472.CAN-16-2074>
 217. Zhang Y, Narayanan SP, Mannan R, et al (2021) Single-cell analyses of renal cell cancers reveal insights into tumor microenvironment, cell of origin, and therapy response. *Proc Natl Acad Sci* 118:e2103240118. <https://doi.org/10.1073/pnas.2103240118>
 218. Su C, Lv Y, Lu W, et al (2021) Single-Cell RNA Sequencing in Multiple Pathologic Types of Renal Cell Carcinoma Revealed Novel Potential Tumor-Specific Markers. *Front Oncol* 11:4211. <https://doi.org/10.3389/fonc.2021.719564>
 219. Dementia. <https://www.who.int/news-room/fact-sheets/detail/dementia>. Accessed 4 Nov 2021
 220. Bali J, Gheinani AH, Zurbriggen S, Rajendran L (2012) Role of genes linked to sporadic Alzheimer’s disease risk in the production of β -amyloid peptides. *Proc Natl Acad Sci* 109:15307–15311. <https://doi.org/10.1073/PNAS.1201632109>
 221. Piaceri I, Nacmias B, Sorbi S (2013) Genetics of familial and sporadic Alzheimer’s disease. *Front Biosci - Elit* 5 E:167–177. <https://doi.org/10.2741/e605>
 222. Dorszewska J, Prendecki M, Oczkowska A, et al (2016) Molecular Basis of Familial and Sporadic Alzheimer’s Disease. *Curr Alzheimer Res* 13:952–963. <https://doi.org/10.2174/1567205013666160314150501>
 223. Association A (2019) 2019 Alzheimer’s disease facts and figures. *Alzheimer’s Dement* 15:321–387. <https://doi.org/10.1016/j.jalz.2019.01.010>
 224. Liu PP, Xie Y, Meng XY, Kang JS (2019) History and progress of hypotheses and clinical trials for alzheimer’s disease. *Signal Transduct Target Ther* 4:1–22. <https://doi.org/10.1038/s41392-019-0063-8>
 225. Breijyeh Z, Karaman R (2020) Comprehensive Review on Alzheimer’s Disease: Causes and Treatment. *Molecules* 25:5789. <https://doi.org/10.3390/MOLECULES25245789>
 226. Davies P, Maloney AJF (1976) SELECTIVE LOSS OF CENTRAL CHOLINERGIC NEURONS IN ALZHEIMER’S DISEASE. *Lancet* 308:1403. [https://doi.org/10.1016/S0140-6736\(76\)91936-X](https://doi.org/10.1016/S0140-6736(76)91936-X)
 227. Siegfried K (1993) The cholinergic hypothesis of Alzheimer’s disease. *Eur Neuropsychopharmacol* 3:170–171. [https://doi.org/10.1016/0924-977X\(93\)90007-9](https://doi.org/10.1016/0924-977X(93)90007-9)
 228. Sharma K (2019) Cholinesterase inhibitors as Alzheimer’s therapeutics (Review). *Mol Med Rep* 20:1479–1487. <https://doi.org/10.3892/MMR.2019.10374>
 229. Haake A, Nguyen K, Friedman L, et al (2020) An update on the utility and safety of cholinesterase inhibitors for the treatment of Alzheimer’s disease. *Expert Opin Drug Saf* 19:147–157. <https://doi.org/10.1080/14740338.2020.1721456>
 230. Hardy J, Higgins G (1992) Alzheimer’s disease: the amyloid cascade hypothesis. *Science* 256:184–185. <https://doi.org/10.1126/SCIENCE.1566067>
 231. Reitz C (2012) Alzheimer’s disease and the amyloid cascade hypothesis: A critical review. *Int J Alzheimers Dis* 2012:. <https://doi.org/10.1155/2012/369808>
 232. Lambert MP, Barlow AK, Chromy BA, et al (1998) Diffusible, nonfibrillar ligands

- derived from A β 1-42 are potent central nervous system neurotoxins. *Proc Natl Acad Sci* 95:6448–6453. <https://doi.org/10.1073/pnas.95.11.6448>
233. Ferreira ST, Lourenco M V., Oliveira MM, De Felice FG (2015) Soluble amyloid- β oligomers as synaptotoxins leading to cognitive impairment in Alzheimer's disease. *Front Cell Neurosci* 9:191. <https://doi.org/10.3389/fncel.2015.00191>
 234. Kent SA, Spires-Jones TL, Durrant CS (2020) The physiological roles of tau and A β : implications for Alzheimer's disease pathology and therapeutics. *Acta Neuropathol* 140:417–447. <https://doi.org/10.1007/s00401-020-02196-w>
 235. Rapoport M, Dawson HN, Binder LI, et al (2002) Tau is essential to β -amyloid-induced neurotoxicity. *Proc Natl Acad Sci* 99:6364–6369. <https://doi.org/10.1073/PNAS.092136199>
 236. Sengupta U, Nilson AN, Kaye R (2016) The Role of Amyloid- β Oligomers in Toxicity, Propagation, and Immunotherapy. *EBioMedicine* 6:42–49. <https://doi.org/10.1016/J.EBIOM.2016.03.035>
 237. Ricciarelli R, Fedele E (2017) The Amyloid Cascade Hypothesis in Alzheimer's Disease: It's Time to Change Our Mind. *Curr Neuropharmacol* 15:. <https://doi.org/10.2174/1570159X15666170116143743>
 238. García-Ayllón M-S, Small DH, Avila J, Saez-Valero J (2011) Revisiting the Role of Acetylcholinesterase in Alzheimer's Disease: Cross-Talk with P-tau and β -Amyloid. *Front Mol Neurosci* 0:22. <https://doi.org/10.3389/FNMOL.2011.00022>
 239. Doig AJ (2018) Positive Feedback Loops in Alzheimer's Disease: The Alzheimer's Feedback Hypothesis. *J Alzheimer's Dis* 66:25–36. <https://doi.org/10.3233/JAD-180583>
 240. Rao C V., Asch AS, Carr DJJ, Yamada HY (2020) “Amyloid-beta accumulation cycle” as a prevention and/or therapy target for Alzheimer's disease. *Aging Cell* 19:e13109. <https://doi.org/10.1111/ACEL.13109>
 241. Vincent I, Jicha G, Rosado M, Dickson DW (1997) Aberrant Expression of Mitotic Cdc2/Cyclin B1 Kinase in Degenerating Neurons of Alzheimer's Disease Brain. *J Neurosci* 17:3588–3598. <https://doi.org/10.1523/JNEUROSCI.17-10-03588.1997>
 242. Smith MZ, Nagy Z, Esiri MM (1999) Cell cycle-related protein expression in vascular dementia and Alzheimer's disease. *Neurosci Lett* 271:45–48. [https://doi.org/10.1016/S0304-3940\(99\)00509-1](https://doi.org/10.1016/S0304-3940(99)00509-1)
 243. Absalon S, Kochanek DM, Raghavan V, Krichevsky AM (2013) MiR-26b, Upregulated in Alzheimer's Disease, Activates Cell Cycle Entry, Tau-Phosphorylation, and Apoptosis in Postmitotic Neurons. *J Neurosci* 33:14645–14659. <https://doi.org/10.1523/JNEUROSCI.1327-13.2013>
 244. Nagy Z, Esiri MM, Cato A-M, Smith AD (1997) Cell cycle markers in the hippocampus in Alzheimer's disease. *Acta Neuropathol* 1997 941 94:6–15. <https://doi.org/10.1007/S004010050665>
 245. van Leeuwen LAG, Hoozemans JJM (2015) Physiological and pathophysiological functions of cell cycle proteins in post-mitotic neurons: implications for Alzheimer's disease. *Acta Neuropathol* 129:511–525. <https://doi.org/10.1007/s00401-015-1382-7>
 246. Huang F, Wang M, Liu R, et al (2019) CDT2-controlled cell cycle reentry regulates the pathogenesis of Alzheimer's disease. *Alzheimer's Dement* 15:217–231. <https://doi.org/10.1016/J.JALZ.2018.08.013>
 247. Marlier Q, D'aes T, Verteneuil S, et al (2020) Core cell cycle machinery is crucially involved in both life and death of post-mitotic neurons. *Cell Mol Life Sci* 77:4553–4571. <https://doi.org/10.1007/s00018-020-03548-1>

248. Yang Y, Mufson EJ, Herrup K (2003) Neuronal Cell Death Is Preceded by Cell Cycle Events at All Stages of Alzheimer's Disease. *J Neurosci* 23:2557–2563. <https://doi.org/10.1523/JNEUROSCI.23-07-02557.2003>
249. Yang Y, Varvel NH, Lamb BT, Herrup K (2006) Ectopic Cell Cycle Events Link Human Alzheimer's Disease and Amyloid Precursor Protein Transgenic Mouse Models. *J Neurosci* 26:775–784. <https://doi.org/10.1523/JNEUROSCI.3707-05.2006>
250. Park KHJ, Hallows JL, Chakrabarty P, et al (2007) Neurobiology of Disease Conditional Neuronal Simian Virus 40 T Antigen Expression Induces Alzheimer-Like Tau and Amyloid Pathology in Mice. <https://doi.org/10.1523/JNEUROSCI.0186-07.2007>
251. Barrett T, Stangis KA, Saito T, et al (2021) Neuronal Cell Cycle Re-Entry Enhances Neuropathological Features in App NLF Knock-In Mice. *J Alzheimer's Dis* 82:1683–1702. <https://doi.org/10.3233/JAD-210091>
252. Giovanni A, Wirtz-Brugger F, Keramaris E, et al (1999) Involvement of Cell Cycle Elements, Cyclin-dependent Kinases, pRb, and E2F·DP, in B-amyloid-induced Neuronal Death *. *J Biol Chem* 274:19011–19016. <https://doi.org/10.1074/JBC.274.27.19011>
253. McShea A, Lee H gon, Petersen RB, et al (2007) Neuronal cell cycle re-entry mediates Alzheimer disease-type changes. *Biochim Biophys Acta - Mol Basis Dis* 1772:467–472. <https://doi.org/10.1016/J.BBADIS.2006.09.010>
254. Veas-Pérez De Tudela M, Maestre C, Delgado-Esteban M, et al (2015) Cdk5-mediated inhibition of APC/C-Cdh1 switches on the cyclin D1-Cdk4-pRb pathway causing aberrant S-phase entry of postmitotic neurons. *Sci Rep* 5:1–9. <https://doi.org/10.1038/srep18180>
255. Baumann K, Mandelkow EM, Biernat J, et al (1993) Abnormal Alzheimer-like phosphorylation of tau-protein by cyclin-dependent kinases cdk2 and cdk5. *FEBS Lett* 336:417–424. [https://doi.org/10.1016/0014-5793\(93\)80849-P](https://doi.org/10.1016/0014-5793(93)80849-P)
256. Kametani F, Hasegawa M (2018) Reconsideration of amyloid hypothesis and tau hypothesis in Alzheimer's disease. *Front Neurosci* 12:25. <https://doi.org/10.3389/fnins.2018.00025>
257. Pei JJ, Braak H, Gong CX, et al (2002) Up-regulation of cell division cycle (cdc) 2 kinase in neurons with early stage Alzheimer's disease neurofibrillary degeneration. *Acta Neuropathol* 104:369–376. <https://doi.org/10.1007/s00401-002-0565-1>
258. Lee HG, Casadesus G, Zhu X, et al (2009) Cell cycle re-entry mediated neurodegeneration and its treatment role in the pathogenesis of Alzheimer's disease. *Neurochem Int* 54:84–88. <https://doi.org/10.1016/J.NEUINT.2008.10.013>
259. Allnut AB, Waters AK, Kesari S, Yenugonda VM (2020) Physiological and Pathological Roles of Cdk5: Potential Directions for Therapeutic Targeting in Neurodegenerative Disease. *ACS Chem Neurosci* 11:1218–1230. <https://doi.org/10.1021/ACSCHEMNEURO.0C00096>
260. Harney D, Smith A, Simanski S, et al (2009) The Anaphase Promoting Complex Induces Substrate Degradation during Neuronal Differentiation. *J Biol Chem* 284:4317–4323. <https://doi.org/10.1074/JBC.M804944200>
261. Delgado-Esteban M, García-Higuera I, Maestre C, et al (2013) APC/C-Cdh1 coordinates neurogenesis and cortical size during development. *Nat Commun* 4:1–12. <https://doi.org/10.1038/ncomms3879>
262. Frade JM, Ovejero-Benito MC (2015) Neuronal cell cycle: The neuron itself and its circumstances. *Cell Cycle* 14:712–720.

- <https://doi.org/10.1080/15384101.2015.1004937>
263. Yan G, Ziff E (1995) NGF regulates the PC12 cell cycle machinery through specific inhibition of the Cdk kinases and induction of cyclin D1. *J Neurosci* 15:6200–6212. <https://doi.org/10.1523/JNEUROSCI.15-09-06200.1995>
 264. Odajima J, Wills ZP, Ndassa YM, et al (2011) Cyclin E Constrains Cdk5 Activity to Regulate Synaptic Plasticity and Memory Formation. *Dev Cell* 21:655–668. <https://doi.org/10.1016/J.DEVCEL.2011.08.009>
 265. Cicero S, Herrup K (2005) Cyclin-Dependent Kinase 5 Is Essential for Neuronal Cell Cycle Arrest and Differentiation. *J Neurosci* 25:9658–9668. <https://doi.org/10.1523/JNEUROSCI.1773-05.2005>
 266. Shah K, Lahiri DK (2014) Cdk5 activity in the brain – multiple paths of regulation. *J Cell Sci* 127:2391–2400. <https://doi.org/10.1242/JCS.147553>
 267. Akashiba H, Matsuki N, Nishiyama N (2006) p27 small interfering RNA induces cell death through elevating cell cycle activity in cultured cortical neurons: A proof-of-concept study. *Cell Mol Life Sci* 63:2397–2404. <https://doi.org/10.1007/s00018-006-6194-4>
 268. Ogawa O, Lee H, Zhu X, et al (2003) Increased p27, an essential component of cell cycle control, in Alzheimer’s disease. *Aging Cell* 2:105–110. <https://doi.org/10.1046/J.1474-9728.2003.00042.X>
 269. Chambard JC, Lefloch R, Pouyssegur J, Lenormand P (2007) ERK implication in cell cycle regulation. *Biochim Biophys Acta - Mol Cell Res* 1773:1299–1310. <https://doi.org/10.1016/J.BBAMCR.2006.11.010>
 270. Chen JY, Lin JR, Cimprich KA, Meyer T (2012) A Two-Dimensional ERK-AKT Signaling Code for an NGF-Triggered Cell-Fate Decision. *Mol Cell* 45:196–209. <https://doi.org/10.1016/j.molcel.2011.11.023>
 271. Ryu H, Chung M, Dobrzyński M, et al (2016) Frequency modulation of ERK activation dynamics rewires cell fate. *Mol Syst Biol* 12:866. <https://doi.org/10.15252/MSB.20166982>
 272. Sharma P, Veeranna V, Sharma M, et al (2002) Phosphorylation of MEK1 by cdk5/p35 down-regulates the mitogen-activated protein kinase pathway. *J Biol Chem* 277:528–534. <https://doi.org/10.1074/jbc.M109324200>
 273. Modi PK, Komaravelli N, Singh N, Sharma P (2012) Interplay between MEK-ERK signaling, cyclin D1, and cyclin-dependent kinase 5 regulates cell cycle reentry and apoptosis of neurons. *Mol Biol Cell* 23:3722–3730. <https://doi.org/10.1091/mbc.E12-02-0125>
 274. Modi PK, Jaiswal S, Sharma P (2015) Regulation of Neuronal Cell Cycle and Apoptosis by MicroRNA 34a. *Mol Cell Biol MCB*.00589-15. <https://doi.org/10.1128/MCB.00589-15>
 275. Zhang J, Li H, Herrup K (2010) Cdk5 Nuclear Localization Is p27-dependent in Nerve Cells: implications for cell cycle suppression and caspase-3 activation. *J Biol Chem* 285:14052–14061. <https://doi.org/10.1074/JBC.M109.068262>
 276. Sumrejkanchanakij P, Tamamori-Adachi M, Matsunaga Y, et al (2003) Role of cyclin D1 cytoplasmic sequestration in the survival of postmitotic neurons. *Oncogene* 22:8723–8730. <https://doi.org/10.1038/sj.onc.1206870>
 277. Jaiswal S, Sharma P (2017) Role and regulation of p27 in neuronal apoptosis. *J Neurochem* 140:576–588. <https://doi.org/10.1111/jnc.13918>
 278. Harper JW, Burton JL, Solomon MJ (2002) The anaphase-promoting complex: it’s not just for mitosis any more. *Genes Dev* 16:2179–2206.

- <https://doi.org/10.1101/GAD.1013102>
279. Lee MS, Kwon YT, Li M, et al (2000) Neurotoxicity induces cleavage of p35 to p25 by calpain. *Nature* 405:360–364. <https://doi.org/10.1038/35012636>
 280. Mucke L, Selkoe DJ (2012) Neurotoxicity of amyloid β -protein: Synaptic and network dysfunction. *Cold Spring Harb Perspect Med* 2:a006338. <https://doi.org/10.1101/cshperspect.a006338>
 281. Patrick GN, Zukerberg L, Nikolic M, et al (1999) Conversion of p35 to p25 deregulates Cdk5 activity and promotes neurodegeneration. *Nature* 402:615–622. <https://doi.org/10.1038/45159>
 282. Futatsugi A, Utreras E, Rudrabhatla P, et al (2012) Cyclin-dependent kinase 5 regulates E2F transcription factor through phosphorylation of Rb protein in neurons. *Cell Cycle* 11:1603–1610. <https://doi.org/10.4161/cc.20009>
 283. Fuchsberger T, Martínez-Bellver S, Giraldo E, et al (2016) A β Induces Excitotoxicity Mediated by APC/C-Cdh1 Depletion That Can Be Prevented by Glutaminase Inhibition Promoting Neuronal Survival. *Sci Rep* 6:1–16. <https://doi.org/10.1038/srep31158>
 284. Herrero-Mendez A, Almeida A, Fernández E, et al (2009) The bioenergetic and antioxidant status of neurons is controlled by continuous degradation of a key glycolytic enzyme by APC/C–Cdh1. *Nat Cell Biol* 2009 116 11:747–752. <https://doi.org/10.1038/ncb1881>
 285. Copley JN, Fiorello ML, Bailey DM (2018) 13 reasons why the brain is susceptible to oxidative stress. *Redox Biol* 15:490–503. <https://doi.org/10.1016/J.REDOX.2018.01.008>
 286. Fischer M, Grossmann P, Padi M, DeCaprio JA (2016) Integration of TP53, DREAM, MMB-FOXM1 and RB-E2F target gene analyses identifies cell cycle gene regulatory networks. *Nucleic Acids Res* 44:6070–6086. <https://doi.org/10.1093/NAR/GKW523>
 287. Liao G Bin, Li XZ, Zeng S, et al (2018) Regulation of the master regulator FOXM1 in cancer. *Cell Commun Signal* 16:1–15. <https://doi.org/10.1186/s12964-018-0266-6>
 288. Veas-Pérez De Tudela M, Delgado-Esteban M, Maestre C, et al (2015) Regulation of Bcl-xL–ATP synthase interaction by mitochondrial cyclin B1–cyclin-dependent kinase-1 determines neuronal survival. *J Neurosci* 35:9287–9301. <https://doi.org/10.1523/JNEUROSCI.4712-14.2015>
 289. Redza-Dutordoir M, Averill-Bates DA (2016) Activation of apoptosis signalling pathways by reactive oxygen species. *Biochim Biophys Acta - Mol Cell Res* 1863:2977–2992. <https://doi.org/10.1016/J.BBAMCR.2016.09.012>
 290. De Caluwé J, Dupont G (2013) The progression towards Alzheimer’s disease described as a bistable switch arising from the positive loop between amyloids and Ca²⁺. *J Theor Biol* 331:12–18. <https://doi.org/10.1016/j.jtbi.2013.04.015>
 291. Müller M, Ahumada-Castro U, Sanhueza M, et al (2018) Mitochondria and Calcium Regulation as Basis of Neurodegeneration Associated With Aging. *Front Neurosci* 0:470. <https://doi.org/10.3389/FNINS.2018.00470>
 292. Folch J, Junyent F, Verdaguer E, et al (2012) Role of cell cycle re-entry in neurons: A common apoptotic mechanism of neuronal cell death. *Neurotox Res* 22:195–207. <https://doi.org/10.1007/s12640-011-9277-4>
 293. Mungenast AE, Tsai L-H (2011) Addressing the complex etiology of Alzheimer’s disease: the role of p25/Cdk5. <http://dx.doi.org/102217/fnl1122> 6:481–496. <https://doi.org/10.2217/FNL.11.22>
 294. Stevens C, Smith L, La Thangue NB (2003) Chk2 activates E2F-1 in response to DNA

- damage. *Nat Cell Biol* 5:401–409. <https://doi.org/10.1038/ncb974>
295. Stevens C, La Thangue NB (2004) The emerging role of E2F-1 in the DNA damage response and checkpoint control. *DNA Repair (Amst)* 3:1071–1079. <https://doi.org/10.1016/j.dnarep.2004.03.034>
 296. Schwartz EI, Smilenov LB, Price MA, et al (2007) Cell cycle activation in postmitotic neurons is essential for DNA repair. *Cell Cycle* 6:318–329. <https://doi.org/10.4161/cc.6.3.3752>
 297. Castillo DS, Campalans A, Belluscio LM, et al (2015) E2F1 and E2F2 induction in response to DNA damage preserves genomic stability in neuronal cells. *Cell Cycle* 14:1300–1314. <https://doi.org/10.4161/15384101.2014.985031>
 298. Tian B, Yang Q, Mao Z (2009) Phosphorylation of ATM by Cdk5 mediates DNA damage signalling and regulates neuronal death. *Nat Cell Biol* 11:211–218. <https://doi.org/10.1038/ncb1829>
 299. Patil M, Pabla N, Dong Z (2013) Checkpoint kinase 1 in DNA damage response and cell cycle regulation. *Cell Mol Life Sci* 70:4009–4021. <https://doi.org/10.1007/s00018-013-1307-3>
 300. Fridman JS, Lowe SW (2003) Control of apoptosis by p53. *Oncogene* 22:9030–9040. <https://doi.org/10.1038/sj.onc.1207116>
 301. Zhang T, Brazhnik P, Tyson JJ (2009) Computational analysis of dynamical responses to the intrinsic pathway of programmed cell death. *Biophys J* 97:415–434. <https://doi.org/10.1016/j.bpj.2009.04.053>
 302. Zhang XP, Liu F, Wang W (2010) Coordination between cell cycle progression and cell fate decision by the p53 and E2F1 pathways in response to DNA damage. *J Biol Chem* 285:31571–31580. <https://doi.org/10.1074/jbc.M110.134650>
 303. Zhang Y, Song X, Herrup K (2020) Context-Dependent Functions of E2F1: Cell Cycle, Cell Death, and DNA Damage Repair in Cortical Neurons. *Mol Neurobiol* 57:2377–2390. <https://doi.org/10.1007/s12035-020-01887-5>
 304. Croxton R, Ma Y, Song L, et al (2002) Direct repression of the Mcl-1 promoter by E2F1. *Oncogene* 21:1359–1369. <https://doi.org/10.1038/sj.onc.1205157>
 305. Huang CYF, Ferrell JE (1996) Ultrasensitivity in the mitogen-activated protein kinase cascade. *Proc Natl Acad Sci* 93:10078–10083. <https://doi.org/10.1073/PNAS.93.19.10078>
 306. Pandey N, Vinod PK (2018) Mathematical modelling of reversible transition between quiescence and proliferation. *PLoS One* 13:e0198420. <https://doi.org/10.1371/JOURNAL.PONE.0198420>
 307. Moldoveanu T, Hosfield CM, Lim D, et al (2002) A Ca²⁺ switch aligns the active site of calpain. *Cell* 108:649–660. [https://doi.org/10.1016/S0092-8674\(02\)00659-1](https://doi.org/10.1016/S0092-8674(02)00659-1)
 308. Xu M, Zhang D-F, Luo R, et al (2018) A systematic integrated analysis of brain expression profiles reveals YAP1 and other prioritized hub genes as important upstream regulators in Alzheimer’s disease. *Alzheimer’s Dement* 14:215–229. <https://doi.org/10.1016/J.JALZ.2017.08.012>
 309. Zhang D-F, Fan Y, Xu M, et al (2019) Complement C7 is a novel risk gene for Alzheimer’s disease in Han Chinese. *Natl Sci Rev* 6:257–274. <https://doi.org/10.1093/nsr/nwy127>
 310. Edgar R, Domrachev M, Lash AE (2002) Gene Expression Omnibus: NCBI gene expression and hybridization array data repository. *Nucleic Acids Res* 30:207–210. <https://doi.org/10.1093/NAR/30.1.207>
 311. Barrett T, Wilhite SE, Ledoux P, et al (2013) NCBI GEO: archive for functional

- genomics data sets—update. *Nucleic Acids Res* 41:D991–D995. <https://doi.org/10.1093/NAR/GKS1193>
312. Blalock EM, Geddes JW, Chen KC, et al (2004) Incipient Alzheimer’s disease: Microarray correlation analyses reveal major transcriptional and tumor suppressor responses. *Proc Natl Acad Sci* 101:2173–2178. <https://doi.org/10.1073/pnas.0308512100>
 313. Patel H, Hodges AK, Curtis C, et al (2019) Transcriptomic analysis of probable asymptomatic and symptomatic alzheimer brains. *Brain Behav Immun* 80:644–656. <https://doi.org/10.1016/J.BBI.2019.05.009>
 314. Sean D, Meltzer PS (2007) GEOquery: A bridge between the Gene Expression Omnibus (GEO) and BioConductor. *Bioinformatics* 23:1846–1847. <https://doi.org/10.1093/bioinformatics/btm254>
 315. Castanho I, Murray TK, Hannon E, et al (2020) Transcriptional Signatures of Tau and Amyloid Neuropathology. *Cell Rep* 30:2040–2054.e5. <https://doi.org/10.1016/J.CELREP.2020.01.063>
 316. Benfeitas R, Bidkhorji G, Mukhopadhyay B, et al (2019) Characterization of heterogeneous redox responses in hepatocellular carcinoma patients using network analysis. *EBioMedicine* 40:471–487. <https://doi.org/10.1016/J.EBIOM.2018.12.057>
 317. Mack SC, Singh I, Wang X, et al (2019) Chromatin landscapes reveal developmentally encoded transcriptional states that define human glioblastoma. *J Exp Med* 216:1071–1090. <https://doi.org/10.1084/jem.20190196>
 318. Zhang J, Li H, Yabut O, et al (2010) Cdk5 Suppresses the Neuronal Cell Cycle by Disrupting the E2F1–DP1 Complex. *J Neurosci* 30:5219–5228. <https://doi.org/10.1523/JNEUROSCI.5628-09.2010>
 319. Zhou Y, Gopalakrishnan V, Richardson JS (1996) Actions of Neurotoxic β -Amyloid on Calcium Homeostasis and Viability of PC12 Cells Are Blocked by Antioxidants but Not by Calcium Channel Antagonists. *J Neurochem* 67:1419–1425. <https://doi.org/10.1046/J.1471-4159.1996.67041419.X>
 320. Ekshyyan O, Aw TY (2005) Decreased susceptibility of differentiated PC12 cells to oxidative challenge: Relationship to cellular redox and expression of apoptotic protease activator factor-1. *Cell Death Differ* 12:1066–1077. <https://doi.org/10.1038/sj.cdd.4401650>
 321. Zhu X, Lee H gon, Perry G, Smith MA (2007) Alzheimer disease, the two-hit hypothesis: An update. *Biochim Biophys Acta - Mol Basis Dis* 1772:494–502. <https://doi.org/10.1016/j.bbadis.2006.10.014>
 322. Wu X, Levine AJ (1994) p53 and E2F-1 cooperate to mediate apoptosis. *Proc Natl Acad Sci* 91:3602–3606. <https://doi.org/10.1073/PNAS.91.9.3602>
 323. Walton CC, Zhang W, Patiño-Parrado I, et al (2019) Primary neurons can enter M-phase. *Sci Rep* 9:1–15. <https://doi.org/10.1038/s41598-019-40462-4>
 324. Shats I, Deng M, Davidovich A, et al (2017) Expression level is a key determinant of E2F1-mediated cell fate. *Cell Death Differ* 24:626–637. <https://doi.org/10.1038/cdd.2017.12>
 325. Nandakumar S, Rozich E, Buttitta L (2021) Cell Cycle Re-entry in the Nervous System: From Polyploidy to Neurodegeneration. *Front Cell Dev Biol* 9:1511. <https://doi.org/10.3389/fcell.2021.698661>
 326. Scharfman HE, Chao M V. (2013) The entorhinal cortex and neurotrophin signaling in Alzheimer’s disease and other disorders. *Cogn Neurosci* 4:123–135. <https://doi.org/10.1080/17588928.2013.826184>

327. Maruszak A, Thuret S (2014) Why looking at the whole hippocampus is not enough—a critical role for anteroposterior axis, subfield and activation analyses to enhance predictive value of hippocampal changes for Alzheimer’s disease diagnosis. *Front Cell Neurosci* 8:95. <https://doi.org/10.3389/fncel.2014.00095>
328. Mu Y, Gage FH (2011) Adult hippocampal neurogenesis and its role in Alzheimer’s disease. *Mol Neurodegener* 6:1–9. <https://doi.org/10.1186/1750-1326-6-85>
329. García-Osta A, Dong J, Moreno-Aliaga MJ, Ramirez MJ (2022) p27, The Cell Cycle and Alzheimer’s Disease. *Int J Mol Sci* 23:1211. <https://doi.org/10.3390/ijms23031211>
330. Hooper C, Meimaridou E, Tavassoli M, et al (2007) p53 is upregulated in Alzheimer’s disease and induces tau phosphorylation in HEK293a cells. *Neurosci Lett* 418:34–37. <https://doi.org/10.1016/J.NEULET.2007.03.026>
331. De La Monte SM, Sohn YK, Wands JR (1997) Correlates of p53- and Fas (CD95)-mediated apoptosis in Alzheimer’s disease. *J Neurol Sci* 152:73–83. [https://doi.org/10.1016/S0022-510X\(97\)00131-7](https://doi.org/10.1016/S0022-510X(97)00131-7)
332. Ohyagi Y, Asahara H, Chui D-H, et al (2005) Intracellular A β 42 activates p53 promoter: a pathway to neurodegeneration in Alzheimer’s disease. *FASEB J* 19:1–29. <https://doi.org/10.1096/FJ.04-2637FJE>
333. LaFerla FM, Hall CK, Ngo L, Jay G (1996) Extracellular deposition of beta-amyloid upon p53-dependent neuronal cell death in transgenic mice. *J Clin Invest* 98:1626–1632. <https://doi.org/10.1172/JCI118957>
334. Hradek AC, Lee HP, Siedlak SL, et al (2015) Distinct Chronology of Neuronal Cell Cycle Re-Entry and Tau Pathology in the 3xTg-AD Mouse Model and Alzheimer’s Disease Patients. *J Alzheimer’s Dis* 43:57–65. <https://doi.org/10.3233/JAD-141083>
335. Petersen RB, Nunomura A, Lee HG, et al (2007) Signal transduction cascades associated with oxidative stress in Alzheimer’s disease. *J Alzheimers Dis* 11:143–152. <https://doi.org/10.3233/JAD-2007-11202>
336. Chen Z, Zhong C (2014) Oxidative stress in Alzheimer’s disease. *Neurosci Bull* 2014 302 30:271–281. <https://doi.org/10.1007/S12264-013-1423-Y>
337. Haque MM, Murale DP, Kim YK, Lee JS (2019) Crosstalk between oxidative stress and tauopathy. *Int J Mol Sci* 20:1959. <https://doi.org/10.3390/ijms20081959>
338. Lee HG, Perry G, Moreira PI, et al (2005) Tau phosphorylation in Alzheimer’s disease: Pathogen or protector? *Trends Mol Med* 11:164–169. <https://doi.org/10.1016/j.molmed.2005.02.008>
339. Roe CM, Behrens MI, Xiong C, et al (2005) Alzheimer disease and cancer. *Neurology* 64:895–898. <https://doi.org/10.1212/01.WNL.0000152889.94785.51>
340. Seo J, Park M (2020) Molecular crosstalk between cancer and neurodegenerative diseases. *Cell Mol Life Sci* 77:2659–2680. <https://doi.org/10.1007/s00018-019-03428-3>
341. Halazonetis TD, Gorgoulis VG, Bartek J (2008) An oncogene-induced DNA damage model for cancer development. *Science* 319:1352–1355. <https://doi.org/10.1126/science.1140735>
342. Luo M, Wicha MS (2019) Targeting Cancer Stem Cell Redox Metabolism to Enhance Therapy Responses. *Semin Radiat Oncol* 29:42–54. <https://doi.org/10.1016/J.SEMRADONC.2018.10.003>
343. Greene LA, Liu DX, Troy CM, Biswas SC (2007) Cell cycle molecules define a pathway required for neuron death in development and disease. *Biochim Biophys Acta - Mol Basis Dis* 1772:392–401. <https://doi.org/10.1016/J.BBADIS.2006.12.003>
344. Ding X-L, Husseman J, Tomashevski A, et al (2000) The Cell Cycle Cdc25A Tyrosine

- Phosphatase Is Activated in Degenerating Postmitotic Neurons in Alzheimer's Disease. *Am J Pathol* 157:1983–1990. [https://doi.org/10.1016/S0002-9440\(10\)64837-7](https://doi.org/10.1016/S0002-9440(10)64837-7)
345. Leung JY, Ehmann GL, Giangrande PH, Nevins JR (2008) A role for Myc in facilitating transcription activation by E2F1. *Oncogene* 27:4172–4179. <https://doi.org/10.1038/onc.2008.55>
 346. Brunet A, Datta SR, Greenberg ME (2001) Transcription-dependent and -independent control of neuronal survival by the PI3K–Akt signaling pathway. *Curr Opin Neurobiol* 11:297–305. [https://doi.org/10.1016/S0959-4388\(00\)00211-7](https://doi.org/10.1016/S0959-4388(00)00211-7)
 347. Castedo M, Perfettini JL, Roumier T, Kroemer G (2002) Cyclin-dependent kinase-1: Linking apoptosis to cell cycle and mitotic catastrophe. *Cell Death Differ* 9:1287–1293. <https://doi.org/10.1038/sj.cdd.4401130>
 348. Konishi Y, Lehtinen M, Donovan N, Bonni A (2002) Cdc2 Phosphorylation of BAD Links the Cell Cycle to the Cell Death Machinery. *Mol Cell* 9:1005–1016. [https://doi.org/10.1016/S1097-2765\(02\)00524-5](https://doi.org/10.1016/S1097-2765(02)00524-5)
 349. Yuan Z, Becker EBE, Merlo P, et al (2008) Activation of FOXO1 by Cdk1 in cycling cells and postmitotic neurons. *Science* 319:1665–1668. <https://doi.org/10.1126/science.1152337>
 350. Abbott JJ, Howlett DR, Francis PT, Williams RJ (2008) A β 1–42 modulation of Akt phosphorylation via α 7 nAChR and NMDA receptors. *Neurobiol Aging* 29:992–1001. <https://doi.org/10.1016/J.NEUROBIOLAGING.2007.01.003>
 351. Lee HK, Kumar P, Fu Q, et al (2009) The insulin/Akt signaling pathway is targeted by intracellular β -amyloid. *Mol Biol Cell* 20:1533–1544. <https://doi.org/10.1091/mbc.E08-07-0777>
 352. Kamei H, Saito T, Ozawa M, et al (2007) Suppression of calpain-dependent cleavage of the CDK5 activator p35 to p25 by site-specific phosphorylation. *J Biol Chem* 282:1687–1694. <https://doi.org/10.1074/jbc.M610541200>
 353. Nikhi K, Shah K (2017) The Cdk5-Mcl-1 axis promotes mitochondrial dysfunction and neurodegeneration in a model of Alzheimer's disease. *J Cell Sci* 130:3023–3039. <https://doi.org/10.1242/jcs.205666>
 354. Ippati S, Deng Y, Hoven J van der, et al (2021) Rapid initiation of cell cycle reentry processes protects neurons from amyloid- β toxicity. *Proc Natl Acad Sci* 118:. <https://doi.org/10.1073/PNAS.2011876118>
 355. Kruman II, Wersto RP, Cardozo-Pelaez F, et al (2004) Cell Cycle Activation Linked to Neuronal Cell Death Initiated by DNA Damage. *Neuron* 41:549–561. [https://doi.org/10.1016/S0896-6273\(04\)00017-0](https://doi.org/10.1016/S0896-6273(04)00017-0)
 356. Nathans JF, Cornwell JA, Afifi MM, et al (2021) Cell cycle inertia underlies a bifurcation in cell fates after DNA damage. *Sci Adv* 7:eabe3882. <https://doi.org/10.1126/sciadv.abe3882>
 357. Alberts B, Johnson A, Lewis J et al. (2002) *The Adaptive Immune System*. New York: Garland Science (<https://www.ncbi.nlm.nih.gov/books/NBK21070/>)
 358. Bhat J, Kabelitz D (2020) An introduction to immunology and epigenetics. In: *Epigenetics of the Immune System*. BioMed Central Ltd., pp 1–23
 359. Chaplin DD (2010) Overview of the immune response. *J Allergy Clin Immunol* 125:. <https://doi.org/10.1016/J.JACI.2009.12.980>
 360. Bonilla FA, Oettgen HC (2010) Adaptive immunity. *J Allergy Clin Immunol* 125:. <https://doi.org/10.1016/J.JACI.2009.09.017>
 361. Murphy K, Travers P, Walport M (2009) *Janeway's Immunobiology*, 7th Edition by Kenneth Murphy, Paul Travers, and Mark Walport. *Biochem Mol Biol Educ* 37:134–

134. <https://doi.org/10.1002/BMB.20272>
362. Lewis DA, Ly T (2021) Cell Cycle Entry Control in Naïve and Memory CD8+ T Cells. *Front Cell Dev Biol* 9:2700. <https://doi.org/10.3389/fcell.2021.727441>
363. Chapman NM, Chi H (2018) Hallmarks of T-cell Exit from Quiescence. *Cancer Immunol Res* 6:502–508. <https://doi.org/10.1158/2326-6066.CIR-17-0605>
364. Yoon H, Kim TS, Braciale TJ (2010) The Cell Cycle Time of CD8+ T Cells Responding In Vivo Is Controlled by the Type of Antigenic Stimulus. *PLoS One* 5:e15423. <https://doi.org/10.1371/JOURNAL.PONE.0015423>
365. Jones SM, Kazlauskas A (2001) Growth-factor-dependent mitogenesis requires two distinct phases of signalling. *Nat Cell Biol* 3:165–172. <https://doi.org/10.1038/35055073>
366. Kazlauskas A (2005) The priming/completion paradigm to explain growth factor-dependent cell cycle progression. *Growth Factors* 23:203–210. <https://doi.org/10.1080/08977190500096020>
367. Chaussepied M, Ginsberg D (2004) Transcriptional Regulation of AKT Activation by E2F. *Mol Cell* 16:831–837. <https://doi.org/10.1016/J.MOLCEL.2004.11.003>
368. Traverse S, Seedorf K, Paterson H, et al (1994) EGF triggers neuronal differentiation of PC12 cells that overexpress the EGF receptor. *Curr Biol* 4:694–701. [https://doi.org/10.1016/S0960-9822\(00\)00154-8](https://doi.org/10.1016/S0960-9822(00)00154-8)
369. Sasagawa S, Ozaki YI, Fujita K, Kuroda S (2005) Prediction and validation of the distinct dynamics of transient and sustained ERK activation. *Nat Cell Biol* 7:365–373. <https://doi.org/10.1038/ncb1233>
370. Marqués M, Kumar A, Cortés I, et al (2008) Phosphoinositide 3-Kinases p110 α and p110 β Regulate Cell Cycle Entry, Exhibiting Distinct Activation Kinetics in G 1 Phase. *Mol Cell Biol* 28:2803–2814. <https://doi.org/10.1128/mcb.01786-07>
371. Watanabe M, Moon KD, Vacchio MS, et al (2014) Downmodulation of tumor suppressor p53 by T cell receptor signaling is critical for antigen-specific CD4+ T cell responses. *Immunity* 40:681–691. <https://doi.org/10.1016/j.immuni.2014.04.006>
372. Tan H, Yang K, Li Y, et al (2017) Integrative Proteomics and Phosphoproteomics Profiling Reveals Dynamic Signaling Networks and Bioenergetics Pathways Underlying T Cell Activation. *Immunity* 46:488–503. <https://doi.org/10.1016/j.immuni.2017.02.010>
373. Obst R (2015) The timing of T cell priming and cycling. *Front Immunol* 6:563. <https://doi.org/10.3389/fimmu.2015.00563>
374. Au-Yeung BB, Zikherman J, Mueller JL, et al (2014) A sharp T-cell antigen receptor signaling threshold for T-cell proliferation. *Proc Natl Acad Sci* 111:E3679–E3688. <https://doi.org/10.1073/pnas.1413726111>
375. Zikherman J, Parameswaran R, Weiss A (2012) Endogenous antigen tunes the responsiveness of naive B cells but not T cells. *Nature* 489:160–164. <https://doi.org/10.1038/nature11311>
376. Liao W, Lin JX, Leonard WJ (2013) Interleukin-2 at the crossroads of effector responses, tolerance, and immunotherapy. *Immunity* 38:13–25. <https://doi.org/10.1016/J.IMMUNI.2013.01.004>
377. Damasio MP, Marchingo JM, Spinelli L, et al (2021) Extracellular signal-regulated kinase (ERK) pathway control of CD8+ T cell differentiation. *Biochem J* 478:79–98. <https://doi.org/10.1042/BCJ20200661>
378. Au-Yeung BB, Smith GA, Mueller JL, et al (2017) IL-2 Modulates the TCR Signaling Threshold for CD8 but Not CD4 T Cell Proliferation on a Single-Cell Level. *J*

- Immunol 198:2445–2456. <https://doi.org/10.4049/jimmunol.1601453>
379. Wang R, Dillon CP, Shi LZ, et al (2011) The Transcription Factor Myc Controls Metabolic Reprogramming upon T Lymphocyte Activation. *Immunity* 35:871–882. <https://doi.org/10.1016/j.immuni.2011.09.021>
380. Marchingo JM, Sinclair L V., Howden AJ, Cantrell DA (2020) Quantitative analysis of how myc controls T cell proteomes and metabolic pathways during T cell activation. *Elife* 9:. <https://doi.org/10.7554/eLife.53725>
381. Heinzl S, Binh Giang T, Kan A, et al (2017) A Myc-dependent division timer complements a cell-death timer to regulate T cell and B cell responses. *Nat Immunol* 18:96–103. <https://doi.org/10.1038/ni.3598>
382. Kumar A, Marqués M, Carrera AC (2006) Phosphoinositide 3-kinase activation in late G1 is required for c-Myc stabilization and S phase entry. *Mol Cell Biol* 26:9116–9125. <https://doi.org/10.1128/MCB.00783-06>
383. Sears RC (2004) The life cycle of c-Myc: From synthesis to degradation. *Cell Cycle* 3:1131–1135. <https://doi.org/10.4161/cc.3.9.1145>
384. Wang X, Simeoni L, Lindquist JA, et al (2008) Dynamics of Proximal Signaling Events after TCR/CD8-Mediated Induction of Proliferation or Apoptosis in Mature CD8+ T Cells. *J Immunol* 180:6703–6712. <https://doi.org/10.4049/JIMMUNOL.180.10.6703>
385. Koike T, Yamagishi H, Hatanaka Y, et al (2003) A novel ERK-dependent signaling process that regulates interleukin-2 expression in a late phase of T cell activation. *J Biol Chem* 278:15685–15692. <https://doi.org/10.1074/jbc.M210829200>
386. Patterson AR, Endale M, Lampe K, et al (2018) Gimap5-dependent inactivation of GSK3 β is required for CD4+ T cell homeostasis and prevention of immune pathology. *Nat Commun* 9:1–15. <https://doi.org/10.1038/s41467-018-02897-7>
387. Tsai CC, Tsai CK, Tseng PC, et al (2020) Glycogen Synthase Kinase-3 β Facilitates Cytokine Production in 12-O-Tetradecanoylphorbol-13-Acetate/Ionomycin-Activated Human CD4+ T Lymphocytes. *Cells* 9:1424. <https://doi.org/10.3390/cells9061424>
388. Swamy M, Pathak S, Grzes KM, et al (2016) Glucose and glutamine fuel protein O-GlcNAcylation to control T cell self-renewal and malignancy. *Nat Immunol* 17:712–720. <https://doi.org/10.1038/ni.3439>
389. Kamemura K, Hayes BK, Comer FI, Hart GW (2002) Dynamic Interplay between O-Glycosylation and O-Phosphorylation of Nucleocytoplasmic Proteins Alternative glycosylation/phosphorylation of THR-58, a known mutational hot spot of c-Myc in lymphomas, is regulated by mitogens. *J Biol Chem* 277:19229–19235. <https://doi.org/10.1074/jbc.M201729200>
390. Bennett TJ, Udupa VAV, Turner SJ (2020) Running to stand still: Naive CD8+ T cells actively maintain a program of quiescence. *Int J Mol Sci* 21:1–15. <https://doi.org/10.3390/ijms21249773>
391. Lindsten T, June CH, Thompson CB (1988) Multiple mechanisms regulate c-myc gene expression during normal T cell activation. *EMBO J* 7:2787–2794. <https://doi.org/10.1002/j.1460-2075.1988.tb03133.x>
392. Buckley AF, Kuo CT, Leiden JM (2001) Transcription factor LKLF is sufficient to program T cell quiescence via a c-Myc-dependent pathway. *Nat Immunol* 2:698–704. <https://doi.org/10.1038/90633>
393. Bhattacharyya ND, Feng CG (2020) Regulation of T Helper Cell Fate by TCR Signal Strength. *Front Immunol* 11:624. <https://doi.org/10.3389/fimmu.2020.00624>
394. Howden AJM, Hukelmann JL, Brenes A, et al (2019) Quantitative analysis of T cell

- proteomes and environmental sensors during T cell differentiation. *Nat Immunol* 20:1542–1554. <https://doi.org/10.1038/s41590-019-0495-x>
395. Wang X, Arceci A, Bird K, et al (2017) VprBP/DCAF1 Regulates the Degradation and Nonproteolytic Activation of the Cell Cycle Transcription Factor FoxM1. *Mol Cell Biol* 37:. <https://doi.org/10.1128/mcb.00609-16>
 396. Schabla NM, Mondal K, Swanson PC (2019) DCAF1 (VprBP): emerging physiological roles for a unique dual-service E3 ubiquitin ligase substrate receptor. *J Mol Cell Biol* 11:725–735. <https://doi.org/10.1093/JMCB/MJY085>
 397. Guo Z, Kong Q, Liu C, et al (2016) DCAF1 controls T-cell function via p53-dependent and -independent mechanisms. *Nat Commun* 7:1–13. <https://doi.org/10.1038/ncomms10307>
 398. Mohamed WI, Schenk AD, Kempf G, et al (2021) The CRL4DCAF1 cullin-RING ubiquitin ligase is activated following a switch in oligomerization state. *EMBO J* 40:e108008. <https://doi.org/10.15252/EMBJ.2021108008>
 399. Marchingo JM, Cantrell DA (2022) Protein synthesis, degradation, and energy metabolism in T cell immunity. *Cell Mol Immunol* 19:303–315. <https://doi.org/10.1038/s41423-021-00792-8>
 400. Metur SP, Klionsky DJ (2021) Adaptive immunity at the crossroads of autophagy and metabolism. *Cell Mol Immunol* 18:1096–1105. <https://doi.org/10.1038/s41423-021-00662-3>
 401. Sinclair L V., Rolf J, Emslie E, et al (2013) Control of amino-acid transport by antigen receptors coordinates the metabolic reprogramming essential for T cell differentiation. *Nat Immunol* 14:500–508. <https://doi.org/10.1038/ni.2556>
 402. Nakaya M, Xiao Y, Zhou X, et al (2014) Inflammatory T cell responses rely on amino acid transporter ASCT2 facilitation of glutamine uptake and mTORC1 kinase activation. *Immunity* 40:692–705. <https://doi.org/10.1016/j.immuni.2014.04.007>
 403. Nachef M, Ali AK, Almutairi SM, Lee SH (2021) Targeting SLC1A5 and SLC3A2/SLC7A5 as a Potential Strategy to Strengthen Anti-Tumor Immunity in the Tumor Microenvironment. *Front Immunol* 12:1311. <https://doi.org/10.3389/fimmu.2021.624324>
 404. Wang W, Zou W (2020) Amino Acids and Their Transporters in T Cell Immunity and Cancer Therapy. *Mol Cell* 80:384–395. <https://doi.org/10.1016/J.MOLCEL.2020.09.006>
 405. Schaub FX, Dhankani V, Berger AC, et al (2018) Pan-cancer Alterations of the MYC Oncogene and Its Proximal Network across the Cancer Genome Atlas. *Cell Syst* 6:271-281.e7. <https://doi.org/https://doi.org/10.1016/j.cels.2018.03.003>
 406. Foulds KE, Zenewicz LA, Shedlock DJ, et al (2002) Cutting Edge: CD4 and CD8 T Cells Are Intrinsically Different in Their Proliferative Responses. *J Immunol* 168:1528–1532. <https://doi.org/10.4049/JIMMUNOL.168.4.1528>
 407. Mishima T, Fukaya S, Toda S, et al (2017) Rapid G0/1 transition and cell cycle progression in CD8+ T cells compared to CD4+ T cells following in vitro stimulation. *Microbiol Immunol* 61:168–175. <https://doi.org/10.1111/1348-0421.12479>
 408. Smith GA, Taunton J, Weiss A (2017) IL-2R β abundance differentially tunes IL-2 signaling dynamics in CD4 + and CD8 + T cells. *Sci Signal* 10:. <https://doi.org/10.1126/SCISIGNAL.AAN4931>
 409. Preston GC, Sinclair L V, Kaskar A, et al (2015) Single cell tuning of Myc expression by antigen receptor signal strength and interleukin-2 in T lymphocytes. *EMBO J* 34:2008–2024. <https://doi.org/10.15252/EMBJ.201490252>

410. Kelly B, Pearce EL (2020) Amino Assets: How Amino Acids Support Immunity. *Cell Metab* 32:154–175. <https://doi.org/10.1016/J.CMET.2020.06.010>
411. Wolf T, Jin W, Zoppi G, et al (2020) Dynamics in protein translation sustaining T cell preparedness. *Nat Immunol* 21:927–937. <https://doi.org/10.1038/s41590-020-0714-5>
412. Seder RA, Ahmed R (2003) Similarities and differences in CD4+ and CD8+ effector and memory T cell generation. *Nat Immunol* 4:835–842. <https://doi.org/10.1038/ni969>
413. Demers KR, Reuter MA, Betts MR (2013) CD8+ T-cell effector function and transcriptional regulation during HIV pathogenesis. *Immunol Rev* 254:190–206. <https://doi.org/10.1111/IMR.12069>
414. O’Garra A (1998) Cytokines induce the development of functionally heterogeneous T helper cell subsets. *Immunity* 8:275–283. [https://doi.org/10.1016/S1074-7613\(00\)80533-6](https://doi.org/10.1016/S1074-7613(00)80533-6)
415. Murphy KM, Ouyang W, Farrar JD, et al (2000) Signaling and transcription in T helper development. *Annu Rev Immunol* 18:451–494. <https://doi.org/10.1146/annurev.immunol.18.1.451>
416. Kaech SM, Ahmed R (2001) Memory CD8+ T cell differentiation: Initial antigen encounter triggers a developmental program in naïve cells. *Nat Immunol* 2:415–422. <https://doi.org/10.1038/87720>
417. Wherry EJ, Ahmed R (2004) Memory CD8 T-Cell Differentiation during Viral Infection. *J Virol* 78:5535–5545. <https://doi.org/10.1128/jvi.78.11.5535-5545.2004>
418. Ananieva EA, Powell JD, Hutson SM (2016) Leucine Metabolism in T Cell Activation: mTOR Signaling and Beyond. *Adv Nutr* 7:798S-805S. <https://doi.org/10.3945/AN.115.011221>
419. Sinclair L V., Howden AJM, Brenes A, et al (2019) Antigen receptor control of methionine metabolism in T cells. *Elife* 8:. <https://doi.org/10.7554/ELIFE.44210>
420. Yang K, Shrestha S, Zeng H, et al (2013) T Cell Exit from Quiescence and Differentiation into Th2 Cells Depend on Raptor-mTORC1-Mediated Metabolic Reprogramming. *Immunity* 39:1043–1056. <https://doi.org/10.1016/j.immuni.2013.09.015>
421. Werlen G, Jain R, Jacinto E (2021) MTOR Signaling and Metabolism in Early T Cell Development. *Genes (Basel)* 12:728. <https://doi.org/10.3390/genes12050728>
422. Dejure FR, Royle N, Herold S, et al (2017) The MYC mRNA 3’-UTR couples RNA polymerase II function to glutamine and ribonucleotide levels. *EMBO J* 36:1854–1868. <https://doi.org/10.15252/EMBJ.201796662>

APPENDIX A

Model details of quiescence to proliferation reversible transition

$\frac{d[Myc]}{dt} = k_{sm} * [S] - k_{dm} * [Myc]$	1
$\frac{d[CycD_T]}{dt} = k_{scycdm} * [Myc] + k_{scycds} * [S] - k_{dcycd} * [CycD_T]$	2
$\frac{d[CycE_T]}{dt} = k_{scyceb} + k_{scycem} * [Myc] + k_{scyce} * \frac{[E2F]}{(k_{ms} + [E2F])} - (k_{dcyce} + k_{dcycea} * [CycA]) * [CycE_T]$	3
$\frac{d[CycA_T]}{dt} = k_{scyca} * \frac{[E2F]}{(k_{msa} + [E2F])} - (k_{dcyca} + k_{dcycac} * [Cdh1]) * [CycA_T]$	4
$\frac{d[E2F_T]}{dt} = k_{se2fb} + k_{se2fm} * [Myc] + k_{se2f} * \frac{[E2F]}{(k_{me2f} + [E2F])} - (k_{de2f} + k_{de2fa} * [CycA]) * [E2F_T]$	5
$\frac{d[Comp1]}{dt} = k_{as1} * [E2F] * [Rb] + k_{rbdp} * [PP2A] * \frac{[Comp2]}{(k_{mpp} + [Comp2])} - k_{dis} * [Comp1] - k_{rbp} * [CycD] * \frac{[Comp1]}{(k_{md} + [Comp1])} - k_{rbp2} * ([CycE] + [CycA]) * \frac{[Comp1]}{(k_{md2} + [Comp1])} - (k_{de2f} + k_{de2fa} * [CycA]) * [Comp1]$	6
$\frac{d[Comp2]}{dt} = k_{as1} * [E2F] * [Rbp] + k_{rbp} * [CycD] * \frac{[Comp1]}{(k_{md} + [Comp1])} - k_{dis} * [Comp2] - k_{rbdp} * [PP2A] * \frac{[Comp2]}{(k_{mpp} + [Comp2])} - k_{rbpp} * ([CycE] + [CycA]) * \frac{[Comp2]}{(k_{me} + [Comp2])} - (k_{de2f} + k_{de2fa} * [CycA]) * [Comp2]$	7
$\frac{d[Rbp]}{dt} = k_{rbp} * [CycD] * \frac{[Rb]}{(k_{md} + [Rb])} + k_{dis} * [Comp2] - k_{as1} * [E2F] * [Rbp] - k_{rbdp} * [PP2A] * \frac{[Rbp]}{(k_{mpp} + [Rbp])} - k_{rbpp} * ([CycE] + [CycA]) * \frac{[Rbp]}{(k_{me} + [Rbp])} - (k_{de2f} + k_{de2fa} * [CycA]) * [Comp2]$	8
$\frac{d[Rbpp]}{dt} = k_{rbpp} * ([CycE] + [CycA]) * \frac{[Rbp]}{(k_{me} + [Rbp])} + k_{rbpp} * ([CycE] + [CycA]) * \frac{[Comp2]}{(k_{me} + [Comp2])} + k_{rbp2} * ([CycE] + [CycA]) * \frac{[Rb]}{(k_{md2} + [Rb])} + k_{rbp2} * ([CycE] + [CycA]) * \frac{[Comp1]}{(k_{md2} + [Comp1])} - k_{rbdp} * [PP2A] * \frac{[Rbpp]}{(k_{mpp} + [Rbpp])}$	9

$\frac{d[Cki_T]}{dt} = k_{scki} - (k_{acki} + k_{ackic} * ([CycE] + [CycA]) * [Ubl]) * [Cki_T]$	10
$\frac{d[CycEcki]}{dt} = k_{ascki} * [CycE] * ([Cki_T] - [CycEcki] - [CycDcki] - [CycACKi]) - (k_{discki} + k_{dcyce} + k_{dcycea} * [CycA] + k_{acki} + k_{ackic} * ([CycE] + [CycA]) * [Ubl]) * [CycEcki]$	11
$\frac{d[CycACKi]}{dt} = k_{ascki} * [CycA] * ([Cki_T] - [CycEcki] - [CycDcki] - [CycACKi]) - (k_{discki} + (k_{dcyca} + k_{dcyac} * [Cdh1]) + k_{acki} + k_{ackic} * ([CycE] + [CycA]) * [Ubl]) * [CycACKi]$	12
$\frac{d[CycDcki]}{dt} = k_{ascki} * [CycD] * ([Cki_T] - [CycEcki] - [CycDcki] - [CycACKi]) - (k_{discki} + k_{dcycd} + k_{dcki} + k_{ackic} * ([CycE] + [CycA]) * [Ubl]) * [CycDcki]$	13
$\frac{d[Cdh1dp]}{dt} = k_{acdh1} * \frac{([Cdh1_T] - [Cdh1dp])}{(k_{m1cdh} + ([Cdh1_T] - [Cdh1dp]))} - (k_{icdh1e} * [CycE] + k_{icdh1a} * [CycA]) * \frac{[Cdh1dp]}{(k_{m2cdh} + [Cdh1dp])}$	14
$\frac{d[Emi1_T]}{dt} = k_{semi1} * \frac{[E2F]}{(k_{memi} + [E2F])} - (k_{demi1} + k_{demi1c} * [Cdh1]) * [Emi1_T]$	15
$\frac{d[EmiC]}{dt} = k_{asec} * ([Cdh1_T] - [EmiC]) * ([Emi1_T] - [EmiC]) - (k_{diec} + k_{demi1} + k_{demi1c} * [Cdh1]) * [EmiC]$	16
$\frac{d[Cdh1]}{dt} = k_{acdh1} * \frac{([Cdh1_T] - [EmiC] - [Cdh1])}{(k_{m1cdh} + ([Cdh1_T] - [Cdh1dp]))} + (k_{diec} + k_{demi1} + k_{demi1c} * [Cdh1]) * ([Cdh1dp] - [Cdh1]) - (k_{icdh1e} * [CycE] + k_{icdh1a} * [CycA]) * \frac{[Cdh1]}{(k_{m2cdh} + [Cdh1dp])} - k_{asec} * [Cdh1] * ([Emi1_T] - [EmiC])$	17
$\frac{d[Ubl]}{dt} = k_{subl} - (k_{dubl} + k_{dublc} * [Cdh1]) * [Ubl]$	18

Algebraic Equations

$[E2F] = [E2F_T] - [Comp1] - [Comp2]$	19
$[Rb] = [Rb_T] - [Rbp] - [Rbpp] - [Comp1] - [Comp2]$	20
$[CycE] = [CycE_T] - [CycEcki]$	21
$[CycD] = [CycD_T] - [CycDcki]$	22
$[CycA] = [CycA_T] - [CycACKi]$	23
$[Cdh1^P] = [Cdh1_T] - [Cdh1] - [EmiC]$	24

Model parameter description

Symbol	Description	Value
S	Mitogen level	1
k_{sm}	Rate constant of Myc synthesis driven by Mitogen	0.1min ⁻¹
k_{dm}	Rate constant of Myc degradation	0.1min ⁻¹
k_{scycdm}	Rate constant of Cyclin D synthesis driven by Myc	0.004min ⁻¹
k_{scycds}	Rate constant of Cyclin D synthesis driven by Mitogen	0.004min ⁻¹
k_{dcycd}	Rate constant of Cyclin D degradation	0.008min ⁻¹
k_{scyceb}	Rate constant of basal(constitutive) Cyclin E synthesis	0.0001min ⁻¹

k_{scycem}	Rate constant of Cyclin E synthesis driven by Myc	0.0005min ⁻¹
k_{scyce}	Rate constant of Cyclin E synthesis driven by E2F	0.004min ⁻¹
k_{dcyce}	Rate constant of Cyclin E degradation	0.001min ⁻¹
k_{dcycea}	Rate constant of Cyclin E degradation driven by Cyclin A	0.01min ⁻¹
k_{ms}	Activation coefficient of E2F for Cyclin E synthesis	0.25
k_{scyca}	Rate constant of Cyclin A synthesis driven by E2F	0.008min ⁻¹
k_{dcyca}	Rate constant of Cyclin A degradation	0.004min ⁻¹
k_{dcycac}	Rate constant of Cyclin A degradation driven by APC/C-Cdh1	0.5min ⁻¹
k_{msa}	Activation coefficient of E2F for Cyclin A synthesis	0.1
k_{se2fb}	Rate constant of basal(constitutive) E2F synthesis	0.0003min ⁻¹
k_{se2fm}	Rate constant of E2F synthesis driven by Myc	0.0015min ⁻¹
k_{se2f}	Rate constant of auto-regulated E2F synthesis	0.004min ⁻¹
k_{de2f}	Rate constant of E2F degradation	0.003min ⁻¹
k_{de2fa}	Rate constant of E2F degradation driven by Cyclin A	0.01min ⁻¹
k_{me2f}	Activation coefficient of E2F for its synthesis	0.25
Rb_T	Total concentration of Rb	1
$PP2A$	Total concentration of PP2A	1
k_{as1}	Association rate constant of E2F and dephosphorylated Rb, E2F and mono-phosphorylated Rb	100min ⁻¹
k_{dis}	Dissociation rate constant of Comp1 and Comp2	1min ⁻¹
k_{rbp}	Phosphorylation rate constant of Rb/Comp1 by Cyclin D-Cdk4/6	5min ⁻¹
k_{rbdp}	Dephosphorylation rate constant of mono-phosphorylated Rb/Comp2 by phosphatase (PP2A)	1min ⁻¹
$k_{rbpp'}$	Phosphorylation rate constant of Rb/Comp1 by Cyclin E-Cdk2	0.5min ⁻¹
k_{rbdpp}	Dephosphorylation rate constant of hyper-phosphorylated Rb by phosphatase (PP2A)	0.1min ⁻¹
k_{rbpp}	Phosphorylation rate constant of mono-phosphorylated Rb/Comp2 by Cyclin E-Cdk2	2min ⁻¹
k_{md}	Michaelis constant for Rb/Comp1 mono-phosphorylation	0.01
k_{me}	Michaelis constant for mono-phosphorylated Rb/Comp2 hyper-phosphorylation	0.05
k_{mpp}	Michaelis constant for mono-phosphorylated Rb/Comp2/hyper-phosphorylated Rb dephosphorylation	0.05
k_{md2}	Michaelis constant for Rb/Comp1 hyper-phosphorylation	0.5
k_{scki}	Rate constant of basal(constitutive) CKI synthesis	0.04min ⁻¹
k_{dcki}	Rate constant of CKI degradation	0.2min ⁻¹
k_{dckic}	Rate constant of CKI degradation driven by ubiquitin ligase	1min ⁻¹
k_{ascki}	Association rate constant of CKI and Cdk	100min ⁻¹
k_{discki}	Dissociation rate constant of CKI-Cdk complex	0.1min ⁻¹
k_{subl}	Rate constant of basal(constitutive) ubiquitin ligase synthesis	0.004min ⁻¹
k_{dubl}	Rate constant of ubiquitin ligase degradation	0.002min ⁻¹
k_{dubl}	Rate constant of ubiquitin ligase degradation driven by APC/C-Cdh1	0.2min ⁻¹
k_{semi1}	Rate constant of Emi1 synthesis driven by E2F	0.45min ⁻¹
k_{demi1}	Rate constant of Emi1 degradation	0.2min ⁻¹
k_{demi1c}	Rate constant of Emi1 degradation driven by APC/C-Cdh1	2min ⁻¹
k_{memi}	Activation coefficient of E2F for Emi1 synthesis	0.1
k_{asec}	Association rate constant of Emi1 and APC/C-Cdh1	100min ⁻¹
k_{diec}	Dissociation rate constant of Emi1-APC/C-Cdh1 complex	0.1min ⁻¹
$Cdh1_T$	Total concentration of APC/C-Cdh1	1
k_{acdh1}	Rate constant for activation of APC/C-Cdh1 by dephosphorylation	0.1min ⁻¹
k_{icdh1e}	Rate constant for inactivation of APC/C-Cdh1 by Cyclin E-Cdk2-dependent phosphorylation	0.14min ⁻¹
k_{icdh1a}	Rate constant for inactivation of APC/C-Cdh1 by Cyclin A-Cdk2-dependent phosphorylation	0.2min ⁻¹
k_{m1cdh}	Michaelis constant for APC/C-Cdh1 dephosphorylation	0.02

k_{m2cdh}	Michaelis constant for APC/C-Cdh1 phosphorylation	0.25
-------------	---	------

Dynamic variable description

Symbol	Description	Initial Condition
[Myc]	Concentration of Myc	0
[CycD _T]	The total concentration of Cyclin D	0
[CycE _T]	The total concentration of Cyclin E	0.119
[CycA _T]	The total concentration of Cyclin A	0
[E2F _T]	The total concentration of E2F transcription factor	0.106
[Comp1]	Concentration of Rb-E2F complex	0.105
[Comp2]	Concentration of Rbp-E2F complex	0
[Rbp]	Mono-phosphorylated Rb	0
[Rbpp]	Hyper-phosphorylated Rb	0.001
[Cki _T]	The total concentration of Cyclin dependent Kinase (CDK) Inhibitors	0.2
[CycEcki]	Concentration of CycE-Cki complex	0.115
[CycDcki]	Concentration of CycD-Cki complex	0
[Cdh1dp]	The total concentration of APC/C-Cdh1 in dephosphorylated form (includes both free APC/C-Cdh1 and APC/C-Cdh1 bound to Emi1)	1
[Emi1 _T]	The total concentration of Emi1	0.002
[EmiC]	Concentration of Emi1-APC/C-Cdh1 complex (includes both phosphorylated and dephosphorylated APC/C-Cdh1 in complex with Emi1)	0.002
[Cdh1]	Concentration of free, dephosphorylated APC/C-Cdh1	0.998
[Ubl]	The total concentration of Ubiquitin ligases	0.02
[E2F]	Concentration of free E2F	0.001
[Rb]	Concentration of free, dephosphorylated Rb	0.894
[CycE]	Concentration of free CycE	0
[CycD]	Concentration of free CycD	0
[Cdh1 ^P]	Concentration of free, phosphorylated APC/C-Cdh1	0

APPENDIX B

Model details of neurodegeneration (module 1)

$\frac{d[p35_n]}{dt} = k_{disp35} * [p35Cdk5_n] + k_{imp} * [p35_c] - k_{asp35} * [p35_n] * [Cdk5_n] - k_{exp} * [p35_n]$	1
$\frac{d[Cdk5_n]}{dt} = k_{disp35} * [p35Cdk5_n] + k_{imp} * [Cdk5_c] - k_{asp35} * [p35_n] * [Cdk5_n] - k_{exp} * [Cdk5_n]$	2
$\frac{d[p35Cdk5_n]}{dt} = k_{asp35} * [p35_n] * [Cdk5_n] + (k_{dis35ckib} + k_{dis35cki} * [A\beta]) * [p35CdkCKI_n] + k_{imp} * [p35Cdk5_c] - k_{disp35} * [p35Cdk5_n] - k_{asp35cki} * [p35Cdk5_n] * [CKI_n] - k_{exp} * [p35Cdk5_n]$	3
$\frac{d[p35CdkCKI_n]}{dt} = k_{asp35cki} * [p35Cdk5_n] * [CKI_n] - (k_{dis35ckib} + k_{dis35cki} * [A\beta]) * [p35CdkCKI_n]$	4
$\frac{d[p35Cdk5_c]}{dt} = k_{asp35} * [p35_c] * [Cdk5_c] + (k_{dis35ckib} + k_{dis35cki} * [A\beta]) * [p35CdkCKI_c] + k_{exp} * [p35Cdk5_n] - k_{disp35} * [p35Cdk5_c] - k_{asp35cki} * [p35Cdk5_c] * [CKI_c] - k_{imp} * [p35Cdk5_c]$	5
$\frac{d[p35CdkCKI_c]}{dt} = k_{asp35cki} * [p35Cdk5_c] * [CKI_c] - (k_{dis35ckib} + k_{dis35cki} * [A\beta]) * [p35CdkCKI_c]$	6
$\frac{d[CKI_n]}{dt} = k_{impcki} * [CKI_c] + (k_{dis35ckib} + k_{dis35cki} * [A\beta]) * [p35CdkCKI_n] - (k_{expckib} + k_{expcki} * [A\beta]) * [CKI_n] - k_{asp35cki} * [p35Cdk5_n] * [CKI_n]$	7
$\frac{d[Erk_i]}{dt} = k_{ierk} * [p35Cdk5_c] * \frac{[Erk_a]}{([I_{ierk}] + [Erk_a])} - k_{aerk} * \frac{[Erk_i]}{([I_{aerk}] + [Erk_i])}$	8
$\frac{d[CycD_T]}{dt} = k_{scycdb} + k_{scycd} * [Erk_a] - k_{dcycd} * [CycD_T]$	9
$\frac{d[CycDCdk5_c]}{dt} = k_{ascycd} * [CycD] * [Cdk5_c] + k_{discyccki} * [CycDCdkCKI_c] - (k_{discycd} + k_{ascycdcki} * [CKI_c] + k_{dcycd}) * [CycDCdk5_c]$	10
$\frac{d[CycCdkCKI_c]}{dt} = k_{ascycdcki} * [CKI_c] * [CycDCdk5_c] - (k_{discyccki} + k_{dcycd}) * [CycCdkCKI_c]$	11
$[p35_c] = [p35_T] - [p35_n] - [p35Cdk5_n] - [p35CdkCKI_n] - [p35Cdk5_c] - [p35CdkCKI_c]$	12
$[Cdk5_c] = [Cdk5_T] - [Cdk5_n] - [p35Cdk5_n] - [p35CdkCKI_n] - [p35Cdk5_c] - [p35CdkCKI_c] - [CycDCdk5_c] - [CycCdkCKI_c]$	13
$[CKI_c] = [CKI_T] - [CKI_n] - [p35CdkCKI_n] - [p35CdkCKI_c] - [CycCdkCKI_c]$	14
$[Erk_a] = [Erk_T] - [Erk_i]$	15
$[CycD] = [CycD_T] - [CycDCdk5_c] - [CycCdkCKI_c]$	16
$[p35_{nT}] = [p35_n] + [p35Cdk5_n] + [p35CdkCKI_n]$	17

$[p35_{cT}] = [p35_c] + [p35Cdk5_c] + [p35CdkCKI_c]$	18
$[CKI_{nT}] = [CKI_n] + [p35CdkCKI_n]$	19

Parameter description

Symbol	Description	Value
A β	Amyloid beta protein level	Varied
CKI _T	Total concentration of Cdk inhibitor (CDKI)	4
Cdk5 _T	Total concentration of Cdk5	2
p35 _T	Total concentration of p35	2
k_{imp}	Nuclear import rate constant of p35, Cdk5 and p35-Cdk5 complex	0.4time ⁻¹
k_{exp}	Nuclear export rate constant of p35, Cdk5 and p35-Cdk5 complex	10time ⁻¹
k_{asp35}	Association rate constant of p35 and Cdk5	100time ⁻¹
k_{disp35}	Dissociation rate constant of p35-Cdk5 complex	1time ⁻¹
$k_{asp35cki}$	Association rate constant of p35-Cdk5 complex and CDKI	10time ⁻¹
$k_{dis35ckib}$	Dissociation rate constant of p35-Cdk5-CDKI complex	1time ⁻¹
$k_{dis35cki}$	A β driven dissociation rate constant of p35-Cdk5-CDKI complex	10time ⁻¹
k_{impcki}	Nuclear import rate constant of CDKI	10time ⁻¹
$k_{expckib}$	Basal nuclear export rate constant of CDKI	0.01time ⁻¹
k_{expcki}	A β driven nuclear export rate constant of CDKI	10time ⁻¹
Erk _T	Total concentration of ERK	1
k_{ierk}	Rate constant for inactivation of ERK	0.25time ⁻¹
k_{aerk}	Rate constant for activation of ERK	0.1time ⁻¹
J_{ierk}	Michaelis constant for ERK inactivation	0.1
J_{aerk}	Michaelis constant for ERK activation	0.1
k_{scycdb}	Rate constant of basal(constitutive) Cyclin D synthesis	0time ⁻¹
k_{scycd}	Rate constant of Cyclin D synthesis driven by ERK	0.01time ⁻¹
k_{dcycd}	Rate constant of Cyclin D degradation	0.002time ⁻¹
k_{ascycd}	Association rate constant of Cyclin D and Cdk5	10time ⁻¹
$k_{ascycdcki}$	Association rate constant of CycD-Cdk5 and CDKI	10time ⁻¹
$k_{discycd}$	Dissociation rate constant of CycD-Cdk5 complex	0.1time ⁻¹
$k_{discyccki}$	Dissociation rate constant of CycD-Cdk5-CDKI complex	0.1time ⁻¹

Dynamic variable description

Symbol	Description	Initial Condition
$[p35_n]$	Concentration of free nuclear p35	0.016
$[Cdk5_n]$	Concentration of free nuclear Cdk5	0.003
$[p35Cdk5_n]$	Concentration of nuclear p35-Cdk5 complex	0.027
$[p35CdkCKI_n]$	Concentration of nuclear p35-Cdk5-CDKI complex	0.838
$[p35Cdk5_c]$	Concentration of cytoplasmic p35-Cdk5 complex	0.741
$[p35CdkCKI_c]$	Concentration of cytoplasmic p35-Cdk5-CDKI complex	0.023
$[CKI_n]$	Concentration of free nuclear CDKI	3.056
$[Erk_i]$	Concentration of inactive ERK	0.905
$[CycD_T]$	The total concentration of Cyclin D	0.473
$[CycDCdk5_c]$	Concentration of cytoplasmic CycD-Cdk5 complex	0.266
$[CycDCdkCKI_c]$	Concentration of cytoplasmic CycD-Cdk5-CDKI complex	0.08
$[p35_c]$	Concentration of free cytoplasmic p35	0.355
$[Cdk5_c]$	Concentration of free cytoplasmic Cdk5	0.022
$[CKI_c]$	Concentration of free cytoplasmic CDKI	0.003

[<i>Erk_a</i>]	Concentration of active ERK	0.095
[<i>CycD</i>]	Concentration of free Cyclin D	0.127
[<i>p35_{nT}</i>]	Concentration of total nuclear p35	0.881
[<i>p35_{cT}</i>]	Concentration of total cytoplasmic p35	1.119
[<i>CKI_{nT}</i>]	Concentration of total nuclear CDKI	3.894

Model details of neurodegeneration (module 2)

$\frac{d[C]}{dt} = k_{inb} + k_{inab} * [A\beta] + k_{inglu} * [Glu] + k_{inros} * [ROS] - k_{out} * [C]$	20
$\frac{d[Cal]}{dt} = k_{scalb} + k_{scal} * \frac{[C]^{ncc}}{(k_{hcal}^{ncc} + [C]^{ncc})} - k_{dcal} * [Cal]$	21
$\frac{d[p25]}{dt} = k_{sp25} * [Cal] * ([p35_T] - [p25]) - k_{dp25} * [p25]$	22
$\frac{d[Cdh1dp]}{dt} = k_{acdh1} * \frac{[Cdh1p]}{(J_{acdh1} + [Cdh1p])} - k_{icdh1} * ([p25] + [CycB]) * \frac{[Cdh1dp]}{(J_{icdh1} + [Cdh1dp])}$	23
$\frac{d[Gls]}{dt} = k_{sgls} - (k_{dgl} + k_{dglsc} * [Cdh1dp]) * [Gls]$	24
$\frac{d[CycB]}{dt} = k_{scycb} + k_{scyc} * \frac{[E2F]}{(k_{hcyc} + [E2F])} - (k_{dcycb} + k_{dcycbc} * [Cdh1dp]) * [CycB]$	25
$\frac{d[Glu]}{dt} = k_{sglub} + k_{sglu} * [Gls] * [Gln] - k_{dglu} * [Glu]$	26
$\frac{d[ROS]}{dt} = k_{srosb} + k_{srosca} * [C] + k_{srosc} * [CycB] - k_{dros} * [ROS] - k_{igsh} * [ROS] * [GSH]^2$	27
$\frac{d[NADPH]}{dt} = (k_{anadphb} + k_{anadphcdh} * [Cdh1dp]) * ([NADP_T] - [NADPH]) - (k_{inadph} + k_{agsh} * [GSSG]) * [NADPH]$	28
$\frac{d[GSH]}{dt} = 2 * k_{agsh} * [GSSG] * [NADPH] - 2 * k_{igsh} * [ROS] * [GSH]^2$	29
$\frac{d[E2F_T]}{dt} = k_{se2fb} + k_{se2f} * \frac{[E2F]}{(k_{he2f} + [E2F])} - k_{de2f} * [E2F_T]$	30
$\frac{d[Comp1]}{dt} = k_{ase2f} * [E2F] * [Rb] - k_{dise2f} * [Comp1] - k_{pprb} * ([p25] + [CycB]) * \frac{[Comp1]}{(J_{pprb} + [Comp1])} - k_{de2f} * [Comp1]$	31
$\frac{d[Rbpp]}{dt} = k_{pprb} * ([p25] + [CycB]) * \frac{[Rb]}{(J_{pprb} + [Rb])} + k_{pprb} * ([p25] + [CycB]) * \frac{[Comp1]}{(J_{pprb} + [Comp1])} - k_{dprb} * \frac{[Rbpp]}{(J_{dprb} + [Rbpp])}$	32
[<i>Cdh1p</i>] = [<i>Cdh1_T</i>] - [<i>Cdh1dp</i>]	33
[<i>GSSG</i>] = $\frac{([GSH_T] - [GSH])}{2}$	34
[<i>E2F</i>] = [<i>E2F_T</i>] - [<i>Comp1</i>]	35
[<i>Rb</i>] = [<i>Rb_T</i>] - [<i>Comp1</i>] - [<i>Rbpp</i>]	36

Parameter description

Symbol	Description	Value
A β	Amyloid beta protein level	Varied
Cdh1 _T	Total concentration of APC/C-Cdh1	1
GSH _T	Total concentration of Glutathione (GSH)	2
NADP _T	Total concentration of NADP	1
p35 _T	Total concentration of p35	2
k_{inb}	Basal rate constant of Ca ²⁺ influx	0.005time ⁻¹
k_{inab}	A β dependent rate constant of Ca ²⁺ influx	1time ⁻¹
k_{inglu}	Glutamate (Glu) dependent rate constant of Ca ²⁺ influx	0.4time ⁻¹
k_{inros}	Reactive oxygen species (ROS) dependent rate constant of Ca ²⁺ influx	0.3time ⁻¹
k_{out}	Rate constant of Ca ²⁺ efflux	0.5time ⁻¹
k_{scalb}	Basal rate constant of calpain activity regulation	0.001time ⁻¹
k_{scal}	Ca ²⁺ modulated rate constant of calpain activity regulation	0.4time ⁻¹
ncc	Cooperativity of Ca ²⁺ binding to calpain protein	2
k_{hcal}	Half saturation constant of Ca ²⁺ for calpain activity regulation	0.5
k_{dcal}	Rate constant of calpain degradation	0.3time ⁻¹
k_{sp25}	Rate constant of p25 synthesis driven by Calpain activity	0.1time ⁻¹
k_{dp25}	Rate constant of p25 degradation	0.05time ⁻¹
k_{icdh1}	Rate constant for inactivation of APC/C-Cdh1 by CycB, p25	0.1time ⁻¹
J_{icdh1}	Michaelis constant for APC/C-Cdh1 phosphorylation by CycB, p25	0.1
k_{acdh1}	Rate constant for activation of APC/C-Cdh1 by dephosphorylation	0.1time ⁻¹
J_{acdh1}	Michaelis constant for APC/C-Cdh1 dephosphorylation	0.1
k_{sgls}	Rate constant of glutaminase (Gls) synthesis	0.01time ⁻¹
k_{dglg}	Basal rate constant of Gls degradation	0.01time ⁻¹
k_{dglsc}	Rate constant of APC/C-Cdh1 dependent Gls degradation	0.15time ⁻¹
k_{scycb}	Basal rate constant of Cyclin B (CycB) synthesis	0.001time ⁻¹
k_{scyc}	Rate constant of E2F dependent CycB synthesis	0.01time ⁻¹
k_{hcyc}	Half saturation constant of CycB for its synthesis	0.25
k_{dcycb}	Rate constant of CycB degradation	0.01time ⁻¹
k_{dcycbc}	Rate constant of APC/C-Cdh1 dependent CycB degradation	0.1time ⁻¹
k_{sglub}	Basal rate constant of glutamate (Glu) synthesis	0.0001time ⁻¹
k_{sglu}	Rate constant of glutaminase catalysed Glu synthesis	0.01time ⁻¹
k_{dglu}	Rate constant of Glu degradation	0.01time ⁻¹
Gln	Total concentration of glutamine (Gln)	1
k_{srosb}	Rate constant of basal ROS synthesis	0.001time ⁻¹
k_{srosca}	Rate constant of Ca ²⁺ dependent ROS synthesis	0.15time ⁻¹
k_{srosc}	Rate constant of CycB dependent ROS synthesis	0.1time ⁻¹
k_{dros}	Basal rate constant of ROS degradation	0.15time ⁻¹
k_{igsh}	Rate constant of ROS scavenging by GSH	0.5time ⁻¹
k_{agsh}	Rate constant of GSSG reduction to GSH by NADPH	0.5time ⁻¹
$k_{anadphb}$	Basal rate constant of NADPH generation	0.001time ⁻¹
$k_{anadphcdh}$	Rate constant of NADPH generation by APC/C-Cdh1	0.04time ⁻¹
k_{inadph}	Basal rate constant of NADPH inactivation	0.01time ⁻¹
k_{se2fb}	Rate constant of basal (constitutive) E2F synthesis	0.0003time ⁻¹
k_{se2f}	Rate constant of auto-regulated E2F synthesis	0.004time ⁻¹
k_{de2f}	Rate constant of E2F degradation	0.003time ⁻¹
k_{he2f}	Half saturation constant of E2F for its synthesis	0.25
Rb _T	Total concentration of Rb	1

k_{ase2f}	Association rate constant of E2F and Rb	100time^{-1}
k_{dise2f}	Dissociation rate constant of Comp1	1time^{-1}
k_{pprb}	Phosphorylation rate constant of Rb/Comp1 by p25 and CycB	0.25time^{-1}
k_{dprbpb}	Dephosphorylation rate constant of Rbpb	0.1time^{-1}
J_{pprb}	Michaelis constant for hyper-phosphorylation of Rb/Comp1	0.05
J_{dprb}	Michaelis constant for dephosphorylation of Rbpb	0.05

Dynamic variable description

Symbol	Description	Initial Condition
[C]	Concentration of intracellular Ca^{2+} ion	0.072
[Cal]	Concentration of activated calpain	0.031
[p25]	Concentration of p25-Cdk5 complex	0.116
[Cdh1dp]	Concentration of APC/C-Cdh1 in dephosphorylated form	0.987
[Gls]	Concentration of glutaminase enzyme	0.063
[CycB]	Concentration of CycB-Cdk1 complex	0.01
[Glu]	Concentration of glutamate	0.073
[ROS]	Concentration of reactive oxygen species	0.006
[NADPH]	Concentration of NADPH (in the scavenger form)	0.567
[GSH]	Concentration of glutathione in reduced form	1.916
[E2F _T]	The total concentration of E2F transcription factor	0.108
[Comp1]	Concentration of Rb-E2F complex	0.107
[Rbpb]	Concentration of hyper-phosphorylated Rb	0.052
[Cdh1p]	Concentration of APC/C-Cdh1 in phosphorylated form	0.013
[GSSG]	Concentration of glutathione in oxidized form	0.042
[E2F]	Concentration of free E2F transcription factor	0.001
[Rb]	Concentration of free dephosphorylated Rb	0.841

Model details of neurodegeneration (module 3)

$\frac{d[p53_T]}{dt} = k_{sp53} - (k_{dp53p} + k_{dp53pp} * [Mdm2]) * [p53_T]$	37
$\frac{d[p53a_T]}{dt} = k_{ap53} * dnadamage * ([p53_T] - [p53a_T]) - k_{ip53} * [p53a_T] - (k_{dp53p} + k_{dp53pp} * [Mdm2]) * [p53a_T]$	38
$\frac{d[p53_{killer}]}{dt} = k_{kip53} * [p53DINP] * \frac{[p53_{helper}]}{(J_{pp53} + [p53_{helper}])} - k_{kidp53} * \frac{[p53_{killer}]}{(J_{dpp53} + [p53_{killer}])} - (k_{dp53p} + k_{dp53pp} * [Mdm2]) * [p53_{killer}]$	39
$\frac{d[Mdm2_T]}{dt} = k_{smdm2p} + k_{smdm2pp} * [p53_T] - k_{dmdm2} * [Mdm2_T]$	40
$\frac{d[Arf_T]}{dt} = k_{sarfp} + k_{sarfpp} * [E2F] - k_{darf} * [Arf_T]$	41
$\frac{d[ArfMdm]}{dt} = k_{asam} * [Arf] * [Mdm2] - k_{dsam} * [ArfMdm] - k_{dmdm2} * [ArfMdm] - k_{darf} * [ArfMdm]$	42

$\frac{d[p53DINP]}{dt} = k_{sdinp1} + k_{sdinp2} * \frac{[p53_{helper}^3]}{(k_{hdinp}^3 + [p53_{helper}^3])} + k_{sdinp3} * \frac{[p53_{killer}^3]}{(k_{hdinp1}^3 + [p53_{killer}^3])} * \frac{[E2F^3]}{(k_{hdinp2}^3 + [E2F^3])} - k_{adinp} * [p53DINP]$	43
$\frac{d[CycD_T]}{dt} = k_{scycds} * [S] + k_{scycdg} * dnadamage - k_{dcycd} * [CycD_T]$	44
$\frac{d[CycE_T]}{dt} = k_{scyceb} + k_{scyce} * \frac{[E2F]}{(k_{hcyce} + [E2F])} - k_{dcyce} * [CycE_T]$	45
$\frac{d[E2F_T]}{dt} = k_{se2fb} + k_{se2f} * \frac{[E2F]}{(k_{he2f} + [E2F])} - k_{de2f} * k_{de2fdnada} * [E2F_T]$	46
$\frac{d[Comp1]}{dt} = k_{ase2f} * [E2F] * [Rb] + k_{dprbp} * \frac{[Comp2]}{(J_{dprb} + [Comp2])} - k_{dise2f} * [Comp1] - k_{prb} * [CycD] * \frac{[Comp1]}{(J_{prb} + [Comp1])} - k_{pprbcyce} * [CycE] * \frac{[Comp1]}{(J_{pprb} + [Comp1])} - k_{pprb} * [p25] * \frac{[Comp1]}{(J_{pprb} + [Comp1])} - k_{de2f} * k_{de2fdnada} * [Comp1]$	47
$\frac{d[Comp2]}{dt} = k_{ase2f} * [E2F] * [Rbp] + k_{prb} * [CycD] * \frac{[Comp1]}{(J_{prb} + [Comp1])} - k_{dise2f} * [Comp2] - k_{dprbp} * \frac{[Comp2]}{(J_{dprb} + [Comp2])} - k_{prbp} * ([CycE] + [p25]) * \frac{[Comp2]}{(J_{prbp} + [Comp2])} - k_{de2f} * k_{de2fdna} * [Comp2]$	48
$\frac{d[Rbp]}{dt} = k_{prb} * [CycD] * \frac{[Rb]}{(J_{prb} + [Rb])} + k_{dise2f} * [Comp2] + k_{de2f} * k_{de2fdnada} * [Comp2] - k_{ase2f} * [E2F] * [Rbp] - k_{dprbp} * \frac{[Rbp]}{(J_{dprb} + [Rbp])} - k_{prbp} * ([CycE] + [p25]) * \frac{[Rbp]}{(J_{prbp} + [Rbp])}$	49
$\frac{d[Rbpp]}{dt} = k_{prbp} * ([CycE] + [p25]) * \frac{[Rbp]}{(J_{prbp} + [Rbp])} + k_{prbp} * ([CycE] + [p25]) * \frac{[Comp2]}{(J_{prbp} + [Comp2])} + k_{pprbcyce} * [CycE] * \frac{[Rb]}{(J_{pprb} + [Rb])} + k_{pprbcyce} * [CycE] * \frac{[Comp1]}{(J_{pprb} + [Comp1])} + k_{pprb} * [p25] * \frac{[Rb]}{(J_{pprb} + [Rb])} + k_{pprb} * [p25] * \frac{[Comp1]}{(J_{pprb} + [Comp1])} - k_{dprbpp} * \frac{[Rbpp]}{(J_{dprb} + [Rbpp])}$	50
$\frac{d[CKI_T]}{dt} = k_{sckib} + k_{sckip53h} * [p53_{helper}] + k_{sckip53k} * [p53_{killer}] - (k_{dcki} + k_{dckic} * [CycE] * [Ubl]) * [CKI_T]$	51
$\frac{d[CycECKI]}{dt} = k_{ascki} * [CycE] * ([CKI_T] - [CycECKI] - [CycDCKI]) - (k_{discki} + k_{dcyce} + k_{dcki} + k_{dckic} * [CycE] * [Ubl]) * [CycECKI]$	52

$\frac{d[CycDCKI]}{dt} = k_{ascki} * [CycD] * ([CKI_T] - [CycECKI] - [CycDCKI]) - (k_{discki} + k_{acycd} + k_{acki} + k_{ackic} * [CycE] * [Ubl]) * [CycDCKI]$	53
$\frac{d[Ubl]}{dt} = k_{subl} - (k_{dubl} + k_{dublc} * [Cdh1dp]) * [Ubl]$	54
$[E2F] = [E2F_T] - [Comp1] - [Comp2]$	55
$[Rb] = [Rb_T] - [Comp1] - [Comp2] - [Rbp] - [Rbpp]$	56
$[CycE] = [CycE_T] - [CycECKI]$	57
$[CycD] = [CycD_T] - [CycDCKI]$	58
$[Arf] = [Arf_T] - [ArfMdm]$	59
$[Mdm2] = [Mdm2_T] - [ArfMdm]$	60
$[p53_{helper}] = [p53a_T] - [p53_{killer}]$	61
$k_{dp53pp} = \frac{1}{(1 + fac1 * dnadamage)}$	62
$k_{dmdm2} = k_{dmdm2p} + k_{dmdm2pp} * dnadamage$	63
$k_{de2fdnada} = \frac{1}{(1 + fac2 * dnadamage)}$	64

Parameter description

Symbol	Description	Value
dnadamage	Magnitude of DNA damage	Varied
k_{sp53}	Rate constant of constitutive p53 synthesis	0.5time^{-1}
k_{dp53p}	Rate constant of basal p53 degradation	0.1time^{-1}
k_{ap53}	Rate constant of DNA damage driven p53 activation	0.5time^{-1}
k_{jp53}	Rate constant of p53 inactivation	0.05time^{-1}
k_{kip53}	Rate constant of p53 killer activation driven by p53DINP1	0.07time^{-1}
k_{kidp53}	Rate constant of p53 killer inactivation	0.14time^{-1}
J_{pp53}	Michaelis constant for phosphorylation of p53 helper	0.5
J_{dpp53}	Michaelis constant for dephosphorylation of p53 killer	0.1
k_{smdm2p}	Rate constant of constitutive Mdm2 synthesis	0.02time^{-1}
$k_{smdm2pp}$	Rate constant of Mdm2 synthesis driven by p53	0.3time^{-1}
k_{dmdm2p}	Rate constant of basal Mdm2 degradation	0.1time^{-1}
$k_{dmdm2pp}$	Rate constant of Mdm2 degradation driven by DNA damage	1time^{-1}
k_{sarfp}	Rate constant of constitutive Arf synthesis	0.01time^{-1}
k_{sarfpp}	Rate constant of Arf synthesis driven by E2F	0.3time^{-1}
k_{darf}	Rate constant of Arf degradation	0.1time^{-1}
k_{sam}	Association rate constant of Arf and Mdm2	10time^{-1}
k_{dsam}	Dissociation rate constant of Arf-Mdm2 complex	2time^{-1}
k_{sdinp1}	Rate constant of basal (constitutive) p53DINP1 synthesis	0.0006time^{-1}
k_{sdinp2}	Rate constant of p53DINP1 synthesis driven by p53 helper	0.016time^{-1}
k_{sdinp3}	Rate constant of p53DINP1 synthesis driven by p53 killer and E2F	0.1time^{-1}
k_{ddinp}	Rate constant of p53DINP1 degradation	0.01time^{-1}
k_{hdinp}	Half saturation constant of p53 helper for p53DINP1 synthesis	0.5
k_{hdinp1}	Half saturation constant of p53 killer for p53DINP1 synthesis	0.5
k_{hdinp2}	Half saturation constant of E2F for p53DINP1 synthesis	1.2
S	Mitogen level	0
k_{scycds}	Rate constant of Cyclin D(CycD) synthesis driven by Mitogen	0.008time^{-1}
k_{scycdg}	Rate constant of CycD nuclear activity induction driven by DNA damage	0.01time^{-1}

k_{dcycd}	Rate constant of CycD degradation	0.001time^{-1}
k_{scyceb}	Rate constant of basal (constitutive) Cyclin E(CycE) synthesis	0.0002time^{-1}
k_{scyce}	Rate constant of CycE synthesis driven by E2F	0.004time^{-1}
k_{dcyce}	Rate constant of CycE degradation	0.001time^{-1}
k_{hcyce}	Half saturation constant of E2F for CycE synthesis	0.25
k_{se2fb}	Rate constant of basal(constitutive) E2F synthesis	0.0003time^{-1}
k_{se2f}	Rate constant of auto-regulated E2F synthesis	0.004time^{-1}
k_{de2f}	Rate constant of E2F degradation	0.004time^{-1}
k_{he2f}	Half saturation constant of E2F for its synthesis	0.25
[Rb _T]	Total concentration of Rb	1
k_{ase2f}	Association rate constant of E2F and Rb; E2F and Rbp	100time^{-1}
k_{dise2f}	Dissociation rate constant of Comp1 and Comp2	1time^{-1}
k_{prb}	Phosphorylation rate constant of Rb/Comp1 by CycD-Cdk4/6	5time^{-1}
k_{prbp}	Phosphorylation rate constant of Rbp/Comp2 by CycE-Cdk2/p25-Cdk5	2time^{-1}
$k_{pprbcyce}$	Phosphorylation rate constant of Rb/Comp1 by CycE-Cdk2	0.5time^{-1}
k_{pprb}	Phosphorylation rate constant of Rb/Comp1 by p25-Cdk5	0.25time^{-1}
k_{dprbp}	Dephosphorylation rate constant of Rbp/Comp2	1time^{-1}
k_{dprbpb}	Dephosphorylation rate constant of Rbpb	0.1time^{-1}
[p25]	Total concentration of p25	0
J_{prb}	Michaelis constant for phosphorylation of Rb/Comp1	0.01
J_{prbp}	Michaelis constant for hyper-phosphorylation of Rbp/Comp2	0.05
J_{pprb}	Michaelis constant for hyper-phosphorylation of Rb/Comp1	0.05
J_{dprb}	Michaelis constant for dephosphorylation of Rbp/Comp2/Rbpb	0.05
k_{sckib}	Rate constant of basal(constitutive) CDKI synthesis	0.04time^{-1}
$k_{sckip53h}$	Rate constant of CDKI synthesis driven by p53 helper	0.2time^{-1}
$k_{sckip53k}$	Rate constant of CDKI synthesis driven by p53 killer	0time^{-1}
k_{dcki}	Rate constant of basal CDKI degradation	0.2time^{-1}
k_{dckic}	Rate constant of CDKI degradation driven by ubiquitin ligase	1time^{-1}
k_{ascki}	Association rate constant of CKI and Cyclin-Cdk complex	100time^{-1}
k_{discki}	Dissociation rate constant of CDKI-Cyclin-Cdk complex	0.1time^{-1}
fac1	Weighted factor representing effect of DNA damage on p53 stability	0.1
fac2	Weighted factor representing effect of DNA damage on E2F stability	0.3
k_{subl}	Rate constant of basal(constitutive) ubiquitin ligase synthesis	0.004time^{-1}
k_{dubl}	Rate constant of ubiquitin ligase degradation	0.002time^{-1}
k_{dublc}	Rate constant of ubiquitin ligase degradation driven by APC/C-Cdh1	0.2time^{-1}
[Cdh1dp]	Total concentration of dephosphorylated APC/C-Cdh1	1

Dynamic variable description

Symbol	Description	Initial Condition
[p53 _T]	The total concentration of p53	0.374
[p53 _{aT}]	The total concentration of activated p53	0
[p53 _{killer}]	Concentration of p53 killer	0
[Mdm2 _T]	The total concentration of Mdm2	1.323
[Arf _T]	The total concentration of Arf	0.103
[ArfMdm]	Concentration of Arf-Mdm2 complex	0.087

[p53DINP]	Concentration of p53DINP1	0.06
[CycD _T]	The total concentration of Cyclin D(CycD)	0
[CycE _T]	The total concentration of Cyclin E(CycE)	0.216
[E2F _T]	The total concentration of E2F transcription factor	0.079
[Comp1]	Concentration of Rb-E2F complex	0.078
[Comp2]	Concentration of Rbp-E2F complex	0
[Rbp]	Mono-phosphorylated Rb	0
[Rb _{pp}]	Hyper-phosphorylated Rb	0.017
[CKI _T]	The total concentration of cyclin dependent kinase inhibitors (CDKI)	0.2
[CycECKI]	Concentration of CycE-CDKI complex	0.183
[CycDCKI]	Concentration of CycD-CDKI complex	0
[Ubl]	The total concentration of Ubiquitin ligases	0.02
[E2F]	Concentration of free E2F transcription factor	0.001
[Rb]	Concentration of free dephosphorylated Rb	0.905
[CycE]	Concentration of free CycE complex	0.033
[CycD]	Concentration of free CycD complex	0
[Arf]	Concentration of free Arf	0.016
[Mdm2]	Concentration of free Mdm2	1.236
[p53 _{helper}]	Concentration of p53 helper	0

APPENDIX C

Model details of naïve T cell activation on antigen recognition

(Additions to quiescence \leftrightarrow proliferation reversible transition model described in Appendix A)

$\frac{d[Myc]}{dt} = k_{sm} * [TCR] - k_{dm} * [Myc]$	1
$\frac{d[Dcaf1]}{dt} = k_{sdcaf1} * [Myc] - k_{ddcaf1} * [Dcaf1]$	2
$\frac{d[Mdm2]}{dt} = k_{smdm2} * [TCR] - k_{dmdm2} * [Mdm2]$	3
$\frac{d[p53]}{dt} = k_{sp53b} + k_{sp53} * [TCR] - k_{dp53} * [p53] * [Mdm2] * [Dcaf1] - k_{dp53b} * [p53]$	4
$\frac{d[CycD_T]}{dt} = k_{scyedm} * [Myc] + k_{scyeds} * [TCR] - k_{dcycd} * [CycD_T]$	5
$\frac{d[Cki_T]}{dt} = k_{sckib} + k_{scki} * [p53] - (k_{dcki} + k_{dckic} * ([CycE] + [CycA]) * [Ubl]) * [Cki_T]$	6

Model parameter description

Symbol	Description	Value
TCR	Antigen signal strength	1
k_{sm}	Rate constant of Myc synthesis driven by antigen	0.1min^{-1}
k_{dm}	Rate constant of Myc degradation	0.1min^{-1}
k_{sdcaf1}	Rate constant of Dcaf1 synthesis driven by Myc	0.0005min^{-1}
k_{ddcaf1}	Rate constant of Dcaf1 degradation	0.0005min^{-1}
k_{smdm2}	Rate constant of Mdm2 synthesis driven by antigen	0.001min^{-1}
k_{dmdm2}	Rate constant of Mdm2 degradation	0.001min^{-1}
k_{sp53b}	Basal synthesis rate of p53	0.0002min^{-1}
k_{sp53}	Rate constant of p53 synthesis driven by antigen	0.01min^{-1}
k_{dp53b}	Basal rate of p53 degradation	0.002min^{-1}
k_{dp53}	Rate constant of p53 degradation driven by Mdm2 and Dcaf1	0.02min^{-1}
k_{scyedm}	Rate constant of Cyclin D synthesis driven by Myc	0.004min^{-1}
k_{scyeds}	Rate constant of Cyclin D synthesis driven by antigen	0.004min^{-1}
k_{dcycd}	Rate constant of Cyclin D degradation	0.008min^{-1}
k_{sckib}	Rate constant of basal(constitutive) CKI synthesis	0min^{-1}
k_{scki}	Rate constant of p53 driven CKI synthesis	0.2min^{-1}
k_{dcki}	Rate constant of CKI degradation	0.2min^{-1}
k_{dckic}	Rate constant of CKI degradation driven by ubiquitin ligase	1min^{-1}

Dynamic variable description

Symbol	Description	Initial Condition
$[Dcaf1]$	Concentration of Dcaf1	0
$[Mdm2]$	Concentration of Mdm2	0
$[p53]$	Concentration of p53	0.1

Model details of Myc protein stability

$k_{degpro} = d_m * [Myc] + d_{mg} * [MycT58M] + d_{ms} * [MycS62P] + d_{mgs} * [MycS62PT58M] + d_{mt} * [MycT58P] + k_{dgl} * [Gls] + k_{dslc} * [SLC]$	1
$k_{synpro} = (k_{smb} * [TCR] + k_{sgls} * \frac{[Myc_T^n]}{K_{hgls}^n + [Myc_T^n]} + k_{sslc} * \frac{[Myc_T^n]}{K_{hslc}^n + [Myc_T^n]}) * \frac{[aa_{pool}]}{K_{maa} + [aa_{pool}]}$	2
$\frac{d[Myc]}{dt} = k_{smb} * [TCR] * \frac{[aa_{pool}]}{K_{maa} + [aa_{pool}]} + k_{md} * \frac{[MycT58M]}{K_{dmet} + [MycT58M]} - k_{ms} * [Erk] * \frac{[Myc]}{K_{mserk} + [Myc]} - V_{maxn} * \frac{[Met1]}{K_{met} + [Met1]} * \frac{[Myc]}{K_{mgn} + [Myc]} - d_m * [Myc]$	3
$\frac{d[MycT58M]}{dt} = V_{maxn} * \frac{[Met1]}{K_{met} + [Met1]} * \frac{[Myc]}{K_{mgn} + [Myc]} - k_{md} * \frac{[MycT58M]}{K_{dmet} + [MycT58M]} - k_{ms} * [Erk] * \frac{[MycT58M]}{K_{mserk} + [MycT58M]} - d_{mg} * [MycT58M]$	4
$\frac{d[MycS62P]}{dt} = k_{ms} * [Erk] * \frac{[Myc]}{K_{mserk} + [Myc]} + k_{md} * \frac{[MycS62PT58M]}{K_{dmet} + [MycS62PT58M]} - k_{mt} * [Gsk3\beta] * \frac{[MycS62P]}{K_{mtgsk} + [MycS62P]} - V_{max} * \frac{[Met1]}{K_{met} + [Met1]} * \frac{[MycS62P]}{K_{mg} + [MycS62P]} - d_{ms} * [MycS62P]$	5
$\frac{d[MycS62PT58M]}{dt} = V_{max} * \frac{[Met1]}{K_{met} + [Met1]} * \frac{[MycS62P]}{K_{mg} + [MycS62P]} + k_{ms} * [Erk] * \frac{[MycT58M]}{K_{mserk} + [MycT58M]} - k_{md} * \frac{[MycS62PT58M]}{K_{dmet} + [MycS62PT58M]} - d_{mgs}$	6
$\frac{d[MycT58P]}{dt} = k_{mt} * [Gsk3\beta] * \frac{[MycS62P]}{K_{mtgsk} + [MycS62P]} - d_{mt} * [MycT58P]$	7
$\frac{d[AktP]}{dt} = k_{ap} * [Pi3k] * \frac{[Akt]}{K_{appi3k} + [Akt]} - k_{ad} * \frac{[AktP]}{K_{adpp} + [AktP]}$	8
$\frac{d[Gsk3\beta]}{dt} = k_{ga} * \frac{[Gsk3\beta P]}{K_{gdpp} + [Gsk3\beta P]} - k_{gp} * [AktP] * \frac{[Gsk3\beta]}{K_{gpakt} + [Gsk3\beta]}$	9
$\frac{d[Gls]}{dt} = \left(k_{sgls} * \frac{[Myc_T^n]}{K_{hgls}^n + [Myc_T^n]} \right) * \frac{[aa_{pool}]}{K_{maa} + [aa_{pool}]} - k_{dgl} * [Gls]$	10
$\frac{d[Met1]}{dt} = k_{cathex} * [Glucose] * \frac{[aa_{pool}]}{K_{cathexogt} + [aa_{pool}]} - V_{max} * \frac{[Met1]}{K_{met} + [Met1]} * \frac{[MycS62P]}{K_{mg} + [MycS62P]} - V_{maxn} * \frac{[Met1]}{K_{met} + [Met1]} * \frac{[Myc]}{K_{mgn} + [Myc]}$	11

$\frac{d[aa_{pool}]}{dt} = (k_{dpro} + scalefac2 * k_{imp} * [SLC] * [aa_{ext}]) * [TCR] + k_{degpro} - (k_{exp} + k_{daap}) * [aa_{pool}] - k_{synpro} - k_{cat} * [Gls] * \frac{[aa_{pool}]}{K_{catgls} + [aa_{pool}]} - k_{cathex} * [Glucose] * \frac{[aa_{pool}]}{K_{cathexogt} + [aa_{pool}]}$	12
$\frac{d[aa_{ext}]}{dt} = k_{aaex} + scalefac1 * k_{exp} * [aa_{pool}] - (k_{daaex} + k_{imp} * [SLC] * [TCR]) * [aa_{ext}]$	13
$\frac{d[SLC]}{dt} = \left(k_{sslc} * \frac{[Myc_T^n]}{K_{hslc}^n + [Myc_T^n]} \right) * \frac{[aa_{pool}]}{K_{maa} + [aa_{pool}]} - k_{dslc} * [SLC]$	14
$\frac{d[Met2]}{dt} = k_{cat} * [Gls] * \frac{[aa_{pool}]}{K_{catgls} + [aa_{pool}]} - k_{dmet2} * [Met2]$	15
$[Gsk3\beta P] = [Gsk3\beta_T] - [Gsk3\beta]$	16
$[Akt] = [Akt_T] - [AktP]$	17
$[Myc_T] = [Myc] + [MycS62P] + [MycT58P] + [MycT58M] + [MycT58MS62P]$	18
$[Erk] = [Erk_{max}] \text{ for } ((t \leq t1) \text{ OR } (t2 \leq t \leq t3)) \text{ else } [Erk_{residual}]$	19
$[Pi3k] = [Pi3k_{max}] \text{ for } ((t \leq t1) \text{ OR } (t2 \leq t \leq t3)) \text{ else } [Pi3k_{residual}]$	20

Model parameter description

Symbol	Description	Value
TCR	T cell receptor specific antigen level	1
K_{maa}	Activation coefficient of aa_{pool} for protein synthesis	3
K_{appi3k}	Michaelis constant for Akt phosphorylation	0.01
k_{ap}	Rate constant of Akt phosphorylation	360hr ⁻¹
K_{adpp}	Michaelis constant for Akt dephosphorylation	0.01
k_{ad}	Rate constant of Akt dephosphorylation	72hr ⁻¹
K_{gpakt}	Michaelis constant for GSK3 β phosphorylation	0.01
k_{gp}	Rate constant of GSK3 β phosphorylation	360hr ⁻¹
K_{gdpp}	Michaelis constant for GSK3 β dephosphorylation	0.01
k_{gd}	Rate constant of GSK3 β dephosphorylation	72hr ⁻¹
K_{mserk}	Michaelis constant for MycS62 phosphorylation	0.01
k_{ms}	Rate constant of MycS62 phosphorylation	6hr ⁻¹
K_{mtgsk}	Michaelis constant for MycT58 phosphorylation	0.01
k_{mt}	Rate constant of MycT58 phosphorylation	0.6hr ⁻¹
d_m	Rate constant of Myc degradation	2.08hr ⁻¹
d_{mg}	Rate constant of MycT58M degradation	0.3hr ⁻¹
d_{mgs}	Rate constant of MycS62PT58M degradation	0.3hr ⁻¹
d_{ms}	Rate constant of MycS62P degradation	0.3hr ⁻¹
d_{mt}	Rate constant of MycT58P degradation	2.08hr ⁻¹
$t1_{erk}$	Timing of first phase of ERK activation	1
$t2_{erk}$	Timing of second phase of ERK activation	0
$t3_{erk}$	Timing of end of second phase of ERK activation	0
Erk_{max}	Maximum activity of ERK	1
$Erk_{residual}$	Residual activity of ERK	0.1
$t1_{pi3k}$	Timing of first phase of PI3K activation	1
$t2_{pi3k}$	Timing of second phase of PI3K activation	0
$t3_{pi3k}$	Timing of end of second phase of PI3K activation	0

$Pi3k_{max}$	Maximum activity of PI3K	1
$Pi3k_{residual}$	Residual activity of PI3K	0.1
Akt_T	Total concentration of Akt	1
$Gsk3\beta_T$	Total concentration of GSK3 β	1
V_{max}	Rate constant of MycS62P glycosylation	2.5hr ⁻¹
V_{maxn}	Rate constant of Myc glycosylation	0.5hr ⁻¹
k_{md}	Rate constant of Myc deglycosylation	0.1hr ⁻¹
K_{mg}	Michaelis constant for MycS62P glycosylation	0.01
K_{mgn}	Michaelis constant for Myc glycosylation	0.5
K_{dmet}	Michaelis constant for Myc deglycosylation	0.01
K_{met}	Michaelis constant of Met1 for Myc deglycosylation	0.01
n	Cooperativity of Myc binding to target gene promoter	1
k_{hgls}	Activation coefficient for Gls synthesis	0.5
k_{sgls}	Rate constant of Gls synthesis	0.3hr ⁻¹
k_{dgl}	Rate constant of Gls degradation	0.025hr ⁻¹
k_{cat}	Rate constant of glutaminolysis	10hr ⁻¹
K_{catgls}	Michaelis constant for glutaminolysis	0.01
k_{cathex}	Rate constant of glutamine metabolism in hexosamine biosynthesis pathway	1hr ⁻¹
$K_{cathexogt}$	Michaelis constant for glutamine utilization in hexosamine biosynthesis pathway	0.5
Glucose	Glucose level	1
k_{dmet2}	Rate constant of Met2 degradation	1hr ⁻¹
k_{exp}	SLC mediated cytosolic export rate constant of amino acids	1
k_{imp}	SLC mediated cytosolic import rate constant of amino acids	1
k_{smb}	Rate constant of Myc synthesis driven by TCR signaling	5hr ⁻¹
k_{sslc}	Rate constant of SLC synthesis	0.05hr ⁻¹
k_{hslc}	Activation coefficient for SLC synthesis	0.5
k_{dslc}	Rate constant of SLC degradation	0.02hr ⁻¹
k_{dpro}	Rate constant of protein degradation by autophagy	15hr ⁻¹
k_{daap}	Utilization rate constant of amino acids in non-protein components (e.g., nucleotides, GSH etc.)	1hr ⁻¹
k_{aaex}	Basal cytosolic export rate constant of amino acids	100hr ⁻¹
k_{daaex}	Basal cytosolic import rate constant of amino acids	1hr ⁻¹
$scalefac1$	Scaling factor to adjust for cytosol and extra-cellular volume ratio	0.1
$scalefac2$	Scaling factor to adjust for cytosol and extra-cellular volume ratio	1

Dynamic variable description

Symbol	Description	Initial Condition
[Myc]	Concentration of Myc	0
[MycT58M]	Concentration of T58 glycosylated Myc	0
[MycS62P]	Concentration of S62 phosphorylated Myc	0
[MycS62PT58M]	Concentration of S62 phosphorylated T58 glycosylated Myc	0
[MycT58P]	Concentration of T58 phosphorylated Myc	0
[AktP]	Concentration of phosphorylated Akt	0.01
[Gsk3 β]	Concentration of unphosphorylated Gsk3 β	1
[Gls]	Concentration of Gls	0
[Met1]	Concentration of Met1	0
[aa _{pool}]	Concentration of amino acids in cytosol	0
[aa _{ext}]	Concentration of amino acids in extra-cellular space	100
[SLC]	Concentration of SLC	0
[Met2]	Concentration of Met2	0
[Myc _T]	The total concentration of Myc	0

[Akt]	Concentration of unphosphorylated Akt	0.99
[Gsk3βP]	Concentration of phosphorylated <i>Gsk3β</i>	0

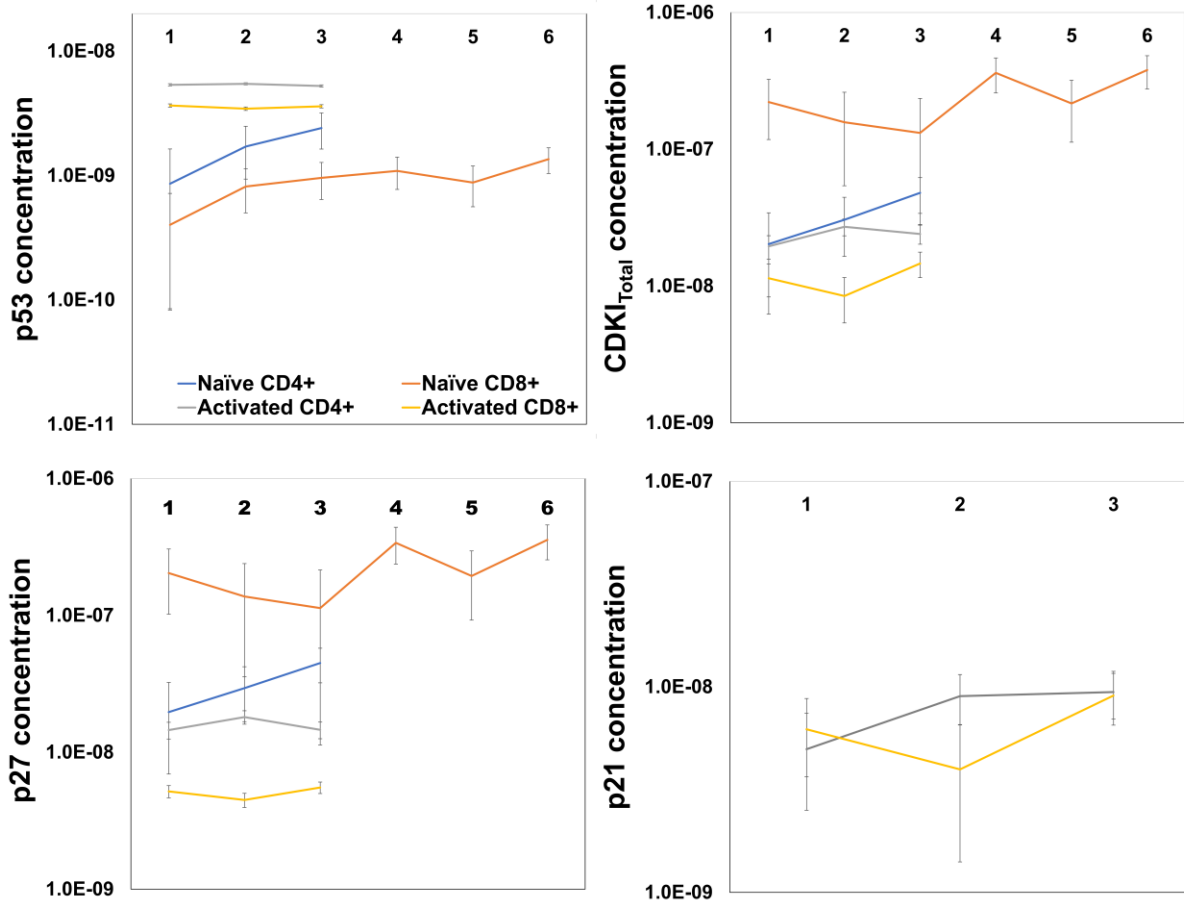


Figure S1: Protein concentration data [380] of cell cycle inhibitors was used for CD4⁺ and CD8⁺ T cells comparison. Y axis represents concentration measured in $\mu\text{g}/\text{million cells}$; numbers along X axis represent the biological replicates. Error bars denote the standard deviation across replicates, data linked to figure 5.7.

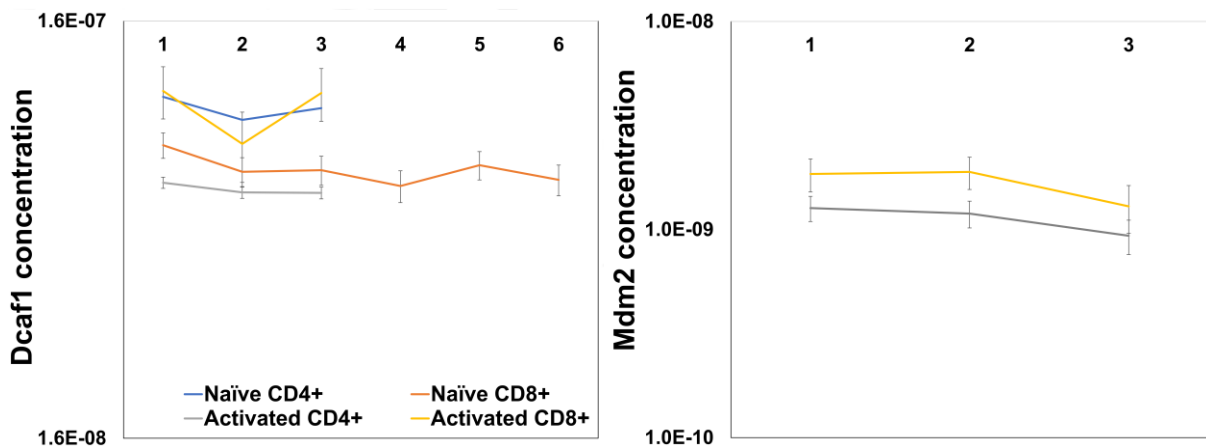


Figure S2: Protein concentration data [380] of cell cycle activators that regulate anti-proliferative response dynamics was used for CD4⁺ and CD8⁺ T cells comparison. Y axis represents concentration measured in $\mu\text{g}/\text{million cells}$; numbers along X axis represent the biological replicates. Error bars denote the standard deviation across replicates, data linked to figure 5.7.

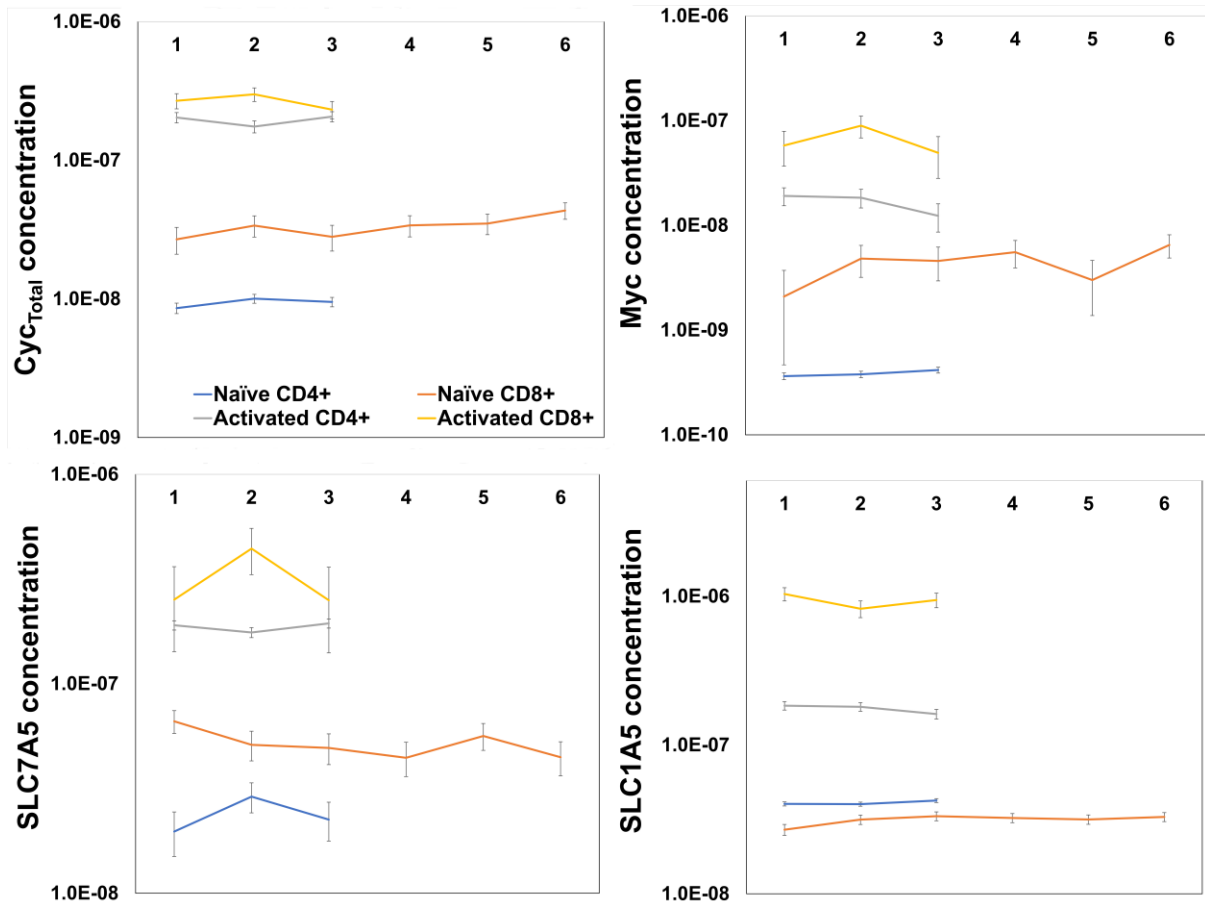


Figure S3: Protein concentration data of Myc and its targets [380] was used for CD4⁺ and CD8⁺ T cells comparison. Y axis represents concentration measured in $\mu\text{g}/\text{million cells}$; X axis represents the biological replicates. Error bars denote the standard deviation across biological replicates, data linked to figure 5.7.